Functional Block Molecules with Nanoscale Order

Functional Block Molecules with Nanoscale Order

PROEFSCHRIFT

ter verkrijging van de graad van doctor aan de Technische Universiteit Eindhoven,
op gezag van de rector magnificus prof.dr.ir. F.P.T. Baaijens,
voor een commissie aangewezen door het College voor Promoties,
in het openbaar te verdedigen op vrijdag 24 februari 2023 om 16:00 uur

door

Martinus Henricus Cornelius van Son

geboren te Eindhoven

Dit proefschrift is goedgekeurd door de promotoren en de samenstelling van de promotiecommissie is als volgt:

Voorzitter:	prof. dr. J.A.M. Kuipers
1e Promotor:	prof. dr. E.W. Meijer
Copromotor:	dr. G.M.E. Vantomme
Leden:	prof. dr. ir. A.R.A. Palmans
	prof. dr. J. Gómez Rivas
	prof. dr. L.M. Campos (University of Columbia)
	dr. S.C.J. Meskers
Advisor:	dr. F.R. Eisenreich

Het onderzoek dat in dit proefschrift wordt beschreven is uitgevoerd in overeenstemming met de TU/e gedragscode voor wetenschapsbeoefening.

It is music and dancing that make me at peace with the world

- Nelson Mandela

Cover design: Martin van Son
Printed by: Ridderprint – the Netherlands

A catalogue record is available from the Eindhoven University of Technology Library
ISBN: 978-90-386-5670-0

This work has been financially supported by the Dutch Ministry of Education, Culture and Science (Gravitation program 024.001.035) and NWO (TOP-PUNT Grant 10018944).

Table of Contents

Chapter 3
The influence of block molecule co-assembly on their optical properties

Chapter 4
Highly ordered supramolecular materials of phase-separated block molecules for long-range exciton transport

Chapter 5
Highly ordered 2D-assemblies of phase-separated block molecules for upconverted, linearly polarized emission

Chapter 6
Epilogue

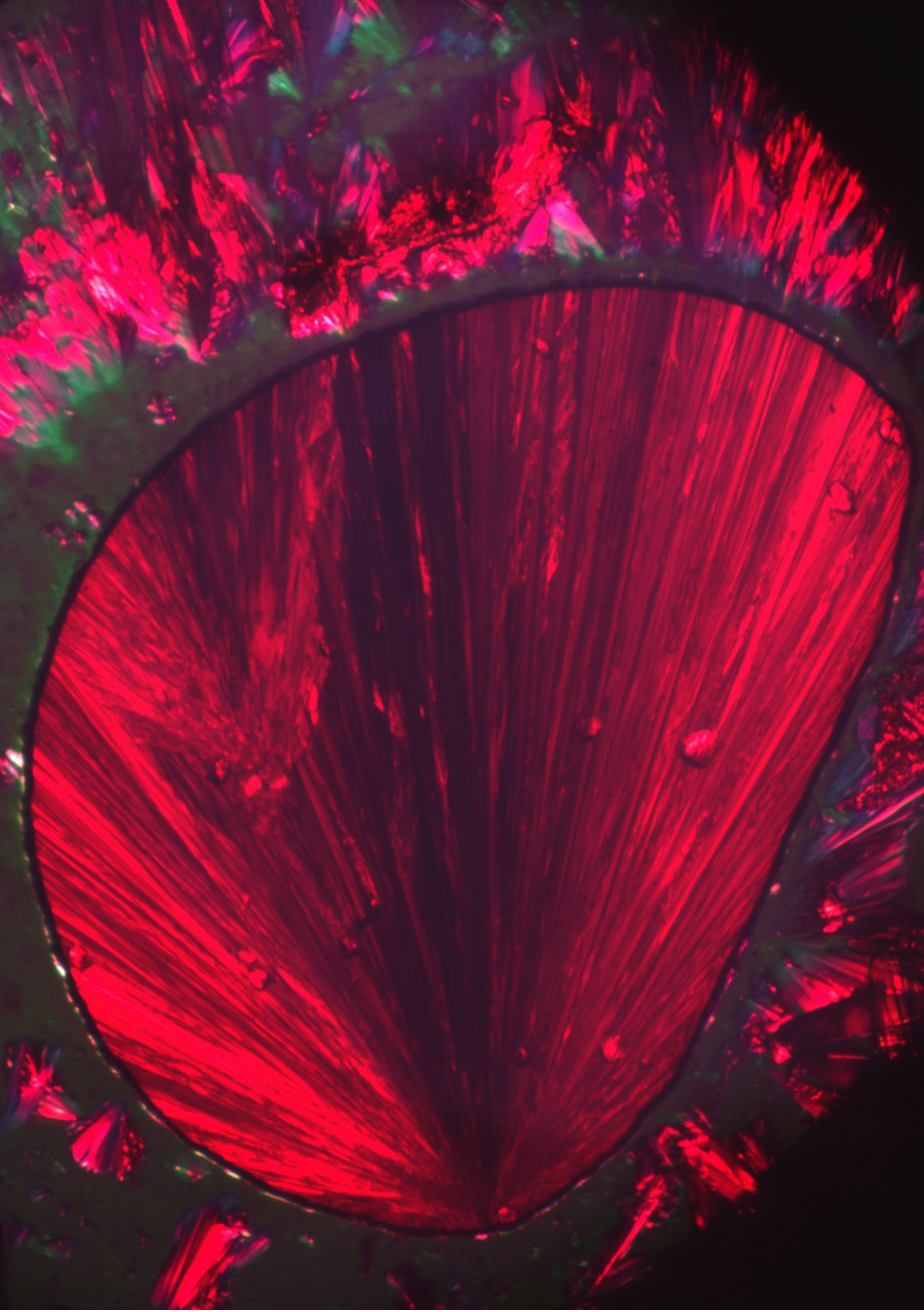

Chapter 1

The influence of structural control on optoelectronic properties

ABSTRACT: Molecular self-assembly can result in ordered materials at the nano-, meso- and macro-scale. This ordering across multiple length scales has a significant impact on the resulting properties of these materials. Therefore, a detailed understanding of how molecular packing can be influenced is essential for both optimizing existing optoelectronic devices and developing new optoelectronic applications. In this chapter, we introduce how 2D crystals, supramolecular materials, liquid crystals, and polymers assemble, and how their ordering can be controlled. The many similarities between these assembly areas have led to blurring boundaries between them, which is accelerated by the recent development of phase separating block molecules, which consists of hard blocks covalently bonded to oligodimethylsiloxane of discrete length. We present a literature review of the recent progress of this new type of material that has order over multiple length scales.

1.1 Introduction

A plethora of organic molecules has been developed for optoelectronic applications such as organic photovoltaics (OPVs), liquid crystalline displays (LCDs), and organic field effect transistors (OFETs). The spatial arrangement of the utilized molecules over multiple length scales determines their energy transfer efficiency.[1–6] Control over their molecular arrangement is therefore essential to their practical implementation. While in the past chemical modifications have been used to change the molecular arrangement at the nanoscale, new processing techniques can also be used to change the molecular arrangement.[7]

There are various types of optoelectronic molecules, of which the smallest type usually forms crystals. Crystals have a well-defined molecular arrangement in three dimensions. This precise arrangement allows for efficient energy transfer through the bulk material. When the thickness of a crystal is reduced to only a few molecules thick, a 2D crystal is obtained where the energy transfer between adjacent molecules is more directional, and thereby a usually more efficient.[8] Similarly, energy transfer is enhanced in fibers, a 1D structure where the fiber thickness is significantly smaller than its length. This reduced dimensionality can additionally lead to new and unique features.[9,10] 2D and 1D crystals can be obtained through molecular self-assembly directed by careful processing steps, aided by side chain engineering.[6,11] Side chain engineering also enables crystalline interactions in self-assembled, supramolecular energy materials in solution.[12] These can be transferred to surfaces, although this generally does not result in complete surface coverage or fiber alignment, limiting solid-state applications. Liquid crystals (LCs) also rely on supramolecular interactions combined with shape anisotropy and phase separation. As a result, they form hierarchically organized nanostructures that provide their function. For macromolecules, similar nanostructures can be formed by side chain engineering of polymers or phase separation in block copolymers (BCPs). All these types of materials combine molecular design and processing to gain nano-, meso- and macroscopic control over the material and the resulting properties. Synthetic advances allow the combination of molecular designs of the different optoelectronic materials. For example, short polymers without molar mass dispersity ($Đ$) can be coupled with small molecules. When there is a large dissimilarity between the different blocks, phase separation as usually found in BCPs can be combined with crystalline interactions in these so-called "block molecules". The combination of these driving forces leads to materials with well-defined molecular arrangements over macroscopic distances. By studying these new materials, the correlation between molecular organization and corresponding optoelectronic properties can be elucidated. The main research question in this thesis is therefore how we can use the nanoscale order obtainable with block molecules to improve optoelectronic properties, here studied by exciton mobility and photon upconversion, while simultaneously elucidating the molecular requirements to obtain this nanoscale order. This knowledge will facilitate the technological development of devices relying on energy transport.

The introductory chapter of this thesis will discuss the different types of optoelectronic materials and how to influence their properties. This will first be done for crystals, followed by supramolecular materials and liquid crystals, and finally for polymers. Next, previous research on phase-separating block molecules will be discussed with an emphasis on design characteristics. Finally, the aim and outline of this thesis will be presented.

1.2 Optoelectronic crystals toward the 2D limit

Crystals of organic semiconducting molecules can be used as optoelectronic active materials; their function being determined by both the molecular structure and their intermolecular interactions. Different packing motifs for the same molecule can be obtained by controlling the crystallization conditions, creating polymorphs. These polymorphs have different properties due to the different electronic coupling between adjacent chromophores, as shown visually in Figure 1A.[13,14] For example, carrier multiplication by singlet fission can either be enhanced or suppressed depending on the molecular packing.[15–19] Similarly, in crystals of charge-transfer forming mixtures, the formation of a separated stack or a mixed stack of donor and acceptor molecules can change the properties from insulating to superconducting (Figure 1B).[20–22]

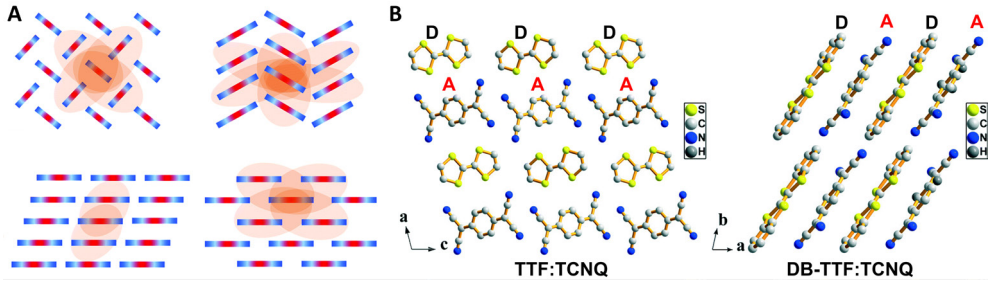

Figure 1. (A) Several common molecular packing motifs of organic semiconductor crystals. The red circles indicate the hopping dimers between neighboring molecules. (B) Molecular packing of donor-acceptor molecules in separated stacking (left) for **TTF**:**TCNQ** and in mixed stacking (right) for **DB-TTF**:**TCNQ**. Images adapted from refs 13 and 20.

In addition to crystallization conditions, side chain engineering is also used to change the crystalline packing.[11] For example, the interactions between the crystalline layers can be weakened, creating a 2D+1D structure.[23,24] Here, the crystalline interactions are directed in plane, with the third dimension consisting of multiple layers that are not electronically coupled. These 2D+1D structures have a more compact molecular packing in the 2D layer compared to the bulk material. As a result, there is better intermolecular orbital overlap, which improves, for example, the transfer of photo-generated carriers.[25] When the 1D thickness is significantly smaller than the 2D surface, these materials are called 2D crystals, with the reduced dimensionality enabling new electronic applications such as thermoelectrics, power conversion devices, and energy storage.[23]

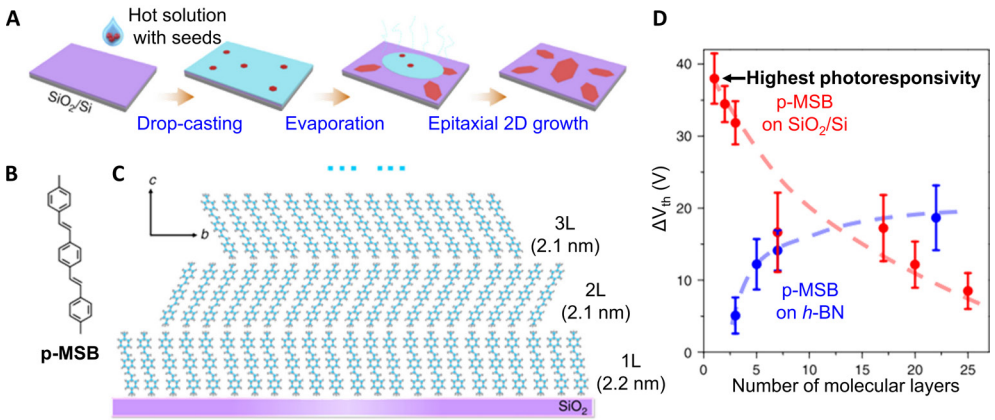

Figure 2. (A) Schematic representation of the 2D crystal growth. (B) A free-standing **p-MSB** molecule. (C) Schematic representation of the molecular packing of the different layers on SiO_2/Si. (D) Molecular layer dependence of the threshold voltage shift correlated to the photoresponsivity. Images adapted from ref 25.

New processing techniques made it possible to form mono- and multilayer crystalline structures. This made it possible to study the thickness effect on energy processes. For 1,4-bis(4-methylstyryl)benzene (**p-MSB**), it was found that when monolayers of compactly packed molecules are formed on SiO_2/Si, 2–3 orders of magnitude higher photoresponsivity is obtained compared to the bulk material (Figure 2).[25] As the layer thickness increases beyond the monolayer, the molecular packing becomes less compact, reducing the photoresponsivity. A less efficient packing is obtained on hexagonal boron nitride (*h*-BN) due to stronger molecule-substrate interactions. As a result, multilayer structures outperform monolayers on *h*-BN although the photoresponsivity is still below that of monolayer **p-MSB** on SiO_2/Si. For different compounds, it was found that monolayers exhibit higher field effect mobilities than bulk or multilayer structures.[26–28] This has been shown to result, for example, in highly sensitive and highly selective gas sensors with a NH_3 detection limit as low as 100 ppb.[28] 2D monolayers are flexible, allowing applications in displays, image sensors, or artificial skin.[13,23]

There is an ongoing development in the processing of crystalline materials to obtain monolayer thick 2D materials that are aligned, with many reviews devoted to this topic.[6,8,23,29–31] One method for obtaining crystalline monolayers is solution-shearing, in which a semiconductor solution is passed over a substrate to achieve alignment of crystalline domains by controlled evaporation of the solvent.[30] By varying the shear rate in this technique, it was found that the intermolecular distance between TIPS-pentacene molecules can be reduced from 3.33 Å to 3.08 Å, leading to a 6-fold increase in charge carrier mobility (Figure 3).[7] This packing is a kinetically trapped polymorph that would otherwise be inaccessible. These examples clearly illustrate the importance of controlling molecular packing to improve existing applications while enabling more fundamental structure-property studies and the development of new applications. For organic crystals, research in the 2D limit is far from complete.[30,32] One of the main challenges is to develop environmentally stable 2D organic crystals by, for example, encapsulating these organic crystals to increase the stability of the materials.

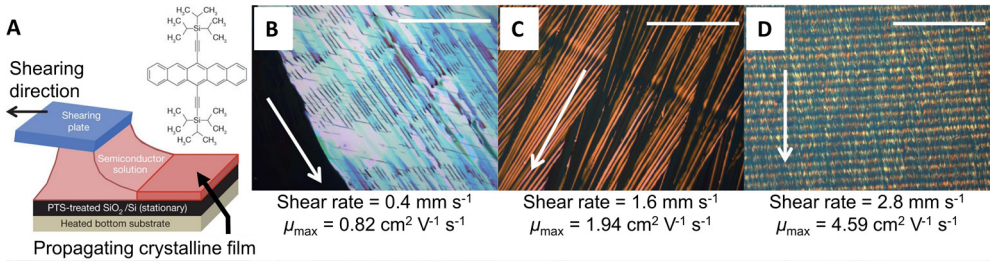

Figure 3. (A) Schematic representation of the solution-shearing method used to align the TIPS-pentacene molecules. (B–D) Polarized optical microscope images with crossed polarizers of solution-sheared TIPS-pentacene thin films formed at different shear rates (scale bars are all 200 μm). The white arrows indicate the shearing direction. The maximum mobility obtained for the films is reported as μ_{max}. Increased shear rates decreased the μ_{max}. Images adapted from ref 7.

1.3 The supramolecular assembly of small molecules in solution and condensed matter

Supramolecular assemblies in solution can be obtained by attractive, non-covalent interactions that can be controlled by side chain engineering. When assembled with favorable π-stacking, these supramolecular assemblies can exhibit a greater propensity to interact with light than their monomeric or macromolecular counterparts (Figure 4A).[12] The resulting electronic coupling and delocalization of π-systems depend on the degree of structural order and are unique to this assembly mechanism (Figure 4C).[33,34] For example, supramolecular nanostructures of hydrogen-bonded oligo(*p*-phenylenevinylene) derivatives have electronic properties midway between crystals and polymeric semiconductors.[35,36] The nanostructures formed are also affected by processing conditions. This pathway complexity allows the formation of either face-to-face (H-aggregate) or brick-layer-type (slipped stacked, J-aggregate) arrangements of the same molecule (Figure 4B), leading to distinctly different (photo)physical properties and spectroscopic features.[37–39] Moreover, dense assemblies can be formed

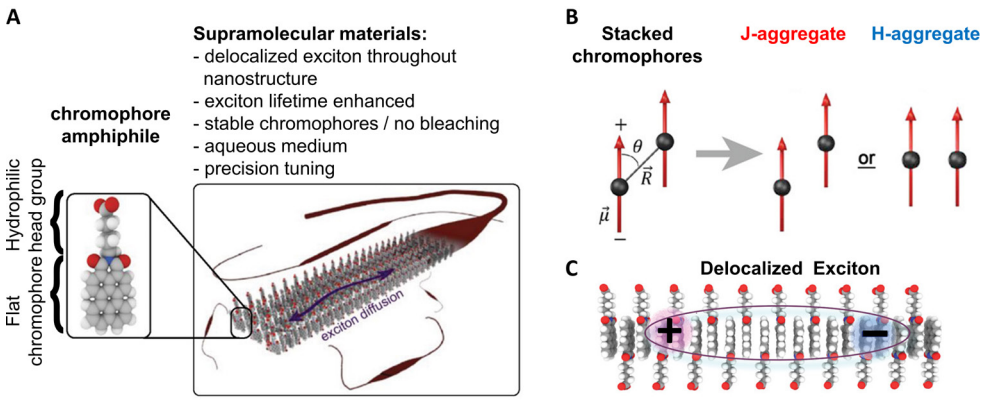

Figure 4. (A) Concepts of self-assembled chromophores in supramolecular materials. (B) Schematic packing of traditional J- and H-aggregates. H-aggregates result in a spectral blue shift and suppressed radiative decay, while in J-aggregates a spectral red shift is observed with an enhanced radiative decay. (C) Schematic of the delocalization of an exciton across a self-assembled structure. Images adapted from refs 12.

that prevent the quenching of photogenerated states by oxygen.[40] Supramolecular energy materials find application in photocatalysis,[41–44] or enhanced (chiral) photoluminescent emission,[45] with the potential for a variety of new phenomena and applications.[46–49] However, although these assemblies can be transferred to surfaces, complete surface coverage or fiber alignment is generally not possible.[50] Applying these 2D or 1D ordered assembled structures for solvent-free nanotechnology applications requires extensive knowledge of all intermolecular interactions as well as the interactions with the substrate.[51,52] Understanding how to control supramolecular assemblies will advance developments that depend sensitively on charge mobility, such as photovoltaics and light emission, as well as piezoelectricity and ferroelectricity.[12,50,53–58]

Supramolecular interactions in condensed matter can lead to the formation of liquid crystalline (LC) phases. LC phases are self-organized, anisotropic fluids that are thermodynamically between the crystalline phase and the isotropic phase.[59] Their dynamic order determines their properties. The most common LC assemblies are smectic and columnar phases, although more complex phases also exist.[60] The smectic phase is a layered nanostructure and can therefore be considered a 2D+1D structure, although there is no positional or rotational ordering of molecules within the layer.[61] LC molecules are widely used in everyday applications such as liquid crystal displays (LCDs),[62] and there is ongoing research into the use of semiconducting LCs in field-effect transistors,[63] ferroelectrics,[53] stimuli-responsive sensors,[64] non-volatile memories[65] and photovoltaic applications.[66]

Smectic and columnar LC phases are formed by a combination of partial rigidity of the LC core and phase separation with their flexible side chains.[67] Figure 5A shows how phase separation leads to improved order for discotic liquid crystals, although the resulting structure should be called a soft crystal rather than a liquid crystal.[67] The stabilization induced by phase separation arises from improved order, while also preventing diffusion of molecules between different layers. The strongest stabilization of the formed nanostructures occurs when the side chains fill the available space (Figure 5B–C).[67] Therefore, the bulkiness of the side chains is an important design parameter of LCs. Phase separation in LCs is often induced by oligodimethylsiloxane (*o*DMS) dimers or trimers because of their high thermodynamic incompatibility of the core and side chains.[68–72] Moreover, *o*DMS has a cross-sectional area twice as large as linear alkanes making this a more bulky side chain.[73]

One of the main advantages of liquid crystalline materials is the ability to align the molecules over large (mm) distances.[74] The alignment of LC materials is done by external stimuli such as electromagnetic fields, mechanical stress, or by rubbed polyimide alignment layers.[75–77] Thus, densely packed, directed nanostructures are formed that increase the order of the system, enabling efficient and anisotropic energy transport as well as linearly polarized emission for luminescent LCs.[78–80] The alignment of LCs has mostly been studied in columnar phases,[81,82] although it has also been reported for smectic phases.[83,84] An advantage of smectic phases is that charge transport is less prone to structural defects than 1D transport in columnar phases.[83]

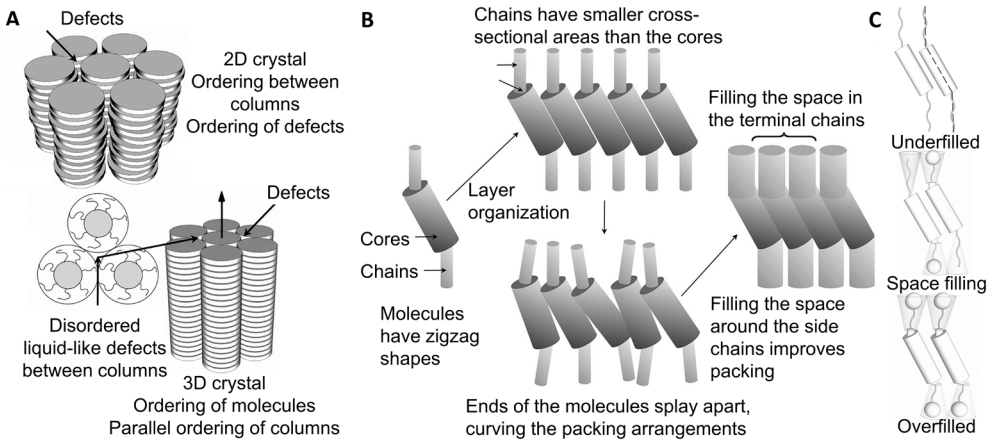

Figure 5. (A) The columnar structure of disordered (top) and ordered (bottom) hexagonally packed columnar stacks. (B) Schematic showing how space filling of side chains in liquid crystals stabilizes the formed nanostructure. (C) Schematic showing how space filling of the side chains can stabilize the smectic phase. Here, the middle structure has the least free space and is therefore the most stable. In the bottom structure the available space is underfilled, while the bulkiness of the side chains in the bottom structure leads to overfilling of the available space, thereby preventing the formation of a smectic phase. Image adapted from ref 67.

1.4 Polymer and block copolymer bulk assembly by thermodynamic incompatibility

The self-assembled morphology of optoelectronically active polymers and block copolymers determines their properties and thereby their application. Side chains can make a polymer more soluble, thereby increase the obtainable molecular weight and processability, but also affect the morphology of the polymer through their intermolecular interactions.[85,86] Conventional approaches increase the length of alkyl side chains or introduce branching points for improved solubility.[87] However, the use of oligodimethylsiloxane derivatives as side chains is becoming increasingly popular because of their thermodynamic incompatibility with conjugated polymer backbones, described by the Flory-Huggins interaction parameter χ. For example, χ of polystyrene-polydimethylsiloxane block polymers is 0.11, while χ of polystyrene-poly(methyl methacrylate) is only 0.030.[88] *o*DMS side chains both improve solubility while reducing the π-stacking distance of the polymer. Consequently, the hole mobilities of an isoindigo-based conjugated polymer are increased from 0.57 $cm^2\ V^{-1}\ s^{-1}$ for branched alkyl side chains to 2.00 $cm^2\ V^{-1}\ s^{-1}$ for an *o*DMS trimer.[89] This functionalization of conjugated polymers with *o*DMS side chains up to the heptamer appears to be a common method to improve OFET performance.[73,90] The immiscibility of conjugated polymers with fluoralkyl chains has also been used to control molecular packing.[91–93] However, the limited solubility of fluoralkyl chains poses problems in purification and processing.[86] Therefore, unlike *o*DMS side chains, fluoralkylated compounds have rarely been used for OFET or OPV applications.

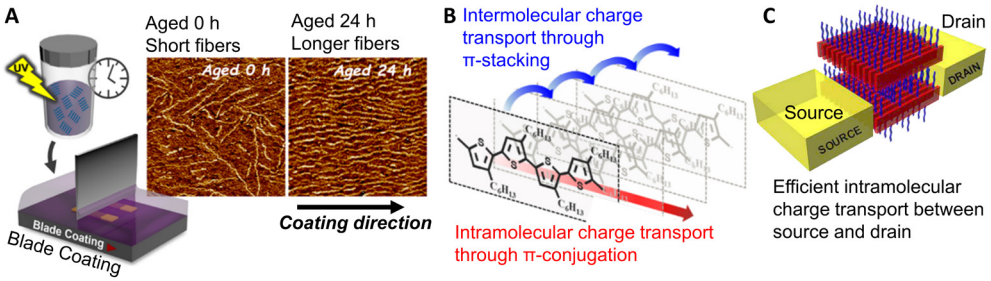

Figure 6. (A) Schematic of the blade coating process used to align **P3HT** fibers in an amorphous **P3HT** matrix. The fibers are formed by supramolecular interactions in solution, with longer assembly times leading to longer fibers. (B) Directions of charge transport in crystalline **P3HT**. (C) This OFET geometry is identified as the most optimal because the charge transport is intramolecular along the π-conjugation direction, which is faster than intermolecular charge transport by hopping in the π-stacking direction. Furthermore, it was found that an edge-on orientation of the fibers onto the bottom layer yields a 100-fold increase compared to a face-on orientation, where the conjugated backbone is in direct contact with the bottom substrate. Images adapted from refs 102 and 103.

In addition to controlling the nanoscale ordering of polymeric systems, the optoelectronic properties can be improved by increasing the meso- and macroscale ordering, which can be achieved by material processing. Long-range ordering of polymers results in percolation paths with high mobility by reducing the number of defects and by increasing the conjugation length through alignment of the conjugated polymer backbone.[94,95] Alignment techniques for polymers are similar to those for liquid crystals (e.g., mechanical rubbing, epitaxy, shear, electric field), with the main difference being that aligned polymer films consist of both ordered (crystallized) and disordered domains.[96–101] This is shown in Figure 6 for **P3HT** films consisting of crystalline nanofibers in a disordered polymer matrix.[102] The macroscopic alignment of these nanofibers by shear force leads to an increase in charge transport by favoring the intramolecular charge transport over the less efficient intermolecular charge transport (Figure 6B).[102,103] Liquid crystalline behavior can be induced in polymers by including both flexible and rigid fragments in the form of rods and disks. The alignment of these LC polymers can then take place under external stimuli, making this class of materials promising for applications in optoelectronics, such as optical sensors or spectrum band filters.[104] These examples clearly show how different self-assembly fields overlap through the pursuit of crystallinity for improved electronic coupling and the use of LC alignment techniques for long-range order in self-assembled polymeric systems.[105] Regardless of the self-assembly field, advances in fundamental knowledge and processing techniques are paramount to further improve existing applications, as well as to target novel applications.

Although phase-separated block copolymers (BCPs) are studied primarily for nanolithography purposes[106–108] and only to a limited extent for optoelectronics,[109] understanding how the chemical incompatibility of different blocks affects morphology may help in the development of all systems that rely on self-assembly. BCPs consist of two or more chemically distinct blocks that are covalently bonded. Because of thermodynamic incompatibility between the different blocks, they self-assemble into nanostructured morphologies driven by phase separation. For BCPs consisting of two flexible blocks (coil-coil), the morphology formed can be predicted in the simplest

approximation via self-consistent mean-field theory.[110] As shown in Figure 7, the Flory-Huggins interaction parameter χ and the BCP length (degree of polymerization N) determine whether the blocks phase separate, while the volume fraction of the blocks (*f*) determines the morphology. When the product of χ and N is smaller than 10.5, the different blocks do not phase separate. Smaller periodicities can thus be obtained with low molecular weight materials only when there is a large incompatibility between the different blocks. These "high χ - low N" BCPs can lead to ordered morphologies with features of less than 10 nm. However, predicting the formed morphology becomes more complicated when self-assembly occurs in the 2D limit or in a confined space.[111–115] Moreover, the formed morphology is also determined by molecular architecture, architectural asymmetry, shape anisotropy, block stiffness (rod-coil instead of coil-coil), and molecular weight dispersity.[109,116–119]

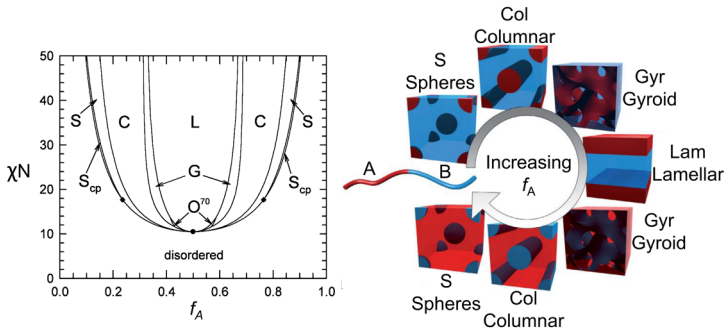

Figure 7. Theoretical phase diagram of a diblock copolymer calculated using self-consistent mean-field theory. The x-axis corresponds to the volume fraction of one of the two blocks, as described by f. The most accessible morphologies are shown graphically on the right: Lamellar (Lam), Columnar (Col), Gyroid (Gyr), body-centered cubic spheres (S). The less common phases are hexagonal close packed spheres (S_{cp}) and *Fddd* (O^{70}). Images adapted from refs 118 and 119.

1.5 Oligodimethylsiloxane for nanoscale phase-separated materials

In the pursuit of well-defined nanoscale materials with meso- to macroscale ordering, the phase separation of BCPs can be combined with the processability of polymers and the molecular design of LCs of an aromatic core with flexible side groups. Moreover, when the appropriate aromatic core is used, it can be combined with the crystalline interactions that occur in crystals. To this end, flexible oligomers were attached to aromatic blocks to obtain a type of material that will be referred to as block molecules in this thesis. This term was introduced by Tschierske to encompass all macromolecules with at least two dissimilar blocks that assemble through a combination of enthalpic and entropic forces.[72] As such, this term links both BCP and LC assembly. According to BCP theory, a high χ value is required when using oligomers (low N, *vide infra*). For this purpose, oligodimethylsiloxane (*o*DMS) has been used because of its high χ values with a range of different monomers.[120] This section discusses previous research efforts focused on *o*DMS-containing block molecules.

1.5.1 The effect of *o*DMS dispersity on the self-assembling properties of block molecules

The iterative synthesis of *o*DMS and oligo(lactic acid) (*o*LA) allowed the precise length of both blocks to be varied.[121] This resulted in lamellar, cylindrical and gyroid morphologies with feature sizes down to 6.5 nm depending on the volume fraction of the blocks, thereby following BCP theory.[122] Furthermore, the *o*DMS-*o*LA block molecules allowed for a comparison of the block dispersity on the thermal transitions and the degree of ordering. Following calculations of diblock copolymers in the "high χ - low N" regime", a higher molar mass dispersity ($Đ$) of both blocks would result in a more readily formed nanostructure than its monodisperse counterpart.[123] This can be visualized by the phase diagram of Figure 7 shifting to lower χN values, or an increase in the order-disorder temperature (T_{ODT}).[124] For *o*DMS-*o*LA, this dispersity-induced stabilization of the microphase-separated state was observed as a shift of the T_{ODT} to higher values when either one or both blocks were polydisperse.[121] In contrast, an increase in the dispersity of the *o*DMS block in *o*DMS-oligomethylmetacrylate with discrete length oligomethylmetacrylate (*o*MMA) lead to a reduction of the T_{ODT}.[124] Similar contradicting effects on the T_{ODT} were observed for triblocks whose center block is poly-1,4-butadiene with the peripheral blocks being either polylactide or polystyrene.[125–127] However, the effect on the morphology for both *o*DMS-containing block molecules was similar. For both *o*DMS-*o*LA and *o*DMS-*o*MMA, the sharpest scattering peaks and smallest periodicities were observed by small-angle X-ray scattering (SAXS) when both blocks of *o*DMS-*o*LA and *o*DMS-*o*MMA are monodisperse. Monodisperse blocks are therefore required when targeting a well-defined morphology where all intermolecular interactions of the non-*o*DMS groups are the same.

The effect of dispersity was also studied in a series of hydrazone-*o*DMS-hydrazone materials with different discrete lengths of *o*DMS.[128] These materials exhibited a high degree of morphological order, as observed by SAXS, that was retained when a disperse mixture under a $Đ$ of 1.10 was artificially created. Similar to *o*DMS-*o*LA, a volume fraction dependence on the formed morphology was observed, although different morphologies could be obtained by varying the melt cooling rate.[128] For both the *o*LA and hydrazone block molecules, the enthalpic changes measured by differential scanning calorimetry (DSC) corresponded to the values usually found for phase-separated block copolymers ($\Delta H_{Order\text{-}Disorder} < 5$ kJ mol^{-1}).[129] These results indicate the importance of discrete length *o*DMS for the formation of phase-separated ordered structures at the nanoscale in *o*DMS-containing block molecules.

1.5.2 Crystallization combined with phase separation in block molecules

In addition to phase separation, crystallization of the hard block can affect the nanostructure formed in *o*DMS-containing block molecules. Crystallization for these types of molecules can be inferred from sharp scattering peaks in the wide-angle X-ray scattering (WAXS) region, combined with melting enthalpies greater than ~15 kJ mol^{-1}.[129] The combination of crystallization and phase separation leads to long-scale ordering, as evidenced by the medium-angle X-ray scattering (MAXS) region. These characteristics are found in *o*DMS-containing block molecules of isotactic *o*DMS-

oligo(lactic acid), *o*DMS-oligoprolines and *o*DMS-oligomethylene.[128,130,131] Interestingly, although the oligomeric non-*o*DMS blocks were able to crystallize, the formed morphologies were depended on the volume fraction. In contrast, for naphthalene dimide-*o*DMS structures, columnar morphologies were observed with core-centered block molecules (*o*DMS-NDI-*o*DMS) regardless of volume fractions, whereas telechelic block molecules (NDI-*o*DMS-NDI) always formed lamellar morphologies.[132] Although both molecules have the same crystallizable NDI blocks, it appears that in addition to the crystallization potential of the core, the molecular architecture also contributes to the formation of the nanostructure. This was further investigated by comparing heterotelechelic pyrene-*o*DMS-NDI with a mixture of homotelechelic pyrene-*o*DMS-pyrene and NDI-*o*DMS-NDI, where the charge transfer interaction was more pronounced in the one-component system.[133] Similar to the NDI block molecules, columnar phases were observed for core-centered block molecules of an azobenzene derivative with different lengths of *o*DMS.[134] In contrast, *o*DMS length changes the morphology between lamellar, gyroid and columnar with increasing *o*DMS length for a core-centered block molecule with two diphenyl groups connected by a triple bond as a central rigid rod (Figure 8).[135] Different morphologies were also obtained by varying the alkyl spacer length between the rigid block and the *o*DMS. These results show that in addition to crystallization, the architecture of the block molecule and the length of the alkyl spacer are also important, although the exact influence remains to be elucidated.

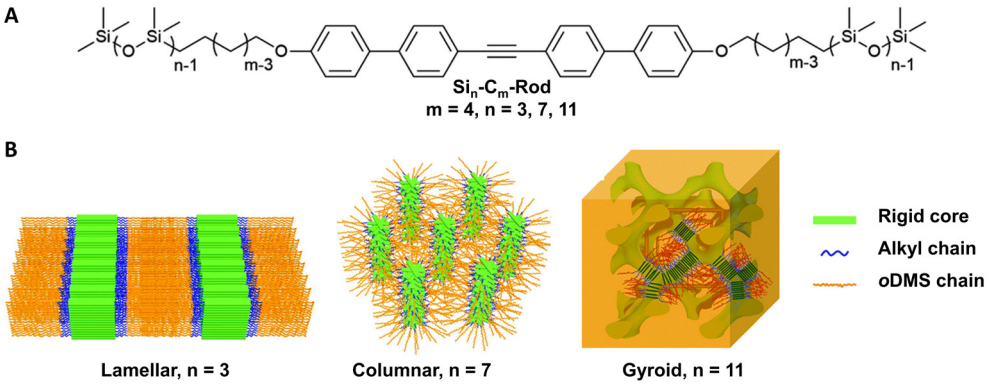

Figure 8. (A) Chemical structure of the core-centered aromatic block molecule. (B) Graphical representations of the formed nanostructures with an increase in *o*DMS length. Images adapted from ref 135.

The effect of crystallization behavior on the formed morphology is also clearly observed for telechelic triptycene block molecules. When a crystallizable triptycene block was used, lamellar morphologies were obtained even with disperse polydimethylsiloxane with a molecular weight of 24 kDa (Figure 9).[136] However, by changing the position of an undecylene chain on the triptycene block, crystallization was prevented and a less defined morphology was obtained. Similarly, telechelic block molecules with a methoxy-capped azobenzene and discrete *o*DMS exhibit a lamellar morphology in the crystallizable trans configuration, while an isotropic liquid is formed when the azobenzene is switched to the *cis* configuration.[137] This photoisomerization leads to rapid transitions from solid to liquid. When a hydrogen-bonding hydroxy-capped azobenzene

was used, the crystallization of azobenzene was inhibited and the morphology formed followed BCP theory. Minor modifications to the non-*o*DMS block also showed a change from BCP to more LC behavior when the peripheral ureidopyrimidinone block can either bond or aggregate in planar geometry, respectively.[137]

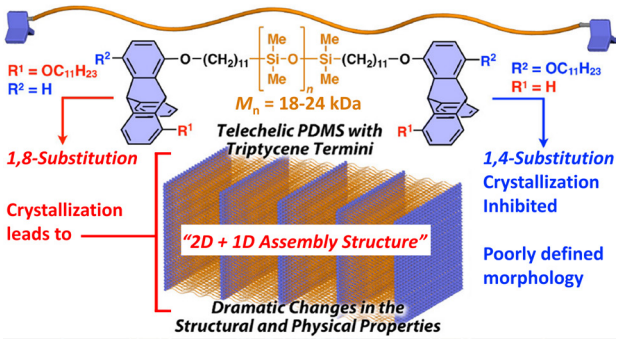

Figure 9. Schematic representation of the telechelic PDMS block molecule containing triptycene. The 1,8-substituted core can crystallize, forming a 2D+1D assembly structure. In the 2D-triptycene layer, the nuclei have well-defined crystalline packing. The 1,4-substituted core does not form this lamellar morphology because crystallization is inhibited. Images adapted from ref 136.

Previous studies of these *o*DMS-containing block molecules have provided the first insights into the various aspects that drive their self-assembly. The formed nanostructure of *o*DMS-containing block molecules appears to be a complex sum of phase separation, non-covalent directional core-core interactions (*e.g.* π-stacking, H-bonding), and molecular architecture. The ability of these molecules to form ordered nanostructures, even with macroscopic domain sizes up to 5 mm,[128] offers great potential for similar optoelectronic applications as for 2D crystals and semiconducting polymers.

1.6 Aim and outline of this thesis

The above literature review shows that controlling intermolecular arrangement at the nanoscale for improved optoelectronic properties is being actively investigated from crystal, liquid crystal, and block copolymer directions. Moreover, it shows the many similarities between these assembly fields and the blurring boundaries between them. The field of *o*DMS-containing block molecules has been introduced as a different way to obtain nanoscale ordered materials via phase separation and directional interactions. However, these block molecules have not yet been studied for their optoelectronic applications. Moreover, questions were raised about the molecular design related to the effect of the architecture of the block molecules. In this thesis, we aim to synthesize and characterize new block molecules to deepen the fundamental understanding of the self-assembly of block molecules while also studying their potential in optoelectronic applications. On the fundamental side, we focus on the effect of molecular architecture and alkyl spacer length. Furthermore, we study the effect of doping with non-functionalized cores and charge transfer forming compounds on the formed nanostructure. The studied optoelectronic properties are long-range exciton diffusion and triplet-triplet annihilation upconversion based on triplet energy migration.

In **Chapter 2**, we describe how the molecular architecture affects the formed nanostructure. For this purpose, a library of four different cores with a core-centered, telechelic or head-tail architecture was synthesized. The effect of volume fraction was excluded by using similar *o*DMS lengths per core. Moreover, the core symmetry has been varied to also study the requirements of the core. This study elucidates the role of intermolecular distances in the crystal structure on the ability to form 2D morphologies. Moreover, the effect of the alkyl spacer length in between the diphenylanthracene core and *o*DMS has been studied.

Chapter 3 focuses on mixing both arylene diimide block molecules with either non-functionalized arylene diimide or pyrene. Pyrene is found to form charge transfer complexes with these block molecules. Charge transfer complexation is also observed in mixtures with viologen block molecules. The luminescent properties of diphenylanthracene block molecules are influenced through intercalation of halogenated benzene rings in the crystalline layer. This chapter extends the intermolecular distances requirements described in Chapter 2 to multicomponent systems.

The effect of ordering at the nanoscale is shown in **Chapter 4**, which examines the difference between non-functionalized and *o*DMS-functionalized carbonyl-bridged triarylamines. We show the formation of well-defined columnar stacks of aligned *o*DMS-containing block molecules. The enhanced order results in high exciton mobilities that are usually only found in crystals. Here the high exciton mobilities were observed in a thermal and solution-processable material.

The ability to align aromatic groups in domains up to one centimeter, while maintaining ordering at the nanoscale, is used in **Chapter 5** to study the enhancement of triplet-triplet annihilation upconversion based on triplet energy migration. While the amorphous diphenylanthracene block molecules showed low upconversion intensities, a 100-fold increase in upconverted signal is reported by ordering the materials by thermal annealing.

Finally, **Chapter 6** reviews the scope and limitations of *o*DMS-containing block molecules. Herein, we report on outstanding fundamental questions by relating them to pentacene block molecules studied for their singlet fission properties and provide guidelines for future optoelectronic research directions.

1.7 References

(1) De Luca, G.; Pisula, W.; Credgington, D.; Treossi, E.; Fenwick, O.; Lazzerini, G. M.; Dabirian, R.; Orgiu, E.; Liscio, A.; Palermo, V.; Mullen, K.; Cacialli, F.; Samori, P. *Adv. Funct. Mater.* **2011**, *21*, 1279.

(2) Beaujuge, P. M.; Fréchet, J. M. J. *J. Am. Chem. Soc.* **2011**, *133*, 20009.

(3) Henson, Z. B.; Müllen, K.; Bazan, G. C. *Nat. Chem.* **2012**, *4*, 699.

(4) Graetzel, M.; Janssen, R. A. J.; Mitzi, D. B.; Sargent, E. H. *Nature* **2012**, *488*, 304.

(5) Hull, R.; Keblinski, P.; Lewis, D.; Maniatty, A.; Meunier, V.; Oberai, A. A.; Picu, C. R.; Samuel, J.; Shephard, M. S.; Tomozawa, M.; Vashishth, D.; Zhang, S. *Appl. Phys. Rev.* **2018**, *5*.

(6) Yao, Y.; Zhang, L.; Orgiu, E.; Samorì, P. *Adv. Mater.* **2019**, *31*, 1.

(7) Giri, G.; Verploegen, E.; Mannsfeld, S. C. B.; Atahan-Evrenk, S.; Kim, D. H.; Lee, S. Y.; Becerril, H. A.; Aspuru-Guzik, A.; Toney, M. F.; Bao, Z. *Nature* **2011**, *480*, 504.

(8) Park, S. K.; Kim, J. H.; Park, S. Y. *Adv. Mater.* **2018**, *30*, 1.

(9) Zhuang, X.; Mai, Y.; Wu, D.; Zhang, F.; Feng, X. *Adv. Mater.* **2015**, *27*, 403.

(10) Cai, S. L.; Zhang, W. G.; Zuckermann, R. N.; Li, Z. T.; Zhao, X.; Liu, Y. *Adv. Mater.* **2015**, *27*, 5762.

(11) Krishna, G. R.; Devarapalli, R.; Lal, G.; Reddy, C. M. *J. Am. Chem. Soc.* **2016**, *138*, 13561.

(12) Dumele, O.; Chen, J.; Passarelli, J. V.; Stupp, S. I. *Adv. Mater.* **2020**, *32*, 1907247.

(13) Wang, Y.; Sun, L.; Wang, C.; Yang, F.; Ren, X.; Zhang, X.; Dong, H.; Hu, W. *Chem. Soc. Rev.* **2019**, *48*, 1492.

(14) Salzillo, T.; Della Valle, R. G.; Venuti, E.; Brillante, A.; Siegrist, T.; Masino, M.; Mezzadri, F.; Girlando, A. *J. Phys. Chem. C* **2016**, *120*, 1831.

(15) Kolata, K.; Breuer, T.; Witte, G.; Chatterjee, S. *ACS Nano* **2014**, *8*, 7377.

(16) Pensack, R. D.; Tilley, A. J.; Grieco, C.; Purdum, G. E.; Ostroumov, E. E.; Granger, D. B.; Oblinsky, D. G.; Dean, J. C.; Doucette, G. S.; Asbury, J. B.; Loo, Y. L.; Seferos, D. S.; Anthony, J. E.; Scholes, G. D. *Chem. Sci.* **2018**, *9*, 6240.

(17) Yang, C. H.; Hsu, C. P. *J. Phys. Chem. Lett.* **2015**, *6*, 1925.

(18) Jones, A. C.; Kearns, N. M.; Ho, J. J.; Flach, J. T.; Zanni, M. T. *Nat. Chem.* **2020**, *12*, 40.

(19) Levine, A. M.; He, G.; Bu, G.; Ramos, P.; Wu, F.; Soliman, A.; Serrano, J.; Pietraru, D.; Chan, C.; Batteas, J. D.; Kowalczyk, M.; Jang, S. J.; Nannenga, B. L.; Sfeir, M. Y.; Tsai, E. H. R.; Braunschweig, A. B. *J. Phys. Chem. C* **2021**, *125*, 12207.

(20) Jiang, H.; Yang, X.; Cui, Z.; Liu, Y.; Li, H.; Hu, W.; Kloc, C. *CrystEngComm* **2014**, *16*, 5968.

(21) Dar, A. A.; Rashid, S. *CrystEngComm* **2021**, *23*, 8007.

(22) Engler, E. M.; Fox, W. B.; Interrante, L. V.; Miller, J. S.; Wudl, F.; Yoshimura, S.; Heeger, A.; Baughman, R. H. In *Molecular Metals*; 1978; pp 541–544.

(23) Yang, F.; Cheng, S.; Zhang, X.; Ren, X.; Li, R.; Dong, H.; Hu, W. *Adv. Mater.* **2018**, *30*, 1702415.

(24) Shi, Y.; Jiang, L.; Liu, J.; Tu, Z.; Hu, Y.; Wu, Q.; Yi, Y.; Gann, E.; McNeill, C. R.; Li, H.; Hu, W.; Zhu, D.; Sirringhaus, H. *Nat. Commun.* **2018**, *9*.

(25) Cao, M.; Zhang, C.; Cai, Z.; Xiao, C.; Chen, X.; Yi, K.; Yang, Y.; Lu, Y.; Wei, D. *Nat. Commun.* **2019**, *10*, 1.

(26) Peng, B.; Huang, S.; Zhou, Z.; Chan, P. K. L. *Adv. Funct. Mater.* **2017**, *27*.

(27) Jiang, L.; Dong, H.; Meng, Q.; Li, H.; He, M.; Wei, Z.; He, Y.; Hu, W. *Adv. Mater.* **2011**, *23*, 2059.

(28) Meng, Q.; Zhang, F.; Zang, Y.; Huang, D.; Zou, Y.; Liu, J.; Zhao, G.; Wang, Z.; Ji, D.; Di, C. A.; Hu, W.; Zhu, D. *J. Mater. Chem. C* **2014**, *2*, 1264.

(29) Shi, Y. L.; Zhuo, M. P.; Wang, X. D.; Liao, L. S. *ACS Appl. Nano Mater.* **2020**, *3*, 1080.

(30) Wang, Z.; Jingjing, Q.; Wang, X.; Zhang, Z.; Chen, Y.; Huang, X.; Huang, W. *Chem. Soc. Rev.* **2018**, *47*, 6128.

(31) He, Z.; Chen, J.; Li, D. *J. Vac. Sci. Technol. A* **2019**, *37*, 040801.

(32) Wang, C.; Fu, B.; Zhang, X.; Li, R.; Dong, H.; Hu, W. *ACS Cent. Sci.* **2020**, *6*, 636.

(33) Grozema, F. C.; Siebbeles, L. D. A. *Int. Rev. Phys. Chem.* **2008**, *27*, 87.

(34) Peng, H. Q.; Niu, L. Y.; Chen, Y. Z.; Wu, L. Z.; Tung, C. H.; Yang, Q. Z. *Chem. Rev.* **2015**, *115*, 7502.

(35) Daniel, C.; Herz, L. M.; Silva, C.; Hoeben, F. J. M.; Jonkheijm, P.; Schenning, A. P. H. J.; Meijer, E. W. *Phys. Rev. B* **2003**, *68*, 1.

(36) Korevaar, P. A.; George, S. J.; Markvoort, A. J.; Smulders, M. M. J.; Hilbers, P. A. J.; Schenning, A. P. H. J.; De Greef, T. F. A.; Meijer, E. W. *Nature* **2012**, *481*, 492.

(37) Ogi, S.; Fukui, T.; Jue, M. L.; Takeuchi, M.; Sugiyasu, K. *Angew. Chemie - Int. Ed.* **2014**, *53*, 14363.

(38) Fukui, T.; Kawai, S.; Fujinuma, S.; Matsushita, Y.; Yasuda, T.; Sakurai, T.; Seki, S.; Takeuchi, M.; Sugiyasu, K. *Nat. Chem.* **2017**, *9*, 493.

(39) Matern, J.; Dorca, Y.; Sánchez, L.; Fernández, G. *Angew. Chemie - Int. Ed.* **2019**, *58*, 16730.

(40) Kouno, H.; Sasaki, Y.; Yanai, N.; Kimizuka, N. *Chem. - A Eur. J.* **2019**, *25*, 6124.
(41) Weingarten, A. S.; Kazantsev, R. V.; Palmer, L. C.; Fairfield, D. J.; Koltonow, A. R.; Stupp, S. I. *J. Am. Chem. Soc.* **2015**, *137*, 15241.rd
(42) Kazantsev, R. V.; Dannenhoffer, A. J.; Weingarten, A. S.; Phelan, B. T.; Harutyunyan, B.; Aytun, T.; Narayanan, A.; Fairfield, D. J.; Boekhoven, J.; Sai, H.; Senesi, A.; O'Dogherty, P. I.; Palmer, L. C.; Bedzyk, M. J.; Wasielewski, M. R.; Stupp, S. I. *J. Am. Chem. Soc.* **2017**, *139*, 6120.
(43) Dannenhoffer, A.; Sai, H.; Huang, D.; Nagasing, B.; Harutyunyan, B.; Fairfield, D. J.; Aytun, T.; Chin, S. M.; Bedzyk, M. J.; Olvera De La Cruz, M.; Stupp, S. I. *Chem. Sci.* **2019**, *10*, 5779.
(44) Weingarten, A. S.; Dannenhoffer, A. J.; Kazantsev, R. V.; Sai, H.; Huang, D.; Stupp, S. I. *J. Am. Chem. Soc.* **2018**, *140*, 4965.
(45) Han, J.; Duan, P.; Li, X.; Liu, M. *J. Am. Chem. Soc.* **2017**, *139*, 9783.
(46) Rybtchinski, B. *ACS Nano* **2011**, *5*, 6791.
(47) Korevaar, P. A.; De Greef, T. F. A.; Meijer, E. W. *Chem. Mater.* **2014**, *26*, 576.
(48) Mattia, E.; Otto, S. *Nat. Nanotechnol.* **2015**, *10*, 111.
(49) Schenning, A. P. H. J.; Meijer, E. W. *Chem. Commun.* **2005**, *26*, 3245.
(50) Wittmann, B.; Wenzel, F. A.; Wiesneth, S.; Haedler, A. T.; Drechsler, M.; Kreger, K.; Köhler, J.; Meijer, E. W.; Schmidt, H. W.; Hildner, R. *J. Am. Chem. Soc.* **2020**, *142*, 8323.
(51) Hoeben, F. J. M.; Jonkheijm, P.; Meijer, E. W.; Schenning, A. P. H. J. *Chem. Rev.* **2005**, *105*, 1491.
(52) Jain, A.; George, S. J. *Nat. Nanotechnol.* **2016**, *11*, 843.
(53) Tayi, A. S.; Kaeser, A.; Matsumoto, M.; Aida, T.; Stupp, S. I. *Nat. Chem.* **2015**, *7*, 281.
(54) Horiuchi, S.; Tokura, Y. *Nat. Mater.* **2008**, *7*, 357.
(55) Tayi, A. S.; Shveyd, A. K.; Sue, A. C. H.; Szarko, J. M.; Rolczynski, B. S.; Cao, D.; Jackson Kennedy, T.; Sarjeant, A. A.; Stern, C. L.; Paxton, W. F.; Wu, W.; Dey, S. K.; Fahrenbach, A. C.; Guest, J. R.; Mohseni, H.; Chen, L. X.; Wang, K. L.; Fraser Stoddart, J.; Stupp, S. I. *Nature* **2012**, *488*, 485.
(56) Gorbunov, A. V.; Haedler, A. T.; Putzeys, T.; Zha, R. H.; Schmidt, H. W.; Kivala, M.; Urbanavičiutec, I.; Wübbenhorst, M.; Meijer, E. W.; Kemerink, M. *ACS Appl. Mater. Interfaces* **2016**, *8*, 15535.
(57) Haedler, A. T.; Kreger, K.; Issac, A.; Wittmann, B.; Kivala, M.; Hammer, N.; Köhler, J.; Schmidt, H. W.; Hildner, R. *Nature* **2015**, *523*, 196.
(58) Wong, K. T.; Bassani, D. M. *NPG Asia Mater.* **2014**, *6*, 1.
(59) Shen, Y.; Dierking, I. *Appl. Sci.* **2019**, *9*, 2512.
(60) Tschierske, C. *Curr. Opin. Colloid Interface Sci.* **2002**, *7*, 69.
(61) Reczek, J. J. *Naphthalenediimide in Modular Columnar Liquid Crystals: Key Component of Donor–Acceptor Columnar Liquid Crystals*; 2017.
(62) Schadt, M. *Annu. Rev. Mater. Sci.* **1997**, *27*, 305.
(63) Iino, H.; Usui, T.; Hanna, J. I. *Nat. Commun.* **2015**, *6*, 1.
(64) Oladepo, S. A. *Molecules* **2022**, *27*, 1453.
(65) Lin, Y. C.; Li, G. S.; Yu, P. J.; Ercan, E.; Chen, W. C. *J. Chin. Chem. Soc.* **2022**, *69*, 1289.
(66) Kumar, M.; Kumar, S. *Polym. J.* **2017**, *49*, 85.
(67) Goodby, J. W.; Mandle, R. J.; Davis, E. J.; Zhong, T.; Cowling, S. J. *Liq. Cryst.* **2015**, *42*, 593.
(68) Newton, J.; Coles, H.; Hodge, P.; Hannington, J. *J. Mater. Chem.* **1994**, *4*, 869.
(69) Zelcer, A.; Donnio, B.; Bourgogne, C.; Cukiernik, F. D.; Guillon, D. *Chem. Mater.* **2007**, *19*, 1992.
(70) Apreutesei, D.; Mehl, G. H. *J. Mater. Chem.* **2007**, *17*, 4711.
(71) Roberts, J. C.; Kapemaum, N.; Giesselmann, F.; Lemieux, R. P. *J. Am. Chem. Soc.* **2008**, *130*, 13842.
(72) Tschierske, C. *J. Mater. Chem.* **1998**, *8*, 1485.
(73) Kamatham, N.; Ibraikulov, O. A.; Durand, P.; Wang, J.; Boyron, O.; Heinrich, B.; Heiser, T.; Lévêque, P.; Leclerc, N.; Méry, S. *Adv. Funct. Mater.* **2021**, *31*, 1.
(74) van Aerle, N. A. J. M.; Tol, A. J. W. *Macromolecules* **1994**, *27*, 6520.
(75) O'Neill, M.; Kelly, S. M. *J. Phys. D. Appl. Phys.* **2000**, *33*, R67.
(76) Stöhr, J.; Samant, M. G. *J. Electron Spectros. Relat. Phenomena* **1999**, *98*, 189.
(77) Markovitsi, D.; Rigaut, F.; Mouallem, M.; Malthête, J. *Chem. Phys. Lett.* **1987**, *135*, 236.
(78) Eisele, D. M.; Arias, D. H.; Fu, X.; Bloemsma, E. A.; Steiner, C. P.; Jensen, R. A.; Rebentrost, P.; Eisele, H.; Tokmakoff, A.; Lloyd, S.; Nelson, K. A.; Nicastro, D.; Knoester, J.; Bawendi, M. G. *Proc. Natl. Acad. Sci. U. S. A.* **2014**, *111*, E3367.
(79) Shimizu, Y. *Liquid Crystals Toward Soft Organic Semiconductors*; 2011.
(80) Wang, Y.; Shi, J.; Chen, J.; Zhu, W.; Baranoff, E. *J. Mater. Chem. C* **2015**, *3*, 7993.
(81) Laschat, S.; Baro, A.; Steinke, N.; Giesselmann, F.; Hägele, C.; Scalie, G.; Judele, R.; Kapatsina, E.; Sauer, S.; Schreivogel, A.; Tosoni, M. *ChemInform* **2007**, *38*, 4832.
(82) Sergeyev, S.; Pisula, W.; Geerts, Y. H. *Chem. Soc. Rev.* **2007**, *36*, 1902.
(83) Wurzbach, I.; Rothe, C.; Bruchlos, K.; Ludwigs, S.; Giesselmann, F. *J. Mater. Chem. C* **2019**, *7*, 2615.

(84) Gryn, I.; Lacaze, E.; Carbone, L.; Giocondo, M.; Zappone, B. *Adv. Funct. Mater.* **2016**, *26*, 7122.
(85) Guo, X.; Baumgarten, M.; Müllen, K. *Prog. Polym. Sci.* **2013**, *38*, 1832.
(86) Mei, J.; Bao, Z. *Chem. Mater.* **2014**, *26*, 604.
(87) Lei, T.; Dou, J. H.; Pei, J. *Adv. Mater.* **2012**, *24*, 6457.
(88) Sinturel, C.; Bates, F. S.; Hillmyer, M. A. *ACS Macro Lett.* **2015**, *4*, 1044.
(89) Yao, Y.; Dong, H.; Hu, W. *Polym. Chem.* **2013**, *4*, 5197.
(90) Zhao, F.; Yuan, Y.; Ding, Y.; Wang, Y.; Wang, X.; Zhang, G.; Gu, X.; Qiu, L. *Macromolecules* **2021**, *54*, 5440.
(91) Wang, B.; Watt, S.; Hong, M.; Domercq, B.; Sun, R.; Kippelen, B.; Collard, D. M. *Macromolecules* **2008**, *41*, 5156.
(92) Yao, K.; Chen, L.; Chen, X.; Chen, Y. *Chem. Mater.* **2013**, *25*, 897.
(93) Geng, Y.; Wei, Q.; Hashimoto, K.; Tajima, K. *Chem. Mater.* **2011**, *23*, 4257.
(94) McCulloch, I.; Heeney, M.; Bailey, C.; Genevicius, K.; MacDonald, I.; Shkunov, M.; Sparrowe, D.; Tierney, S.; Wagner, R.; Zhang, W.; Chabinyc, M. L.; Kline, R. J.; McGehee, M. D.; Toney, M. F. *Nat. Mater.* **2006**, *5*, 328.
(95) Street, R. A.; Northrup, J. E.; Salleo, A. *Phys. Rev. B - Condens. Matter Mater. Phys.* **2005**, *71*, 1.
(96) Hartmann, L.; Tremel, K.; Uttiya, S.; Crossland, E.; Ludwigs, S.; Kayunkid, N.; Vergnat, C.; Brinkmann, M. *Adv. Funct. Mater.* **2011**, *21*, 4047.
(97) Amundson, K.; Helfand, E.; Quan, X.; Smith, S. D. *Macromolecules* **1993**, *26*, 2698.
(98) Salleo, A.; Kline, R. J.; DeLongchamp, D. M.; Chabinyc, M. L. *Adv. Mater.* **2010**, *22*, 3812.
(99) Skotheim, T. A.; Reynolds, J. R. *Handbook of Conducting Polymers: Conjugated Polymers Processing and Applications*; 2007.
(100) Sommer, M.; Huettner, S.; Thelakkat, M. *J. Mater. Chem.* **2010**, *20*, 10788.
(101) Rychkov, I. *Macromol. Theory Simulations* **2005**, *14*, 207.
(102) Chu, P. H.; Kleinhenz, N.; Persson, N.; McBride, M.; Hernandez, J. L.; Fu, B.; Zhang, G.; Reichmanis, E. *Chem. Mater.* **2016**, *28*, 9099.
(103) Botiz, I.; Stingelin, N. *Materials (Basel).* **2014**, *7*, 2273.
(104) Shibaev, V.; Bobrovsky, A.; Boiko, N. *Prog. Polym. Sci.* **2003**, *28*, 729.
(105) Sneyd, A. J.; Fukui, T.; Paleček, D.; Prodhan, S.; Wagner, I.; Zhang, Y.; Sung, J.; Collins, S. M.; Slater, T. J. A.; Andaji-Garmaroudi, Z.; MacFarlane, L. R.; Garcia-Hernandez, J. D.; Wang, L.; Whittell, G. R.; Hodgkiss, J. M.; Chen, K.; Beljonne, D.; Manners, I.; Friend, R. H.; Rao, A. *Sci. Adv.* **2021**, *7*, eabh4232.
(106) Zhang, L.; Cao, C.; Yakimov, A.; Arges, C. G. *ECS Trans.* **2017**, *80*, 971.
(107) Sinturel, C.; Bates, F. S.; Hillmyer, M. A. *ACS Macro Lett.* **2015**, *4*, 1044.
(108) Morris, M. A. *Microelectron. Eng.* **2015**, *132*, 207.
(109) Mitchell, V. D.; Jones, D. J. *Polym. Chem.* **2018**, *9*, 795.
(110) Leibler, L. *Macromolecules* **1980**, *13*, 1602.
(111) He, X.; Song, M.; Liang, H.; Pan, C. *J. Chem. Phys.* **2001**, *114*, 10510.
(112) Binder, K.; Horbach, J.; Vink, R.; De Virgiliis, A. *Soft Matter* **2008**, *4*, 1555.
(113) Albert, J. N. L.; Epps, T. H. *Mater. Today* **2010**, *13*, 24.
(114) Koo, K.; Ahn, H.; Kim, S. W.; Ryu, D. Y.; Russell, T. P. *Soft Matter* **2013**, *9*, 9059.
(115) Li, W.; Liu, M.; Qiu, F.; Shi, A. C. *J. Phys. Chem. B* **2013**, *117*, 5280.
(116) Lohse, D. J.; Hadjichristidis, N. *Curr. Opin. Colloid Interface Sci.* **1997**, *2*, 171.
(117) Chen, J. Z.; Zhang, C. X.; Sun, Z. Y.; An, L. J.; Tong, Z. *J. Chem. Phys.* **2007**, *127*, 024105.
(118) Matsen, M. W. *Macromolecules* **2012**, *45*, 2161.
(119) Tseng, Y. C.; Darling, S. B. *Polymers (Basel).* **2010**, *2*, 470.
(120) Genabeek, B. van; Lamers, B. A. G.; Hawker, C. J.; Meijer, E. W.; Gutekunst, W. R.; Schmidt, B. V. K. J. *J. Polym. Sci.* **2021**, *59*, 373.
(121) Van Genabeek, B.; De Waal, B. F. M.; Ligt, B.; Palmans, A. R. A.; Meijer, E. W. *ACS Macro Lett.* **2017**, *6*, 674.
(122) Van Genabeek, B.; de Waal, B. F. M.; Gosens, M. M. J.; Pitet, L. M.; Palmans, A. R. A.; Meijer, E. W. *J. Am. Chem. Soc.* **2016**, *138*, 4210.
(123) Lynd, N. A.; Meuler, A. J.; Hillmyer, M. A. *Prog. Polym. Sci.* **2008**, *33*, 875.
(124) Oschmann, B.; Lawrence, J.; Schulze, M. W.; Ren, J. M.; Anastasaki, A.; Luo, Y.; Nothling, M. D.; Pester, C. W.; Delaney, K. T.; Connal, L. A.; McGrath, A. J.; Clark, P. G.; Bates, C. M.; Hawker, C. J. *ACS Macro Lett.* **2017**, *6*, 668.
(125) Widin, J. M.; Schmitt, A. K.; Im, K.; Schmitt, A. L.; Mahanthappa, M. K. *Macromolecules* **2010**, *43*, 7913.
(126) Widin, J. M.; Schmitt, A. K.; Schmitt, A. L.; Im, K.; Mahanthappa, M. K. *J. Am. Chem. Soc.* **2012**, *134*, 3834.

(127) Schmitt, A. K.; Mahanthappa, M. K. *Macromolecules* **2017**, *50*, 6779.
(128) Lamers, B. A. G.; Graf, R.; De Waal, B. F. M.; Vantomme, G.; Palmans, A. R. A.; Meijer, E. W. *J. Am. Chem. Soc.* **2019**, *141*, 15456.
(129) Lee, S.; Gillard, T. M.; Bates, F. S. *AIChE J.* **2013**, *59*, 3502.
(130) van Genabeek, B.; de Waal, B. F. M.; Palmans, A. R. A.; Meijer, E. W. *Polym. Chem.* **2018**, *9*, 2746.
(131) Lamers, B. A. G.; Herdlitschka, A.; Schnitzer, T.; Mabesoone, M. F. J.; Schoenmakers, S. M. C.; De Waal, B. F. M.; Palmans, A. R. A.; Wennemers, H.; Meijer, E. W. *J. Am. Chem. Soc.* **2021**, *143*, 4032.
(132) Berrocal, J. A.; Zha, R. H.; de Waal, B. F. M.; Lugger, J. A. M.; Lutz, M.; Meijer, E. W. *ACS Nano* **2017**, *11*, 3733.
(133) Lamers, B. A. G.; Van Son, M. H. C.; De Graaf, F. V.; Van Den Bersselaar, B. W. L.; De Waal, B. F. M.; Komatsu, K.; Sato, H.; Aida, T.; Berrocal, J. A.; Palmans, A. R. A.; Vantomme, G.; Meskers, S. C. J.; Meijer, E. W. *Mater. Horizons* **2022**, *9*, 294.
(134) Nickmans, K.; Murphy, J. N.; de Waal, B.; Leclère, P.; Doise, J.; Gronheid, R.; Broer, D. J.; Schenning, A. P. H. J. *Adv. Mater.* **2016**, *28*, 10068.
(135) Yang, W.; Zhang, W.; Luo, L.; Lyu, X.; Xiao, A.; Shen, Z.; Fan, X. H. *Chem. Commun.* **2020**, *56*, 10341.
(136) Ishiwari, F.; Okabe, G.; Ogiwara, H.; Kajitani, T.; Tokita, M.; Takata, M.; Fukushima, T. *J. Am. Chem. Soc.* **2018**, *140*, 13497.
(137) Zha, R. H.; Vantomme, G.; Berrocal, J. A.; Gosens, R.; De Waal, B.; Meskers, S.; Meijer, E. W. *Adv. Funct. Mater.* **2018**, *28*, 1.

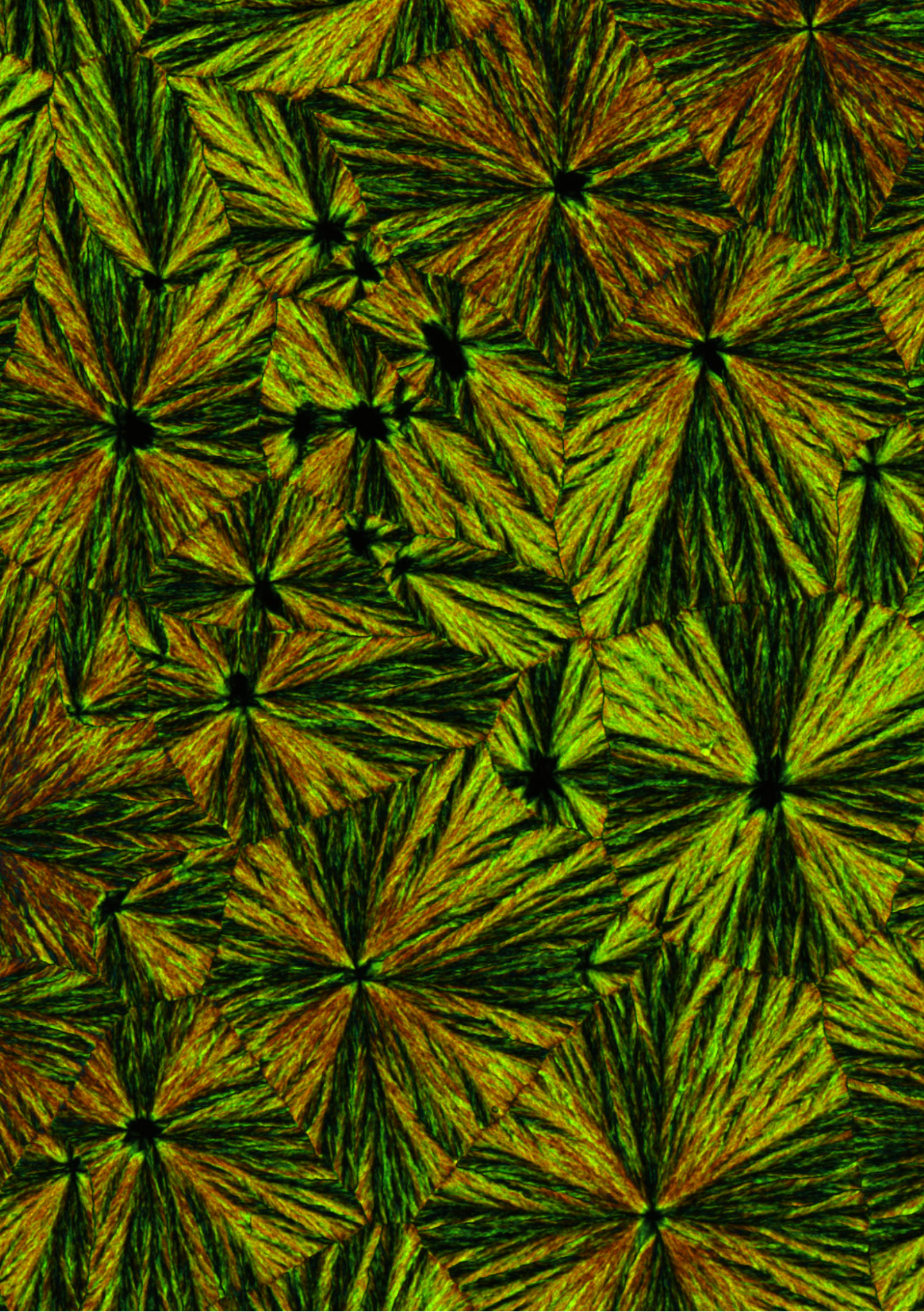

Chapter 2

The characteristics of block molecule design for 2D nanostructures

ABSTRACT: Materials with the ability to phase separate into well-ordered 2D morphologies hold promise for a range of applications, for example, in molecular electronics. However, the prediction of the morphology formed from the molecular structure remains a challenge for the self-assembly of block molecules. Therefore, we report a systematic approach to investigate both the influence of molecular architecture and core symmetry on the morphology of oligodimethylsiloxane (*o*DMS)-based block molecules. We synthesized a library of 20 block molecules with three different architectures (core-centered, head-tail, telechelic), containing four different crystalline blocks (diphenylanthracene, azobenzene, anthraquinone and oligophenylvinylene) and varied the degree of symmetry for two of these cores. In addition, for diphenylanthracene in the core-centered architecture, the effect of alkyl spacer length on morphology was determined. 2D morphologies were obtained when the *o*DMS chains fit into the reported crystal structure. Thus, the core-centered architecture, due to its higher graft density, forms lamellae only with diphenylanthracene. This core has the phenyl rings perpendicular to anthracene, so the distance between the *o*DMS attachment points is greater than for the other, more planar cores. The lower *o*DMS attachment density for the head-tail and telechelic architectures allowed the formation of lamellae for the three other cores. The head-tail architecture has a lower tendency for lamella formation because the *o*DMS can coil onto itself preventing close packing of the cores, which is prevented in the telechelic architecture. A reduction in the length of alkyl end groups in the head-tail and telechelic architectures results in columnar morphologies to minimize the free volume that would otherwise be present in the lamellar morphology. For the core-centered architecture, an increase in the length of the alkyl spacer beyond C_5 was found to result in multiple coexisting lamellar morphologies, which is assigned to minimization of the free volume in the alkane portion of the assembly. The sharpest transitions in the X-ray scattering profile and highest melting and crystallization enthalpies were found when a pentylene spacer connects the core and *o*DMS. This systematic study shows how reported crystal structures can be used in the design of block molecules, enabling *a priori* design of lamellae-forming block molecules, accelerating the development of nanostructured materials for nanoscale lithography and optoelectronics. Some of these applications will be discussed in the following chapters.

Part of the work presented in this chapter will be published:
M. H. C. van Son, B. W. L. van den Bersselaar, B. F. M. de Waal, G. Vantomme, E. W. Meijer, *Manuscript in preparation*
M. H. C. van Son, M. Beslać, B. F. M. de Waal, G. Vantomme, E. W. Meijer, *Manuscript in preparation*

2.1 Introduction

Continued innovation in chemical synthesis and materials processing has led to the ability to create organic 2D materials whose properties differ from those of the bulk.[1,2] For example, the reduced dimensionality of 2D materials results in faster energy transfer through densely packed chromophores.[3–10] When large domains of highly ordered lamellar assemblies are obtained, their applicability in devices is further enhanced by a reduction in packing defects and a smaller number of grain boundaries.[11–13] Organic 2D materials find applications ranging from molecular electronics to photo- and bioactivity, where properties depend on the molecular orientation within the 2D assembly.[14–19]

Spontaneously formed 2D assemblies are ubiquitous in the fields of liquid crystals (LCs),[20] block copolymers (BCPs)[21] and (coil-)rod-coils.[22,23] Liquid crystalline materials can be distinguished into lyotropic and thermotropic, based on the mechanism that results in LC mesophase formation. Lyotropic mesophases are generally formed when amphiphilic molecules self-assemble in the presence of a solvent.[20] Here, the shape anisotropy of the molecules determines the nanostructure obtained by minimization of the free volume between the molecules, following Israelachvili packing parameters.[24] Free volume minimalization also determines which mesophase is formed for thermotropic liquid crystals that self-assemble without solvent.[25–31] Thermotropic liquid crystals consist of a rigid aromatic core segment with one or two side chains.[20] Alkyl and alkoxy side chains are most commonly used, while relatively more bulky side chains, such as perfluorinated alkanes or oligodimethylsiloxanes, are also reported.[29,31] Side chains with a smaller cross-sectional area than the rigid core lead to free volume in the side chain part, while too bulky side chains lead to free volume in the rigid core part.[26] Minimizing this free volume destabilizes the lamellar morphology by reducing the ordering of the aromatic groups. The most stable lamellar morphologies are formed with cross-sectional areas of the side chains and the rigid core (Chapter 1, Figure 5).[25,26] Thus, when aiming for an ordered lamellar morphology for energy transfer applications, space-filling arguments must be considered in the design of the liquid crystal.

Diblock copolymers consist of two covalently linked disperse flexible polymer chains. For these materials, the morphology is determined by the degree of polymerization (N), the block incompatibility, as indicated by the Flory-Huggins parameter (χ), and the volume fraction of the different blocks.[32,33] For 2D morphologies, roughly equal volume fraction of both blocks is required. However, this requirement does not necessarily apply when one of the blocks is rigid. These rigid-flexible BCPs are also called rod-coil BCPs. When the coil has no more than several dozen repeat units and the rod is an aromatic small molecule, these materials are called rod-coil molecules. Like BCPs and LCs, these materials can form 2D morphologies.[22,34,35] Which morphology is formed is determined not only by the phase separation due to the mismatch of the rod and its flexible side chain, but also by the number of coils per rod, as indicated by the grafting density.[36] By controlling the grafting density, the average cross-sectional area of the cores and side chains can be balanced, similar to the free volume arguments described for liquid crystals. The disadvantage of RC and BCP materials is that the length and polydispersity of the flexible chain make them undesirable for certain applications. The longer side chains increase the periodicity compared to LCs and therefore reduce the

amount of active component, while the polydispersity means that the interface between the blocks is poorly defined.[37]

To circumvent the problems associated with polydispersity, our group introduced a class of block molecules in which a crystalline core is coupled to monodisperse ($Đ < 1.00001$) oligodimethylsiloxane (*o*DMS).[38,39] Due to the high immiscibility of *o*DMS with different cores, this design has proven successful for creating well-defined, lamellar morphologies.[40] Moreover, their long-range order and sub-5 nm domain spacings make these block molecules attractive for energy transfer applications that require well-defined molecular ordering.[41,42] For some molecules, an increase in the *o*DMS length resulted in the formation of a different morphology.[43] For naphthalene diimide block molecules, however, the self-assembled morphology did not depend on *o*DMS length, but on molecular design.[44] While the core-centered design of *o*DMS-NDI-*o*DMS reliably yielded columnar structures, the telechelic design of NDI-*o*DMS-NDI consistently resulted in lamellar morphologies. This is in contrast with the block molecule set where the core consisted of two diphenyl groups connected by a triple bond. Here, the morphology depends on both the length of the *o*DMS and the length of the alkyl spacer connecting the *o*DMS and the core (Chapter 1, Figure 8).[45] Moreover, obtaining a columnar or lamellar morphology for hydrazone block molecules depends on careful adjustment of composition and temperature during sample processing.[46] Although the formed morphology of *o*DMS-containing block molecules can generally be explained after synthesis and characterization of the materials, prediction of the morphology would significantly accelerate the development of nanostructured materials. Therefore, we aim to further elucidate the design characteristics of block molecules. Here, we systematically investigate the influence of molecular design and core symmetry on the obtained morphology of *o*DMS-containing block molecules. In addition, we study the effect of alkyl spacer length. The results give insights in how block molecule design can be used to target lamellar morphologies.

2.2 The effect of molecular architecture on block molecule self-assembly

To study the effect of molecular architecture on the self-assembly behavior of block molecules with the intention of creating 2D morphologies, a library of 20 molecules was designed and synthesized (Figure 1, see next page). For this purpose, four different core molecules were chosen: diphenylanthracene (**DPA**), azobenzene (**Azo**), anthraquinone (**AQ**) and oligophenylvinylene (**OPV**). These cores were functionalized with *o*DMS at both ends for the core-centered architecture, at one end for the head-tail architecture and with peripheral cores for the telechelic architecture. For a fair comparison between the block molecules, the *o*DMS content was kept constant throughout the library (14, 15 or 16 silicon atoms per core molecule for core-centered, head-tail or telechelic, respectively). In addition, the degree of symmetry in the **AQ** and **OPV** cores was adjusted by varying the terminal functionalization (**PentO-**, **MeO-** and **H-**). The synthesis of these molecules is described in Chapter 2.5.2 and was performed in collaboration with Bart van den Bersselaar. All molecules were purified by recycling GPC in THF to ensure high purity. The effect of small amounts of impurities is described in Chapter 3.2.6. The molecules

were characterized by differential scanning calorimetry (DSC), medium- and wide-angle X-ray scattering (MAXS and WAXS) and polarized optical microscopy (POM) to obtain detailed information about their thermal and morphological behavior.

Here the results of the core-centered architecture are discussed first, followed by both the head-tail and telechelic architectures with terminal pentoxy groups. Then the differences between the terminal pentoxy (**PentO-**), methoxy (**MeO-**) and hydrogen (**H-**) functionalized **AQ** and **OPV** block molecules are discussed. For the latter comparison, **DPA** is excluded because the electron density is mainly dominated on the anthracene part, and thus the hydrogen-terminated structure will have only a small dipolar moment. **Azo** is excluded to avoid misinterpretation of the results due to altered cis-trans isomerization constants.[47] If the molecules were to follow exclusively block copolymer theory, the *o*DMS volume fraction (0.69–0.79) dictates the formation of a columnar hexagonal phase for all molecules. Although the molecules are not classified as liquid crystals or block copolymers, their mechanistic concepts will be used to explain the differences between the morphologies for the block molecules reported here.

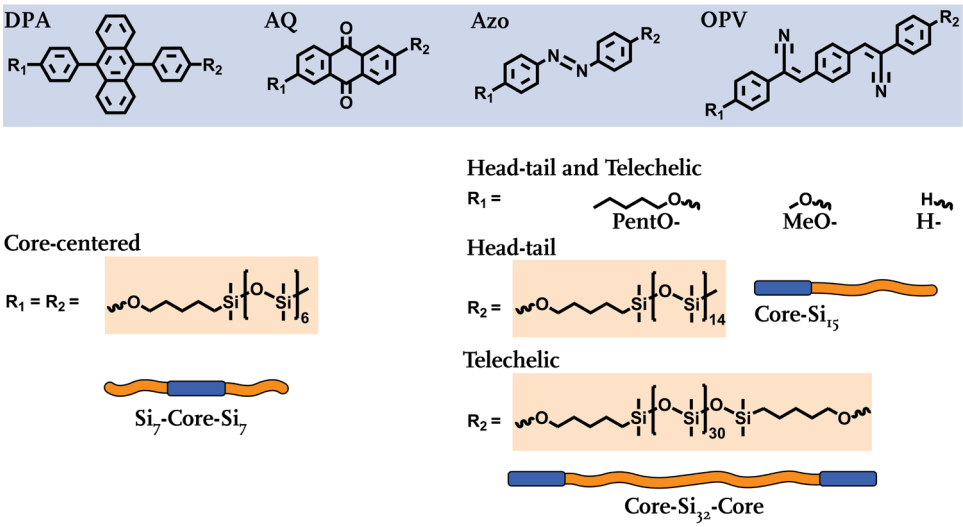

Figure 1. Schematic representation of the molecules used to study the effect of molecular architecture and core symmetry. The four different cores (blue) **DPA**, **AQ**, **Azo** and **OPV** are attached on both sides with $\mathbf{Si_7}$ in the core-centered architecture, on one side with $\mathbf{Si_{15}}$ for the head-tail architecture, or on the periphery of $\mathbf{Si_{32}}$ to obtain the telechelic architecture. The terminus (R_1) of the head-tail and telechelic is pentoxy (**PentO-**) for all four cores, while the terminus for **AQ** and **OPV** is also changed to a methoxy (**MeO-**) or hydrogen (**H-**) group.

2.2.1 Core-centered architecture

The thermal properties of the core-centered molecules were characterized by DSC, with the results shown in Table 1 (Page 24) where they are listed together with the molecules of different architectures to make the comparison easier in the discussion. Two endothermic thermal transitions (T_{endo}) were observed for **Si$_7$-DPA-Si$_7$**, **Si$_7$-Azo-Si$_7$**, and **Si$_7$-OPV-Si$_7$**, while **Si$_7$-AQ-Si$_7$** exhibited only one transition in the studied temperature range –70 – 180 °C. All T_{endo}s had corresponding exothermic thermal transitions (T_{exo}), except for **Si$_7$-Azo-Si$_7$**. The second T_{exo} of **Si$_7$-Azo-Si$_7$** is presumably

below the detection limit of our instrument of –70 °C. The identified thermal transitions were used to analyze the nanoscale ordering of the molecules at temperatures below their T_{exo} using medium-angle X-ray scattering (MAXS). A lamellar morphology was found for **Si$_7$-DPA-Si$_7$** based on the integer reflection peaks of the principal scattering peak q^*. The spacing was calculated at 3.2 nm using $d = 2\pi/q^*$. A double hexagonally packed columnar (2 Col$_h$) phase was found for **Si$_7$-AQ-Si$_7$**, since both principal scattering peaks q' and q^* have consecutive reflection peaks (q, $\sqrt{3}q$, $\sqrt{4}q$, ...) corresponding to a Col$_h$ phase (Figure 2A). The presence of two morphologies is attributed to subtle differences in the packing of the non-*o*DMS part. **Si$_7$-Azo-Si$_7$** also has a columnar morphology, albeit in an oblique arrangement (Col$_{ob}$, Figure 2B). Here, the unit cell dimensions based on the reflection peaks were approximated as a = 3.4 nm, b = 4.1 nm, α = 74°.[48] Finally, **Si$_7$-OPV-Si$_7$** formed a single Col$_h$ phase at 40 °C, a temperature in between the two thermal transitions (Figure 2C). Upon cooling below the lowest T_{exo} (–60 °C), a Col$_{ob}$ phase formed in addition to the previously formed Col$_h$. A visual representation of all observed morphologies is shown in Figure 2D.

Although all four molecules have the same molecular architecture, only **Si$_7$-DPA-Si$_7$** forms a lamellar phase, while **Si$_7$-AQ-Si$_7$**, **Si$_7$-Azo-Si$_7$**, and **Si$_7$-OPV-Si$_7$** form columnar phases. This difference is explained by the different relative bulkiness of the *o*DMS compared to the core. A graphical representation is shown in Chapter 1, Figure 5B and C. The effect of relatively bulky groups on the resulting morphology has been well studied in the field of liquid crystals,[25,26] and has even been used to explain the morphology of liquid crystals with discrete length *o*DMS up to 5 repeat units.[49,50] Here, we extend this knowledge by combining it with the reported crystal structures of the cores before functionalization with *o*DMS. Thus, the relative bulkiness of *o*DMS can be determined. This assumes that the core includes the alkyl spacer if this crystal structures available. Assuming that the reported crystal structures show the most favorable packing of the core molecules, this packing should ideally be maintained after functionalization with *o*DMS. However, *o*DMS has a significantly larger cross-sectional area than the linear alkyls attached to most cores in their crystal structure (21.5 Å^2 (3.5 Å) versus 41 Å^2 (7 Å) for the cross-sectional areas (diameter) of linear alkyls and *o*DMS, respectively).[51,52] Thus, if there is not enough space in the crystal packing of the core for the *o*DMS chain, the preferred packing is disrupted. Based on the reported crystal structure of **DPA** (not shown), **DPA** crystallizes into lamellae with the minimum in plane distances between the attachment points of *o*DMS of 7.5 Å in one direction and 10.4 Å in the other direction.[53] Thus, the *o*DMS can be accommodated without disturbing the packing of non-functionalized **DPA**, leading to a lamellar packing of **Si$_7$-DPA-Si$_7$**. Lamellae can also be observed in the crystal structures of **C$_3$AQC$_3$** and **C$_4$OPVC$_4$**.[54,55] However, for these two molecules the minimum distance between the attachment points of *o*DMS is much smaller than 7 Å at ~4-5 Å. Thus, the relative bulkiness of the *o*DMS cannot be accommodated in the reported crystal structure, which prevents the formation of a lamellar morphology. No lamellar orientation of the cores is observed in the crystal structure of **C$_6$AzoC$_6$**, making a lamellar phase unfavorable after functionalization with *o*DMS.[56] Thus, based on the reported crystal structures and free volume considerations, the formed morphologies of core-centered molecules can be rationalized.

Table 1. Morphological and thermal characterization of the molecules with symmetric cores.

Compound[a]	f_{Si}[b]	Phase[c]	d[d] [nm]	T_{Endo} [°C][e]	ΔH_{Endo} [kJ mol^{-1}][f]	T_{Exo} [°C][e]	ΔH_{Exo} [kJ mol^{-1}][f]
Si$_7$-DPA-Si$_7$	0.74	Lam[g]	3.1[g]	−39 ±1	26	−44 ±1	24
				80±1	44	60 ±1	48
DPA-Si$_{15}$	0.75	Lam	5.8	112 ±1	35	102 ±1	36
DPA-Si$_{32}$-DPA	0.76	Lam	6.1	117 ±2	32[f]	103 ±2	33[f]
Si$_7$-AQ-Si$_7$	0.69	Col$_h$	3.7	−3 ±2	21	−16 ±1	19
		Col$_h$	3.5				
AQ-Si$_{15}$	0.70	Lam	5.9	32 ±1	23	20 ±2	23
AQ-Si$_{32}$-AQ	0.72	Lam	6.3	38 ±2	22[f]	25 ±1	19[f]
Si$_7$-Azo-Si$_7$	0.77	Col$_{ob}$	a = 3.4	4 ±2	26	-2 ±1	24
			b = 4.1	−59 ±2	2		
			α = 74°				
Azo-Si$_{15}$	0.78	Lam[h]	6.3	38 ±1	17	36 ±0.5	17
				13 ±2[h]	1[h]		
Azo-Si$_{32}$-Azo	0.79	Lam	6.7	45 ±2	33[f]	41 ±2	42[f]
Si$_7$-OPV-Si$_7$	0.74	Col$_h$	3.9	30 ±1	11	18 ±1	10
		Col$_{ob}$	a = 2.9	83 ±0.5	2[i]	82 ±0.5	2[i]
			b = 3.5				
			α = 80°				
OPV-Si$_{15}$	0.75	Col$_h$	6.3	107 ±2	14	105 ±1	14
		Col$_{ob}$	a = 4.5	133 ±2	1[i]	131 ±2	1[i]
			b = 5.7				
			α = 82°				
OPV-Si$_{32}$-OPV	0.76	Col$_h$	5.8	107±2	15[f]	104 ±1	17[f]
		Lam	5.1	134 ±[j]	n.d.[i,j]	131 ±2	1[f,i]

[a] Block molecules as shown in Figure 1 and Chapter 2.5.2. [b] Volume fraction of the amorphous *o*DMS, calculated from the bulk densities of PDMS (0.95 g mL^{-1}, converted to ml mol^{-1}),[52] and the densities of the crystal structures of **DPA**,[53] **C$_3$AQC$_3$**,[54] **C$_6$AzoC$_6$**,[56] and **C$_4$OPVC$_4$**.[55] The crystal densities were estimated by dividing the unit cell volume with the number of molecules in the unit cell. [c] Morphology of the nanostructure determined with SAXS, corresponding to the thermal transitions given in the same line. Lam = lamellar, Col$_h$ = columnar hexagonal, Col$_{ob}$ = columnar oblique. [d] Domain spacing (d) calculated with $d = 2\pi/q^*$, with q^* being the principal scattering peak for Lam and Col$_h$. The lattice parameters of the Col$_{ob}$ phases are calculated by fitting the lattice parameters to the experimentally obtained reflection peaks.[48] [e] Thermal transitions as determined by DSC from the second heating and cooling cycle with heating and cooling rates of 10 °C min^{-1}. The endothermic transitions are attributed to melting of the material and the exothermic transitions are attributed to crystallization of the material unless otherwise noted. [f] The enthalpic values are per mole of core molecule and thus are half the measured enthalpic values for the telechelic architecture. [g] An additional principal scattering peak without further reflections was found at 3.2 nm, assigned to a different packing of the non-*o*DMS portion of the molecule. [h] Measured below the order-order transition at 13 °C. [i] Order-disorder (when endothermic) or disorder-order (when exothermic) transition due to their small enthalpic contribution.[57] [j] Not determined as no clear beginning and end of the peak could be identified.

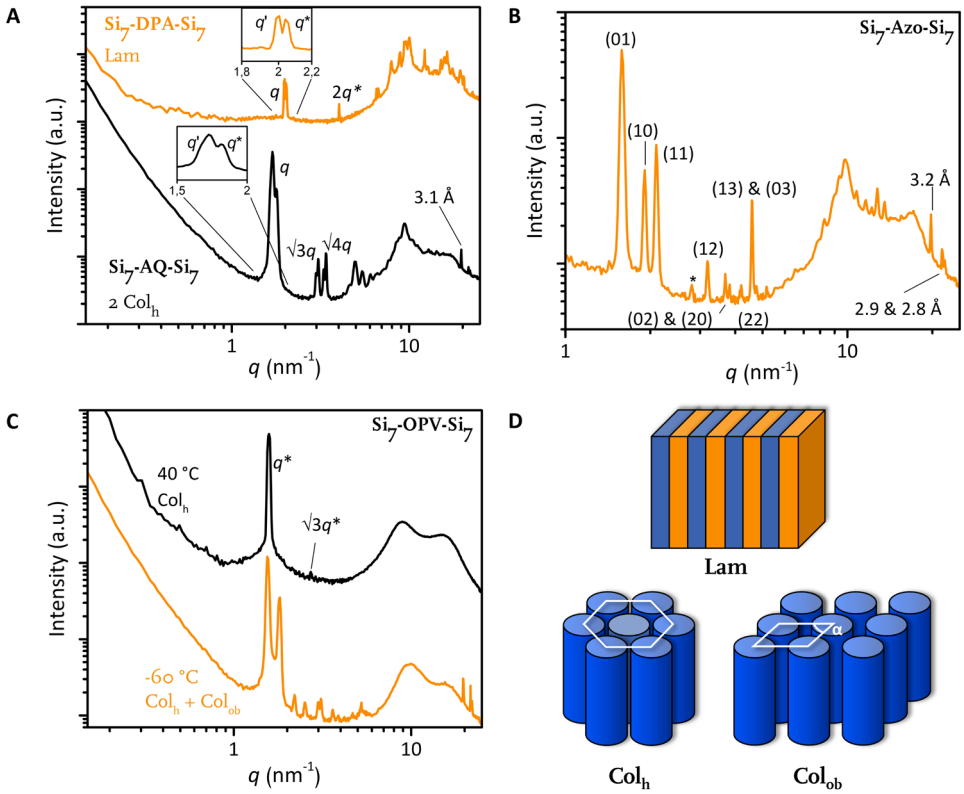

Figure 2. (A) 1D-transmission scattering profiles of **Si$_7$-DPA-Si$_7$** (orange) and **Si$_7$-AQ-Si$_7$** (black). The first peak q consists of two peaks in proximity q^* and q'. The regularly spaced reflection peaks q^* and $2q^*$ for **Si$_7$-DPA-Si$_7$** imply a lamellar ordering. q' is assigned to a different packing of the non-*o*DMS part of the molecule. The $\sqrt{3}q^*$, $\sqrt{4}q^*$ reflection peaks for **Si$_7$-AQ-Si$_7$** imply hexagonally packed columnar order (Col$_h$). (B) 1D-transmission scattering profile of **Si$_7$-Azo-Si$_7$** that forms a columnar oblique packing with lattice parameters: a = 3.4; b = 4.1; α = 74°. (C) 1D-transmission scattering profiles of **Si$_7$-OPV-Si$_7$** showing a columnar hexagonal phase between its two thermal transitions, and an additional columnar oblique below its second transition. (D) Schematic representations of the most common morphologies in this study: lamellar (Lam), hexagonally packed columnar (Col$_h$) and columnar oblique (Col$_{ob}$). For Col$_{ob}$, α indicates the angle of the oblique unit cell.

Additional information about the core-core interactions can be obtained from the wide-angle region (WAXS) (q > 7 nm^{-1}) of the 1D transmission scattering profile. The WAXS region of **Si$_7$-DPA-Si$_7$** shows many sharp peaks indicating the crystallinity of the DPA core. For **Si$_7$-AQ-Si$_7$** and **Si$_7$-Azo-Si$_7$**, the π-π distance was clearly visible at 3.1 Å and 3.2 Å, respectively. For **Si$_7$-OPV-Si$_7$**, two π-π distances were observed at 3.1 Å and 2.9 Å. Two spacings in this region is characteristic of a Col$_{ob}$ phase due to ordering of the molecules within a disk (intradiscoidal stacking) and stacking of the disks in a columnar fashion (intracolumnar stacking).[48] Knowledge about the spatial accommodation of *o*DMS can also be obtained from this region. Here, the peak at ~10 nm^{-1} corresponds to the average diameter of the *o*DMS, while the width provides insight into how fluid it is in the formed nanostructure.[51,52] For **Si$_7$-OPV-Si$_7$**, a broad halo is observed around this peak, implying that the *o*DMS is amorphous. In contrast, the sharpness of this peak for **Si$_7$-DPA-Si$_7$**, **Si$_7$-AQ-Si$_7$**, and **Si$_7$-Azo-Si$_7$** implies that the movement of the *o*DMS chain

in these materials is at least partially restricted. This immobilization of the *o*DMS is probably most pronounced at the alkane-*o*DMS interface and becomes less pronounced further into the *o*DMS matrix. As such, this immobilization is often not observed for longer *o*DMS chains because of the relatively larger contribution of amorphous *o*DMS. For the lamellar **Si$_7$-DPA-Si$_7$**, this immobilization of *o*DMS confirms that the *o*DMS can be incorporated without disrupting the lamellar packing.

2.2.2 Head-tail and telechelic architectures

In both the head-tail and telechelic architectures, the **DPA**, **AQ**, and **Azo** block molecules crystallized into a lamellar nanostructure. For **AQ** and **Azo**, the difference between the lamellae formed for these architectures and the columnar packing for the core-centered architecture can be explained by the relative size of the *o*DMS chain. Here, each core is grafted with a single *o*DMS chain, effectively allowing for more space for the *o*DMS through the formation of an interdigitated packing in which the *o*DMS of adjacent molecules point in alternating directions. This interdigitated lamellar packing fits well with the measured lamellar spacings and calculated volume fractions of *o*DMS, as shown in Figure 3 for **DPA-Si$_{32}$-DPA**. The lamellae in the telechelic architecture are interconnected, while in the head-tail architecture a slipping plane is present (Figure 3). This slipping plane has a pronounced effect on the thermal transitions of the **DPA**, **AQ**, and **Azo**. Although both architectures form lamellae with similar enthalpies per core block, the melting point of the telechelic architecture is ~6 °C higher than for the head-tail architecture due to this interconnectivity between the layers. Since the core packing is not affected by the slipping plane, the observed enthalpies between the two architectures are similar.

A different thermal and morphological behavior was observed for the head-tail and telechelic **OPV** molecules than for the other cores. Both **OPV-Si$_{15}$** and **OPV-Si$_{32}$-OPV** exhibited a crystallization temperature with a subsequent order-disorder transition at higher temperatures (Table 1).[57] A liquid crystalline Col$_h$ phase was observed between the two thermal transitions, as promoted by the *o*DMS volume fraction. Such thermotropic liquid crystalline behavior is often observed in **OPV**-based materials.[58,59] Upon further cooling, crystallization of the material leads to an additional morphology coexisting with the Col$_h$ phase, which was assigned to Col$_{ob}$ for **OPV-Si$_{15}$** and Lam for **OPV-Si$_{32}$-OPV**. The difference between the crystallized morphologies is hypothesized to be caused by shape anisotropy in the head-tail **OPV-Si$_{15}$**. In this head-tail architecture, the *o*DMS is free to collapse onto itself to reduce unfavorable interactions, making it relatively bulkier. However, this collapse of the *o*DMS is suppressed in the telechelic architecture due to the symmetry of the molecule.[24] This difference of **OPV-Si$_{15}$** with the other head-tail molecules that do form lamellae could not be related to the distances between the *o*DMS attachment points, as these were similar for **Azo** and **OPV**. A different hypothesis was that the **OPV** molecules have weaker in-plane crystalline interactions compared to the other cores, which would reduce the propensity for lamella formation. This hypothesis was unvalidated when calculating the total in-plane interaction energies in the crystal lattice using CrystalExplorer and the reported crystal structures of the cores.[60] The largest in-plane interaction energies were found for **OPV** (~ −290 kJ mol^{-1}) compared to **DPA** (~ −190 kJ mol^{-1}), **AQ** (~ −280 kJ mol^{-1}) and **Azo** (~ −200 kJ mol^{-1}).[60–63] Although we propose that **OPV-Si$_{15}$** forms a columnar morphology as the *o*DMS coils onto itself, it

remains to be elucidated why this is only observed with **OPV-Si$_{15}$**. Combining the results of the three architectures shows that the relative size of the *o*DMS with respect to the core must be taken into account for the design of block molecules. For this purpose, the crystal structure of the non-functionalized core can be used, if reported, although the alkylated core would be preferred as the alkyl side chains can induce different core packings.[64]

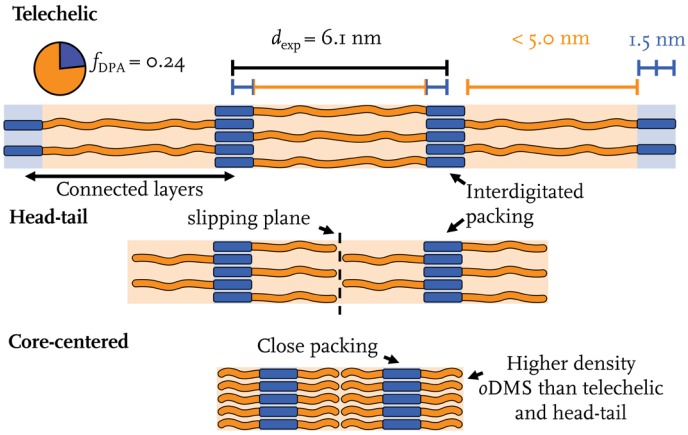

Figure 3. Schematic of the 2D lamellar morphology of the telechelic, head-tail and core-centered molecules. The given distances for the telechelic architecture correspond to **DPA-Si$_{32}$-DPA**, with the *o*DMS length calculated from its stretched length of 0.155 Å per repeat unit,[51,52] and the DPA length is derived from its crystal structure.[53] Arrows are used to clarify the terminology of the main text.

2.2.3 Branched *o*DMS

To further study how the *o*DMS density at the *o*DMS-alkane interface in the core-centered architecture affects the morphology, **Si$_{7b}$-DPA-Si$_{7b}$** was synthesized (Figure 4, see next page). By attaching the alkyl spacer to the central silicon atom of the *o*DMS side chain, branched *o*DMS is obtained, effectively resulting in two linear *o*DMS chains of length 4 per alkyl chain. The lamellar spacing of **Si$_{7b}$-DPA-Si$_{7b}$** of 2.6 nm is therefore smaller than that of **Si$_7$-DPA-Si$_7$** (3.1 nm). The bulkier branched side chains lead to a higher *o*DMS density, which weakens the core-core interactions. This is evident from the lower melting point for **Si$_{7b}$-DPA-Si$_{7b}$** of 5 °C compared to 80 °C for **Si$_7$-DPA-Si$_7$**, and the broader peaks in the WAXS region shown for both molecules below their lowest T_{exo}. These results confirm the requirements for matching the cross-sectional area of the side chain to the available space in the crystal structure. The broad bump below the principal scattering peak indicates that not all material has crystallized.

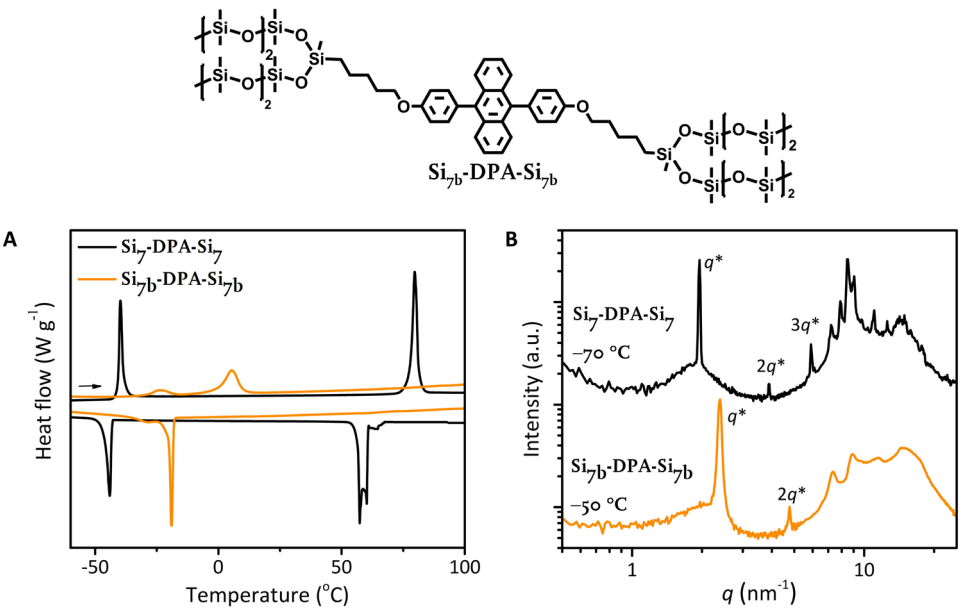

Figure 4. Chemical structure of **Si$_{7b}$-DPA-Si$_{7b}$**, which has the same length *o*DMS as **Si$_7$-DPA-Si$_7$** but with branched *o*DMS. (A) Scaled DSC traces of **Si$_7$-DPA-Si$_7$** (black) and **Si$_{7b}$-DPA-Si$_{7b}$** (orange). Arrows indicate heating. Heating and cooling rate of **Si$_7$-DPA-Si$_7$** was 10 °C min^{-1}, and for **Si$_{7b}$-DPA-Si$_{7b}$** 2 °C min^{-1}. (B) 1D-transmission scattering profiles of **Si$_7$-DPA-Si$_7$** (black) and **Si$_{7b}$-DPA-Si$_{7b}$** (orange). The WAXS region (>7 nm^{-1}) clearly shows less well-defined ordered for **Si$_{7b}$-DPA-Si$_{7b}$** than for **Si$_7$-DPA-Si$_7$**.

2.2.4 Core symmetry

The previous results used aromatic groups with pentoxy spacers on both sides, resulting in a symmetric crystalline core. However, not all aromatic groups are symmetric but can still form well-defined nanoscale morphologies, such as hydrazone or ureidopyrimidinone telechelic block molecules.[40,46] To systematically study the effect of core symmetry, the alkyl end group in the head-tail and telechelic architectures of **AQ** and **OPV** was changed from a pentoxy-chain (**PentO-**), to a methoxy-group (**MeO-**), as well as removed (**H-**). The thermal and morphological properties of these materials are summarized in Table 2.

For the **AQ** molecules, a clear reduction in thermal transitions was observed when going from pentoxy, to methoxy, to hydrogen end groups. This reduction was not found for the **OPV** series. It is assumed that this is caused by the size of the molecules, since change of terminus on the **AQ** core produces a larger relative length difference than in the **OPV**. A pronounced difference between the two cores was also observed in their respective formed morphologies. The **MeO-AQ** and **H-AQ** block molecules, for both architectures, phase separated into a Col$_h$ phase rather than the Lam phase found for **PentO-AQ-Si$_{15}$** and **PentO-AQ-Si$_{32}$-AQ-OPent**. Again, this difference can be attributed to a minimization of free volume as shown schematically in Figure 5.[26] When the same alternating, lamellar packing is adopted that was found for the pentoxy end groups, the shorter end groups lead to an underfilling of the space in the alkane region. The **OPV** block molecules showed a different effect of the end groups on the morphology formed.

Regardless of the end group, the same columnar morphologies were found, the only difference being that **PentO-OPV-Si$_{32}$-OPV-OPent** formed an additional lamellar phase. This shows that core symmetry can stabilize a lamellar morphology by space-filling arguments in a telechelic architecture.

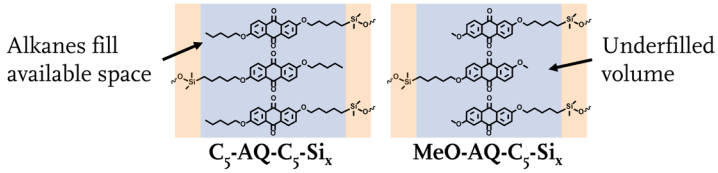

Figure 5. Schematic indication of the free volume that would be present if **MeO-AQ-Si$_{15}$** formed the same interdigitated lamellar structure as **Pent-AQ-Si$_{15}$**. Shown here for the head-tail architecture, but the same arguments hold for **H-AQ-Si$_{15}$**, as well as for the columnar **MeO-AQ-Si$_{32}$-AQ-MeO** and **H-AQ-Si$_{32}$-AQ-H**. This diagram shows how symmetric cores stabilize the lamellar packing.

Table 2. Morphological and thermal characterization of the **AQ** and **OPV** block molecules, depending on the end group.

Compound[a]	End group	Phase[b]	d[c] [nm]	T_{Endo} [°C][d]	ΔH_{Endo} [kJ mol^{-1}][d]	T_{Exo} [°C][d]	ΔH_{Exo} [kJ mol^{-1}][d]
AQ-Si$_{15}$	PentO	Lam	5.9	32 ±1	23	20 ±2	23
	MeO	Col$_h$	5.6	23 ±2	16	14 ±2	18
	H	Col$_h$	5.7	−18 ±3	10	−21 ±3	9
AQ-Si$_{32}$-AQ	PentO	Lam	6.3	38 ±2	44	25 ±1	37
	MeO	Col$_h$	5.7	23 ±5	16	14 ±4	18
	H	Col$_h$	5.9	−10 ±1	19	−13 ±2	19
OPV-Si$_{15}$	PentO	Col$_h$	6.3	107 ±2	14	105 ±1	14
		Col$_{ob}$	[f]	133 ±2	1[e]	131 ±2	1[e]
	MeO	Col$_h$	6.1	110 ±5	9	102 ±1	16[i]
		Col$_{ob}$	[g]			107 ±1[i]	
	H	Col$_h$	6.0	108 ±1	21	102 ±1	22
		Col$_{ob}$	[h]				
OPV-Si$_{32}$-OPV	PentO	Col$_h$	5.8	107 ±2	30	104 ±1	35
		Lam	5.1	134 ±[j]	n.d.[j]	131 ±2	2[e]
	MeO	Col$_h$	6.5	123 ±2	27	117 ±2	24
	H	Col$_h$	6.2	104 ±3	18	95 ±5	41

[a] Block molecules as shown in Figure 1 and in Chapter 2.5.2. [b] Morphology of the nanostructure determined with SAXS under the temperature of the lowest exothermic peak. Lam = lamellar, Col$_h$ = columnar hexagonal, Col$_{ob}$ = columnar oblique. [c] Domain spacing (d) calculated with $d = 2\pi/q^*$, with q^* being the principal scattering peak for Lam and Col$_h$. The lattice parameters of the Col$_{ob}$ phases are calculated by fitting the lattice parameters to the experimentally obtained reflection peaks.[48] [d] Thermal transitions and enthalpies as determined by DSC from the second heating and cooling cycle with heating and cooling rates of 10 °C min^{-1}. [e] Order-disorder (when endothermic) or disorder-order (when exothermic) transition due to their small enthalpic contribution.[57] [f] Columnar oblique lattice parameters **PentO-OPV-Si$_{15}$**: a = 4.5; b = 5.7; α = 82°. [g] Columnar oblique lattice parameters **MeO-OPV-Si$_{15}$**: a = 4.9; b = 5.7; α = 83°. [h] Columnar oblique lattice parameters **MeO-OPV-Si$_{15}$**: a = 4.3; b = 5.6; α = 82°. [i] Two temperatures are given as two clear maxima could be distinguished, while a single enthalpy is given as the peaks were overlapping. [j] Not determined as no clear begin and end of the peak could be resolved.

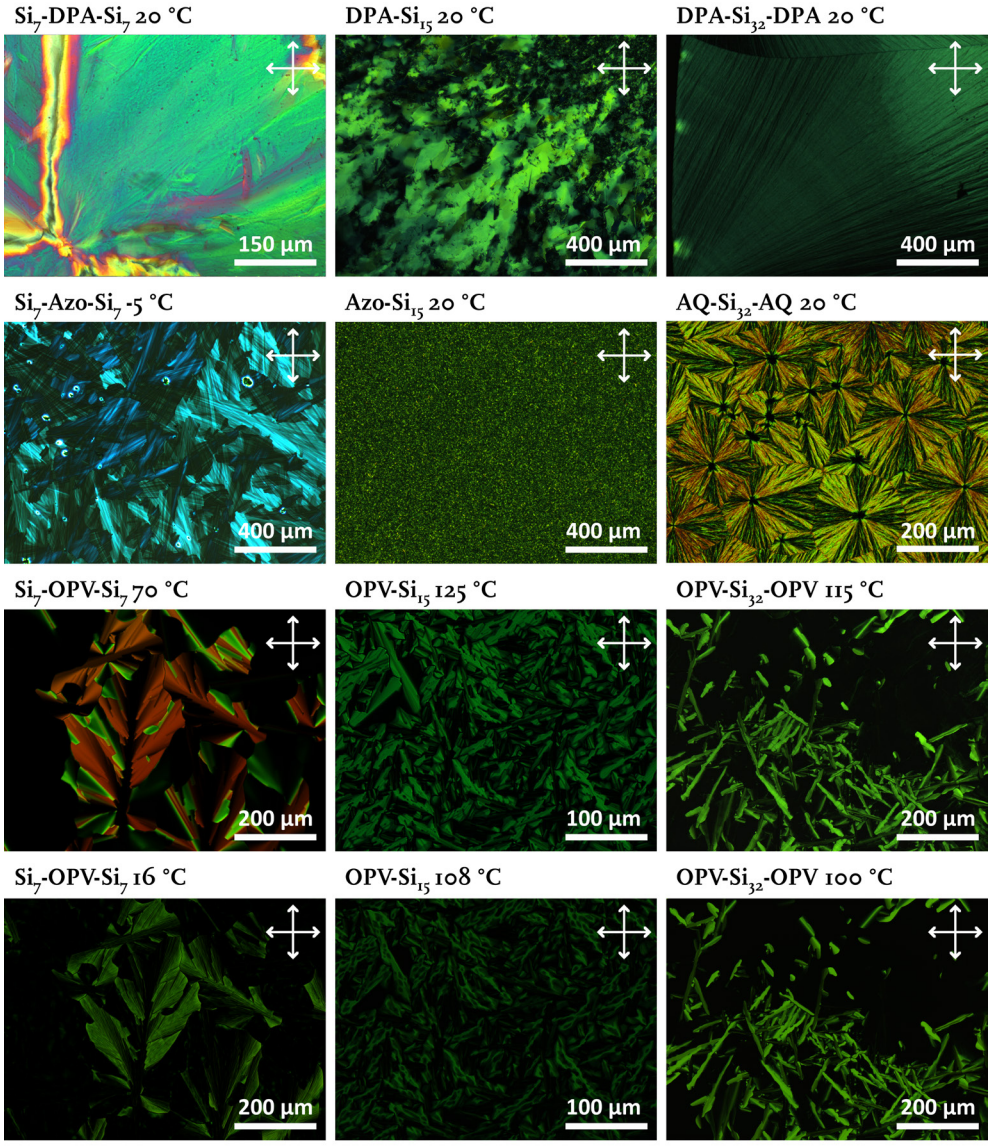

Figure 6. Polarized optical microscopy images after cooling with 1 °C min^{-1} from their isotropic melt. The DPA block molecules form large domains regardless of architecture. For Azo and AQ, only **Si_7-Azo-Si_7** and **AQ-Si_{32}-AQ** formed large domains. The POM-image of **Azo-Si_{15}** is representative for the molecules not shown here, with domain sizes that could not be resolved. The POM-images of the OPV block molecules initially form large domains below their highest thermal transition (row 3) to which an additional texture is added upon cooling below their lower thermal transition (row 4).

2.2.5 Polarized optical microscopy analysis

Application of the synthesized materials in devices that rely on energy transport requires the formation of domains with aromatic groups aligned over tens of micrometers.[65,66] To this end, the molecules were additionally analyzed using polarized optical microscopy (POM). Under their T_{exo}, birefringent domains were formed upon cooling from the melt at 1 °C min^{-1}, although these domains were not observed for **H-AQ-Si$_{15}$** and **H-AQ-Si$_{32}$-AQ-H**. About half of the molecules in the library formed large birefringent domains of tens of micrometers to centimeters in size under their T_{exo} (Figure 6) while the other half showed only small domains that could not be resolved in size. Large domains are obtained with a small number of crystal nuclei or by rapid domain growth after a crystal nucleus is formed. It could therefore be expect that a correlation could be made between the domain size and both X-ray scattering and DSC data, since these techniques provide information about the crystallization behavior of the material. However, although the reported compounds allow a thorough comparison of the requirements for large domains, the precise correlation between the three techniques could not be made. This is discussed here for the compounds with symmetric cores (Table 1). The domain size could not be related to the crystallization enthalpy. All **DPA** compounds show large domains and have high crystallization enthalpies (>30 kJ mol^{-1}), while all **OPV** compounds show large domains and have significantly lower enthalpies (~13 kJ mol^{-1}). In contrast, all **AQ** and **Azo** compounds have enthalpies in between these two values, but they do not all form large domains. Additionally, the domain size could not be related to the sharpness of the crystallization peak nor the sharpness of the peaks in the WAXS region. This is clearly exemplified by **Si$_7$-DPA-Si$_7$**, **Si$_7$-AQ-Si$_7$** and **Si$_7$-Azo-Si$_7$** that all have pronounced peaks in their WAXS region (Figure 3). The crystallization peak for **Si$_7$-DPA-Si$_7$** is poorly defined (Figure 4), while the crystallization peaks are sharp for **Si$_7$-AQ-Si$_7$** and **Si$_7$-Azo-Si$_7$**. However, only **Si$_7$-DPA-Si$_7$** and **Si$_7$-Azo-Si$_7$** form large domains. The small domains for **Si$_7$-AQ-Si$_7$** might be related to its coexisting double columnar morphology, but all three **OPV** molecules also have coexisting phases and still show large domains. This difference might be explained by a combination of the X-ray scattering and DSC data. For **Si$_7$-AQ-Si$_7$** the two coexisting phases crystallize at the same temperature. For the **OPV** molecules, first micrometer sized domains are formed with the first phase, while crystallization of the coexisting phase added texture to the existing domains. The precise relation between the X-ray scattering and DSC data to the domain size remains to be elucidated.

2.2.6 Conclusions on molecular architecture

A library of 20 molecules was synthesized to study the influence of molecular design on the bulk self-assembly properties of block molecules consisting of aromatic cores functionalized with amorphous oligodimethylsiloxane (*o*DMS). Both the molecular architecture and the degree of symmetry of the aromatic core were varied. For this purpose, diphenylanthracene (**DPA**), anthraquinone (**AQ**), azobenzene (**Azo**), and oligophenylvinylene (**OPV**) were used as aromatic cores with different alkyl end groups. The obtained results are explained by space-filling arguments in conjunction with the reported crystal structures. The core-centered architecture is found to be best suited for bulkier cores, due to the higher *o*DMS density at the alkane-*o*DMS interface. For the head-tail and telechelic architectures, the cores exhibit an interdigitated packing with

adjacent molecules having the *o*DMS pointing outward in alternating directions. For the lamellae-forming diphenylanthracene (**DPA**), anthraquinone (**AQ**), and azobenzene (**Azo**), the telechelic architecture results in ~6 °C higher thermal transitions than for the head-tail architecture. This difference is explained by the interconnection of the different crystalline layers in the telechelic architecture, whereas in the head-to-tail architecture a slipping plane is present. An additional difference between these two architectures is illustrated by the **OPV** block molecules. In the head-tail architecture, the *o*DMS is assumed to coil on to itself which increases its relative bulkiness and leads to a columnar phase. In contrast, the telechelic architecture prevents this coiling, leading to a lamellar phase for **OPV-Si$_{32}$-OPV**. The templating effect for the telechelic architecture is observed only for symmetric cores, as it allows space filling in the non-*o*DMS layer. Why we only see this difference between the head-tail and telechelic architectures for the **OPV** molecules might be related to the strength of the interactions within the crystal structure. This is currently under investigation.

Combining these results, we show how space-filling arguments can be used to explain the formed morphology of *o*DMS-containing block molecules. Combined with the distances between the attachment points of *o*DMS from a reported crystal structure of the core, preferably with alkyl chains, this enables an *a priori* design of block molecules.

2.3 The effect of alkyl spacer length on the properties of core-centered DPA block molecules

In addition to molecular architecture and core symmetry, there is another fundamental design question related to the length of alkyl spacers connecting the aromatic core with the *o*DMS chain. Previously, both pentylene and undecylene spacers were used in the design of block molecules. Only for telechelic NDI block molecules with *o*DMS of length 8 (**Si$_8$**) have both spacer lengths been reported, albeit in separate articles.[44,67] Comparing their thermal behavior, a ~15 °C higher melting temperature is found for the block molecule with the pentylene spacer, but with a lower enthalpy (26 and 18 kJ mol^{-1} for pentylene and undecylene, respectively). This shows that the alkyl length can have a significant influence on the material properties of block molecules. However, a clear rationale for the choice of a particular alkyl length is lacking. Therefore, we report here the systematic study of alkyl spacer length. For this purpose, **DPA** was chosen as the core in a core-centered architecture. This choice is based on lamellae-forming **Si$_7$-DPA-Si$_7$**, where the strong intralayer interactions based on the WAXS region leads to high melting enthalpies and the formation of domains up to 1 cm in size. For this design, it is thus expected that differences in spacer length will have clearly distinguishable effects on the thermal, morphological and crystallization behavior of the material.

For this systematic study, the alkyl spacer length was varied between **C$_4$** and **C$_{11}$** with a constant *o*DMS length of 7 (**Si$_7$**). The molecules are shown in Figure 7 and will be referred to by their alkyl length. In addition, both no spacer and a chiral spacer were used, which will be referred to as **Si$_{11}$** and **C$_5$*** respectively. The molecules with an alkyl spacer were synthesized by first synthesizing *o*DMS functionalized bromoalkanes via hydrosilylation, which were then coupled to 9,10-diphenolanthracene. **Si$_{11}$** was

synthesized from 9,10-diphenolanthracene using Strykers' reagent to couple with hydride-functionalized *o*DMS of length 11. Unfortunately, not all intermediates are fully characterized (see Chapter 2.5.2.5), but ^{1}H NMR spectroscopy confirmed the structure assigned. All final molecules were purified with recycling GPC to ensure high purity, which was confirmed by ^{1}H NMR, ^{13}C NMR, MALDI-ToF-MS, and GPC.

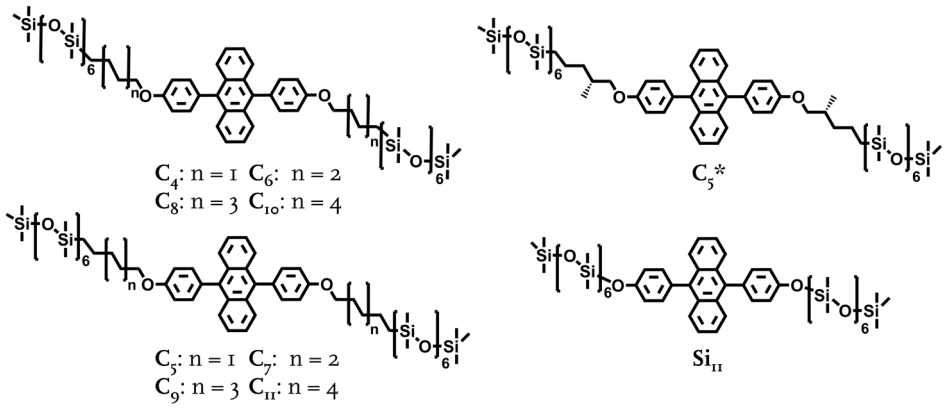

Figure 7. Molecular structures of $\mathbf{C_4}$ - $\mathbf{C_{11}}$, $\mathbf{C_5}$* and $\mathbf{Si_{11}}$.

The thermal behavior was studied with differential scanning calorimetry (DSC) with the results reported in Table 3 on the next page. All molecules with alkyl spacers are solid at room temperature, while $\mathbf{Si_{11}}$ is a liquid for which no thermal transitions are observed down to –70 °C. This shows that the alkyl spacer is required to increase the distance between the bulky *o*DMS and the aromatic block to allow crystallization of the core. As shown in the table, both $\mathbf{C_4}$ and $\mathbf{C_5}$ exhibit multiple thermal transitions, while $\mathbf{C_6}$ to $\mathbf{C_{11}}$ and $\mathbf{C_5}$* exhibit a single thermal transition. The single thermal transitions are sharp, while the transitions for $\mathbf{C_4}$ and $\mathbf{C_5}$ exhibit a more complex shape, indicating different crystallization behavior (Figure 8A, page 35). A clear odd-even effect is observable for $\mathbf{C_x}$ with $6 \leq x \leq 11$ on both T_m and T_c and the corresponding enthalpy changes (Figure 8B). For $\mathbf{C_x}$ with x odd, the T_m, T_c and enthalpies are higher than the immediately adjacent analogs with even numbers. This is similar to what has been observed for the solid/solid transitions of 2,5-di-*n*-alkoxy-1,4-benzoquinones,[68] or the melting point of dialkylsuccinates.[69] There, the odd-even effect is explained by a more favorable packing for odd alkyl lengths. To study the molecular packing of the DPA derivatives, X-ray scattering is used. $\mathbf{C_4}$ and $\mathbf{C_5}$ exhibit many crystalline interactions in the WAXS region (>7 nm^{-1}, Figure 2C), which explains why their enthalpies and thermal transitions are higher than for longer alkyl lengths. $\mathbf{C_5}$* and $\mathbf{C_6}$ show two sharp peaks around 20 nm^{-1} (3.1 and 2.8 Å) that are not observed for the other molecules. These values are assigned to close core-core interactions. $\mathbf{C_5}$*, $\mathbf{C_7}$, $\mathbf{C_9}$ and $\mathbf{C_{11}}$ exhibit peaks at 9 nm^{-1} corresponding to 7Å, the diameter of *o*DMS.[52] It is hypothesized that the odd lengths of the spacers can accommodate the *o*DMS better through a more perpendicular orientation of the *o*DMS with respect to the **DPA** monolayer, as is common for self-assembled monolayers.[70–72] This results in partial immobilization of *o*DMS and therefore higher thermal transitions and enthalpies.

Table 3. Thermal and morphological properties of the **DPA** molecules with various alkyl spacers.

Compound	T_m [a,b] [°C]	ΔH_m [a,c] [kJ mol^{-1}]	T_c [a,b] [°C]	ΔH_c [a,c] [kJ mol^{-1}]	d_{lam} [d] [nm]
$\mathbf{C_4}$	0 ±2	10	−7 ±3	9	3.3[e]
	83 ±2	24	76 ±3	26	
$\mathbf{C_5}$	−39 ±1	26	−44 ±1	24	3.1[f]
	80 ±1	44	60 ±2	48	
$\mathbf{C_6}$	26 ±2	15	9 ±1	16	4.1; 4.5; 5.4
$\mathbf{C_7}$	42 ±1	20	28 ±1	21	4.2; 4.5; 5.5
$\mathbf{C_8}$	40 ±1	18	23 ±1	18	4.3; 4.5; 5.8
$\mathbf{C_9}$	60 ±2	24	48 ±0.5	25	4.5; 4.7; 6.2
$\mathbf{C_{10}}$	59 ±2	21	47 ±0.2	22	4.5; 4.7; 6.2
$\mathbf{C_{11}}$	69 ±1	25	60 ±0.5	26	4.5; 4.7; 6.2
$\mathbf{C_5}$*	39 ±2	20	27 ±0.5	20	4.1; 4.4; 5.1
$\mathbf{Si_{11}}$	< −70 °C	-	< −70 °C	-	-

[a] Thermal transitions and enthalpies as determined by DSC from the second heating and cooling cycle with heating and cooling rates of 10 °C min^{-1}. [b] Error margins taken as the FWHM. [c] The error margin on enthalpy is ~5%. [d] Lamellar spacing as calculated from the principal scattering peak q^* with $d_{lam} = 2\pi/q^*$, measured at room temperature. [e] An additional broad peak is observed at 4.8 nm with no reflections. [f] An additional sharp peak is observed at 3.2 nm without reflections.

In the MAXS region of the X-ray scattering profiles (< 7 nm^{-1}), for $\mathbf{C_4}$ and $\mathbf{C_5}$ lamellae are clearly observable as integer reflection peaks from the principal scattering peak (Figure 8C). The lamellar spacings were calculated to be 3.3 nm and 3.1 nm for $\mathbf{C_4}$ and $\mathbf{C_5}$, respectively. This larger spacing for the smaller spacer length indicates a different packing of the core, as also evidenced by the difference in WAXS region. For $\mathbf{C_4}$, an additional broad peak is observed at 4.8 nm, indicating imperfect packing of the material throughout the sample. An additional peak is also observed for $\mathbf{C_5}$. However, the sharpness of the peak and its similar spacing of 3.2 nm as the lamellar arrangement (3.1 nm) indicate that this peak originates from a slightly different crystalline packing within the lamellar arrangement with regular spacing. While for $\mathbf{C_4}$ the broad peak is preserved upon cooling below the lowest exothermic transition, the additional scattering peak of $\mathbf{C_5}$ disappears. Combined with the higher melting enthalpy for $\mathbf{C_5}$, it is assumed that for these two materials $\mathbf{C_5}$ leads to the most favorable crystalline ordering. The spectra for $\mathbf{C_6}$ to $\mathbf{C_{11}}$ and $\mathbf{C_5}$* show three co-existing lamellae, of which two have similar spacings while the other has a larger spacing. These peaks are assigned for $\mathbf{C_5}$* in Figure 8E and the peak assignments are similar for $\mathbf{C_6}$ to $\mathbf{C_{11}}$. The two similar packings are likely the result of small differences in alkyl orientation, while the less defined, larger spacing is likely the result of packing defects. As expected, longer alkyl lengths lead to longer lamellar spacings (Figure 8D, Table 3). Different thermal treatments, such as slow or fast cooling or keeping the sample isothermal just below the melting point did not change the scattering profiles. These results indicate that for short alkyls, the alkyl can really be considered as the spacer and the block molecule consists only of *o*DMS and non-*o*DMS blocks. However, by increasing the length of the spacer, the alkyl spacer must be considered as a separate entity that requires less space than *o*DMS (Figure 8F). This underfilling leads to destabilization of a single lamellar morphology. Therefore, to reduce the complexity of the system, it is recommended to use pentylene spacers.

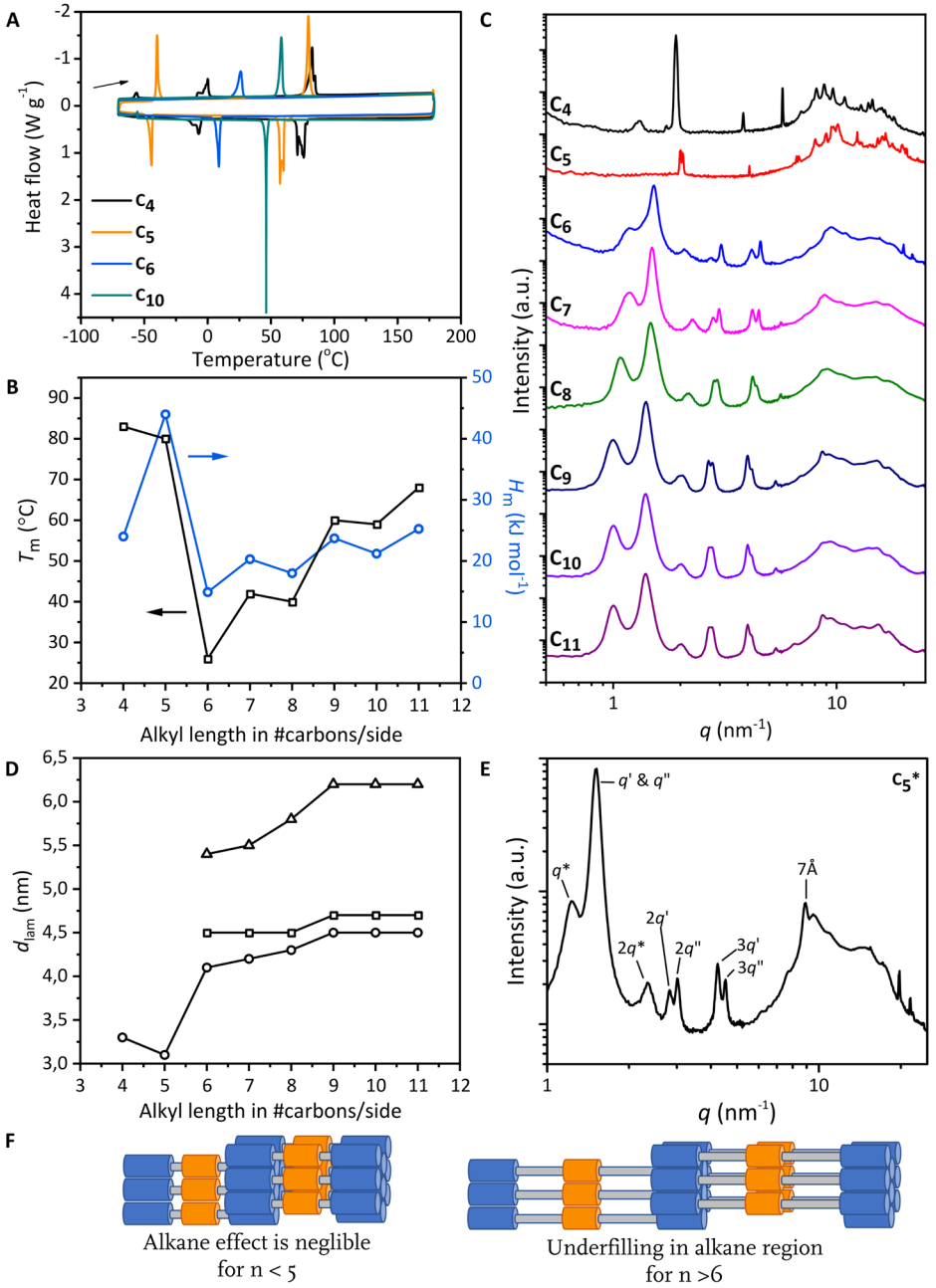

Figure 8. (A) Differential scanning calorimetry traces of the second cycle of C_4 - C_6 and C_{10} at 10 °C min^{-1} showing melting and crystallization peaks (exothermic down). The arrow indicates heating. The second heating and cooling cycle is shown. (B) Alkyl length dependence of melting temperature (black) and enthalpy (blue). (C) 1-D transmission scattering data of compounds C_4 – C_{11}. (D) Alkyl length dependence of lamellar spacing. Multiple entry points indicate multiple co-existing morphologies. (E) 1-D transmission scattering data of C_5* with assigned peaks. The assignment is representative of C_6 – C_{11}. (F) Schematic showing how longer alkyl spacer lengths increase the free volume in the alkane region.

To study how the alkyl length changes the domain sizes, the materials were cooled at 1 °C min^{-1} from their melt and analyzed by polarized optical microscopy (POM). Both **C**$_4$ and **C**$_5$ exhibit domains several millimeters in size, while **C**$_6$ forms a solidification-induced band texture.[73] **C**$_7$ to **C**$_{11}$ and **C**$_5$***** form domains that cannot be resolved in size (Figure 9). This discrepancy can be related to the X-ray scattering results. A single morphology and strong crystalline interactions facilitate the formation of large domains, whereas co-existing morphologies lead to too many nuclei and limited domain growth. For **C**$_5$*****, the absence of a single morphology and large domains lead to achiral assemblies based on circular dichroism measurements. It is hypothesized that the amorphous *o*DMS layers prevent the transfer of chiral information from one layer to another. The combination of all these results shows that **C**$_5$ is the ideal spacer length to obtain the most well-defined long-range crystalline arrangement in the **DPA** block molecule system.

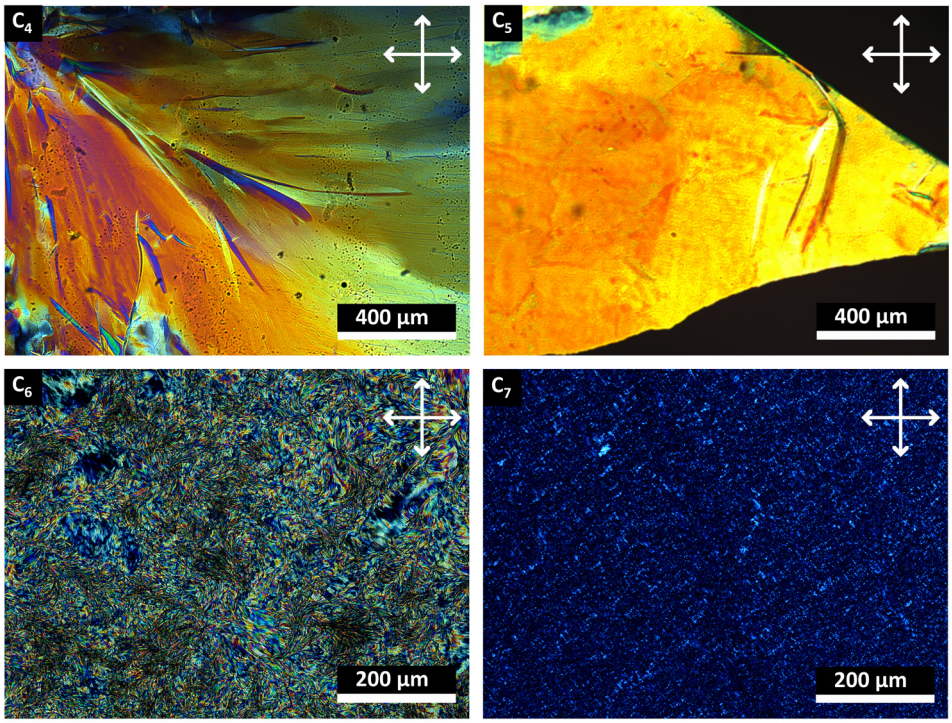

Figure 9. Polarized optical microscopy images of the crystallized structures of **C**$_4$ – **C**$_7$ under crossed polarizers 10 °C below their crystallization temperature after cooling by 1 °C min^{-1} from their isotropic phase. **C**$_4$ and **C**$_5$ show domains of millimeter size, while the size could not be resolved for **C**$_6$ and **C**$_7$. The POM image shown for **C**$_7$ is representative of **C**$_7$ – **C**$_{11}$ and **C**$_5$*****.

2.4 Conclusions

In summary, a library of 30 *o*DMS-containing block molecules was synthesized and characterized for their thermal and morphological behavior to elucidate the design requirements for a well-defined arrangement at the nanoscale. It was found that a 2D morphology arises only when functionalization with *o*DMS does not lead to free volume in the alkyl or core region of the assembly. This requirement can be checked *a priori* by

looking at the distance between the *o*DMS attachment points in the reported crystal structure of the core. If the distance between the *o*DMS attachment points is greater than the *o*DMS diameter of 7 Å, and the crystal structure already showed a preference for lamellar formation, it is expected that a 2D morphology will be obtained. For the core-centered architecture, this requirement is met only for bulky cores as the two *o*DMS groups per core lead to a high density of *o*DMS at the interface between *o*DMS and alkyl. In contrast, there is more space available for the *o*DMS in the head-tail and telechelic architectures, as the single *o*DMS chains per core point in opposite directions for two adjacent molecules. Their lower grafting density allows lamella formation for more densely packed chromophores. When targeting a lamellar morphology, the interconnectivity of multiple layers with the telechelic architecture acts as a template for the formation of 2D structures and as such is preferred over the head-to-tail architecture. Since *o*DMS has a cross-sectional area roughly twice that of alkanes, it is recommended to use short alkyl spacers to prevent the destabilizing formation of free volume in the alkane portion of the assembly. For short alkyls, the alkyl can be considered part of the core and therefore the crystal structure of an alkylated core should be used in the prediction of the formed morphology. This is also additionally useful since alkylation of the core can lead to different polymorphs. We hereby show how reported crystal structures can be used to design block molecules by minimizing free volume, thereby accelerating their development for optoelectronic applications.

2.5 Experimental section

2.5.1 Materials and methods.

All chemicals were purchased from commercial sources and used without further purification. The K_2CO_3 that was used was in anhydrous powder form and of analytical grade. For the hydrosilylation reactions, the following preparation of Karstedt's catalyst from Sigma Aldrich is used; Platinum(0)-1,3-divinyl-1,1,3,3-tetramethyldisiloxane complex solution in xylene, Pt ~2 %. The discrete length oligodimethylsiloxanes (*o*DMS) monohydride with a length of 7 (**HSi$_7$**) or 15 (**HSi$_{15}$**) silicon atoms, and *o*DMS dihydride with a length of 32 silicon atoms (**HSi$_{32}$H**) were synthesized according to literature procedure.[1] Dry solvents were obtained with an MBRAUN solvent purification system (MB-SPS). Oven-dried round bottom flasks (120 °C) or flame-dried Schlenk flasks were used for all reactions carried out under argon atmosphere. Reactions were followed by thin-layer chromatography (TLC) using 60-F254 silica gel plates from Merck and visualized by UV light at 254 nm. Automated column chromatography was conducted on a Grace system using Biotage KP-SIL Silica Flash Cartridges. **Nuclear magnetic resonance (NMR) spectra** were recorded on Bruker 400 MHz Ultrashield spectrometers (400 MHz for ^{1}H NMR, 100 MHz for ^{13}C NMR). Deuterated chloroform is used in each case with its shifts used as internal standard (7.26 ppm for ^{1}H NMR; 77.16 ppm for ^{13}C NMR). Chemical shifts (δ) are expressed in ppm values relative to tetramethylsilane. Peak multiplicity is abbreviated as s: singlet; d: doublet; t: triplet; q: quartet; m: multiplet. **Matrix assisted laser desorption/ionization time of flight mass spectroscopy (MALDI-ToF-MS) spectra** were acquired using a Bruker Autoflex Speed MALDI-ToF-MS using α-cyano-4-hydroxycinnamic acid (CHCA) or trans-2-[3-(4-tert-butylphenyl)-2-methyl-2-propenylidene]malononitrile (DCTB) as matrices. All samples were dissolved in chloroform. **Differential scanning calorimetry (DSC)** data were collected on a DSC Q2000 from TA instruments, calibrated with an indium standard. The samples (4-8 mg) were weighed directly into aluminium pans and hermetically sealed. The samples were initially heated to 180 °C and then subjected to two cooling/heating cycles from -70 °C to 180 °C with a rate of 10 K min^{-1}. The data that is presented, represents the second heating and/or cooling cycle, with the third cycle similar to the second. The thermal transition temperatures were assigned at the maximum of the transition. **Recycling GPC** was performed in stabilized tetrahydrofuran solution with a Shodex-GPC H-2002.5 column (20 mm i.d. x 500 mm, MW up to 20.000 calibrated to PS standards). A Shimadzu SPD-10AV VP was used as UV VIS detector in conjunction with Dax 9.0 software from Van Mierlo Software Consultancy. **Polarized Optical Microscopy** (POM) samples were sandwiched between glass substrates and imaged using Nikon ECLIPSE Ci-POL microscope with 5x, or 20x magnification. The samples were heated and cooled using a Linkam LTS 420 heating stage mounted in the POM set-up. All samples were heated to their isotropic phase

(10 – 20 °C above their melting point, isothermal for 5 – 10 minutes) and subsequently cooled with 5 °C min^{-1} to their melting point. The samples were further cooled with 1 K min^{-1} to form birefringent domains. Temperatures below room temperature were reached through controlled cooling with liquid nitrogen. Bulk **small angle X-ray scattering (SAXS)** was performed on an instrument from Ganesha Lab. The flight tube and sample holder are all under vacuum in a single housing, with a GeniX-Cu ultra-low divergence X-ray generator. The source produces X-rays with a wavelength (λ) of 0.154 nm and a flux of 1 × 108 ph s^{-1}. Scattered X-rays were captured on a 2-dimensional Pilatus 300K detector with 487 × 619 pixel resolution. The sample-to-detector distance was 0.084 m (WAXS mode) or 0.48 m (MAXS mode). The instrument was calibrated with diffraction patterns from silver behenate. All room temperature measurements were performed after overnight cooling from their melt. Domain spacings (d) are calculated using $d = 2\pi/q^*$, with q^* the principal scattering peak. **Crystal lattice energy** calculations were performed by Tobias Schnitzer with the program CrystalExplorer.[60] Here, the interaction energies for all neighbouring molecules are calculated using a B3LYP functional for a central molecule using reported crystal structures.[74] **Volume fractions** were estimated as the ratio between the *o*DMS volume and the core volume. For this, the bulk density of PDMS was taken as 0.95 g ml^{-1} which was converted to volume with the respective molecular weights of the three lengths *o*DMS ($M_{w,HSi7}$ = 519.1 g mol^{-1} gives $V_{HSi7} \approx 546$ ml mol^{-1}; $M_{w,HSi15}$ = 1112.4 g mol^{-1} gives $V_{HSi15} \approx 1170$ ml mol^{-1}; $M_{w,HSi32H}$ = 2359 g mol^{-1} gives $V_{HSi32H} \approx 2483$ ml mol^{-1}).[39] The volume of the cores were calculated using the densities of the crystal structures of compounds similar to used cores. The crystal densities were estimated from the crystal structures of unfunctionalized 9,10-diphenylanthracene,[53] **C_3AQC$_3$**,[54] **C_6AzoC$_6$**,[56] and **C_4OPVC$_4$**[55] by dividing the unit cell volume in Å^3 with the number of molecules in the unit cell followed by conversion to ml mol^{-1}. For the calculations for the volume of the cores, their molecular weights were taken including alkyl spacer on both sides. The calculated volume fractions thus give an upper limit of the core volume fractions.

2.5.2 Synthesis

The synthesis of the linear *o*DMS is described in the literature and performed by Bas de Waal,[38] who also synthesized the branched *o*DMS. The synthesis of 9,10-bis(4-hydroxyphenyl)anthracene and **C_5** (**Si$_7$DPASi$_7$**) are reported in Chapter 5. The synthesis for the molecular architecture part was partially performed by Bart van den Bersselaar, and the synthesis for the alkyl spacer effect on the DPA morphology was partially performed by Marko Beslać. For the chiral spacer, (*S*)-2-methylpent-4-en-1-yl 4-ethylbenzenesulfonate was purchased from ChemSpace and is used as received. All final products are characterized by ^{1}H-NMR, ^{13}C-NMR and MALDI-ToF-MS after purification by recycling GPC in THF.

2.5.2.1 Molecular architecture: diphenylanthracene derivatives

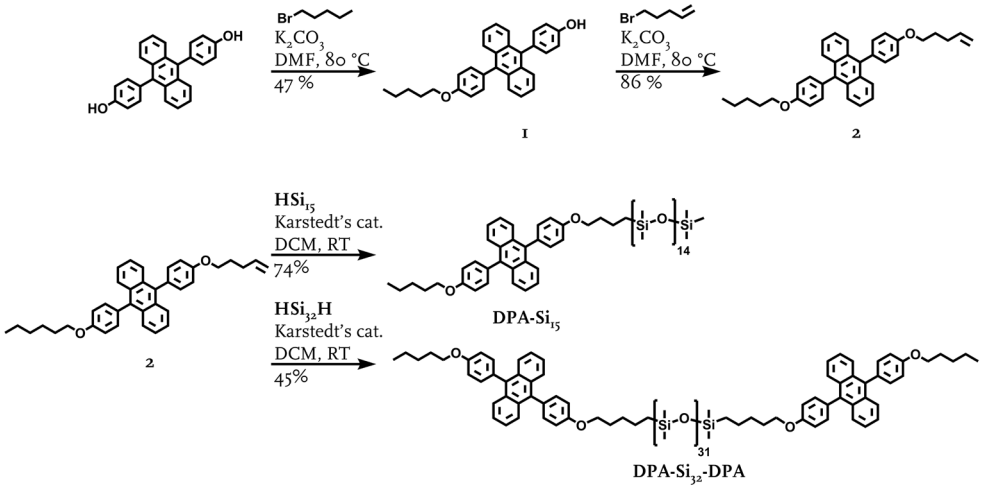

Scheme 1. Synthetic route to the **DPA** block molecules.

4-(10-(4-(Pentyloxy)phenyl)anthracen-9-yl)phenol (1)
An oven-dried round bottom flask was charged with 4,4'-(9,10-anthracenediyl)bis-phenol (812 mg, 2.24 mmol, 2 eq.), 1-bromopentane (167 mg, 1.12 mmol, 1 eq.) and K_2CO_3 (454 mg, 3.28 mmol, 2.9 eq.) in dry DMF (50 mL). This mixture was stirred at 80 °C under argon atmosphere for 18 hours. Consequently, the mixture was cooled to room temperature and precipitated in cold 1M HCl (500 mL). The precipitate was filtered with a Büchner funnel and the mother liquor was filtered again over the same filter paper. The precipitate was impregnated on celite and purified using column chromatography (Solid loading, eluent heptane 100%) to yield the target compound as slightly yellow crystals (225 mg, 0.53 mmol, 47%).
^{1}H NMR (400 MHz, $CDCl_3$) δ 7.75 (td, *J* = 6.0, 2.4 Hz, 4H), 7.41 – 7.29 (m, 8H), 7.13 (d, *J* = 8.4 Hz, 2H), 7.11 – 7.04 (m, 2H), 5.04 (s, 1H), 4.12 (t, *J* = 6.5 Hz, 2H), 1.91 (p, *J* = 6.7 Hz, 2H), 1.64 – 1.42 (m, 4H), 0.99 (t, *J* = 7.1 Hz, 3H) ppm. ^{13}C NMR was not recorded due to poor solubility.

9-(4-(Pent-4-en-1-yloxy)phenyl)-10-(4-(pentyloxy)phenyl)anthracene (2)
An oven-dried round bottom flask was charged with **1** (140 mg, 0.32 mmol, 1 eq.), 5-bromo-1-pentene (271 mg, 1.82 mmol, 5.7 eq.) and K_2CO_3 (144 mg, 1.04 mmol, 3.3 eq.) in dry DMF (50 mL). This mixture was stirred at 80 °C under argon atmosphere for 18 hours. Consequently, the mixture was cooled to room temperature and precipitated in cold DI water (500 mL) to yield the target compound after gravity filtration as white crystals (140 mg, 0.28 mmol, 86%).
^{1}H NMR (400 MHz, $CDCl_3$) δ 7.79 – 7.73 (m, 4H), 7.41 – 7.30 (m, 8H), 7.17 – 7.11 (m, 4H), 5.94 (dddd, *J* = 18.8, 10.3, 7.5, 5.7 Hz, 1H), 5.21 – 5.02 (m, 2H), 4.13 (q, *J* = 6.9 Hz, 4H), 2.35 (q, *J* = 7.7, 7.2 Hz, 2H), 2.01 (qd, *J* = 8.4, 7.5, 5.6 Hz, 2H), 1.96 – 1.86 (m, 2H), 1.60 – 1.40 (m, 4H), 1.00 (td, *J* = 7.2, 1.9 Hz, 3H) ppm. ^{13}C NMR was not recorded due to poor solubility.

DPA-Si_{15}
A flame dried Schlenk flask was charged with **2** (29.4 mg, 60 µmol, 1 eq.), **HSi_{15}** (133.6 mg, 120 µmol, 2 eq.) and dry DCM (1.5 mL). Subsequently, 1 drop Karstedt's catalyst was added and the mixture was stirred under argon at room temperature. After 5 hours of reaction, another drop of catalyst was added. The mixture was left to stir over the weekend. The crude mixture was impregnated on celite and purified by column chromatography (Solid loading, eluent heptane/$CHCl_3$ 0/100 – 100/0) to yield the target compound as a slightly yellow waxy solid (70.0 mg, 44 µmol, 74%).
^{1}H NMR (400 MHz, $CDCl_3$) δ 7.76 (dd, *J* = 6.8, 3.3 Hz, 4H), 7.38 (d, *J* = 8.5 Hz, 4H), 7.33 (dd, *J* = 6.8, 3.3 Hz, 4H), 7.13 (d, *J* = 8.5 Hz, 4H), 4.12 (t, *J* = 6.6 Hz, 4H), 1.95 – 1.87 (m, 4H), 1.64 – 1.42 (m, 8H), 1.00 (t, *J* = 7.1 Hz, 3H), 0.68 – 0.61 (m, 2H), 0.14 – 0.07 (m, 93H) ppm. ^{13}C NMR (100 MHz, $CDCl_3$) δ 158.76, 136.97, 132.51, 131.08, 131.07, 130.43, 127.23, 124.98, 114.53, 68.27, 32.05, 30.04, 29.36, 29.29, 29.19, 28.50, 23.33, 22.85, 22.71, 18.43, 14.27, 14.24, 1.94, 1.58, 1.37, 1.30, 1.26, 1.23, 1.21, 0.84, 0.39, 0.15 ppm. MALDI-ToF-MS M_w calculated for $C_{67}H_{130}O_{16}Si_{15}$: 1610.6 Da, m/z found = 1612.6 Da $[M+H]^+$.

DPA-Si_{32}-DPA
A flame dried Schlenk flask was charged with **2** (69.2 mg, 0.14 mmol, 2.8 eq.), **$HSi_{32}H$** (110.1 mg, 0.05 mmol, 1 eq.) and dry toluene (2.5 mL). The mixture was heated to 100 °C and subsequently, 1 drop Karstedt's catalyst was added and the mixture was stirred under argon. After 18 hours, the mixture was cooled to room temperature and impregnated on celite, after which the crude mixture was purified by column chromatography (Solid loading, eluent heptane/$CHCl_3$ 0/100 – 100/0) to yield the target compound as a yellowish wax (70.0 mg, 0.02 mmol, 45%).
^{1}H NMR (400 MHz, $CDCl_3$) δ 7.78 – 7.72 (m, 8H), 7.40 – 7.35 (m, 8H), 7.35 – 7.29 (m, 8H), 7.16 – 7.10 (m, 8H), 4.11 (td, *J* = 6.6, 2.2 Hz, 8H), 1.95 – 1.86 (m, 8H), 1.64 – 1.41 (m, 16H, H_2O), 0.99 (t, *J* = 7.2 Hz, 6H), 0.67 – 0.60 (m, 4H), 0.15 – 0.02 (m, 192H). ^{13}C NMR (100 MHz, $CDCl_3$) δ 158.76, 136.97, 132.51, 131.08, 131.07, 130.43, 127.23, 124.98, 114.53, 68.27, 32.05, 30.05, 29.36, 29.29, 29.19, 28.50, 23.33, 22.86, 22.71, 18.43, 14.27, 14.24, 1.56, 1.36, 1.25, 1.23, 1.19, 0.82, 0.38, 0.15. MALDI-ToF-MS M_w calculated for $C_{136}H_{266}O_{35}Si_{32}$: 3355.2 Da, m/z found = 3359.1 Da $[M+H]^+$.

2.5.2.2 Molecular architecture: anthraquinone derivatives

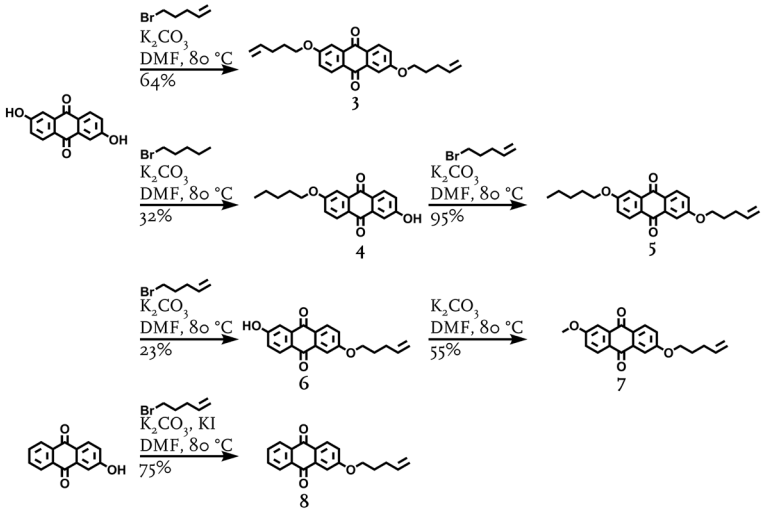

Scheme 2. Synthetic route to the precursors of the **AQ** block molecules.

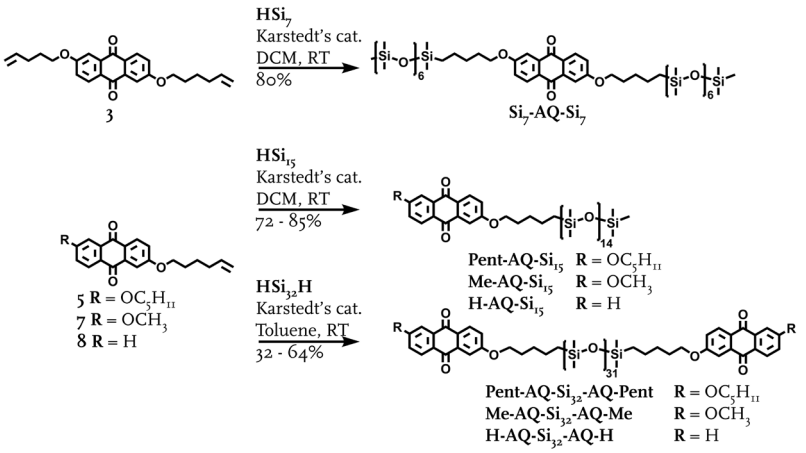

Scheme 3. Synthetic route to the **AQ** block molecules.

2-(Pent-4-en-1-yloxy)-6-(pent-4-en-1-yloxy)anthracene-9,10-dione (3)
An oven-dried round bottom flask was charged with 2,6-dihydroxyanthraquinone (123 mg, 0.51 mmol, 1 eq.), 5-bromo-1-pentene (213 mg, 1.43 mmol, 2.8 eq.) and K_2CO_3 (217 mg, 1.57 mmol, 3.1 eq.) in dry DMF (6 mL). This mixture was stirred at 80 °C under argon atmosphere for 20 hours. Consequently, the mixture was cooled to room temperature and precipitated in cold DI water. The precipitate was filtered by gravity filtration and impregnated on celite, after which the crude mixture was purified by column chromatography (Solid loading, eluent heptane, 100%) to yield the target compound as slightly yellow fluffy crystals (123 mg, 0.33 mmol, 64%). ^{1}H NMR (400 MHz, $CDCl_3$) δ 8.23 (d, J = 8.7 Hz, 2H), 7.71 (d, J = 2.6 Hz, 2H), 7.22 (dd, J = 8.7, 2.7 Hz, 2H), 5.86 (ddt, J = 16.9, 10.2, 6.6 Hz, 2H), 5.17 – 4.95 (m, 4H), 4.16 (t, J = 6.4 Hz, 4H), 2.28 (q, J = 7.2 Hz, 4H), 1.96 (p, J = 6.7 Hz, 4H) ppm. ^{13}C NMR (100 MHz, $CDCl_3$) δ 182.30, 163.96, 137.40, 135.87, 129.68, 127.07, 120.91, 115.58, 110.57, 67.93, 29.97, 28.18.

2-Hydroxy-6-(pentyloxy)anthracene-9,10-dione (4)
An oven-dried round bottom flask was charged with 2,6-dihydroxyanthraquinone (1.64 g, 6.83 mmol, 1.7 eq.), 1-bromopentane (591 mg, 3.91 mmol, 1 eq.) and K_2CO_3 (1.00 g, 7.24 mmol, 1.9 eq.) in dry DMF (200 mL). This mixture was stirred at 100 °C under argon atmosphere for 18 hours. Consequently, the mixture was cooled to room temperature and precipitated in cold 1M HCl (500 mL). The precipitate was filtered by gravity filtration and impregnated on celite, after which the crude mixture was purified by column chromatography (Solid loading, eluent DCM 100%) to yield the target compound as yellow crystals (388 mg, 1.25 mmol, 32%).
^{1}H NMR (400 MHz, $CDCl_3$) δ 8.22 (t, *J* = 8.4 Hz, 2H), 7.79 (d, *J* = 2.6 Hz, 1H), 7.71 (d, *J* = 2.7 Hz, 1H), 7.22 (dt, *J* = 8.5, 2.6 Hz, 2H), 6.75 (s, 1H), 4.15 (t, *J* = 6.6 Hz, 2H), 1.94 – 1.75 (m, 2H), 1.55 – 1.35 (m, 4H), 0.95 (t, *J* = 7.1 Hz, 3H) ppm. ^{13}C NMR was not recorded.

2-(Pent-4-en-1-yloxy)-6-(pentyloxy)anthracene-9,10-dione (5)
An oven-dried round bottom flask was charged with **4** (388 mg, 1.25 mmol, 1 eq.), 5-bromo-1-pentene (377 mg, 2.53 mmol, 2 eq.) and K_2CO_3 (265.0 mg, 1.92 mmol, 1.5 eq.) in dry DMF (50 mL). This mixture was stirred at 80 °C under argon atmosphere for 20 hours. Consequently, the mixture was cooled to room temperature and precipitated in cold 1M HCl (250 mL). The precipitate was filtered by gravity filtration and impregnated on celite, after which the crude mixture was purified by column chromatography (Solid loading, eluent heptane 100%) to yield the target compound as crashed out yellow crystals (450 mg, 1.19 mmol, 95%).
^{1}H NMR (400 MHz, $CDCl_3$) δ 8.22 (dd, *J* = 8.7, 1.1 Hz, 2H), 7.70 (d, *J* = 2.6 Hz, 2H), 7.22 (ddd, *J* = 8.7, 2.7, 1.1 Hz, 2H), 5.86 (ddt, *J* = 16.9, 10.2, 6.7 Hz, 1H), 5.14 – 4.98 (m, 2H), 4.15 (q, *J* = 6.6 Hz, 4H), 2.34 – 2.20 (m, 2H), 1.96 (p, *J* = 6.7 Hz, 2H), 1.85 (p, *J* = 6.8 Hz, 2H), 1.52 – 1.32 (m, 4H), 0.95 (t, *J* = 7.0 Hz, 3H) ppm. ^{13}C NMR (100 MHz, $CDCl_3$) δ 182.32, 164.08, 163.95, 137.40, 135.88, 135.86, 129.67, 127.09, 126.99, 120.93, 120.90, 115.58, 110.57, 68.82, 67.93, 29.97, 28.73, 28.19, 28.10, 22.41, 14.00 ppm.

2-Hydroxy-6-(pent-4-en-1-yloxy)anthracene-9,10-dione (6)
An oven-dried round bottom flask was charged with 2,6-dihydroxyanthraquinone (619 mg, 2.58 mmol, 5.1 eq.), 5-bromo-1-pentene (197 mg, 0.51 mmol, 1 eq.) and K_2CO_3 (414.0 mg, 3.0 mmol, 6 eq.) in dry DMF (80 mL). This mixture was stirred at 80 °C under argon atmosphere for 18 hours. Consequently, the mixture was cooled to room temperature and filtered with a gravity filter. The residue was washed with DCM, MeOH and acetone to bring the product to the filtrate while removing the K_2CO_3. The filtrate was reduced in vacuo until 0.5 mL and dropwise added to 1M HCl (300 mL). The precipitate was filtered by gravity filtration and impregnated on celite, after which the crude mixture was purified by column chromatography (Solid loading, eluent heptane/DCM 100/0 – 100/0, switch to *iso*-propanol/DCM 10/90) to yield the material as a yellow solid (180 mg, 0.12 mmol, 23%).
^{1}H NMR (400 MHz, $CDCl_3$) δ 8.89 (s, 1H), 8.19 (dd, *J* = 8.3, 2.2 Hz, 2H), 7.77 (d, *J* = 2.6 Hz, 1H), 7.69 (d, *J* = 2.6 Hz, 1H), 7.22 (td, *J* = 8.7, 2.5 Hz, 2H), 5.86 (ddt, *J* = 16.8, 10.1, 6.6 Hz, 1H), 5.13 – 4.98 (m, 2H), 4.15 (t, *J* = 6.4 Hz, 2H), 2.34 – 2.21 (m, 2H), 1.95 (p, *J* = 6.7 Hz, 2H) ppm. ^{13}C NMR (100 MHz, $CDCl_3$) δ 182.65, 182.27, 164.03, 162.97, 162.52, 137.40, 135.98, 135.90, 130.22, 129.65, 127.00, 126.58, 121.13, 120.86, 115.58, 113.22, 110.66, 67.94, 36.80, 31.76, 29.97, 28.17 ppm.

2-Methoxy-6-(pent-4-en-1-yloxy)anthracene-9,10-dione (7)
An oven-dried round bottom flask was charged with **6** (180 mg, 0.59 mmol, 1 eq.), dimethyl sulfide (0.2 mL, 2.34 mmol, 4 eq.), K_2CO_3 (149 mg, 1.08 mmol, 1.9 eq.) and acetone (40 mL). This mixture was stirred at 65 °C under argon atmosphere for 18 hours. Subsequently, the mixture was cooled to room temperature, filtered by gravity filtration to remove K_2CO_3. The filtrate was impregnated on celite and purified by column chromatography (Solid loading, eluent heptane/EtAc 100/0 – 80/20) to yield the product as yellow crystals (104 mg, 0.31 mmol, 55%). The crystals came together with the eluent in the test tubes of the automated column chromatography machine and were obtained by reducing the eluent in vacuo.
^{1}H NMR (400 MHz, $CDCl_3$) δ 8.17 (dd, *J* = 8.6, 1.9 Hz, 2H), 7.64 (dd, *J* = 6.9, 2.7 Hz, 2H), 7.17 (ddd, *J* = 8.6, 2.7, 1.6 Hz, 2H), 5.85 (ddt, *J* = 16.9, 10.2, 6.7 Hz, 1H), 5.11 – 4.96 (m, 2H), 4.12 (t, *J* = 6.4 Hz, 2H), 3.95 (s, 3H), 2.33 – 2.18 (m, 2H), 1.94 (dt, *J* = 8.0, 6.5 Hz, 2H) ppm. ^{13}C NMR (100 MHz, $CDCl_3$) δ 182.13, 182.07, 164.35, 163.89, 137.40, 135.80, 135.74, 129.63, 129.61, 128.31, 127.14, 126.97, 126.10, 120.85, 120.54, 115.57, 110.50, 109.92, 68.48, 67.91, 55.91, 32.27, 31.88, 29.97, 29.02, 28.17, 22.69, 18.05, 14.12 ppm.

2-(Pent-4-en-1-yloxy)anthracene-9,10-dione (8)
An oven-dried round bottom flask was charged with 2-hydroxyanthraquinone (580 mg, 2.57 mmol, 1 eq.), 5-bromo-1-pentene (770 mg, 5.13 mmol, 2 eq.), K_2CO_3 (672 mg, 4.88 mmol, 1.9 eq.) and KI (43 mg, 0.26 mmol, 0.1 eq.) in dry DMF (50 mL). This mixture was stirred at 80 °C under argon atmosphere for 20 hours. Consequently, the mixture was cooled to room temperature and precipitated in cold water (250 mL). The

precipitate was filtered by gravity filtration and dried under vacuum overnight to yield the target compound as a dark green-brown solid (570 mg, 1.93 mmol, 75%).
^{1}H NMR (400 MHz, $CDCl_3$) δ = 8.36 – 8.19 (m, 3H), 7.84 – 7.65 (m, 3H), 7.31 – 7.18 (m, 1H), 5.94 – 5.84 (m, 1H), 5.10 – 5.04 (m, 2H), 4.17 (t, J = 6.4 Hz, 2H), 2.28 (q, *J* = 7.1 Hz, 2H), 2.01 – 1.92 (m, 2H) ppm. ^{13}C NMR (100 MHz, $CDCl_3$) δ = 182.65, 163.83, 137.37, 135.52, 135.12 – 133.22, 129.71, 121.40, 115.59, 110.50, 67.94, 29.97, 28.16 ppm.

Si_7-AQ-Si_7
A flame dried Schlenk flask was charged with **3** (55.3 mg, 0.15 mmol, 1 eq.), **HSi_7** (231.8 mg, 0.45 mmol, 3 eq.) and dry DCM (0.4 mL). Subsequently, 1 drop Karstedt's catalyst was added and the mixture was stirred under argon at room temperature. The mixture was left to stir until full conversion was observed by TLC, after which the mixture was impregnated on celite and purified by column chromatography (Solid loading, eluent heptane/$CHCl_3$ 0/100 – 100/0) to yield the target compound as a yellowish liquid (168.0 mg, 0.12 mmol, 80%).
^{1}H NMR (400 MHz, $CDCl_3$) δ 8.22 (d, *J* = 8.6 Hz, 2H), 7.70 (d, *J* = 2.6 Hz, 2H), 7.21 (dd, *J* = 8.6, 2.7 Hz, 2H), 4.14 (t, *J* = 6.5 Hz, 4H), 1.85 (p, *J* = 6.8 Hz, 4H), 1.62 – 1.37 (m, 8H), 0.64 – 0.53 (m, 4H), 0.14 – 0.01 (m, 90H) ppm. ^{13}C NMR (100 MHz, $CDCl_3$) δ 182.45, 164.21, 136.02, 129.79, 127.16, 121.05, 110.68, 68.97, 29.80, 28.97, 23.22, 18.36, 1.94, 1.34, 1.30, 1.24, 1.22, 0.35 ppm. MALDI-ToF-MS M_w calculated for $C_{54}H_{116}O_{16}Si_{14}$: 1412.5 Da, m/z found = 1437.5 Da $[M+Na]^+$.

Pent-AQ-Si_{15}
A flame dried Schlenk flask was charged with **5** (51 mg, 0.14 mmol, 1 eq.), **HSi_{15}** (226 mg, 0.20 mmol, 1.4 eq.) and dry DCM (1 mL). Subsequently, 2 drops Karstedt's catalyst were added and the mixture was stirred under argon at room temperature. The mixture was left to stir for 20 hours, after which the mixture was impregnated on celite and purified by column chromatography (Solid loading, eluent heptane/$CHCl_3$ 0/100 – 60/40) to yield the target compound as a yellowish wax (145 mg, 0.10 mmol, 72%).
^{1}H NMR (400 MHz, $CDCl_3$) δ 8.22 (d, *J* = 8.6 Hz, 2H), 7.70 (d, *J* = 2.6 Hz, 2H), 7.21 (ddd, *J* = 8.7, 2.7, 1.5 Hz, 2H), 4.14 (td, *J* = 6.6, 2.3 Hz, 4H), 1.92 – 1.76 (m, 4H), 1.58 – 1.35 (m, 8H), 0.95 (t, *J* = 7.1 Hz, 3H), 0.66 – 0.54 (m, 2H), 0.08 (m, 93H) ppm. ^{13}C NMR (100 MHz, $CDCl_3$) δ 182.47, 182.45, 164.20, 136.00, 129.79, 127.14, 121.05, 110.67, 68.95, 29.80, 28.96, 28.87, 28.24, 23.21, 22.56, 18.34, 14.15, 1.93, 1.34, 1.29, 1.23, 1.20, 0.34 ppm. MALDI-ToF-MS M_w calculated for $C_{55}H_{120}O_{18}Si_{15}$: 1488.5 Da, m/z found = 1513.4 Da $[M+Na]^+$.

Pent-AQ-Si_{32}-AQ-Pent
A flame dried Schlenk flask was charged with **5** (49.5 mg, 130 µmol, 2.6 eq.), **$HSi_{32}H$** (125 mg, 50 µmol, 1 eq.) and dry toluene (1 mL). Subsequently, 2 drops Karstedt's catalyst were added and the mixture was stirred under argon at 80 °C. The mixture was left to stir for 5 hours, after which the mixture was cooled to room temperature, impregnated on celite and purified by column chromatography (Solid loading, eluent heptane/$CHCl_3$ 0/100 – 100/0) to yield the target compound as a soft yellowish wax (52.0 mg, 16 µmol, 32%).
^{1}H NMR (400 MHz, $CDCl_3$) δ 8.24 (d, *J* = 8.6 Hz, 4H), 7.72 (d, *J* = 2.6 Hz, 4H), 7.23 (dt, *J* = 8.6, 2.2 Hz, 4H), 4.16 (td, *J* = 6.6, 2.7 Hz, 8H), 1.95 – 1.77 (m, 8H), 1.54 – 1.38 (m, 16H), 0.97 (t, *J* = 7.1 Hz, 6H), 0.67 – 0.50 (m, 4H), 0.09 (s, 192H) ppm. ^{13}C NMR (100 MHz, $CDCl_3$) δ 13C NMR (100 MHz, CDCl3) δ 182.39, 164.09, 135.86, 129.68, 126.98, 120.93, 110.57, 68.82, 29.65, 28.81, 28.72, 28.10, 23.07, 22.41, 18.20, 14.00, 1.41, 1.19, 1.08, 1.06, 0.67, 0.20 ppm. MALDI-ToF-MS M_w calculated for $C_{112}H_{246}O_{39}Si_{32}$: 3110.0 Da, m/z found = 3137.9 Da $[M+Na]^+$.

Me-AQ-Si_{15}
A flame dried Schlenk flask was charged with **7** (15 mg, 47 µmol, 1 eq.), **HSi_{15}** (127 mg, 114 µmol, 2.5 eq.) and dry DCM (0.8 mL). Subsequently, 1 drop Karstedt's catalyst was added and the mixture was stirred under argon at room temperature. The mixture was left to stir for 20 hours, after which the mixture was impregnated on celite and purified by column chromatography (Solid loading, eluent heptane/$CHCl_3$ 100/0 – 50/50) to yield the target compound as a yellowish wax (50 mg, 35 µmol, 75%).
^{1}H NMR (400 MHz, $CDCl_3$) δ 8.22 (dd, *J* = 8.6, 3.5 Hz, 2H), 7.71 (dd, *J* = 8.8, 2.7 Hz, 2H), 7.22 (dd, *J* = 8.4, 5.4, 2.7 Hz, 2H), 4.14 (t, *J* = 6.6 Hz, 2H), 3.98 (s, 3H), 1.90 – 1.80 (m, 2H), 1.61 – 1.37 (m, 4H), 0.63 – 0.54 (m, 2H), 0.13 – 0.01 (m, 93H) ppm. ^{13}C NMR (100 MHz, $CDCl_3$) δ 207.03, 182.42, 182.36, 164.55, 164.22, 136.04, 135.96, 129.81, 127.38, 127.10, 121.09, 120.75, 110.68, 110.10, 68.96, 56.08, 31.07, 29.79, 28.95, 23.21, 18.34, 1.93, 1.33, 1.28, 1.23, 1.19, 0.34 ppm. MALDI-ToF-MS M_w calculated for $C_{51}H_{112}O_{18}Si_{15}$: 1432.4 Da, m/z found = 1457.4 Da $[M+Na]^+$.

Me-AQ-Si_{32}-AQ-Me
A flame dried Schlenk flask was charged with **7** (44 mg, 136.5 µm, 28.5 eq.), **$HSi_{32}H$** (113 mg, 4.79 µmol, 1 eq.) and dry DCM (0.5 mL). Subsequently, 20 µL Karstedt's catalyst was added and the mixture was stirred under argon at room temperature. The mixture was left to stir for 20 hours, after which the mixture was impregnated on celite and purified by column chromatography (Solid loading, eluent heptane/$CHCl_3$ 100/0 – 50/50) to yield the target compound as a yellowish wax (98 mg, 31 µmol, 64%).
^{1}H NMR (400 MHz, $CDCl_3$) δ 8.23 (dd, *J* = 8.6, 3.6 Hz, 4H), 7.71 (dd, *J* = 9.1, 2.7 Hz, 4H), 7.22 (ddd, *J* = 8.5, 5.7, 2.7 Hz, 4H), 4.14 (dt, *J* = 6.5, 3.0 Hz, 4H), 3.98 (s, 6H), 1.91 – 1.78 (m, 4H), 1.60 – 1.36 (m, 8H), 0.65 – 0.52 (m, 4H), 0.07 (s, 192H) ppm. ^{13}C NMR (100 MHz, $CDCl_3$) δ 182.10, 182.04, 164.22, 163.89, 135.71, 135.63, 129.48, 127.04, 126.76, 120.76, 120.42, 110.35, 109.77, 68.63, 55.75, 29.45, 28.61, 22.87, 18.00, 0.99, 0.88, 0.86, 0.84 ppm. MALDI-ToF-MS M_w calculated for $C_{104}H_{230}O_{39}Si_{32}$: 2998.9 Da, m/z found = 3026.8 Da $[M+Na]^+$.

H-AQ-Si_{15}
A flame dried Schlenk flask was charged with **8** (5 mg, 0.176 mmol, 1 eq.), **HSi_{15}** (217. mg, 0.185 mmol, 1.1 eq.) and dry DCM (1 mL). Subsequently, 1 drop Karstedt's catalyst was added and the mixture was stirred under argon at room temperature. The mixture was left to stir for 10 hours, after which the mixture was impregnated on celite and purified by column chromatography (Solid loading, eluent heptane/$CHCl_3$ 100/0 – 50/50) to yield the target compound as a yellowish wax (211 mg, 0.100 mmol, 85%).
^{1}H NMR (400 MHz, $CDCl_3$) δ 8.33 – 8.22 (m, 3H), 7.81 – 7.68 (m, 3H), 7.27 – 7.22 (m, 1H), 4.14 (t, *J* = 6.5 Hz, 2H), 1.86 (p, *J* = 6.7 Hz, 2H), 1.59 – 1.36 (m, 4H), 0.64 – 0.55 (m, 2H), 0.08 (d, *J* = 5.2 Hz, 93H) ppm. ^{13}C NMR (100 MHz, $CDCl_3$) δ 183.46, 182.29, 164.14, 135.72, 134.25, 133.87, 133.77, 133.75, 129.87, 127.27, 127.05, 121.62, 110.64, 68.98, 29.80, 28.95, 23.22, 18.35, 1.93, 1.57, 1.34, 1.29, 1.23, 1.20, 0.83, 0.35 ppm. MALDI-ToF-MS M_w calculated for $C_{50}H_{110}O_{18}Si_{15}$: 1402.4 Da, m/z found = 1427.4 Da $[M+Na]^+$.

H-AQ-Si_{32}-AQ-H
A flame dried Schlenk flask was charged with **5** (61 mg, 0.208 mmol, 2.3 eq.), **$HSi_{32}H$** (212 mg, 0.090 mmol, 1 eq.) and dry DCM (1 mL). Subsequently, 1 drops Karstedt's catalyst was added and the mixture was stirred under argon at room temperature. The mixture was left to stir for 10 hours, after which the mixture was impregnated on celite and purified by column chromatography (Solid loading, eluent heptane/$CHCl_3$ 100/0 – 50/50) to yield the target compound as a soft yellowish wax (139 mg, 0.047 mmol, 52%).
^{1}H NMR (400 MHz, $CDCl_3$) δ 8.35 – 8.19 (m, 6H), 7.83 – 7.64 (m, 6H), 7.27 – 7.22 (m, 2H), 4.14 (t, *J* = 6.5 Hz, 4H), 1.91 – 1.80 (m, 4H), 1.58 – 1.36 (m, 8H), 0.64 – 0.53 (m, 4H), 0.16 – 0.02 (m, 192H) ppm. ^{13}C NMR (100 MHz, $CDCl_3$) δ 183.46, 182.29, 164.14, 135.72, 134.25, 133.87, 133.77, 133.74, 129.87, 127.27, 127.05, 121.62, 110.64, 68.98, 29.80, 28.95, 23.21, 18.35, 2.58, 1.23, 0.82, 0.14 ppm. MALDI-ToF-MS M_w calculated for $C_{102}H_{226}O_{37}Si_{32}$: 2938.8 Da, m/z found = 2965.8 Da $[M+Na]^+$.

2.5.2.3 Molecular architecture: azobenzene derivatives

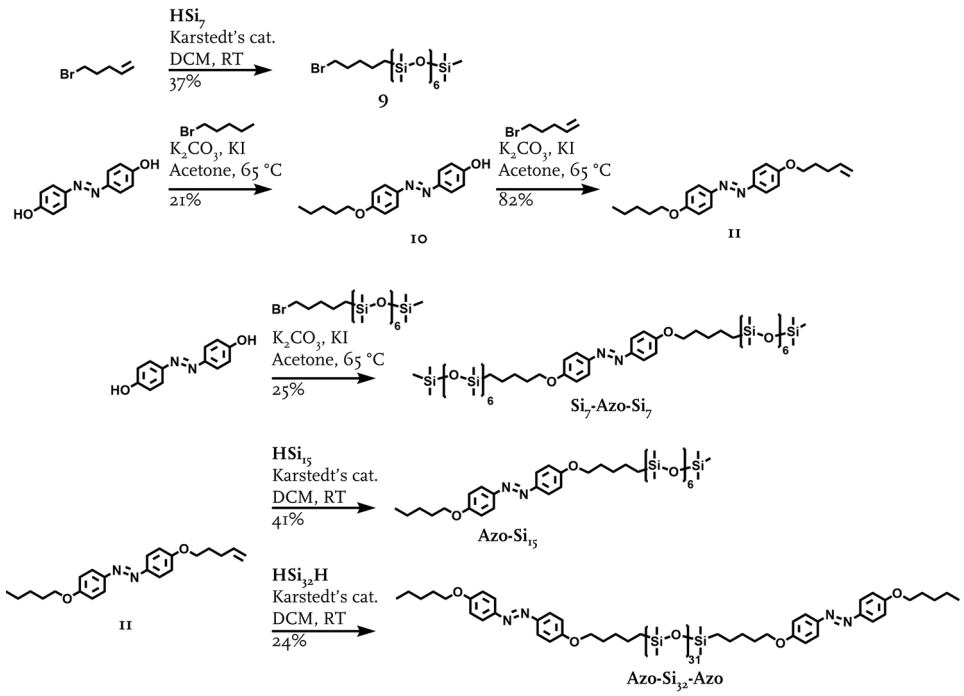

Scheme 4. Synthetic route to the **Azo** block molecules.

1-(5-Bromopentyl)-1,1,3,3,5,5,7,7,9,9,11,11,13,13,13-pentadecamethylheptasiloxane (9)
An oven-dried round bottom flask was charged with **HSi$_7$** (1.015 g, 1.96 mmol, 1 eq.) and 1-bromo-5-pentene (384.5 mg, 2.54 mmol, 1.3 eq.). To this, two drops of Karstedt's catalyst were added under argon. The mixture was stirred for 2 hours until full conversion and purified by column chromatography (Liquid injection from heptane, heptane/EtAc 50/50) to yield the target compounds as a colorless oil (489 mg, 0.73 mmol, 37%).
^{1}H NMR (400 MHz, $CDCl_3$) δ 3.40 (t, J = 6.9 Hz, 2H), 1.94 – 1.79 (m, 2H), 1.50 – 1.34 (m, 4H), 0.58 – 0.52 (m, 2H), 0.10 – 0.03 (m, 48H) ppm. ^{13}C NMR (100 MHz, $CDCl_3$) δ 33.93, 32.61, 31.85, 22.50, 18.09, 1.80, 1.19, 1.16, 1.09, 1.08, 0.17 ppm.

4-((4-(Pentyloxy)phenyl)diazenyl)phenol (10)
An oven-dried round bottom flask was charged with dihydroxy azobenzene (305 mg, 1.42 mmol, 2 eq.) K_2CO_3 (592 mg, 4.28 mmol, 6 eq.) and KI (27 mg, 0.16 mmol, 0.22 eq.) in acetone (30 mL). This suspension was stirred at room temperature and 1-bromopentane (0.09 mL, 0.71 mmol, 1 eq.) was added dropwise. Consequently, the mixture was heated to reflux and stirred overnight. The mixture was cooled to room temperature and filtered by gravity filtration to remove the salts. The residue was rinsed with acetone and $CHCl_3$ and the organic phase was combined and concentrated to remain with approx. 150 mL organic solvent that was extracted with 1M HCl (50 mL). The aqueous phase was extracted with $CHCl_3$ (2x50 mL). The organic phase was combined and dried over Na_2SO_4, upon which the Na_2SO_4 turned deep red. The precipitate was rinsed thoroughly with additional $CHCl_3$ to remove all color. The organic fraction was impregnated on celite and purified by column chromatography (Solid loaded, eluent DCM:MeOH 99/1 – 95/5) to yield the target compound as a yellow solid (41.6 mg, 0.146 mmol, 21%).
^{1}H NMR (400 MHz, $CDCl_3$) δ: 7.92 – 7.76 (m, 4H), 6.99 (d, J = 8.8 Hz, 2H), 6.93 (d, J = 8.8 Hz, 2H), 4.95 (s, 1H), 4.03 (t, J = 6.6 Hz, 2H), 1.82 (p, J = 6.8 Hz, 2H), 1.43 (m, 4H), 0.95 (t, J = 7.0 Hz, 3H) ppm. ^{13}C NMR (100 MHz, $CDCl_3$) δ 161.17, 157.63, 147.31, 146.91, 137.68, 124.56, 124.38, 115.74, 115.36, 114.70, 67.49, 30.08, 28.37 ppm.

1-(4-(Pent-4-en-1-yloxy)phenyl)-2-(4-(pentyloxy)phenyl)diazene (11)
An oven-dried round bottom flask was charged with **9** (33 mg, 0.116 mmol, 1 eq.), K_2CO_3 (72 mg, 0.518 mmol, 4.5 eq.) and KI (2 mg, 0.12 mmol, 1 eq.) in acetone (5 mL) and the mixture was heated to 60 °C under argon. Subsequently, 5-bromo-1-pentene (43 mg, 0.288 mmol, 2.5 eq.) was added dropwise and the mixture is stirred overnight under reflux. The contents of the round bottom flask were filtered by gravity filtration to remove the salts and the residue was washed with acetone and $CHCl_3$. The organic phase was extracted with 0.5M HCl (50 mL) and the aqueous phase was extracted with $CHCl_3$ (2x50 mL). The organic phase was dried over $MgSO_4$ which turned orange so it was rinsed with $CHCl_3$ (3x 10 mL). The organic phase was dried in vacuo, yielding an orange solid. The crude was purified by column chromatography (Liquid injection from heptane, eluent heptane:EtAc 100/0 – 80/20) to yield the target compound as an orange solid (36 mg, 0.102 mmol, 88%).
^{1}H NMR (400 MHz, $CDCl_3$) δ: 7.25 – 7.18 (m, 2H), 6.93 – 6.85 (m, 2H), 5.85 (ddt, *J* = 16.9, 10.1, 6.6 Hz, 1H), 5.15 – 4.92 (m, 2H) 4.04 (q, *J* = 6.7 Hz, 4H), 2.27 (q, *J* = 7.2 Hz, 2H), 1.92 (p, *J* = 6.8 Hz, 2H), 1.87 – 1.78 (m, 2H), 1.43 (m, 2H), 0.95 (t, *J* = 7.0 Hz, 3H) ppm. ^{13}C NMR was not recorded.

Si_7-Azo-Si_7
An oven-dried round bottom flask was charged with dihydroxy azobenzene (59 mg, 0.276 mmol, 1 eq.), K_2CO_3 (122 mg, 0.870 mmol, 3.2 eq.) and KI (7 mg, 0.040 mmol, 0.1 eq.) in acetone (10 mL) and the mixture was heated to 60 °C under argon. Subsequently, **9** (463 mg, 0.694 mmol, 2.5 eq.) was added dropwise and the mixture was stirred overnight under reflux. The content of the round bottom flask was then transferred to a separatory funnel and 100 mL water and 100 mL DCM were added. The organic phase was collected and the water phase was washed with DCM (4x 20 mL). The combined organic fractions were washed with brine (100 mL) and dried over $MgSO_4$. The mixture was concentrated in vacuo and purified by column chromatography (Liquid injection from heptane, eluent heptane/DCM 50/50 – 0/100) to yield the target compound as an orange viscous liquid (91 mg, 0.070 mmol, 25%).
^{1}H NMR (400 MHz, $CDCl_3$) δ: 7.89 – 7.82 (m, 4H), 7.01 – 6.95 (m, 4H), 4.02 (t, *J* = 6.6 Hz, 4H) 1.82 (p, *J* = 6.7 Hz, 4H), 1.52 – 1.46 (m, 4H), 1.42 (t, *J* = 8.3 Hz, 4H), 0.62 – 0.55 (m, 4H), 0.13 – 0.03 (m, 90H) ppm. ^{13}C NMR (100 MHz, $CDCl_3$) δ: 160.08, 145.86, 123.20, 113.57, 67.22, 28.64, 27.90, 22.01, 17.13, 0.71, 0.11, –0.00, –0.88, –1.08 ppm. MALDI-ToF-MS M_w calculated for $C_{52}H_{118}N_2O_{14}Si_{14}$: 1386.5 Da, m/z found = 1387.5 Da $[M+H]^+$.

Azo-Si_{15}
An oven-dried round bottom flask was charged with **11** (52 mg, 0.0616 mmol, 1 eq.), **HSi$_{15}$** (86 mg, 0.0778 mmol, 1.3 eq.) and dry DCM (3 mL). Subsequently, 2 drops Karstedt's catalyst were added and the mixture was stirred under argon at room temperature overnight . The mixture was concentrated in vacuo and purified by column chromatography (Liquid injection from heptane, eluent heptane:EtAc, 100/0 – 80/20) to yield the product as an orange solid (37 mg, 0.025 mmol, 41%).
^{1}H NMR (400 MHz, $CDCl_3$) δ 7.86 (d, *J* = 8.9 Hz, 4H), 6.98 (dd, *J* = 8.9, 1.9 Hz, 4H), 4.03 (td, *J* = 6.6, 2.9 Hz, 4H) 1.82 (p, *J* = 6.6 Hz, 4H), 1.43 (m, 4H), 0.95 (t, *J* = 7.0 Hz, 3H), 0.65 – 0.52 (m, 2H), 0.08 (m, 93H) ppm. ^{13}C NMR (100 MHz, $CDCl_3$) δ: 182.79, 164.48, 130.25, 123.98, 120.74, 113.00, 104.76, 32.06, 28.19, 27.84, 27.18, 25.13, 21.60, 13.08, 1.44, –1.06 ppm. MALDI-ToF-MS M_w calculated for $C_{53}H_{122}N_2O_{16}Si_{15}$: 1462.5 Da, m/z found: 1465.1 Da $[M+H]^+$.

Azo-Si_{32}-Azo
An oven-dried round bottom flask was charged with **11** (29 mg, 0.081 mmol, 2 eq.), **HSi$_{32}$H** (97 mg, 0.041 mmol, 1 eq.) and dry DCM (2 mL). Subsequently, 5 drops of Karstedt's catalyst were added and the mixture was stirred at room temperature under argon until full conversion of the hydride. Hereafter, the material was purified by column chromatography (Liquid injection from heptane, eluent heptane:DCM 100/0 – 50/50) to yield the material as an orange viscous liquid (30 mg, 0.010 mmol, 24%).
^{1}H NMR (400 MHz, $CDCl_3$) δ: 7.88 – 7.83 (m, 8H), 6.99 (d, *J* = 1.9 Hz, 4H), 6.97 (d, *J* = 1.8 Hz, 4H), 4.03 (td, *J* = 6.6, 2.8 Hz, 8H), 1.82 (m, 8H), 1.52 – 1.36 (m, 16H), 0.61 – 0.55 (m, 4H), 0.07 (m, 192H) ppm. ^{13}C NMR (100 MHz, $CDCl_3$) δ 161.31, 147.09, 124.43, 114.80, 68.56, 29.87, 29.22, 29.07, 28.33, 23.23, 22.62, 18.29, 14.17, 1.33, 1.18, 0.34, 0.14 ppm. MALDI-ToF-MS M_w calculated for $C_{108}H_{250}N_4O_{35}Si_{32}$: 3059.1 Da, m/z found: 3060.1 Da $[M+H]^+$.

2.5.2.4 Molecular architecture: oligophenylvinylene derivatives

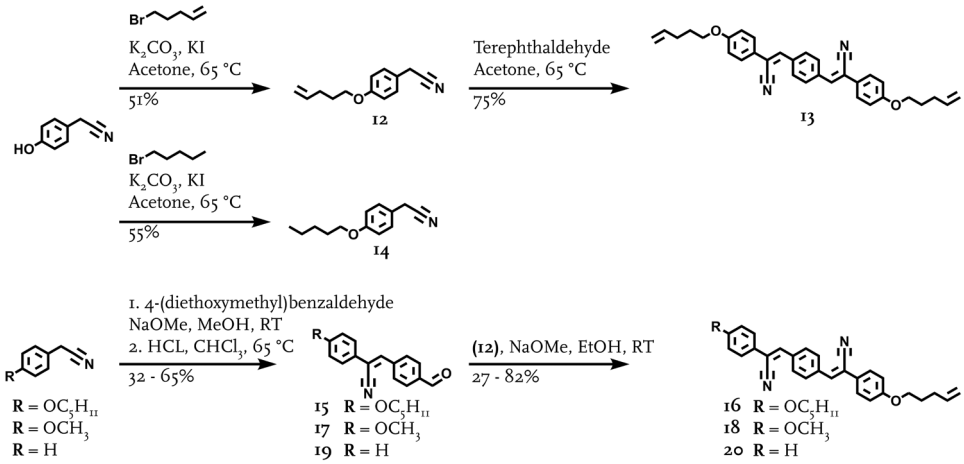

Scheme 5. Synthetic route to the precursors of the **OPV** block molecules.

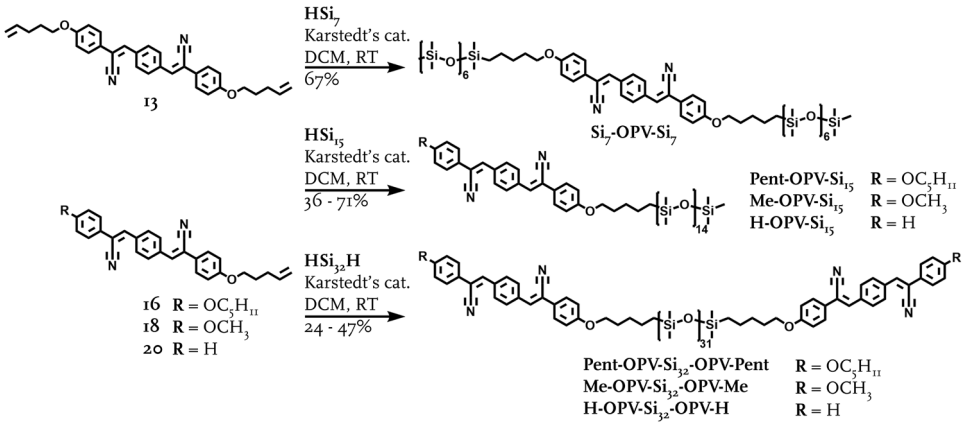

Scheme 6. Synthetic route to the **OPV** block molecules.

2-(4-(Pent-4-en-1-yloxy)phenyl)acetonitrile (12)
An oven-dried round bottom flask was charged with 4-hydroxyphenylacetonitrile (509 mg, 3.82 mmol, 1 eq.), K_2CO_3 (1.059 g, 7.67 mmol, 2 eq.) and KI (74 mg, 0.44 mmol, 0.1 eq.) in acetone (30 mL) and the mixture was heated to 60 °C under argon. Subsequently, 5-bromo-1-pentene (0.8 mL, 6.77 mmol) was added dropwise and the mixture was stirred overnight under reflux. The content of the round bottom flask was then transferred to a separatory funnel and 100 mL water and 100 mL DCM were added. The organic phase was collected and the water phase was washed with DCM (4x 20 mL). The combined organic fractions were washed with brine (100 mL) and dried over $MgSO_4$. The mixture was concentrated in vacuo and purified by column chromatography (Liquid injection from heptane, eluent heptane:DCM, 50/50 – 0/100) to yield the target compound as a transparent liquid (425 mg, 2.11 mmol, 55%).
^{1}H NMR (400 MHz, $CDCl_3$) δ 7.24 – 7.19 (m, 2H), 6.91 – 6.86 (m, 2H), 5.85 (ddt, *J* = 16.9, 10.1, 6.6 Hz, 1H), 5.10 – 4.97 (m, 2H), 3.96 (t, *J* = 6.4 Hz, 2H), 3.67 (s, 2H), 2.28 – 2.19 (m, 2H), 1.89 (dt, *J* = 8.3, 6.7 Hz, 2H) ppm. ^{13}C NMR (100 MHz, $CDCl_3$) δ: 158.84, 137.70, 129.06, 121.62, 118.22, 115.29, 115.10, 67.28, 30.06, 28.34, 22.84 ppm.

3,3'-(1,4-Phenylene)bis(2-(4-(pent-4-en-1-yloxy)phenyl)acrylonitrile) (13)
An oven-dried round bottom flask was charged with **12** (824 mg, 4.097 mmol, 1 eq.) in EtOH (60 mL). Whilst stirring the mixture, 0.5 M NaOMe in MeOH was added (75 mL). Subsequently, terephthaldehyde (1.100 g, 8.194 mmol, 2 eq.) was added and the mixture was stirred overnight, after which the sample turned into a yellow turbid solution and ^{1}H NMR showed full aldehyde conversion. Hereafter, the mixture was quenched with EtOH and filtered through a Büchner funnel. The funnel was rinsed with EtOH and MeOH and the residue was collected and dried in a vacuum oven at 80 °C. To remove remaining sodium salts, the mixture was extracted with $CHCl_3$/water (50 mL/50 mL, 3 x). The organic fraction was dried over $MgSO_4$ and concentrated in vacuo to yield the target compound as a bright yellow solid (1.00 gram, 2.00 mmol, 75%).
^{1}H NMR (400 MHz, $CDCl_3$) δ: 7.95 (s, 4H), 7.63 (d, *J* = 8.9 Hz, 4H), 7.43 (s, 2H), 6.97 (d, *J* = 8.9 Hz, 4H), 5.87 (ddt, *J* = 16.9, 10.2, 6.7 Hz, 2H), 5.13 – 4.95 (m, 4H), 4.03 (t, *J* = 6.4 Hz, 4H), 2.33 – 2.19 (m, 4H), 1.98 – 1.84 (m, 4H) ppm. ^{13}C NMR (100 MHz, $CDCl_3$) δ 160.03, 129.12, 127.35, 123.89, 115.58, 115.06, 29.94, 28.78, 28.24, 25.67 ppm.

2-(4-(Pentyloxy)phenyl)acetonitrile (14)
An oven-dried round bottom flask was charged with 4-hydroxyphenylacetonitrile (494 mg, 3.71 mmol, 1 eq.), K_2CO_3 (1.061 g, 7.67 mmol, 2.1 eq.) and KI (65 mg, 0.39 mmol, 0.1 eq.) in acetone (15 mL) and the mixture was heated to 60 °C under argon. Subsequently, 1-bromopentane (0.6 mL, 4.83 mmol, 1.3 eq.). The content of the round bottom flask was then transferred to a separatory funnel and 100 mL water and 100 mL DCM were added. The organic phase was collected and the water phase was washed with DCM (4x 20 mL). The combined organic fractions were washed with brine (100 mL) and dried over $MgSO_4$. The mixture was concentrated in vacuo and purified by column chromatography (Liquid injection from heptane, eluent heptane:DCM 50/50 – 0/100) to yield the target compound (383.0 mg, 1.8 mmol, 51%).
^{1}H NMR (400 MHz, $CDCl_3$) δ 7.24 – 7.18 (m, 2H), 6.93 – 6.86 (m, 2H), 3.95 (t, *J* = 6.4 Hz, 2H), 3.68 (s, 2H), 1.84 - 1.73 (m, 2H), 1.49 - 1.34 (m, 4H), 0.93 (t, *J* = 7.1 Hz, 3H) ppm. ^{13}C NMR (100 MHz, $CDCl_3$) δ: 158.94, 129.04, 121.51, 118.24, 115.10, 68.14, 31.89, 28.90, 28.18, 22.84, 22.70, 22.45, 14.01 ppm.

3-(4-Formylphenyl)-2-(4-(pentyloxy)phenyl)acrylonitrile (15)
An oven-dried round bottom flask was charged with diethoxymethylbenzaldehyde (306 mg, 1.47 mmol, 1 eq.), **14** (386 mg, 1.90 mmol, 1.3 eq.) and MeOH (17 mL). To this, 1M NaOMe in MeOH (3 mL) was added and the mixture was stirred at room temperature under argon. Conversion was monitored using ^{1}H NMR to check for disappearance of the aldehyde peak. After complete conversion, the mixture was diluted in MeOH and the precipitate was filtered by gravity filtration. The precipitate was dissolved in $CHCl_3$ and concentrated HCl was added. The mixture was stirred at 65 °C for 1 hour until full conversion. Hereafter, the mixture was concentrated in vacuo and purified by column chromatography (Liquid injection from heptane, eluent heptane:DCM 50/50 – 0/100), to yield the target compound as a yellow solid (306 mg, 0.96 mmol, 65%).
^{1}H NMR (400 MHz, $CDCl_3$) δ 10.06 (s, 1H), 7.98 (q, *J* = 8.4 Hz, 4H), 7.64 (d, *J* = 8.9 Hz, 2H), 7.46 (s, 1H), 6.97 (d, *J* = 8.9 Hz, 2H), 4.01 (t, *J* = 6.6 Hz, 2H), 1.87 – 1.77 (m, 2H), 1.52 – 1.35 (m, 4H), 0.95 (t, *J* = 7.0 Hz, 3H) ppm. ^{13}C NMR (100 MHz, $CDCl_3$) δ: 191.35, 160.66, 139.61, 137.70, 136.72, 130.11, 129.49, 127.60, 126.06, 117.60, 115.11, 114.46, 68.30, 28.85, 28.16, 22.45, 14.02 ppm.

3-(4-(2-Cyano-2-(4-(pent-4-en-1-yloxy)phenyl)vinyl)phenyl)-2-(4-(pentyloxy)phenyl)acrylonitrile (16)
An oven-dried round bottom flask was charged with **12** (130 mg, 0.64 mmol, 1 eq.) in EtOH (20 mL) and whilst stirring 0.5 M NaOMe in MeOH (5.5 mL) was added. Subsequently, **14** (205 mg, 0.64 mmol, 1 eq.) was added and the mixture was stirred at room temperature overnight. After confirmation of aldehyde conversion, the mixture was diluted with EtOH and washed through a Büchner funnel. The residue was rinsed with cold EtOH (20 mL) and cold MeOH (20 mL), collected and dried in the oven at 80 °C. The product was obtained as a yellow solid (251 mg, 0.579 mmol, 81%).
^{1}H NMR (400 MHz, $CDCl_3$) δ 7.95 (s, 4H), 7.63 (d, *J* = 8.8 Hz, 4H), 7.43 (s, 2H), 6.97 (d, *J* = 8.8 Hz, 4H), 5.87 (ddt, *J* = 16.9, 10.2, 6.7 Hz, 1H), 5.13 – 4.98 (m, 2H), 4.02 (q, *J* = 6.7 Hz, 4H), 2.26 (q, *J* = 7.2 Hz, 2H), 1.97 – 1.77 (m, 4H), 1.43 (tt, *J* = 14.6, 7.8 Hz, 4H), 0.95 (t, *J* = 7.1 Hz, 3H) ppm. ^{13}C NMR (100 MHz, $CDCl_3$) δ: 158.84, 137.70, 129.06, 121.63, 118.22, 115.29, 115.11, 67.29, 30.06, 28.34, 22.84 ppm.

3-(4-Formylphenyl)-2-(4-methoxyphenyl)acrylonitrile (17)
An oven-dried round bottom flask was charged with diethoxymethylbenzaldehyde (299 mg, 1.43 mmol, 1 eq.), 4-methoxyphenylacetonitrile (278 mg, 1.88 mmol, 1.3 eq.) and MeOH (10 mL). To this, 1M NaOMe in MeOH (6 mL) was added and the mixture was stirred at room temperature under argon. Conversion was monitored using ^{1}H NMR to check for disappearance of the aldehyde peak. After complete conversion, the mixture was

diluted in H_2O and the precipitate was filtered by gravity filtration. The precipitate was dissolved in $CHCl_3$ (10 mL) and concentrated HCl was added. The mixture was stirred at 65 °C for 1 hour until full conversion. Hereafter, the mixture was concentrated in vacuo and purified by column chromatography (Liquid injection from heptane, eluent heptane:DCM 50/50 – 0/100) to yield the product as a yellow solid (208 mg, 0.791 mmol, 55%).
^{1}H NMR (400 MHz, $CDCl_3$) δ 10.05 (d, *J* = 1.4 Hz, 1H), 8.05 – 7.91 (m, 4H), 7.68 – 7.61 (m, 2H), 7.47 (s, 1H), 6.98 (dd, *J* = 8.7, 1.4 Hz, 2H), 3.87 (s, 3H) ppm. ^{13}C NMR (100 MHz, $CDCl_3$) δ 158.85, 137.71, 129.06, 121.63, 115.30, 115.11, 67.29, 30.07, 28.35, 22.85, 22.70 ppm.

3-(4-((2-Cyano-2-(4-(pent-4-en-1-yloxy)phenyl)vinyl)phenyl)-2-(4-methoxyphenyl)acrylonitrile (18)
An oven-dried round bottom flask was charged with **12** (106 mg, 0.530 mmol, 1 eq.) in EtOH (5 mL) and whilst stirring 0.5 M NaOMe in MeOH (5 mL) was added. Subsequently, **17** (134 mg, 0.510 mmol, 1 eq.) was added and the mixture was stirred at room temperature overnight. After confirmation of aldehyde conversion, the mixture was diluted with H_2O and washed through a Büchner funnel. The residue was rinsed with cold EtOH (20 mL) and cold MeOH (20 mL), collected and dried in the oven at 80 °C. The product was obtained as a yellow solid (61 mg, 0.137 mmol, 27%).
^{1}H NMR (400 MHz, $CDCl_3$) δ 7.96 (s, 4H), 7.68 – 7.61 (m, 4H), 7.43 (d, *J* = 1.9 Hz, 2H), 6.98 (dd, *J* = 8.5, 5.3 Hz, 4H), 5.87 (ddt, *J* = 16.8, 10.1, 6.6 Hz, 1H), 5.15 – 4.95 (m, 2H), 4.03 (t, *J* = 6.4 Hz, 2H), 3.87 (s, 3H), 2.32 – 2.17 (m, 2H), 1.99 – 1.84 (m, 2H) ppm. ^{13}C NMR (100 MHz, $CDCl_3$) δ 160.73, 160.24, 138.56, 138.42, 137.63, 135.42, 135.36, 129.52, 127.48, 127.45, 126.75, 126.58, 118.00, 115.40, 115.06, 114.54, 112.33, 112.26, 67.41, 55.49, 30.06, 28.32 ppm.

3-(4-Formylphenyl)-2-phenylacrylonitrile (19)
An oven-dried round bottom flask was charged with diethoxymethylbenzaldehyde (1.999 g, 9.60 mmol, 1 eq.), benzylacetonitril (1.125 g, 9.60 mmol, 1 eq.) and MeOH (20 mL). To this, 1M NaOMe in MeOH (10 mL) was added and the mixture was stirred at room temperature under argon. Conversion was monitored using ^{1}H NMR to check for disappearance of the aldehyde peak. After complete conversion, the mixture was diluted in MeOH (30 mL) and the green/yellow precipitate was filtered by gravity filtration. The filtrate was poured in water and centrifuged to form a yellow gel at the bottom of the falcon tube. This gel was dissolved in $CHCl_3$ (30 mL) and concentrated HCl was added (10 mL). The mixture was stirred at 65 °C for 1 hour until full conversion. Hereafter, the mixture was reduced in vacuo and purified by column chromatography (Liquid injection from heptane, eluent heptane:DCM 50/50 – 0/100), to yield the target compound as a yellow solid (720 mg, 3.09 mmol, 32%).
^{1}H NMR (400 MHz, $CDCl_3$) δ 10.07 (s, 1H), 8.04 (d, *J* = 8.3 Hz, 2H), 7.98 (d, *J* = 8.5 Hz, 2H), 7.75 – 7.67 (m, 2H), 7.53 – 7.41 (m, 3H) ppm. ^{13}C NMR (100 MHz, $CDCl_3$) δ 191.43, 140.37, 139.32, 137.16, 133.96, 130.24, 130.07, 129.84, 129.53, 129.36, 126.34, 117.54, 114.96, 76.84, 0.14 ppm.

3-(4-(2-Cyano-2-(4-(pent-4-en-1-yloxy)phenyl)vinyl)phenyl)-2-phenylacrylonitrile (20)
An oven-dried round bottom flask was charged with **12** (0.41 g, 2.06 mmol, 1 eq.) in EtOH (20 mL) and whilst stirring 0.5 M NaOMe in MeOH (20 mL) was added. Subsequently, **19** (0.48 g, 2.06 mmol, 1 eq.) was added and the mixture was stirred at room temperature overnight. After confirmation of aldehyde conversion, the mixture was diluted with EtOH (10 mL) and washed through a Büchner funnel. The residue was rinsed with cold EtOH (10 mL) and cold MeOH (100 mL), collected and dried in the oven at 80 °C. The product was obtained as a yellow solid (417 mg, 1.68 mmol, 82%).
^{1}H NMR (400 MHz, $CDCl_3$) δ 8.05 – 7.92 (m, 4H), 7.75 – 7.67 (m, 2H), 7.66 – 7.60 (m, 2H), 7.55 (s, 1H), 7.51 – 7.39 (m, 4H), 7.00 – 6.94 (m, 2H), 5.87 (ddt, *J* = 17.0, 10.2, 6.7 Hz, 1H), 5.14 – 4.96 (m, 2H), 4.03 (t, *J* = 6.4 Hz, 2H), 2.34 – 2.19 (m, 2H), 1.93 (dt, *J* = 8.0, 6.5 Hz, 2H) ppm. ^{13}C NMR (100 MHz, $CDCl_3$) δ 160.30, 140.80, 138.31, 137.62, 135.84, 135.05, 134.27, 129.76, 129.54, 129.17, 127.49, 126.53, 126.12, 117.94, 117.84, 115.41, 115.07, 112.71, 112.66, 67.41, 30.05, 28.32 ppm.

Si_7-OPV-Si_7
A flame dried Schlenk flask was charged with **12** (69 mg, 0.14 mmol, 1 eq.), **HSi_7** (236 mg, 0.46 mmol, 3.3 eq.) and dry DCM (0.5 mL). subsequently, 2 drops Karstedt's catalyst were added and the mixture was stirred for 2 hours under argon. The mixture was reduced in vacuo and purified by column chromatography (Liquid injection from heptane, eluent heptane:$CHCl_3$ 100/0 – 70/30) to yield the target compound as a yellow crystal (142 mg, 0.093 mmol, 67%).
^{1}H NMR (400 MHz, $CDCl_3$) δ 7.95 (s, 4H), 7.67 – 7.57 (m, 4H), 7.43 (s, 2H), 6.96 (d, *J* = 8.8 Hz, 4H), 4.00 (t, *J* = 6.6 Hz, 4H), 1.82 (p, *J* = 7.1, 6.7 Hz, 4H), 1.53 – 1.35 (m, 8H), 0.63 – 0.53 (m, 4H), 0.10 – 0.04 (m, 90H) ppm. ^{13}C NMR (100 MHz, $CDCl_3$) δ 183.35, 160.25, 129.40, 127.85, 125.25, 115.04, 109.05, 69.75, 66.61, 50.46, 46.91, 30.74, 4.82, 1.80, 1.16, 1.08, 0.14 ppm. MALDI-ToF-MS M_w calculated for $C_{64}H_{124}N_2O_{14}Si_{14}$: 1536.6 Da, m/z found: 1561.6 Da $[M+Na]^+$.

Pent-OPV-Si_{15}
An oven-dried round bottom flask was charged with **16** (52 mg, 0.104 mmol, 1 eq.), **HSi_{15}** (124 mg, 0.112 mmol, 1.1 eq.) and dry DCM (3 mL). Subsequently, 2 drops Karstedt's catalyst were added and the mixture was stirred under argon at room temperature overnight. The mixture was reduced in vacuo and purified by column chromatography (Liquid injection from heptane, eluent heptane:$CHCl_3$ 100/0 – 0/100) to yield the target compound as a sticky, bright yellow solid (89.6 mg, 0.056 mmol, 54%).
^{1}H NMR (400 MHz, $CDCl_3$) δ 7.95 (s, 4H), 7.63 (d, *J* = 8.7 Hz, 4H), 7.43 (s, 2H), 6.96 (dd, *J* = 8.9, 2.0 Hz, 5H), 4.01 (dt, *J* = 6.5, 3.3 Hz, 4H), 1.87 – 1.77 (m, 4H), 1.52– 1.36 (m, 8H), 0.95 (t, *J* = 7.1 Hz, 3H), 0.61 – 0.55 (m, 2H), 0.10 – 0.04 (m, 93H) ppm. ^{13}C NMR (100 MHz, $CDCl_3$) δ: 160.03, 138.60, 135.55, 129.65, 127.58, 118.30, 115.18, 112.54, 68.41, 29.86, 29.09, 29.03, 28.92, 28.35, 26.26, 23.23, 22.60, 18.38, 14.17, 1.93, 1.34, 1.29, 1.20, 0.34, 0.14 ppm. MALDI-ToF-MS M_w calculated for $C_{65}H_{127}N_2O_{16}Si_{15}$: 1612.6 Da, m/z found: 1612.6 Da $[M]^+$.

Pent-OPV-Si_{32}-OPV-Pent
An oven-dried round bottom flask was charged with **16** (101 mg, 0.200 mmol, 2.1 eq.), **$HSi_{32}H$** (230 mg, 0.097 mmol, 1 eq.) and dry DCM (2 mL). Subsequently, 2 drops Karstedt's catalyst were added, and the mixture was stirred under argon at room temperature overnight. The mixture was reduced in vacuo and purified by column chromatography (Liquid injection from heptane, eluent heptane:$CHCl_3$ 100/0 – 80/20) to yield the target compound as a brittle yellow solid (153 mg, 0.045 mmol, 47%).
^{1}H NMR (400 MHz, $CDCl_3$) δ: 7.97 (s, 8H), 7.65 (d, *J* = 8.7 Hz, 8H), 7.45 (s, 4H), 6.98 (dd, *J* = 8.9, 2.1 Hz, 8H), 4.03 (td, *J* = 6.6, 3.5 Hz, 8H), 1.85 (h, *J* = 6.5 Hz, 8H), 1.46 (m, 8H), 0.97 (t, *J* = 7.1 Hz, 6H), 0.64 – 0.56 (m, 4H), 0.09 (s, 192H) ppm. ^{13}C NMR (100 MHz, $CDCl_3$) δ: ^{13}C NMR (100 MHz, $CDCl_3$) δ 160.37, 138.71, 129.50, 127.44, 117.51, 115.04, 112.11, 68.14, 47.70, 29.71, 28.87, 28.10, 23.55, 22.50, 22.46, 18.53, 14.20, 1.19, 1.09, 1.04, 0.20 ppm. MALDI-ToF-MS M_w calculated for $C_{132}H_{262}N_4O_{35}Si_{32}$: 3359.2 Da, m/z found: 3382.0 Da $[M+Na]^+$.

Me-OPV-Si_{15}
An oven-dried round bottom flask was charged with **18** (19 mg, 0.0421 mmol, 1 eq.), **HSi_{15}** (63 mg, 0.056 mmol, 1.3 eq.) and dry DCM (3 mL). Subsequently, 2 drops Karstedt's catalyst were added and the mixture was stirred under argon at room temperature overnight. The mixture was reduced in vacuo and purified by column chromatography (Liquid injection from heptane, eluent heptane:$CHCl_3$ 100/0 – 0/100) to yield the target compound as a sticky yellow solid (23 mg, 0.015 mmol, 36%).
^{1}H NMR (400 MHz, $CDCl_3$) δ 7.96 (s, 4H), 7.70 – 7.56 (m, 4H), 7.43 (d, *J* = 2.7 Hz, 2H), 7.02 – 6.94 (m, 4H), 4.00 (t, *J* = 6.6 Hz, 2H), 3.87 (s, 3H), 1.81 (p, *J* = 6.7 Hz, 2H), 1.53 – 1.37 (m, 4H), 0.62 – 0.54 (m, 2H), 0.08 (dt, *J* = 3.9, 1.5 Hz, 93H) ppm. ^{13}C NMR (100 MHz, $CDCl_3$) δ 160.73, 160.35, 138.60, 138.35, 135.46, 135.35, 129.52, 127.48, 127.43, 126.78, 126.48, 117.99, 115.03, 114.54, 112.41, 112.28, 68.26, 55.49, 29.71, 28.94, 23.09, 18.21, 1.79, 1.43, 1.19, 1.15, 1.09, 1.06, 0.68, 0.20 ppm. MALDI-ToF-MS M_w calculated for $C_{61}H_{119}N_2O_{16}Si_{15}$: 1556.51 Da, m/z found 1579.53 Da $[M+Na]^+$

Me-OPV-Si_{32}-OPV-Me
An oven-dried round bottom flask was charged with **18** (49 mg, 0.109 mmol, 1.9 eq.), **$HSi_{32}H$** (131 mg, 0.056 mmol, 1 eq.) and dry DCM (2 mL). Subsequently, 1 drop of Karstedt's catalyst was added and the mixture was stirred under argon at room temperature overnight. The mixture was reduced in vacuo and purified by column chromatography (Liquid injection from heptane, eluent heptane:EtAc, 100/0 – 50/50) to yield the target compound as a bright yellow solid (94 mg, 0.029 mmol, 52%).
^{1}H NMR (400 MHz, $CDCl_3$) δ: 7.95 (s, 8H), 7.69 – 7.55 (m, 8H), 7.43 (d, *J* = 2.7 Hz, 4H), 6.97 (t, *J* = 8.5 Hz, 8H), 4.00 (t, *J* = 6.5 Hz, 4H), 3.87 (s, 6H), 1.81 (p, *J* = 6.6 Hz, 4H), 1.52 – 1.37 (m, 8H), 0.63 – 0.52 (m, 4H),

0.07 (d, J = 2.0 Hz, 198H) ppm. ^{13}C NMR (100 MHz, $CDCl_3$) δ 160.73, 160.35, 138.59, 138.34, 135.46, 135.34, 129.52, 129.50, 127.48, 127.43, 126.77, 126.48, 117.99, 115.03, 114.54, 112.40, 112.27, 68.25, 55.48, 29.72, 28.95, 23.09, 18.21, 1.41, 1.19, 1.07, 1.04, 0.68, 0.20 ppm. MALDI-ToF-MS M_w calculated for $C_{124}H_{246}N_4O_{35}Si_{32}$: 3247.0 Da, m/z found 3274.0 Da $[M+Na]^+$.

H-OPV-Si$_{15}$
An oven-dried round bottom flask was charged with **20** (53 mg, 0.130 mmol, 1 eq.), **HSi$_{15}$** (182 mg, 0.160 mmol, 1.2 eq.) and dry DCM (3 mL). Subsequently, 2 drops Karstedt's catalyst were added and the mixture was stirred under argon at room temperature overnight. The mixture was concentrated in vacuo and purified by column chromatography (Liquid injection from heptane, eluent heptane:$CHCl_3$ 100/0 – 0/100) to yield the target compound as a sticky bright yellow solid (140 mg, 0.092 mmol, 71%).
^{1}H NMR (400 MHz, $CDCl_3$) δ 7.98 (d, J = 2.7 Hz, 4H), 7.74 – 7.68 (m, 2H), 7.63 (d, J = 8.8 Hz, 2H), 7.55 (s, 1H), 7.50 – 7.38 (m, 5H), 6.96 (d, J = 8.9 Hz, 2H), 4.00 (t, J = 6.7 Hz, 2H), 1.81 (dt, J = 8.2, 6.5 Hz, 2H), 1.54 – 1.36 (m, 4H), 0.62 – 0.55 (m, 2H), 0.10 – 0.04 (m, 90H) ppm. ^{13}C NMR (100 MHz, $CDCl_3$) δ 160.20, 140.60, 138.02, 135.67, 134.82, 134.08, 130.08, 129.55, 129.33, 129.07, 128.96, 128.64, 127.26, 126.21, 125.91, 117.74, 117.64, 114.84, 112.50, 68.06, 29.51, 28.74, 22.89, 18.01, 1.59, 1.22, 0.99, 0.95, 0.88, 0.86, 0.48 ppm. MALDI-ToF-MS M_w calculated for $C_{60}H_{117}N_2O_{15}Si_{15}$: 1526.5 Da, m/z found 1549.5 Da $[M+Na]^+$.

H-OPV-Si$_{32}$-OPV-H
An oven-dried round bottom flask was charged with **20** (74 mg, 0.1777 mmol, 2.1 eq.), **HSi$_{32}$H** (203 mg, 0.086 mmol, 1 eq.) and dry DCM (3 mL). Subsequently, 2 drops Karstedt's catalyst were added and the mixture was stirred under argon at room temperature overnight. The mixture was reduced in vacuo and purified by column chromatography (Liquid injection from heptane, eluent heptane:$CHCl_3$ 100/0 – 0/100) to yield the target compound as a yellow solid (79.9 mg, 0.029 mmol, 24%).
^{1}H NMR (400 MHz, $CDCl_3$) δ 8.01 – 7.94 (m, 8H), 7.71 (d, J = 7.2 Hz, 4H), 7.63 (d, J = 8.8 Hz, 4H), 7.55 (s, 2H), 7.50 – 7.41 (m, 8H), 6.96 (d, J = 8.8 Hz, 4H), 4.00 (t, J = 6.5 Hz, 4H), 1.82 (dt, J = 14.3, 7.3 Hz, 4H), 1.51 – 1.39 (m, 8H), 0.61 – 0.55 (m, 4H), 0.07 (s, 192H) ppm. ^{13}C NMR (100 MHz, $CDCl_3$) δ 160.41, 140.80, 138.22, 135.86, 134.94, 134.35, 129.75, 129.53, 129.16, 127.46, 126.11, 115.04, 112.70, 67.30, 29.71, 28.94, 23.09, 18.21, 1.08, 1.04, 0.20 ppm. MALDI-ToF-MS M_w calculated for $C_{122}H_{242}N_4O_{33}Si_{32}$: 3187.0 Da, found 3210.0 Da $[M+Na]^+$.

2.5.2.5 Synthesis of DPA block molecules with various side chains

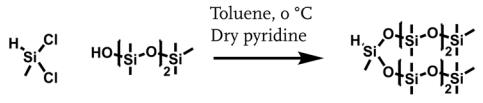

Scheme 7. Synthetic route to the branched *o*DMS **HSi$_{7b}$**.

Branched *o*DMS Si7b
To toluene (56 ml), cooled with an ice/water bath, was added dichloromethylsilane (2.60 ml, 25.0 mmol, 1 eq.), followed by dry pyridine (9.12 mL, 112 mmol, 4.5 eq.). A solution of $MeSi_3OH$ (12.28 g, 55.2 mmol, 2.2 eq.) in toluene (27 mL) was added dropwise over 2 minutes. The cooling was removed after 20 minutes and the reaction was let to stir at room temperature under argon. After 26 hours, the reaction mixture was shaken with DI water (3x 100 mL) in a separatory funnel. The organic phase was concentrated in vacuo and purified by column chromatography (SiO_2, eluent heptane/chloroform 100/0 – 0/100) The product was obtained as a clear liquid (10.13 g, 19.5 mmol, 77%).
^{1}H-NMR (400 MHz, $CDCl_3$): δ = 4.69 (s, 1H, H-Si-CH_3), 0.15 (s, 3H, H-Si-CH_3), 0.11 – 0.08 (m, 30H, $(CH_3)_3$-Si), 0.05 (s, 18H, H-Si-O-Si-$(CH_3)_2$) ppm. ^{13}C NMR (100 MHz, $CDCl_3$) δ = 32.21, 29.34, 23.01, 14.42, 2.37, 2.08, 1.78, 1.71, 1.62, 1.44, 1.35, 1.32, 1.27, 1.16, 0.97 ppm. ^{29}Si NMR (79 MHz, $CDCl_3$) δ = 7.32, –20.73, –21.17, –37.66 ppm. GCMS found: 503 Da = $[M-15]^+$.

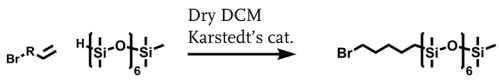

Scheme 8. Synthetic route to the bromo-alkane-*o*DMS molecules.

General procedure for Karstedt's hydrosilylation reaction
In a flame dried Schlenk tube, **HSi**$_7$ (1 eq.) and bromo-alkene (1.5 eq.) were charged. The compounds are dissolved in dry DCM after which 1 or 2 drops Karstedt's catalyst were added under argon. After complete conversion (indicated by the absence of the *H*-Si hydrogen in ^{1}H-NMR at 4.70 ppm in $CDCl_3$) the mixture was diluted with DCM and reduced in vacuo. Excess bromo-alkene was partially removed with column chromatography (Liquid injection from heptane, eluent heptane/DCM 100/0 – 0/100). Byproducts could not be removed completely, and the compounds were used as is. All compounds were obtained as colorless oils.

BrC$_4$Si$_7$
HSi$_7$ (500 mg, 0.96 mmol, 1 eq.), 4-bromo-1-butene (286 mg, 2.12 mmol, 2.2 eq.), dry DCM (0.3 mL). Product: 545 mg, 0.83 mmol, 85 %, obtained as a colorless liquid.
^{1}H NMR (400 MHz, $CDCl_3$): δ 3.41 (t, *J* = 6.8 Hz, 2H), 1.92 – 1.83 (m, 2H), 1.52 – 1.43 (m, 2H), 0.57 – 0.52 (m, 2H), 0.11 – 0.03 (m, 45H) ppm. ^{13}C NMR (100 MHz, $CDCl_3$) δ 36.26, 33.73, 22.02, 17.40, 1.94, 1.33, 1.30, 1.24, 1.22, 1.20, 0.29 ppm.

BrC$_6$Si$_7$
HSi$_7$ (1000 mg, 1.93 mmol, 1 eq.), 6-bromo-1-hexene (500 mg, 3.06 mmol, 1.6 eq.), dry DCM (0.3 mL). Product: 1100 mg, 1.58 mmol, 82 %, obtained as a colorless liquid.
^{1}H NMR (400 MHz, $CDCl_3$): δ 3.44-3.41 (m, 2H), 1.90 – 1.75 (m, 2H), 1.48 – 1.25 (m, 6H), 0.60 – 0.45 (m, 2H), 0.13 – 0.0 (m, 45H) ppm.

BrC$_7$Si$_7$
HSi$_7$ (330 mg, 0.63 mmol, 1 eq.), 7-bromo-1-heptene (180 mg, 1.02 mmol, 1.6 eq.), dry DCM (0.5 mL). Product: 262 mg, 0.37 mmol, 59 %, obtained as a colorless liquid.
^{1}H NMR (400 MHz, $CDCl_3$): δ 3.41 (t, *J* = 6.9 Hz, 2H), 1.90 – 1.80 (m, 2H), 1.48 – 1.36 (m, 2H), 1.35 – 1.28 (m, 6H), 0.57 – 0.49 (m, 2H), 0.10 – 0.03 (m, 45H) ppm. ^{13}C NMR (100 MHz, $CDCl_3$) δ 34.35, 33.54, 33.23, 28.85, 28.48, 23.48, 18.57, 2.15, 1.54, 1.51, 1.43, 0.54 ppm.

BrC$_8$Si$_7$
HSi$_7$ (330 mg, 0.63 mmol, 1 eq.), 8-bromo-1-octene (160 mg, 0.84 mmol, 1.3 eq.), dry DCM (1 mL). Product: 282 mg, 0.39 mmol, 62 %, obtained as a colorless liquid.
^{1}H NMR (400 MHz, $CDCl_3$): δ 3.40 (t, *J* = 6.9 Hz, 2H), 1.90 – 1.81 (m, 2H), 1.47 – 1.37 (m, 2H), 1.35 – 1.23 (m, 8H), 0.55 – 0.47 (m, 2H), 0.10 – 0.02 (m, 45H) ppm.

BrC$_9$Si$_7$
HSi$_7$ (325 mg, 0.62 mmol, 1 eq.), 9-bromo-1-nonene (154 mg, 0.75 mmol, 1.2 eq.), dry DCM (1 mL). Product: 414 mg, 0.56 mmol, 90 %, obtained as a colorless liquid.
^{1}H NMR (400 MHz, $CDCl_3$): δ 3.40 (t, *J* = 6.9 Hz, 2H), 1.89 – 1.81 (m, 2H), 1.46 – 1.38 (m, 2H), 1.35 – 1.24 (m, 10H), 0.56 – 0.48 (m, 2H), 0.11 – 0.02 (m, 45H) ppm.

BrC$_{10}$Si$_7$
HSi$_7$ (1000 mg, 1.93 mmol, 1 eq.), 10-bromo-1-decene (659 mg, 3.01 mmol, 1.6 eq.), dry DCM (0.3 mL). Product: 760 mg, 1.03 mmol, 53 %, obtained as a colorless liquid.
^{1}H NMR (400 MHz, $CDCl_3$): δ 3.40 (t, *J* = 6.9 Hz, 2H), 1.90 – 1.79 (m, 2H), 1.47 – 1.37 (m, 2H), 1.36 – 1.20 (m, 12H), 0.56 – 0.48 (m, 2H), 0.11 –0.02 (m, 45H) ppm.

BrC$_{11}$Si$_7$
HSi$_7$ (780 mg, 1.50 mmol, 1 eq.), 11-bromo-1-undecene (350 mg, 1.50 mmol, 1.0 eq.), dry DCM (0.5 mL). Product: 913 mg, 1.33 mmol, 88 %, obtained as a colorless liquid.
^{1}H NMR (400 MHz, $CDCl_3$): δ 3.40 (t, *J* = 6.9 Hz, 2H), 1.90 –1.80 (m, 2H), 1.46 – 1.37 (m, 2H), 1.34 –1.23 (m, 14H), 0.56 – 0.49 (m, 2H), 0.11 –0.03 (m, 45H) ppm.

TsChiralSi$_7$
HSi$_7$ (570 mg, 1.10 mmol, 1.4 eq.), (S)-2-methylpent-4-en-1-yl 4-ethylbenzenesulfonate (200 mg, 0.79 mmol, 1 eq.), dry DCM (1 mL). Product: 565 mg, 1.04 mmol, 95 %, obtained as a colorless liquid.
^{1}H NMR (400 MHz, $CDCl_3$): δ 7.79 (d, *J* = 8.3 Hz, 2H), 7.34 (d, *J* = 7.9 Hz, 2H), 3.90 – 3.75 (m, 2H), 1.84 – 1.72 (m, 1H), 1.40 – 1.07 (m, 4H), 0.90 – 0.85 (d, *J* = 6.7, 3H), 0.50-0.40 (m, 2H), 0.10-0.01 (m, 45H) ppm.

Si$_{7b}$-DPA-Si$_{7b}$
HSi$_{7b}$ (156 mg, 0.3 mmol, 3 eq.), 9,10-bis(4-(pent-4-en-1-yloxy)phenyl)anthracene (50 mg, 0.1 mmol, 1 eq.), dry DCM (4 mL). Product: 135 mg, 0.088 mmol, 88 %, obtained as a colorless liquid.
^{1}H NMR (400 MHz, $CDCl_3$): δ 7.77-7.71 (m, 4H), 7.39 – 7.35 (m, 4H), 7.35 – 7.29 (m, 4H), 7.15 – 7.10 (m, 4H), 4.10 (t, *J* = 6.8 Hz, 4H), 1.94 – 1.84 (m, 4H), 1.61 – 1.45 (m, 4H), 1.51 – 1.37 (4H), 0.64 – 0.57 (m, 4H), 0.13 – 0.04 (m, 90H) ppm. ^{13}C NMR (100 MHz, $CDCl_3$): δ 158.96, 137.17, 132.69, 131.26, 130.63, 127.42, 125.16, 114.73, 68.47, 30.11, 29.58, 23.28, 17.88, 2.19, 1.89, 1.57, 1.52, 0.36 ppm. MALDI-ToF-MS: m/z calcd. for $C_{68}H_{130}O_{14}Si_{14}$ 1534.6; found: 1536.6 [M$^+$].

General procedure Williamson etherification
To a solution of 9,10-bis(4-hydroxyphenyl)anthracene (1 eq.) and K_2CO_3 (2.3-3.6 eq.) in ACN, bromo-alkane-*o*DMS (2.6-4.3 eq.) was dropwise added before reaction at 80 °C under argon atmosphere. The mixture was cooled to RT after reacting for 4 days, after which DI water was added. The target compound was extracted with chloroform. The organic phase was impregnated on celite and purified by column chromatography (Solid loading, eluent heptane/chloroform 100/0 – 0/100). This gave a mixture of mono and direacted compound, which was further purified by recycling GPC in THF to yield pure target compound.

C$_4$ ($Si_7C_4DPAC_4Si_7$)
9,10-Bis(4-hydroxyphenyl)anthracene (60 mg, 166 µmol, 1 eq.), K_2CO_3 (82 mg, 600 µmol, 3.6 eq.), ACN (2 mL), BrC_4Si_7 (465 mg, 712 µmol, 4.3 eq.). After recycling GPC, the product was obtained as a yellowish wax that crystallized into a brittle solid.
^{1}H NMR (400 MHz, $CDCl_3$): δ 7.79 – 7.72 (m, 4H), 7.41 – 7.35 (m, 4H), 7.35 – 7.29 (m, 4H), 7.16 – 7.10 (m, 4H), 4.12 (t, *J* = 6.4 Hz, 4H), 1.97 – 1.87 (m, 4H), 1.67 – 1.52 (m, 4H), 0.73 – 0.65 (m, 4H), 0.16 – 0.03 (m, 90H) ppm. ^{13}C NMR (100 MHz, $CDCl_3$): δ 158.97, 137.17, 132.69, 131.25, 130.62, 127.42, 125.17, 114.73, 68.11, 33.33, 20.29, 18.43, 2.16, 1.59, 1.52, 1.49, 1.46, 1.45. 0.59 ppm. MALDI-ToF-MS: m/z calcd. for $C_{64}H_{122}O_{14}Si_{14}$ 1508.9 Da, m/z found 1508.5 Da [M$^+$].

C$_6$ ($Si_7C_6DPAC_6Si_7$)
9,10-Bis(4-hydroxyphenyl)anthracene (40 mg, 110 µmol, 1 eq.), K_2CO_3 (55 mg, 400 µmol, 3.6 eq.), ACN (1 mL), BrC_6Si_7 (324 mg, 475 µmol, 4.3 eq. dissolved in 0.2 mL ACN). Prior to recycling GPC, 41 mg (23%) product was obtained. After recycling GPC, the product was obtained as a yellowish wax.
^{1}H NMR (400 MHz, $CDCl_3$): δ 7.78 – 7.72 (m, 4H), 7.40 – 7.35 (m, 4H), 7.35 – 7.29 (m, 4H), 7.15 – 7.10 (m, 4H), 4.11 (t, *J* = 6.5 Hz, 4H), 1.93 – 1.83 (m, 4H), 1.61 – 1.51 (m, 4H), 1.51 – 1.37 (8H), 0.63 – 0.56 (m, 4H), 0.13 – 0.03 (m, 90H). ^{13}C NMR (100 MHz, $CDCl_3$): δ 158.92, 137.13, 132.67, 131.23, 130.59, 127.39, 125.14, 114.69, 68.48, 33.58, 29.72, 26.24, 23.57, 18.59, 2.13, 1.55, 1.49, 1.45, 1.44, 1.42, 0.55 ppm. MALDI-ToF-MS: m/z calcd. for $C_{68}H_{130}O_{14}Si_{14}$ 1564.9 Da, m/z found 1564.6 Da [M$^+$].

C$_7$ ($Si_7C_7DPAC_7Si_7$)
9,10-Bis(4-hydroxyphenyl)anthracene (35 mg, 97 µmol, 1 eq.), K_2CO_3 (33 mg, 240 µmol, 2.4 eq.), ACN (12 mL), BrC_7Si_7 (222 mg, 319 µmol, 3.3 eq.). After recycling GPC, the product was obtained as a yellowish wax.
^{1}H NMR (400 MHz, $CDCl_3$): δ 7.77 – 7.72 (m, 4H), 7.39 – 7.35 (m, 4H), 7.34 – 7.30 (m, 4H), 7.15 – 7.11 (m, 4H), 4.11 (t, *J* = 6.5 Hz, 4H), 1.94 – 1.84 (m, 4H), 1.59 – 1.49 (m, 4H), 1.48 – 1.31 (12H), 0.61 – 0.56 (m, 4H), 0.13 – 0.03 (m, 90H) ppm. ^{13}C NMR (100 MHz, $CDCl_3$): δ 158.95, 137.15, 132.70, 131.26, 130.62, 127.42, 125.17, 114.71, 68.49, 33.78, 29.84, 29.59, 26.49, 23.59, 18.66, 2.16, 1.57, 1.52, 1.46, 1.45, 1.44, 0.58 ppm. MALDI-ToF-MS: m/z calcd. for $C_{70}H_{134}O_{14}Si_{14}$ 1593.0 Da, m/z found 1592.7 Da [M$^+$].

C$_8$ ($Si_7C_8DPAC_8Si_7$)
9,10-Bis(4-hydroxyphenyl)anthracene (44 mg, 122 µmol, 1 eq.), K_2CO_3 (32 mg, 230 µmol, 2.3 eq.), ACN (14 mL), BrC_7Si_7 (222 mg, 319 µmol, 2.6 eq.). After recycling GPC, the product was obtained as a yellowish wax.
^{1}H NMR (400 MHz, $CDCl_3$): δ 7.78 – 7.73 (m, 4H), 7.40 – 7.35 (m, 4H), 7.34 – 7.30 (m, 4H), 7.15 – 7.11 (m, 4H), 4.11 (t, *J* = 6.6 Hz, 4H), 1.94 – 1.85 (m, 4H), 1.60 – 1.50 (m, 4H), 1.46 – 1.33 (16H), 0.60 – 0.52 (m, 4H), 0.13 – 0.03 (m, 90H) ppm. ^{13}C NMR (100 MHz, $CDCl_3$): δ 158.95, 137.16, 132.70, 131.26, 130.62, 127.42, 125.17,

114.72, 68.50, 33.80, 29.82, 29.81, 29.74, 26.59, 23.62, 18.66, 2.16, 1.56, 1.52, 1.46, 1.44, 0.58 ppm. MALDI-ToF-MS: m/z calcd. for $C_{72}H_{138}O_{14}Si_{14}$ 1621.1 Da, m/z found 1620.7 Da [M+].

C_9 ($Si_7C_9DPAC_9Si_7$)
9,10-Bis(4-hydroxyphenyl)anthracene (33 mg, 91 µmol, 1 eq.), K_2CO_3 (39 mg, 280 µmol, 3.1 eq.), ACN (5 mL), BrC_9Si_7 (188 mg, 265 µmol, 2.9 eq.). After recycling GPC, the product was obtained as a yellowish wax.
^{1}H NMR (400 MHz, $CDCl_3$): δ 7.77 – 7.72 (m, 4H), 7.39 – 7.35 (m, 4H), 7.34 – 7.30 (m, 4H), 7.14 – 7.10 (m, 4H), 4.11 (t, *J* = 6.5 Hz, 4H), 1.94 – 1.84 (m, 4H), 1.59 – 1.49 (m, 4H), 1.46 – 1.31 (20H), 0.58 – 0.52 (m, 4H), 0.11 – 0.03 (m, 90H) ppm. ^{13}C NMR (100 MHz, $CDCl_3$): δ 158.95, 137.15, 132.70, 131.26, 130.61, 127.42, 125.17, 114.72, 68.51, 33.85, 29.96, 29.91, 29.82, 29.76, 26.56, 23.61, 18.65, 2.15, 1.55, 1.51, 1.45, 1.43, 0.57 ppm. MALDI-ToF-MS: m/z calcd. for $C_{74}H_{142}O_{14}Si_{14}$ 1649.1 Da, m/z found 1648.7 Da [M+].

C_{10} ($Si_7C_{10}DPAC_{10}Si_7$)
9,10-Bis(4-hydroxyphenyl)anthracene (32 mg, 88 µmol, 1 eq.), K_2CO_3 (39 mg, 280 µmol, 3.2 eq.), ACN (5 mL), $BrC_{10}Si_7$ (222 mg, 307 µmol, 3.5 eq.). After recycling GPC, the product was obtained as a yellowish wax.
^{1}H NMR (400 MHz, $CDCl_3$): δ 7.76 – 7.72 (m, 4H), 7.39 – 7.35 (m, 4H), 7.34 – 7.30 (m, 4H), 7.14 – 7.10 (m, 4H), 4.11 (t, *J* = 6.5 Hz, 4H), 1.93 – 1.82 (m, 4H), 1.59 – 1.49 (m, 4H), 1.35 – 1.29 (24H), 0.58 – 0.50 (m, 4H), 0.09 – 0.03 (m, 90H) ppm. ^{13}C NMR (100 MHz, $CDCl_3$): δ 158.95, 137.15, 132.70, 131.26, 130.61, 127.42, 125.87, 125.17, 114.72, 68.50, 33.86, 30.68, 30.06, 29.98, 29.88, 29.81, 26.56, 23.62, 18.65, 2.16, 1.55, 1.52, 1.45, 1.44, 0.57 ppm. MALDI-ToF-MS: m/z calcd. for $C_{76}H_{146}O_{14}Si_{14}$ 1677.2 Da, m/z found 1676.8 Da [M+].

C_{11} ($Si_7C_{11}DPAC_{11}Si_7$)
9,10-Bis(4-hydroxyphenyl)anthracene (60 mg, 166 µmol, 1 eq.), K_2CO_3 (82 mg, 596 µmol, 3.6 eq.), ACN (3 mL), $BrC_{11}Si_7$ (536 mg, 712 µmol, 4.3 eq.). After recycling GPC, the product was obtained as a yellowish wax.
^{1}H NMR (400 MHz, $CDCl_3$): δ 7.77 – 7.72 (m, 4H), 7.39 – 7.34 (m, 4H), 7.34 – 7.29 (m, 4H), 7.14 – 7.10 (m, 4H), 4.11 (t, *J* = 6.6 Hz, 4H), 1.93 – 1.84 (m, 4H), 1.59 – 1.51 (m, 4H), 1.41 – 1.26 (28H), 0.57 – 0.51 (m, 4H), 0.10 – 0.03 (m, 90H) ppm. ^{13}C NMR (100 MHz, $CDCl_3$): δ 158.95, 137.15, 132.70, 131.26, 130.61, 127.42, 125.87, 125.17, 114.72, 68.50, 33.86, 30.68, 30.06, 29.98, 29.88, 29.81, 26.56, 23.62, 18.65, 2.16, 1.55, 1.52, 1.45, 1.44, 0.57 ppm. MALDI-ToF-MS: m/z calcd. for $C_{78}H_{150}O_{14}Si_{14}$ 1705.2 Da, m/z found 1704.8 Da [M+].

C_5* (Si_7C_5*$DPAC_5$*Si_7)
9,10-Bis(4-hydroxyphenyl)anthracene (40 mg, 110 µmol, 1 eq.), K_2CO_3 (55 mg, 400 µmol, 3.6 eq.), ACN (3 mL), $BrChiralSi_7$ (367 mg, 475 µmol, 4.3 eq.). After recycling GPC, the product was obtained as a yellowish wax.
^{1}H NMR (400 MHz, $CDCl_3$): δ 7.77 – 7.72 (m, 4H), 7.40 – 7.35 (m, 4H), 7.35 – 7.29 (m, 4H), 7.15 – 7.10 (m, 4H), 4.00 – 3.84 (m, 4H), 2.12 – 2.00 (m, 4H), 1.69 – 1.57 (m, 2H), 1.55 – 1.29 (m, 4H), 1.11 (d, *J* = 6.7 Hz, 6H), 0.66 – 0.56 (m, 4H), 0.13 – 0.02 (m, 90H) ppm. ^{13}C NMR (100 MHz, $CDCl_3$): δ 159.11, 137.17, 132.67, 131.21, 130.62, 127.42, 125.15, 114.74, 73.74, 37.78, 33.45, 21.07, 18.85, 17.45, 2.15, 1.58, 1.51, 1.47, 1.45, 1.43, 0.63, 0.62, 0.35 ppm. MALDI-ToF-MS: m/z calcd. for $C_{68}H_{130}O_{14}Si_{14}$ 1562.6 Da, m/z found 1564.6 Da [M+].

Si_{11} ($Si_{11}DPASi_{11}$, no spacer)
In a flame dried Schlenk tube, 9,10-bis(4-hydroxyphenyl)anthracene (150 mg, 410 µmol, 1 eq.) was suspended in dry DCM (2 mL). To this, **$Si_{11}H$** (642 mg, 870 µmol, 2.1 eq.) and Strykers catalyst (9.2 mg suspended in 2 mL THF) were added. The reaction was let to react for 4 days. The product was impregnated on celite and purified by column chromatography (Solid loading, eluent heptane/EtOAc 100/0 – 0/100) to yield the final product as a colorless oil (400 mg, 206 µmol, 50 %). The liquid product did not show any thermal transitions above –70 °C.
^{1}H NMR (400 MHz, $CDCl_3$): δ 7.81 – 7.76 (m, 4H), 7.40 – 7.34 (m, 8H), 7.20 – 7.17 (m, 4H), 0.42 (s, 12H), 0.21 (s, 12H), 0.17 (s, 12H), 0.15 (s, 12H), 0.14 – 0.11 (m, 78H), 0.10 (s, 12H) ppm. ^{13}C NMR (100 MHz, $CDCl_3$): δ 154.46, 137.24, 132.73, 132.47, 130.60, 129.06, 127.89, 127.44, 125.20, 123.78, 120.29, 120.16, 30.10, 2.18, 1.83, 1.54, 1.49, 1.46, 1.44, 1.08, 0.12 ppm. MALDI-ToF-MS: m/z calcd. for $C_{72}H_{154}O_{22}Si_{22}$ 1986.6 Da, m/z found 1988.6 Da [M+].

2.6 References

(1) Hartmann, L.; Tremel, K.; Uttiya, S.; Crossland, E.; Ludwigs, S.; Kayunkid, N.; Vergnat, C.; Brinkmann, M. *Adv. Funct. Mater.* **2011**, *21*, 4047.
(2) Kamada, A.; Levin, A.; Toprakcioglu, Z.; Shen, Y.; Lutz-Bueno, V.; Baumann, K. N.; Mohammadi, P.; Linder, M. B.; Mezzenga, R.; Knowles, T. P. J. *Small* **2020**, *16*, 1904190.
(3) Giri, G.; Verploegen, E.; Mannsfeld, S. C. B.; Atahan-Evrenk, S.; Kim, D. H.; Lee, S. Y.; Becerril, H. A.; Aspuru-Guzik, A.; Toney, M. F.; Bao, Z. *Nature* **2011**, *480*, 504.
(4) O'Neill, M.; Kelly, S. M. *Adv. Mater.* **2011**, *23*, 566.
(5) Jin, X.; Price, M. B.; Finnegan, J. R.; Boott, C. E.; Richter, J. M.; Rao, A.; Menke, S. M.; Friend, R. H.; Whittell, G. R.; Manners, I. *Science* **2018**, *360*, 897.
(6) Joarder, B.; Yanai, N.; Kimizuka, N. *J. Phys. Chem. Lett.* **2018**, *9*, 4613.
(7) Park, S. K.; Kim, J. H.; Park, S. Y. *Adv. Mater.* **2018**, *30*, 1.
(8) Qin, X.; Han, J.; Yang, D.; Chen, W.; Zhao, T.; Jin, X.; Guo, P.; Duan, P. *Chinese Chem. Lett.* **2019**, *30*, 1923.
(9) Shi, Y. L.; Zhuo, M. P.; Wang, X. D.; Liao, L. S. *ACS Appl. Nano Mater.* **2020**, *3*, 1080.
(10) Cao, M.; Zhang, C.; Cai, Z.; Xiao, C.; Chen, X.; Yi, K.; Yang, Y.; Lu, Y.; Wei, D. *Nat. Commun.* **2019**, *10*, 1.
(11) Jiang, L.; Dong, H.; Meng, Q.; Li, H.; He, M.; Wei, Z.; He, Y.; Hu, W. *Adv. Mater.* **2011**, *23*, 2059.
(12) Yao, Y.; Zhang, L.; Orgiu, E.; Samorì, P. *Adv. Mater.* **2019**, *31*, 1.
(13) Wang, Y.; Sun, L.; Wang, C.; Yang, F.; Ren, X.; Zhang, X.; Dong, H.; Hu, W. *Chem. Soc. Rev.* **2019**, *48*, 1492.
(14) Percec, V.; Ahn, C. H.; Ungar, G.; Yeardley, D. J. P.; Möller, M.; Sheiko, S. S. *Nature* **1998**, *391*, 161.
(15) Neupane, G. P.; Ma, W.; Yildirim, T.; Tang, Y.; Zhang, L.; Lu, Y. *Nano Mater. Sci.* **2019**, *1*, 246.
(16) Yao, W.; Zhao, Y. S. *Nanoscale* **2014**, *6*, 3467.
(17) Huang, H.; Feng, W.; Chen, Y. *Chem. Soc. Rev* **2021**, *50*, 11381.
(18) Yang, F.; Cheng, S.; Zhang, X.; Ren, X.; Li, R.; Dong, H.; Hu, W. *Adv. Mater.* **2018**, *30*, 1702415.
(19) van Son, M. H. C.; Berghuis, A. M.; Eisenreich, F.; de Waal, B.; Vantomme, G.; Gómez Rivas, J.; Meijer, E. W. *Adv. Mater.* **2020**, *32*.
(20) Kloos, J.; Joosten, N.; Schenning, A.; Nijmeijer, K. *J. Memb. Sci.* **2021**, *620*, 118849.
(21) Tschierske, C. *J. Mater. Chem.* **1998**, *8*, 1485.
(22) Chen, Y.; Zhang, F.; Zhu, B.; Han, Y.; Bo, Z. *Chem. Asian J.* **2011**, *6*, 226.
(23) Lee, M.; Kim, J. W.; Hwang, I. W.; Kim, Y. R.; Oh, N. K.; Zin, W. C. *Adv. Mater.* **2001**, *13*, 1363.
(24) Israelachvili, J. N.; Mitchell, D. J.; Ninham, B. W. *J. Chem. Soc., Faraday Trans. 2,* **1976**, *72*, 1525.
(25) Mandle, R. J.; Davis, E. J.; Sarju, J. P.; Stock, N.; Cooke, M. S.; Lobato, S. A.; Cowling, S. J.; Goodby, J. W. *J. Mater. Chem. C* **2015**, *3*, 4333.
(26) Goodby, J. W.; Mandle, R. J.; Davis, E. J.; Zhong, T.; Cowling, S. J. *Liq. Cryst.* **2015**, *42*, 593.
(27) Ichikawa, T.; Yoshio, M.; Hamasaki, A.; Taguchi, S.; Liu, F.; Zeng, X.; Ungar, G.; Ohno, H.; Kato, T. *J. Am. Chem. Soc.* **2012**, *134*, 2634.
(28) Kato, T.; Mizoshita, N. *Curr. Opin. Solid State Mater. Sci.* **2002**, *6*, 579.
(29) Newton, J.; Coles, H.; Hodge, P.; Hannington, J. *J. Mater. Chem.* **1994**, *4*, 869.
(30) Chen, C.; Kieffer, R.; Ebert, H.; Prehm, M.; Zhang, R.; Zeng, X.; Liu, F.; Ungar, G.; Tschierske, C. *Angew. Chem. Int. Ed.* **2020**, *59*, 2725.
(31) Tschierske, C. *Curr. Opin. Colloid Interface Sci.* **2002**, *7*, 69.
(32) Leibler, L. *Macromolecules* **2002**, *13*, 1602.
(33) Bates, C. M.; Bates, F. S. *Macromolecules* **2016**, *50*, 3.
(34) Lee, M.; Cho, B. K.; Kim, H.; Yoon, J. Y.; Zin, W. C. *J. Am. Chem. Soc.* **1998**, *120*, 9168.
(35) Lee, M.; Yoo, Y. S. *J. Mater. Chem.* **2002**, *12*, 2161.
(36) Lee, M.; Cho, B. K.; Oh, N. K.; Zin, W. C. *Macromolecules* **2001**, *34*, 1987.
(37) Van Genabeek, B.; Lamers, B. A. G.; De Waal, B. F. M.; Van Son, M. H. C.; Palmans, A. R. A.; Meijer, E. W. *J. Am. Chem. Soc.* **2017**, *139*, 14869.
(38) Lamers, B. A. G.; Waal, B. F. M. de; Meijer, E. W. *J. Polym. Sci.* **2021**, *59*, 1142.
(39) Van Genabeek, B.; de Waal, B. F. M.; Gosens, M. M. J.; Pitet, L. M.; Palmans, A. R. A.; Meijer, E. W. *J. Am. Chem. Soc.* **2016**, *138*, 4210.
(40) Zha, R. H.; de Waal, B.; Lutz, M.; Teunissen, A. J. P.; Meijer, E. W. *J. Am. Chem. Soc.* **2016**, *138*, 5693.
(41) Genabeek, B. van; Lamers, B. A. G.; Hawker, C. J.; Meijer, E. W.; Gutekunst, W. R.; Schmidt, B. V. K. J. *J. Polym. Sci.* **2021**, *59*, 373.
(42) Lamers, B. A. G.; Van Son, M. H. C.; De Graaf, F. V.; Van Den Bersselaar, B. W. L.; De Waal, B. F.

M.; Komatsu, K.; Sato, H.; Aida, T.; Berrocal, J. A.; Palmans, A. R. A.; Vantomme, G.; Meskers, S. C. J.; Meijer, E. W. *Mater. Horizons* **2022**, *9*, 294.
(43) van Genabeek, B.; de Waal, B. F. M.; Palmans, A. R. A.; Meijer, E. W. *Polym. Chem.* **2018**, *9*, 2746.
(44) Berrocal, J. A.; Zha, R. H.; de Waal, B. F. M.; Lugger, J. A. M.; Lutz, M.; Meijer, E. W. *ACS Nano* **2017**, *11*, 3733.
(45) Yang, W.; Zhang, W.; Luo, L.; Lyu, X.; Xiao, A.; Shen, Z.; Fan, X. H. *Chem. Commun.* **2020**, *56*, 10341.
(46) Lamers, B. A. G.; Graf, R.; De Waal, B. F. M.; Vantomme, G.; Palmans, A. R. A.; Meijer, E. W. *J. Am. Chem. Soc.* **2019**, *141*, 15456.
(47) Zha, R. H.; Vantomme, G.; Berrocal, J. A.; Gosens, R.; De Waal, B.; Meskers, S.; Meijer, E. W. *Adv. Funct. Mater.* **2018**, *28*, 1.
(48) Godbert, N.; Crispini, A.; Ghedini, M.; Carini, M.; Chiaravalloti, F.; Ferrise, A. *J. Appl. Crystallogr.* **2014**, *47*, 668.
(49) Corsellis, E.; Guillon, D.; Kloess, P.; Coles, H. *Liq. Cryst.* **1997**, *23*, 235.
(50) Keith, C.; Reddy, R. A.; Hauser, A.; Baumeister, U.; Tschierske, C. *J. Am. Chem. Soc.* **2006**, *128*, 3051.
(51) Tosaka, M.; Tashiro, K. *Polym. J.* **2018**, *153*, 507.
(52) Kamatham, N.; Ibraikulov, O. A.; Durand, P.; Wang, J.; Boyron, O.; Heinrich, B.; Heiser, T.; Lévêque, P.; Leclerc, N.; Méry, S. *Adv. Funct. Mater.* **2021**, *31*, 1.
(53) Salzillo, T.; Della Valle, R. G.; Venuti, E.; Brillante, A.; Siegrist, T.; Masino, M.; Mezzadri, F.; Girlando, A. *J. Phys. Chem. C* **2016**, *120*, 1831.
(54) Ohta, A.; Hattori, K.; Kusumoto, Y.; Kawase, T.; Kobayashi, T.; Naito, H.; Kitamura, C. *Chem. Lett.* **2012**, *41*, 674.
(55) Varghese, S.; Yoon, S. J.; Casado, S.; Fischer, R. C.; Wannemacher, R.; Park, S. Y.; Gierschner, J. *Adv. Opt. Mater.* **2014**, *2*, 542.
(56) Norikane, Y.; Uchida, E.; Tanaka, S.; Fujiwara, K.; Koyama, E.; Azumi, R.; Akiyama, H.; Kihara, H.; Yoshida, M. *Org. Lett.* **2014**, *16*, 5012.
(57) Bruce, D. W.; Deschenaux, R.; Donnio, B.; Guillon, D. *Metallomesogens*; 2007.
(58) Cimrová, V.; Remmers, M.; Neher, D.; Wegner, G. *Adv. Mater.* **1996**, *8*, 146.
(59) Bao, Z.; Chen, Y.; Cai, R.; Yu, L. *Macromolecules* **1993**, *26*, 5281.
(60) Wolff, S. K.; Grimwood, D. J.; McKinnon, J. J.; Turner, M. J.; Jayatilaka, D.; Spackman, M. A. *Crystal Explorer*; 2012.
(61) Adams, J. M.; Ramdas, S. *Acta Crystallogr. Sect. B Struct. Crystallogr. Cryst. Chem.* **1973**, *35*, 679.
(62) Galigné, J. L. *Acta Crystallogr. Sect. B Struct. Crystallogr. Cryst. Chem.* **1970**, *26*, 1977.
(63) Xu, Y.; Wang, K.; Zhang, Y.; Xie, Z.; Zou, B.; Ma, Y. *J. Mater. Chem. C* **2016**, *4*, 1257.
(64) Maranda-Niedbała, A.; Krzyżewska, K.; Kotwica, K.; Skórka, Ł.; Drapała, J.; Jarzembska, K. N.; Zagórska, M.; Proń, A.; Nowakowski, R. *Langmuir* **2020**, *36*, 15048.
(65) Eisele, D. M.; Arias, D. H.; Fu, X.; Bloemsma, E. A.; Steiner, C. P.; Jensen, R. A.; Rebentrost, P.; Eisele, H.; Tokmakoff, A.; Lloyd, S.; Nelson, K. A.; Nicastro, D.; Knoester, J.; Bawendi, M. G. *Proc. Natl. Acad. Sci. U. S. A.* **2014**, *111*, E3367.
(66) Dumele, O.; Chen, J.; Passarelli, J. V.; Stupp, S. I. *Adv. Mater.* **2020**, *32*, 1907247.
(67) Lamers, B. A. G.; Van Son, M. H. C.; De Graaf, F. V.; Van Den Bersselaar, B. W. L.; De Waal, B. F. M.; Komatsu, K.; Sato, H.; Aida, T.; Berrocal, J. A.; Palmans, A. R. A.; Vantomme, G.; Meskers, S. C. J.; Meijer, E. W. *Mater. Horizons* **2022**, *9*, 294.
(68) Keegstra, E. M. D.; Van Mieden, V. Der; Zwikker, J. W.; Jenneskens, L. W.; Schouten, A.; Kooijman, H.; Veldman, N.; Spek, A. L. *Chem. Mater.* **1996**, *8*, 1092.
(69) Joseph, S.; Sathishkumar, R. *Acta Crystallogr. Sect. B Struct. Sci. Cryst. Eng. Mater.* **2014**, *70*, 839.
(70) Shaporenko, A.; Brunnbauer, M.; Terfort, A.; Johansson, L. S. O.; Grunze, M.; Zharnikov, M. *Langmuir*, **2005**, *21*, 4370.
(71) Dendzik, M.; Terfort, A.; Cyganik, P. *J. Phys. Chem. C* **2012**, *116*, 19535.
(72) Gnatek, D.; Schuster, S.; Ossowski, J.; Khan, M.; Rysz, J.; Krakert, S.; Terfort, A.; Zharnikov, M.; Cyganik, P. *J. Phys. Chem. C* **2015**, *119*, 25929.
(73) Gu, Q.; Wu, C.; Chen, S.; Huang, Y. *Liq. Cryst.* **2004**, *31*, 519.
(74) Maessen, S. J. D. Predicting the Formation of Lamellae in Block Molecules by Crystal Structure Energy Calculations, 2022.

Chapter 3

The influence of block molecule co-assembly on their optical properties

ABSTRACT: Co-assembly of donor and acceptor molecules can improve the optical properties relative to the individual components. This chapter elaborates on the requirements for co-assembly in nanostructured bulk materials and provides a better understanding of the parameters that can be used to change the optical properties. To this end, three series of block molecules mixtures were prepared. First, core-centered and telechelic arylene diimide block molecules were studied. We investigate the difference between charge transfer interactions, homo-interactions and molecular architecture on the formed nanostructure, which we relate to the interaction strength of the aromatic groups and the space available for the *o*DMS group. The charge transfer interactions lead to different colors of the material and result in lamellar morphologies. The second series, consisting of a viologen block molecule mixed with tetrathiafulvalene derivatives, shows that the observations and explanations can be extended to charged assemblies. Finally, in the third series, halogen bonding is used to change the optical properties of diphenylanthracene block molecules while maintaining the same nanostructure. These results show how block molecule systems can be designed with a higher probability of lamellar co-assembly, while simultaneously affecting optical properties. Our findings demonstrate the potential of block molecule co-assembly in the field of optoelectronics.

3.1 Introduction

Analogous to the alloying of inorganic compounds, the mixing of multiple organic components is an established method to obtain a desired function. The best known approaches are bulk heterojunction solar cells consisting of donor-acceptor mixtures for transporting holes and electrons, respectively,[1] as well as organic charge-transfer (CT) compounds where the electronic properties range from insulating to superconducting.[2] In both systems, the spatial arrangement of the various components determines the optoelectronic properties. For example, in bulk heterojunctions, nanomorphology and molecular aggregation influence exciton mobility.[3] In CT co-crystals, different properties arise for mixed stack (...-D-A-D-A-...) or segregated stack (...-A-A-... and ...-D-D-...) systems.[4] Under ambient conditions, mixed stack systems are generally semiconductors or insulators.[4–7] Segregated stacks with incomplete charge transfer between the stacks exhibit high electrical conductivity that can even become metallic-like.[8–12] Although bulk heterojunctions and CT co-crystals both use donor and acceptor molecules, the individual components in bulk heterojunctions perform different functions, while in CT co-crystals the function arises from both components together. CT co-crystals are found to possess a wide range of interesting properties, such as room-temperature phosphorescence,[13] ferroelectricity,[14,15] metallic electrical conductivity,[16] ambipolar charge transport,[17] and even superconductivity.[18] However, the fundamental structure-property relationship of CT co-crystals needs further elucidation to improve their properties, air stability, and use in thin films.[2,19]

The ability of soft CT materials to form organized, multicomponent nanostructures has led to the recent interest in studying the structure-property relationship of CT complexed π-donors and -acceptors.[20] These soft materials consist of gels,[21–23] supramolecular polymers,[24–26] covalent polymers,[27–30] liquid crystals,[31,32] and covalent organic frameworks.[33] However, compared to hydrogen-bonded supramolecular assemblies, the CT materials have relatively low association constants and the materials are therefore limited in their ability to create long-range ordered structures.[23] Their association can be enhanced by combining CT interactions with other noncovalent forces. For this purpose, hydrogen bonds,[21,23,25–27,29,30] ion complexation,[24,34] peptide-mediated assembly,[22,35] or amphiphilicity[24,25,31] are used, leading to larger domains of ordered structures and improved properties.[36]

Similar to amphiphilicity, the high mismatch in cohesive energy density between oligodimethylsiloxane (*o*DMS) and aromatic or aliphatic groups can be used to create well-defined, phase-separated assemblies.[37–43] This phase separation approach with *o*DMS has recently been used to study CT complexation in ordered, nanostructured systems based on pyrene and naphthalene diimide (NDI) and serves as the starting point for the research presented in this chapter.[39,44] To this end, telechelic block molecules were used with either peripheral pyrene (**Pyr-Si$_n$-Pyr**), peripheral NDI (**NDI-Si$_8$-NDI**), as well as an asymmetric structure with pyrene and NDI at opposite ends (**Pyr-Si$_8$-NDI**, Figure 1).[39,44] While **Pyr-Si$_n$-Pyr** and **Pyr-Si$_8$-NDI** used pentylene spacers to attach the aromatic group and *o*DMS, the alkul spacer for the telechelic NDI block molecules was varied between pentylene and undecylene. Using these molecules, it was determined that for co-assembly of pyrene and NDI block molecules, their alkyl spacer lengths must match, as was also found in solution studies of CT complexes of NDIs and

dialkoxynaphthalene.[45] Furthermore, CT interactions were found to lead to better-defined lamellar morphologies than found for their individual components. In the CT co-assembly, the lamellar spacing was found to be the average of the spacings of the individual components, even when a mismatch in *o*DMS length of 32 repeat units was used between **Pyr-Si$_{40}$-Pyr** and **NDI-Si$_8$-NDI**. Asymmetric **Pyr-Si$_8$-NDI** was found to form a thermodynamically more stable structure with more pronounced CT interactions compared to an equimolar mixture of **Pyr-Si$_8$-NDI** and **NDI-Si$_8$-NDI**. This effect was explained by either a higher effective molarity or a smaller number of assembly possibilities for **Pyr-Si$_8$-NDI**. Two π-stacking distances were found in the lamellar morphology of **Pyr-Si$_8$-NDI**, corresponding to the pyrene-NDI dimer and the spacing between two dimers, indicative of CT complexation.[11] Charge delocalization of aromatic cores and thereby the semiconducting properties of the material were shown to be enhanced upon applied pressure up to 6.1 GPa.[46] To study whether CT interactions are required for co-assembly in *o*DMS systems, *o*DMS was functionalized with hydrazone and methoxy-capped azobenzene at opposite ends sharing only their rod-like shape and no other specific interactions. Since this molecule exhibited self-sorted morphologies, it was concluded that specific interactions, such as CT interactions, are required for the co-assembly of telechelic block molecules with different cores, and that merely matching the molecular shape and domain spacings does not result in co-assembled structures.

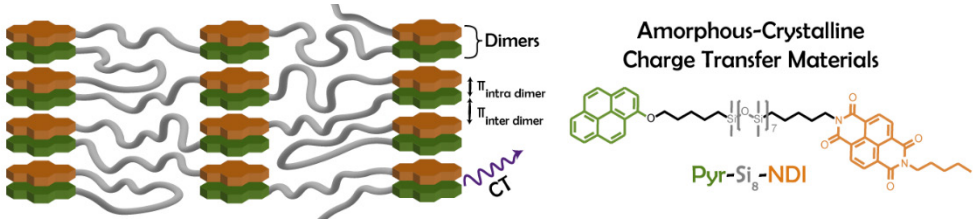

Figure 1. Schematic of the packing of **Pyr-Si$_8$-NDI**.[46] Two distinct spacings at high *q* were observed corresponding to the pyrene-NDI dimer, and the spacing between two dimers. This dimerization leads to the formation of a CT band in the absorbance spectrum.

In this chapter, we continue the study on how to control the co-assembly of *o*DMS-functionalized aromatic blocks using charge transfer interactions. For this purpose, we use pyromellitic diimide (PMDI) systems, as this molecule is known to form CT interactions with pyrene, although weaker than NDI.[47] Both telechelic and core-centered architectures are used to study the influence of molecular architecture on co-assembly with pyrene. In addition, mixtures with alkyl-functionalized PMDI are prepared to study the effect of homo-interactions on co-assembly. Charge transfer interactions are also studied in three-component, non-arylene diimide systems consisting of viologen, bromide ions and tetrathiafulvalene derivatives. Finally, co-assembly is studied with halogen bonding rather than charge transfer as the donor-acceptor interaction. With this, we report on the requirements for co-assembly in phase-separated block molecule systems.

3.2 Co-assembly of arylene diimide block molecules

3.2.1 Synthesis of PMDI and NDI block molecules

The syntheses of **C_5PMDIC$_5$** and the telechelic pyromellitic diimide block molecules (**PMDI-Si$_n$-PMDI**, Figure 2) are reported in the master thesis of Stefan Maessen.[48] Arylene diimide-centered **Si$_7$-PMDI-Si$_7$** and **Si$_7$-NDI-Si$_7$** were prepared from PMDA and naphthalene dianhydride, respectively, by microwave-assisted reaction with 5-pentene-1-amine (Scheme 1). The resulting olefin-terminated PMDI and NDI were then coupled to **HSi$_7$** using Karstedt-catalyzed hydrosilylation to yield **Si$_7$PMDISi$_7$** as a colorless oil (32%) and **Si$_7$NDISi$_7$** as a yellow oil (53%). The structure and the purity of the molecules were confirmed by ^{1}H NMR, ^{13}C NMR, MALDI-ToF-MS, and GPC.

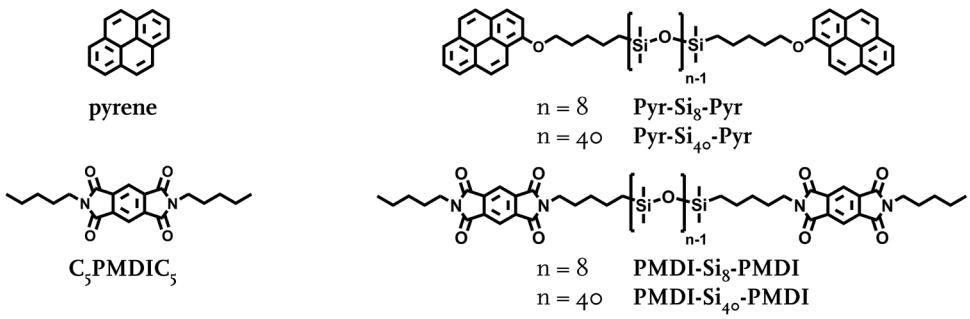

Figure 2. Chemical structures of pyrene, **Pyr-Si$_n$-Pyr**, **C_5PMDIC$_5$** and **PMDI-Si$_n$-PMDI**.

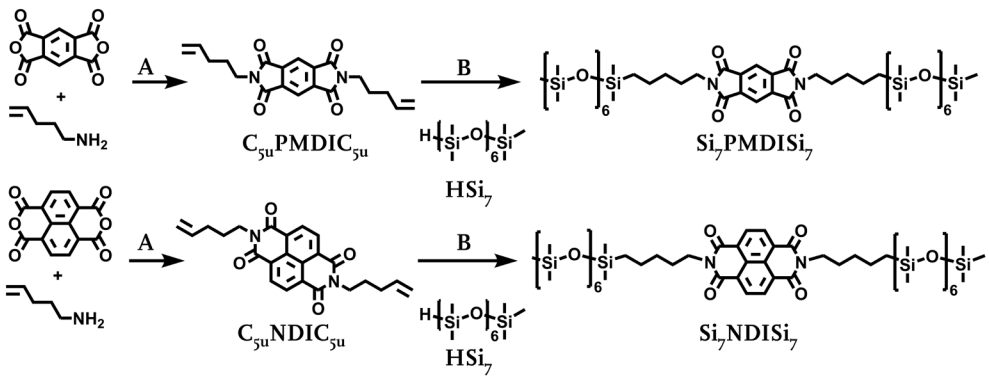

Scheme 1. Synthesis scheme of PMDI and NDI blocks and the corresponding block molecules. Reaction conditions: (A) DMF, 100 °C, 24 h (70 – 85 %). (B) Karstedt's catalyst, dry DCM, 20 °C, overnight (31 – 52%).

3.2.2 Bulk properties of telechelic PMDI block molecules

The bulk material properties of both **PMDI-Si$_n$-PMDI** molecules were studied with differential scanning calorimetry (DSC), medium- and wide-angle X-ray scattering (MAXS and WAXS) and polarized optical microscopy (POM). A single melting and crystallization temperature was found for both compounds (Table 1). As expected, higher thermal transition temperatures were found for **PMDI-Si$_8$-PMDI** due to the lower volume fraction of amorphous *o*DMS compared to **PMDI-Si$_{40}$-PMDI**. The melting enthalpy of **PMDI-Si$_8$-PMDI** (~54 kJ mol^{-1}) is significantly higher than that of

PMDI-Si$_{40}$-PMDI (~35 kJ mol^{-1}). This is unexpected when comparing this system to previously reported telechelic pyrene block molecules **Pyr-Si$_n$-Pyr** (Figure 2) with n = 8 or 40 where the length of the *o*DMS had little influence on the melting enthalpy due to its amorphous nature.[44] Similar enthalpies indicate that the pyrene blocks pack similarly regardless of *o*DMS length, while the difference observed between **PMDI-Si$_8$-PMDI** and **PMDI-Si$_{40}$-PMDI** indicates less defined core interactions for the latter.

Table 1. Thermal properties and morphology of **PMDI-Si$_8$-PMDI** and **PMDI-Si$_{40}$-PMDI**.

Compound	T_m [a,b] [°C]	ΔH_m [a,c] [kJ mol^{-1}]	T_c [a,b] [°C]	ΔH_c [a,c] [kJ mol^{-1}]	f_{Si} [d] [-]	d_{lam} [e] [nm]
PMDI-Si$_8$-PMDI	140 ±2	54	129 ±1	57	0.67	3.3
with pyrene	91 ±1	36	88 ±1	16		3.0
			50 ±3	20		
PMDI-Si$_{40}$-PMDI	76 ±2	35	74 ±2	35	0.91	7.3; 6.8
with pyrene	28 ±2	37	7 ±2	22		7.7

[a] Thermal transitions and enthalpies as determined by DSC from the second heating and cooling cycle with heating and cooling rates of 10 °C min^{-1}. [b] Error margins taken as the FWHM. [c] The error margin on the enthalpies is ~5%. [d] Volume fraction of *o*DMS as calculated from the crystal lattice volume of PMDI[49] and the molecular volume of *o*DMS.[50] [e] Lamellar spacing as calculated from the principal scattering peak q^* using $d_{lam} = 2\pi/q^*$, measured at room temperature.

X-ray scattering was used to further study the packing of **PMDI-Si$_8$-PMDI** and **PMDI-Si$_{40}$-PMDI**, as shown in Figure 3 on the next page. For **PMDI-Si$_8$-PMDI**, sharp peaks were observed with integer reflections from the principal scattering peak, q^*, indicating lamellar ordering with a spacing of 3.3 nm. In contrast, the principal scattering peak of **PMDI-Si$_{40}$-PMDI** is broad and a double lamellar ordering with spacings of 7.3 and 6.8 nm could be distinguished based on the subsequent reflection peaks. The principal scattering peak appears to have a shoulder on both sides of the maximum, which is hypothesized to be a third morphology with a larger spacing than 7.3 nm. The presence of multiple spacings indicates polymorphism in the PMDI layer, which explains the lower enthalpies found for **PMDI-Si$_{40}$-PMDI** compared to **PMDI-Si$_8$-PMDI**. This contradicts the results found for **Pyr-Si$_{40}$-Pyr**, that has a similar *o*DMS content but forms a well-defined lamellar morphology.

To rationalize the different thermal and morphological behavior of **PMDI-Si$_{40}$-PMDI** and **Pyr-Si$_{40}$-Pyr**, we use our recently developed approach of comparing the total interaction energies in the crystal lattice. Pyrene has a stronger total interaction energy in its crystal lattice (~ –260 kJ mol^{-1}) compared to PMDI crystals (~ –200 kJ mol^{-1}). These values are calculated using the program CrystalExplorer from the reported crystal structures of pentoxy pyrene and dimethyl PMDI.[51,52] However, an exact comparison between both cores is hindered as the PMDI groups used in this study have pentylene chains instead of methyl groups. The additional Van der Waals interactions will increase the total interaction energies.[53] Furthermore, especially when going from short to longer alkyls, the molecular packing is expected to change significantly, leading to different interaction energies.[53,54] We are currently investigating how we can relate the calculated total interaction energies to the formed morphology, when combined with the core symmetry and free volume considerations introduced in Chapter 2.

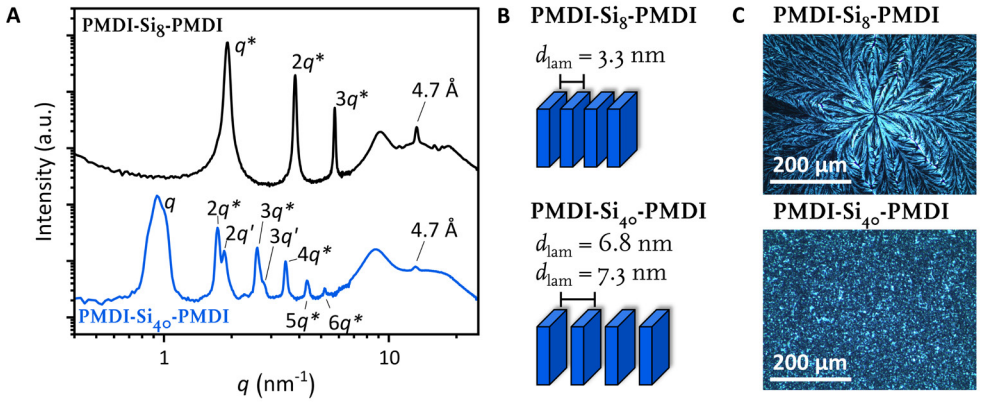

Figure 3. (A) 1-D transmission scattering data of **PMDI-Si8-PMDI** (black) and **PMDI-Si40-PMDI** (blue) after annealing with the corresponding lamellar morphology shown schematically in (B). (C) Polarized optical microscopy images of **PMDI-Si8-PMDI** and **PMDI-Si40-PMDI** after slow cooling from the melt (1 °C min^{-1}). Images were taken between crossed polarizers.

For the lamella of **PMDI-Si8-PMDI** and **PMDI-Si40-PMDI**, adjacent PMDIs are expected to have the *o*DMS directed in opposite directions, thus connecting the different layers (Shown schematically in Chapter 2, Figure 3). This interdigitated packing provides sufficient space for the *o*DMS (*vide infra*) and matches the predicted and experimental lamellar spacings for **PMDI-Si8-PMDI**. For **PMDI-Si40-PMDI**, the observed spacings are smaller than the calculated spacing of ~7.9 nm, which is probably caused by the less well-defined PMDI-PMDI interactions. The WAXS region of both materials shows a sharp peak at 4.7 Å, which is also found in the WAXS region of **C_5PMDIC_5** (not shown). This distance is comparable to the PMDI-PMDI distance in herringbone-stacked PMDI crystals, and suggests a similar herringbone packing of the cores in the PMDI block molecules.[49,55]

Upon cooling from the melt of **PMDI-Si8-PMDI** at 1 °C min^{-1}, large dendritic spherulite structures up to 0.8 cm in size are observed, of which one of the centers is shown in Figure 3C. The large size is attributed to the well-defined morphology, combined with the high propensity for crystallization as indicated by a sharp, narrow T_c with a high crystallization enthalpy (Table 1, Figure 4A). However, the dendritic spherulitic structure indicates that the lamellae do not have the same orientation throughout the domain, but rather that there was a single nucleation point followed by rapid crystallization. In contrast, for slowly cooled **PMDI-Si40-PMDI**, many sub-5 µm domains were found, assigned to the presence of multiple morphologies that crystallize simultaneously, preventing the formation of large domains.

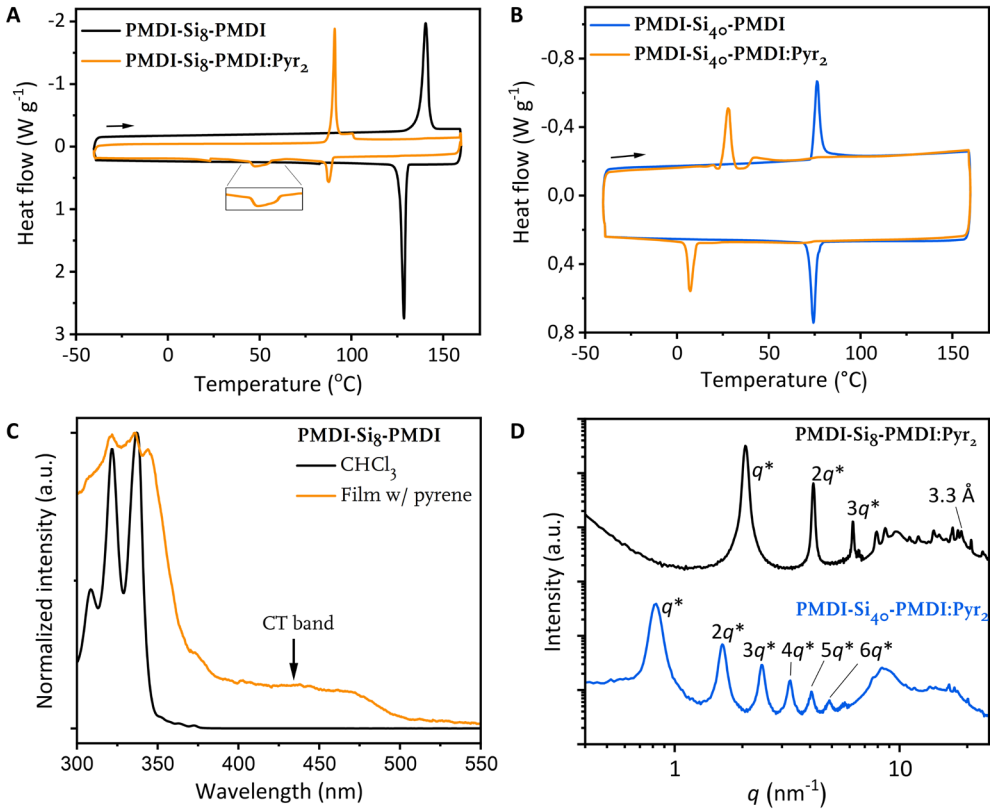

Figure 4. (A, B) DSC traces of **PMDI-Si$_8$-PMDI** (black) and **PMDI-Si$_{40}$-PMDI** (blue) both with (orange) and without pyrene. Arrows indicate heating. Heating and cooling rate 10°C min^{-1}. The second heating and cooling cycle is shown. (C) Absorption spectrum of **PMDI-Si$_8$-PMDI** in 50 µM $CHCl_3$ solution (black), and spin-coated **PMDI-Si$_8$-PMDI:Pyr$_2$** (orange). (D) 1-D transmission scattering data of **PMDI-Si$_8$-PMDI** (black) and **PMDI-Si$_{40}$-PMDI** (blue) with 2 eq. pyrene. **PMDI-Si$_{40}$-PMDI:Pyr$_2$** was cooled to −20 °C to crystallize the sample prior to the measurement.

3.2.3 Co-assembly of telechelic PMDI block molecules with pyrene

The two telechelic PMDI block molecules were mixed with pyrene to study their co-assembly in the presence of possible charge transfer interactions. All mixtures were prepared at a 1:2 ratio between **PMDI-Si$_n$-PMDI** and pyrene to obtain an equal number of PMDI and pyrene molecules in the mixtures, and will be referred to as **PMDI-Si$_n$-PMDI:Pyr$_2$**. The molecules were first dissolved in dichloromethane (DCM), a good solvent for both molecules, followed by evaporation of the solvent during which a color change from colorless to bright yellow was observed. This color change indicates the formation of a charge transfer band, which is shown for **PMDI-Si$_8$-PMDI:Pyr$_2$** in Figure 4C. The yellow color was more pronounced in **PMDI-Si$_8$-PMDI:Pyr$_2$** than in **PMDI-Si$_{40}$-PMDI:Pyr$_2$**, proposedly due to the higher volume fraction of aromatic molecules in the former.

The CT interactions induced by mixing with pyrene have a pronounced influence on the thermal behavior of the block molecules. A reduction in melting and crystallization temperatures of ~50 °C was observed for both mixtures (Table 1, Figure 4). Furthermore, the melting transitions became less Gaussian in shape as an additional transition is observed at higher temperatures as either a shoulder for **PMDI-Si$_8$-PMDI:Pyr$_2$** or a separate transition for **PMDI-Si$_{40}$-PMDI:Pyr$_2$**. The crystallization peaks remained Gaussian, although a second exothermic peak was observed at 47 °C for **PMDI-Si$_8$-PMDI:Pyr$_2$**. Remarkably, similar melting enthalpies of ~36 kJ mol^{-1} are found for both mixtures, indicating similar crystalline packing between the two mixtures. This melting enthalpy is lower than for **PMDI-Si$_8$-PMDI** (~54 kJ mol^{-1}), which is explained by differences in packing motifs in the crystalline layer with or without pyrene. Based on the reported crystal structures, the crystalline layer of the CT mixture consists of a 1D face-to-face packing,[56] while PMDI packs in a herringbone arrangement.[49,55]

The nanostructures of the mixtures were studied by medium- and wide-angle X-ray scattering (MAXS and WAXS, Figure 4D) to determine the morphology and degree of mixing. For **PMDI-Si$_8$-PMDI:Pyr$_2$**, a reduction in the lamellar spacing was observed from 3.3 nm to 3.0 nm compared to **PMDI-Si$_8$-PMDI**. This smaller spacing can be easily explained by geometry. Upon incorporation of pyrene into the PMDI layer, the crystalline layer thickness remains constant while the distance between the *o*DMS groups is increased. This leads to a reduction in the *o*DMS layer thickness to maintain the same volume of *o*DMS. Assuming similar packing of the aromatic groups with and without *o*DMS, the crystal structure of PMDI and the PMDI:pyrene complex shows an increase between the *o*DMS attachment points from ~9 – 10 Å to ~13 – 16 Å, respectively.[49,55,56] These values assume that the adjacent PMDI cores have the *o*DMS directed in opposite directions to minimize the spatial overlap of the *o*DMS (Figure 3 of Chapter 2). The increase in distance between *o*DMS attachment points to > 13 Å would lead to unfavorable free volume at the alkane-*o*DMS interface in the **PMDI-Si$_n$-PMDI** system since the diameter of *o*DMS is only 7 Å.[57] However, the observed lamellar morphology indicates that strong intermolecular interactions stabilize lamella formation for distances between the attachment points of *o*DMS over 10 Å. Many sharp peaks were observed in the WAXS region, some of which are assigned to pyrene-pyrene and PMDI-PMDI interactions. Thus, in this system, there is still partial self-sorting of the molecules. However, a new sharp peak was also observed corresponding to a π-stacking distance of 3.3 Å, indicating the CT interaction distance between PMDI and pyrene.[39]

The **PMDI-Si$_{40}$-PMDI:Pyr$_2$** mixture was cooled to -20 °C to crystallize the sample prior to the X-ray measurement. This CT mixture shows a single lamellar morphology instead of the double lamellar morphology found for **PMDI-Si$_{40}$-PMDI**. Even though the scattering peaks in the MAXS region are broad, there are no visible shoulders present. CT interactions thus appear to increase homogeneity within the crystalline layer by favoring a single packing of the aromatic groups. The spacing of the single lamellar morphology at 7.7 nm is larger than for **PMDI-Si$_{40}$-PMDI**, as a different packing of the crystalline layer is favored with and without pyrene. The WAXS region of **PMDI-Si$_{40}$-PMDI:Pyr$_2$** exhibits similar peaks as for **PMDI-Si$_8$-PMDI:Pyr$_2$**, indicating similar interlayer CT interactions. This similar packing is further confirmed by layer spacing calculations. When the average $Si(CH_3)_2O$ repeat unit is taken as 0.15 nm,[58,59]

the lamellar spacing from **PMDI-Si$_8$-PMDI** to **PMDI-Si$_{40}$-PMDI** should increase by ~4.8 nm. This value corresponds to the experimentally observed increase of ~4.7 nm. The comparison of the mixtures and its individual components clearly shows that for strong interactions within the crystalline layer, the *o*DMS volume fraction becomes less important, as previously demonstrated for a hydrogen-bonding ureidopyrimidinone block molecule system.[60] Thus, the interaction strength within the crystalline layer is an important parameter in the prediction of the morphology formed, a topic which is currently being studied in our group.

3.2.4 Co-assembly of core-centered arylene diimide block molecules

To evaluate the effect of molecular architecture on the assembly of arylene diimide with pyrene, arylene diimide-centered **Si$_7$PMDISi$_7$** and **Si$_7$NDISi$_7$** were studied with and without an equimolar amount of pyrene. The colorless **Si$_7$PMDISi$_7$** became yellow when mixed with pyrene, indicating the presence of a CT band. This CT band was visible in the absorption spectrum as a peak around 425 nm (Figure 5A, next page), similar as found for **PMDI-Si$_8$-PMDI:Pyr$_2$**. There was little effect on the exothermic transition temperature (T_{exo}) of **Si$_7$PMDISi$_7$** with and without pyrene (Table 2). This T_{exo} is assigned to an order-disorder transition because of its low enthalpy (<5 kJ mol^{-1}).[61] The morphology of **Si$_7$PMDISi$_7$** could not be inferred from the transmission scattering profile, although the scattering peaks were sharp (Figure 5B). We suppose that due to steric hindrance of the *o*DMS, no simple morphology could be formed. The steric hindrance can be related to the reported crystal structure of alkylated PMDI.[49] The diameter of *o*DMS is 7 Å,[50,62] while the closest distance between the attachment points of *o*DMS is significantly smaller at 5.0 Å, thereby preventing a lamellar morphology. However, in a PMDI pyrene CT system, the available distance is 6.6 Å[56] and thus a lamellar morphology can more easily be formed for the equimolar **Si$_7$PMDISi$_7$** pyrene mixture. Since the available distance is still slightly too small, the lamellar reflection peaks are relatively broad.

Similar observations on CT formation and morphology changes were made for the **Si$_7$NDISi$_7$** system with pyrene. Here the formation of CT interactions results in a red color due to the formation of a CT band around 490 nm, while **Si$_7$NDISi$_7$** itself is yellow (Figure 5C). The ratio of the CT band and the absorption below 400 nm varied between samples due to the liquid nature of the mixture. The difference in color with the purple **Pyr-Si$_8$-NDI** is due to the different donors, as here pyrene is used instead of alkoxy-pyrene.[39] This was confirmed when mixing **Si$_7$NDISi$_7$** with alkoxy-pyrene, which resulted in a purple color. The thermal transitions of **Si$_7$NDISi$_7$** were higher after incorporation of pyrene, indicating a thermodynamically more stable morphology (Table 2). This incorporation is also evident in the transmission scattering profile (Figure 5D). Without pyrene, **Si$_7$NDISi$_7$** exhibits a cylindrical morphology with a spacing of 3.5 nm, with an additional principal scattering peak at 3.3 nm for which no reflection peaks were observed. Steric hindrance prevents the formation of a lamellar morphology, as the closest distance between *o*DMS attachment points is only 4 Å instead of the required 7 Å.[57] In contrast, the closest distance between *o*DMS attachment points for alternating NDI-pyrene crystals is 7.6 Å,[63] leaving sufficient space for the *o*DMS. Therefore, a well-defined lamellar morphology is observed for the mixture with a spacing of 4.1 nm (Figure 5D). Here the scattering peaks are sharp, indicating a high degree of homogeneity

throughout the sample. The WAXS region shows many sharp peaks indicating possible partial immobilization of the *o*DMS. Furthermore, the close core-core interactions are observed by the sharp peak in the WAXS region around 20 nm^{-1}, corresponding to a π-stacking distance of 3.2 Å.

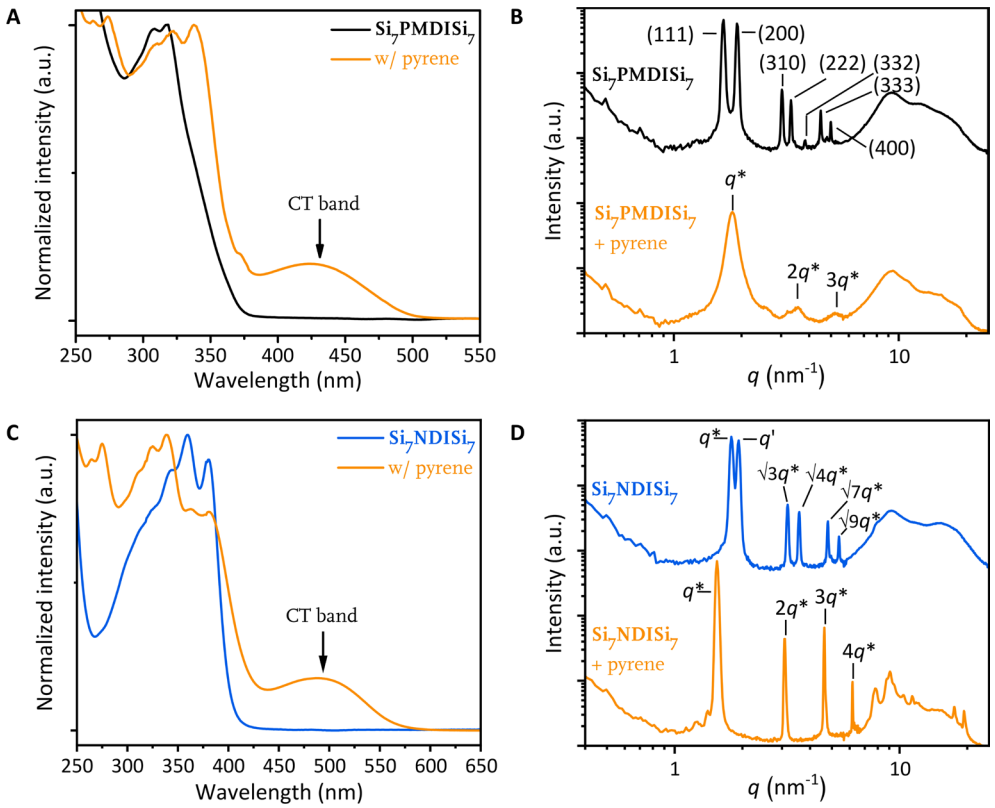

Figure 5. (A, C) Absorption spectra at room temperature of the material without solvent (thickness unknown due to liquid nature of the material) and (B, D) 1-D transmission scattering data of **$Si_7PMDISi_7$** (black), **Si_7NDISi_7** (orange) without and with (orange) equimolar amounts of pyrene.

Table 2. Thermal properties of **$Si_7PMDISi_7$** and **Si_7NDISi_7**, their mixtures with equimolar amounts of pyrene and the equimolar mixture of **$Si_7PMDISi_7$** and **C_5PMDIC_5**.

Mixture composition	T_{exo} [a,b] [°C]	ΔH_{exo} [a,c] [kJ mol^{-1}]	T_{endo} [a,b] [°C]	ΔH_{end} [a,c] [kJ mol^{-1}]
$Si_7PMDISi_7$	−28 ±1	2	−33 ±1	3
with pyrene	−30 ±2	5[d]	−44 ±2	5[d]
with **C_5PMDIC_5**	−22 ±1	2	−26 ±1	2
	158 ±5	2[d]	157 ±6	6[d]
Si_7NDISi_7	2 ±2	11	−12 ±0.5	10
with pyrene	23 ±2	5[d]	12 ±3	12[d]

[a] Thermal transitions and enthalpies as determined by DSC from the second heating and cooling cycle with heating and cooling rates of 10 °C min^{-1}. [b] Error margins taken as the FWHM. [c] The error margin on the enthalpies is ~5%. [d] Enthalpies are calculated from the combined molecular weight of the constituents, assuming a 1:1 mixture. This leads to an overestimate of the true enthalpy.

3.2.5 Co-assembly of PMDI block molecules with PMDI

Following the above results, we were interested in whether co-assembly could also take place without CT interactions. To this end, a 1:1 mixture of **PMDI-Si$_8$-PMDI** and **PMDI-Si$_{40}$-PMDI** was prepared. No obvious melting peaks were observed, while two peaks with low enthalpic values were visible at 112 and 75 °C (Figure 6A, page 69). The highest T_c probably corresponds to a **PMDI-Si$_8$-PMDI** rich phase with partial **PMDI-Si$_{40}$-PMDI** incorporation which lowers the T_c compared to **PMDI-Si$_8$-PMDI**. The T_c at 75 °C corresponds to that of **PMDI-Si$_{40}$-PMDI**, indicating partial self-sorting in the mixture. This is confirmed by X-ray analysis, which shows superposition of both components in the mixture (Figure 6B). The broad principal scattering peak of **PMDI-Si$_{40}$-PMDI** is still visible, albeit with a broader base and a sharper principal scattering peak. This indicates an increased preference for a single spacing, although there is still a large variation in spacing. This contrasts with what was previously found for the equimolar mixture of **NDI-Si$_8$-NDI** and **Pyr-Si$_{40}$-Pyr** that formed a single lamellar morphology, even though it has the same *o*DMS length difference between the two constituents as **PMDI-Si$_8$-PMDI**:**PMDI-Si$_{40}$-PMDI**.[44] A well-defined single lamellar system was also found for a 1:1:1 mixture of telechelic hydrazone block molecules with Si$_8$, Si$_{32}$, and Si$_{40}$.[64] Thus, it appears that the PMDI homo-interactions are not strong enough to result in a single morphology when there are large differences in *o*DMS length. This observation further indicates that the strength of the crystalline interactions plays a role in the bulk self-assembly of block molecules. Quenching of the **PMDI-Si$_8$-PMDI**:**PMDI-Si$_{40}$-PMDI** mixture from the melt shows a single lamellar morphology, indicating a kinetically trapped co-crystallized state. However, the width of the principal scattering peak shows that the lamellae are ill-defined, further confirming that a co-crystallized state is thermodynamically unfavorable for this homosystem.

Table 3. Thermal properties and morphology of **PMDI-Si$_8$-PDMI** mixtures with **C$_5$PMDIC$_5$**.

Mixture composition	T_m[a] [°C]	ΔH_m[a,b] [kJ mol^{-1}]	T_c[a] [°C]	ΔH_c[a,b] [kJ mol^{-1}]	d_{lam}[c] [nm]
1:0	140 ±2	54	129 ±1	57	3.3
1:0.2	162 ±2	39	156 ±0.5	41	3.2
1:0.4	164 ±1	55	160 ±0.5	57	3.1
1:1	164 ±4	85	169 ±3	85	5.5; 2.9; 2.8[d]

[a] Thermal transitions and enthalpies as determined by DSC from the second heating and cooling cycle with heating and cooling rates of 10 °C min^{-1}. Error margins taken as the FWHM. [b] The error margin on the enthalpies is ~5%. [c] Lamellar spacing as calculated from the principal scattering peak q^* using $d_{lam} = 2\pi/q^*$. [d] Spacings correspond to a triple lamellar morphology.

To further study the effect of homo-interactions, **PMDI-Si$_8$-PMDI** was mixed with **C$_5$PMDIC$_5$** in the ratios 1:0.2, 1:0.4, and 1:1 by dissolving both compounds in DCM and evaporating the solvent (Table 3). **C$_5$PMDIC$_5$** was chosen because it meets the requirement of equal alkyl linker length reported previously.[44,45] DSC analyses for the 1:0.2 and 1:0.4 mixtures show a sharp crystallization onset followed by a long decay to the baseline, indicating fast nucleation followed by slow crystallization (Figure 6C). In contrast, a more complex crystallization behavior was observed for the 1:1 mixture, indicating multiple (coexisting) morphologies. These observations are confirmed by the fact that a single lamellar phase is found for the 1:0.2 and 1:0.4 mixtures, whereas the 1:1 mixture exhibits two pronounced lamellar spacings of 2.9 and 2.8 nm as well as an

additional broad principal scattering peak corresponding to a lamellar spacing of 5.5 nm. The spacing of 5.5 nm is presumably caused by an amorphous PMDI layer, creating a repeating layered structure of [crystalline PMDI – *o*DMS – non-crystallized PMDI – *o*DMS]$_n$. The non-crystallized PMDI layer probably has a variable thickness, leading to the width of the scattering peaks assigned to this spacing. The small difference between the other two spacings of 2.8 and 2.9 nm is attributed to a different degree of **C$_5$PMDIC$_5$** incorporation within the lamellar structure of **PMDI-Si$_8$-PMDI**. Since the 1:0.2 and 1:0.4 mixtures exhibit single lamellar morphologies, it appears that **C$_5$PMDIC$_5$** can be incorporated into the lamellar packing of **PMDI-Si$_8$-PMDI** via co-crystallization from the melt, but only to a certain extent. Incorporation of **C$_5$PMDIC$_5$** leads to a smaller lamellar spacing, following the same geometric arguments as for the mixture with pyrene. The limited mixing of **PMDI-Si$_8$-PMDI** and **C$_5$PMDIC$_5$** is explained by the formation of unfavorable free space at the alkane-*o*DMS interface for too high **C$_5$PMDIC$_5$** loadings, as there was already sufficient space for the *o*DMS in **PMDI-Si$_8$-PMDI**.

In contrast, for **Si$_7$PMDISi$_7$** there is not enough space for the *o*DMS to form lamellae. However, for an equimolar mixture of **Si$_7$PMDISi$_7$** and **C$_5$PMDIC$_5$** an ill-defined lamellar morphology is observed below the crystallization temperature of the **C$_5$PMDIC$_5$** rich fraction at ~160 °C (Figure 6E, Table 2, *vide supra*). The formation of this lamellar morphology can again be explained by the space filling arguments, as interdigitation of **C$_5$PMDIC$_5$** in the **Si$_7$PMDISi$_7$** leads to comparable distances between the *o*DMS attachment points as for the lamellar **PMDI-Si$_{40}$-PMDI**. However, the lamellar morphology of the **Si$_7$PMDISi$_7$:C$_5$PMDIC$_5$** mixture is ill-defined due to partial self-sorting. This self-sorting is observed by the presence of the scattering profile of **Si$_7$PMDISi$_7$** below its thermal transition at ~–20 °C. The peaks at 1.7 nm and 4.7 Å correspond to **C$_5$PMDIC$_5$** and thereby further confirm self-sorting in this system. This self-sorting occurs because the homo-interactions are too weak to drive the entire sample into a single lamellar morphology. The comparison of the telechelic and core-centered PMDI block molecule mixtures with non-functionalized PMDI confirms the conclusions of *o*DMS space-filling reported in Chapter 2.

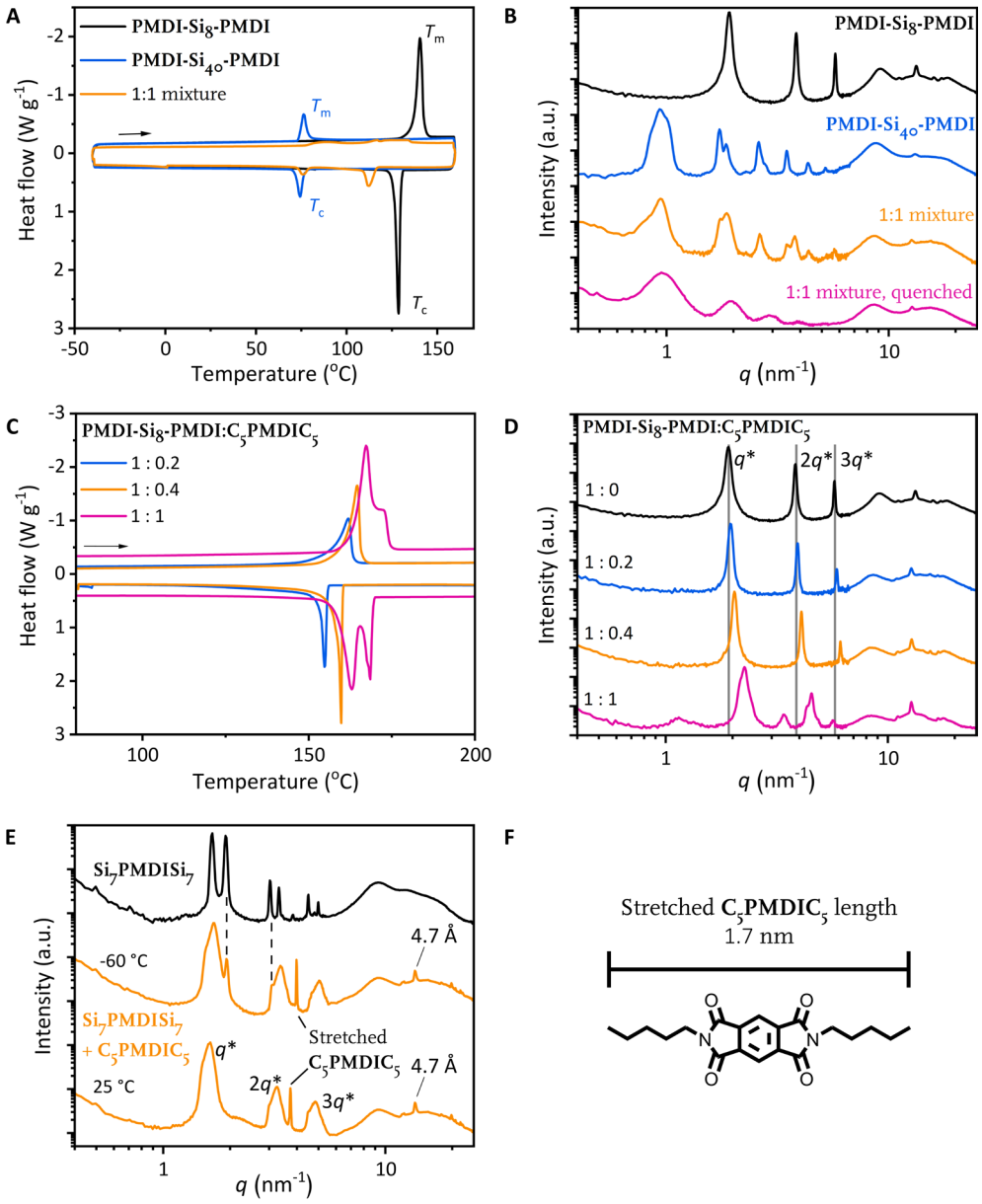

Figure 6. (A) DSC traces and (B) 1-D transmission scattering data of **PMDI-Si$_8$-PMDI** (black) and **PMDI-Si$_{40}$-PMDI** (blue) and their 1:1 mixture (orange). The pink line in 4B is from the 1:1 mixture after quenching from the melt with a mixture of liquid N_2 and ethanol. (C) DSC traces and (D) 1-D transmission scattering data of **PMDI-Si$_8$-PMDI** mixed with **C$_5$PMDIC$_5$** in the ratios 1:0.2 (blue), 1:0.4 (orange), 1:1 (pink). Arrows in the DSC profiles indicate heating. The second heating and cooling cycle is shown. (E) 1-D transmission scattering data of **Si$_7$PMDISi$_7$** (black), and in a 1:1 mixture with **C$_5$PMDIC$_5$** at –60 and 25 °C (orange). (F) Dimensions of fully stretched **C$_5$PMDIC$_5$**.

3.2.6 The effect of purity on the self-assembly of block molecules

The molecules studied in this chapter were considered pure based on their proton and carbon NMRs and a single peak in the MALDI-ToF-MS. However, this does not exclude the presence of very small amounts of non-functionalized core molecules, of which most peaks overlap in the NMR spectrum with the target product and whose size prevents detection by MALDI-ToF-MS. Fortunately, these peaks were visible with GPC through separation by size. To study the effect of these small, unidentified impurities, the differences in DSC, SAXS and POM before and after purification by recycle GPC are shown here for **PMDI-Si$_{40}$-PMDI** and **Si$_{15}$-Azo**, the latter introduced in Chapter 2. It should be noted that all molecules reported in Chapter 2, 4 and 5 were purified by recycling GPC, whereas the molecules in this chapter were not.

As shown in Figure 7, for both **PMDI-Si$_{40}$-PMDI** and **Si$_{15}$-Azo** the onset of the crystallization peak is more abrupt and generally sharper after recycling GPC. However, no significant differences were observed in the melting and crystallization enthalpies. The sharper crystallization peaks indicate that both materials become more crystalline as purity increases. The crystallinity can be studied with SAXS, which for **PMDI-Si$_{40}$-PMDI** did not change with the additional purification. However, the different crystallization behaviors can be observed during POM analyses by the formation of larger domains after recycling GPC upon slow cooling from the melt. For **Si$_{15}$-Azo**, no significant differences were observed by POM, but the SAXS analysis shows a change from three coexisting lamellar phases to a single lamellar phase. Furthermore, the peak at 3.8 Å indicative of the π-π interaction becomes significantly sharper after recycling GPC and additional peaks around 20 nm^{-1} arise. When comparing the other molecules reported in Chapter 2 before and after recycling GPC, either pronounced differences are observed in DSC, POM and/or SAXS or no differences were found in any of these analytical techniques. This is related to the nature and amount of the impurities. The effect of recycling GPC can therefore not be predicted. However, based on these results, we strongly recommend that all new block molecules are purified using recycling GPC prior to analysis to rule out the effect of small amounts of impurities on the self-assembly behavior.

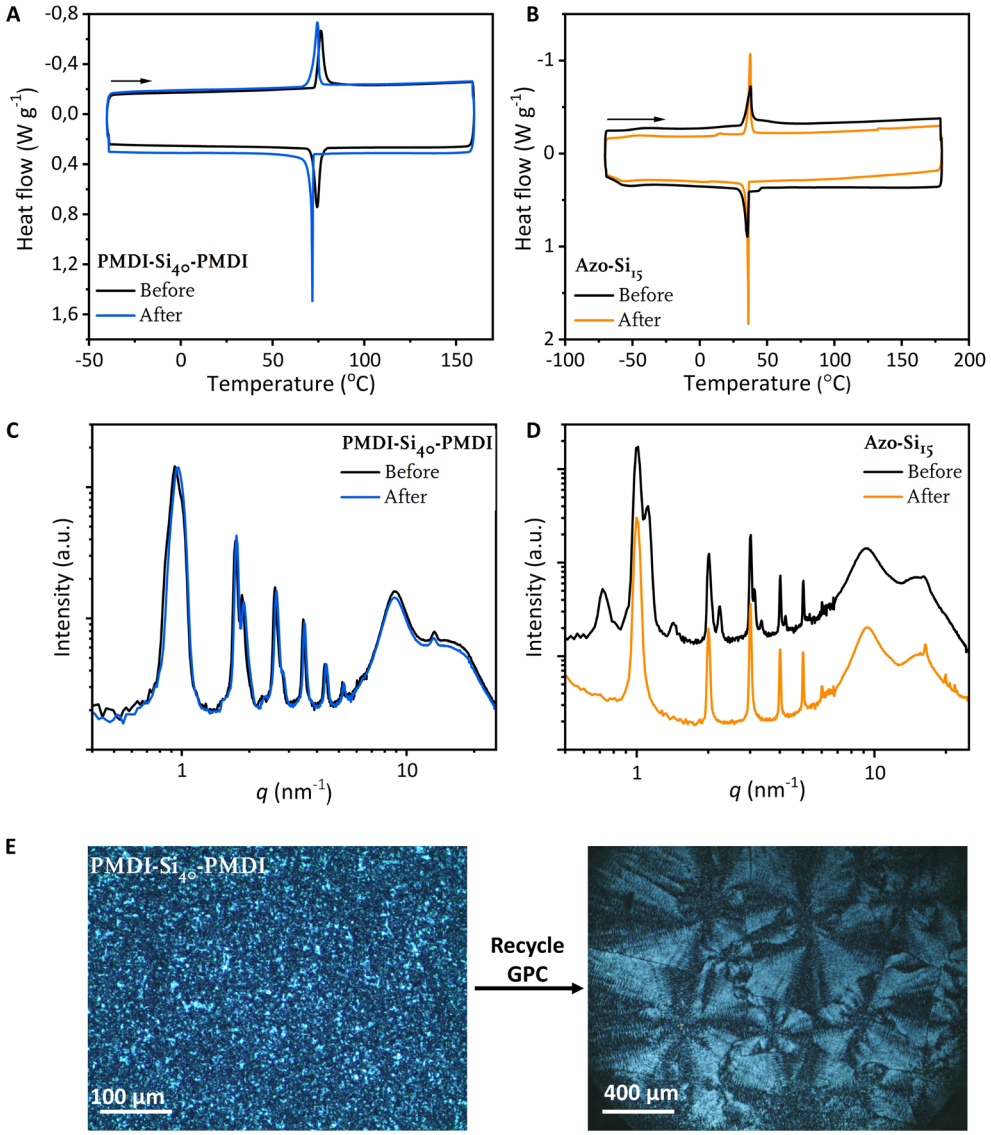

Figure 7. DSC traces of (A) **PMDI-Si$_{40}$-PMDI** and (B) **Si$_{15}$-Azo** before (black) and after (color) additional purification with recycle GPC. The arrow indicates heating. A temperature ramp of 10 °C min^{-1} is used. The second heating and cooling cycle is shown. 1-D transmission scattering data of (C) **PMDI-Si$_{40}$-PMDI** and (D) **Si$_{15}$-Azo** before (black) and after (color) additional purification with recycle GPC. (E) Polarized optical microscopy image between crossed polarizers of **PMDI-Si$_{40}$-PMDI**. Before additional purification, no large domains were observed (left). After purification by recycle GPC, domains of a few mm were observed (right).

3.2.7 Conclusions arylene diimide block molecules co-assembly

In summary, we have successfully synthesized symmetric arylene diimide *o*DMS block molecules with both telechelic and core-centered architectures. Binary mixtures based on either CT interactions with pyrene or homo-interactions with PMDI were studied to investigate the requirements for co-assembly in the bulk material. On its own, **PMDI-Si$_8$-PMDI** forms a well-defined lamellar packing, while a less defined double lamellar packing was found for **PMDI-Si$_{4o}$-PMDI**. This indicates that the *o*DMS length can impose an additional packing constraint when sufficiently short. Moreover, an equimolar mixture of these two telechelic block molecules showed self-sorting, while a similar *o*DMS length difference in the CT complex of pyrene and NDI showed co-assembly.[44] From this, we conclude that PMDI homo-interactions are not strong enough to direct a certain packing, which is further confirmed by the self-sorting mixtures of **PMDI-Si$_8$-PMDI** and **Si$_7$PMDISi$_7$** with **C$_5$PMDIC$_5$**. In contrast, the stronger CT interactions appear to favor a single packing of the aromatic layer regardless of the molecular architecture, forming lamellar structures regardless of the *o*DMS length or the architecture of the block molecules. These results show that when designing systems with multiple components, there must be both strong interactions between the different components as well as sufficient space to accommodate the *o*DMS when targeting a single morphology throughout the bulk. If the interactions between the layers are strong, the required space for the *o*DMS acts as a lower bound and the amorphous *o*DMS occupies additional available space. Finally, the effect of small impurities is shown and thereby it is recommended that block molecules are always purified with recycle GPC prior to the study of their properties.

3.3 Co-assembly of charged *o*DMS block molecules by CT interactions

To extend the scope of *o*DMS functionalized CT compounds beyond arylene diimides, *o*DMS functionalized viologens are studied in mixtures with tetrathiafulvalene derivatives. The **Si$_7$VSi$_7$Br** block molecule used in this study (Scheme 2) was previously synthesized and studied in our group by Alex van de Ven and Fabian Eisenreich.[65] The product was purified by extraction with MeOH/heptane to remove excess *o*DMS and by recrystallization from acetonitrile to remove the unreacted viologen cores. Due to the charged nature of the material, recycling GPC could not be used to further purify the material. Since no thermal transitions were observed, the mixtures were only studied for their morphological and spectral properties. This viologen system allows to further understand the requirements of co-assembly in *o*DMS systems. Viologens have been studied for their organic battery potential and their electronic and electrochromic properties. Thus, greater understanding of how ordering can be affected at the nanoscale will help in the development of functional, electronic, ordered materials.[66–68]

3.3.1 Morphological properties of co-assembled, charged block molecules

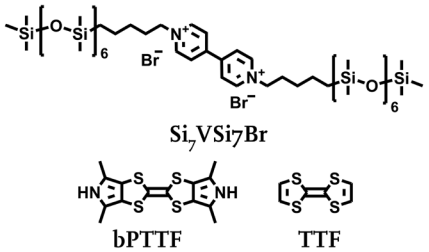

Scheme 2. Molecular structures of **Si$_7$VSi$_7$Br**, **bPTTF** and **TTF**.

Equimolar mixtures of waxy **Si$_7$VSi$_7$Br** with bispyrrolotetrathiafulvalene (**bPTTF**) and tetrathiafulvalene (**TTF**) were prepared by suspension in acetonitrile and evaporation of the solvent under nitrogen flow at 80 °C. The mixtures are referred to as **V:bPTTF** and **V:TTF**, respectively. Acetonitrile was chosen for its ability to break the bromide-viologen ion-pair complex.[69,70] By itself, **Si$_7$VSi$_7$Br** is yellow, while **bPTTF** and **TTF** are red solids. **V:bPTTF** was obtained as a brittle wax with a dark green color. These changes in color and physical properties indicate the incorporation of **bPTTF** into the viologen layer of **Si$_7$-V-Si$_7$Br** via CT interactions. In contrast, **V:TTF** was obtained as a red wax, with the color indicating an absence of CT interactions. These visual observations are confirmed by absorbance measurements. As shown in Figure 8A, for **V:bPTTF** a clear CT band is observed with a maximum at ~640 nm.[71] For **V:TTF**, the reported CT bands around 625 – 650 nm are not observed. The absence of CT formation in the **V:TTF** mixture is attributed to the low binding constant of **TTF** with the viologen.[72] The absence of CT interactions confirms that for block molecule co-assemblies, solely matching the shape and length of both molecules is insufficient. **bPTTF** has better π-donor properties than **TTF** due to a combination of its extended π-surface and low first oxidation potential and can therefore form CT interactions with **Si$_7$VSi$_7$Br**.[73]

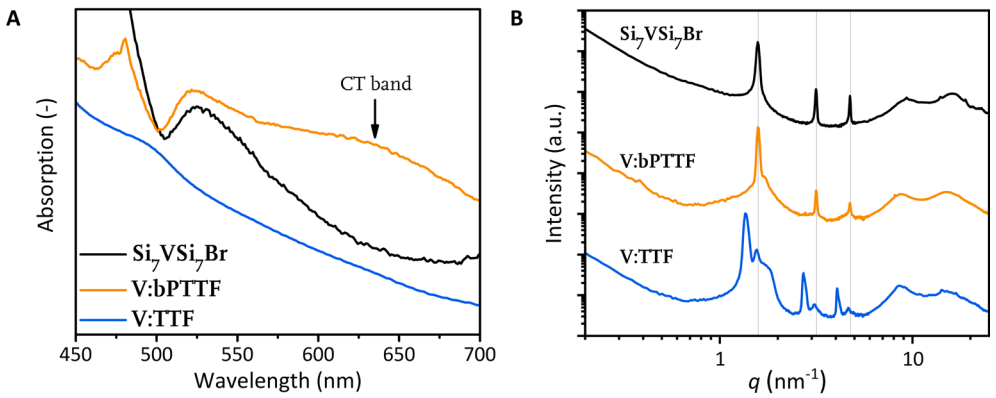

Figure 8. (A) Absorption spectrum and (B) 1-D transmission scattering profile of **Si$_7$VSi$_7$Br** (black) and equimolar mixtures of **Si$_7$VSi$_7$Br** with **bPTFF** (orange) or **TTF** (blue).

To further study the CT formation in these mixtures, the transmission scattering profiles are analyzed (Figure 8B). For **V:bPTTF**, the 4.0 nm spaced lamellar morphology of **Si_7VSi_7Br** is still clearly visible. However, an underlying peak at larger *q*, with smaller spacing, is also observed. This smaller spacing indicates intercalation of **bPTTF** in the viologen layer and further proves CT formation. The partial self-sorting is probably the result of suboptimal mixture preparation due to miscibility differences between the viologen ion-pair complex and **bPTTF**. Since the material could not be melted, thermal annealing could not be used to bring the system into thermodynamic equilibrium. For **V:TTF**, the most pronounced lamellar morphology corresponds to a spacing of 4.6 nm. This increase in spacing from **Si_7VSi_7Br** arises from a different tilt angle of the aromatic layer.[70] Here, the **TTF** is expected to be located in the alkyl portion of **Si_7VSi_7Br**, similar to the reported crystal structure.[70] Thus, intercalation of **TTF** does take place in the aromatic layer, but the molecular complex is mainly formed by CH/π and/or van der Waals interactions rather than CT interactions. The lamellar packing of **Si_7VSi_7Br** can also still be observed, indicating partial self-sorting. For the shorter spacing at 3.4 nm, no clear reflection peaks are observed. This spacing is therefore attributed to undefined ordering caused by packing defects between viologen, bromide ions and **TTF**. Similar to the PMDI mixing studies, these results show that mixing multiple components can be used to alter the optical and morphological properties of the system, although obtaining a perfectly mixed system remains a challenge.

3.4 Co-assembly of diphenylanthracene block molecules by halogen bonding

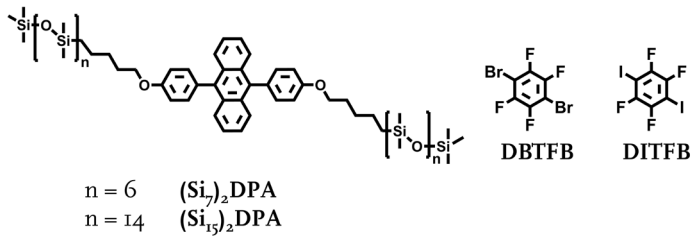

Figure 9. Molecular structures of **$(Si_7)_2$DPA**, **$(Si_{15})_2$DPA**, **DBTFB**, and **DITFB**.

The optical properties of a system can also be modified by mixing with halogen bonding molecules. For example, it has been shown that co-crystals of diphenylanthracene (**DPA**) with halogenated benzene exhibit a >20-fold increase in electrochemiluminescence due to enhanced intermolecular electron transfer, although at the expense of its photoluminescence quantum yield.[74] Therefore, the question arises whether these co-assembled systems can also be formed with *o*DMS-functionalized DPA to study luminescence properties in nanostructured systems. To this end, co-crystals of **$(Si_7)_2$DPA** or **$(Si_{15})_2$DPA** with either dibromotetrafluorobenzene (**DBTFB**) or diiodotetrafluorobenzene (**DITFB**) were prepared (Figure 9). Three co-crystals were prepared at a ratio of 1:1 by evaporation of chloroform to give **$(Si_7)_2$DPA:DBTFB**, **$(Si_{15})_2$DPA:DBTFB**, and **$(Si_{15})_2$DPA:DITFB**. These mixtures were chosen to compare the effect of halogenated benzenes on the strong crystalline packing of **$(Si_7)_2$DPA** and the weaker packing of **$(Si_{15})_2$DPA**, while two halogenated benzenes were chosen to study their

differences. The thermal behavior of the co-crystals was investigated with DSC. For **$(Si_7)_2$DPA**:**DBTFB**, the sharp melting transition at 80 °C of the parent crystal became a broad melting transition between 52 – 71 °C with the maximum at 67 °C in the co-crystal. Moreover, the crystallization occurs at a ~15 °C lower temperature compared to the parent crystal, with the crystallization peak consisting of multiple merged peaks with maxima at 56, 52 and 51 °C. This complicated crystallization behavior could not be elucidated by POM, as the halogenated benzene did not affect the formed birefringent structures. In contrast, for **$(Si_{15})_2$DPA** only a slight (< 6 °C) decrease in melting and crystallization temperature was observed for both co-crystals, while the shape of the peaks remained the same (Table 4). Moreover, **$(Si_7)_2$DPA**:**DBTFB** has a 60% lower crystallization enthalpy than **$(Si_7)_2$DPA**, while this reduction is only 10 – 20% for the **$(Si_{15})_2$DPA** mixtures. These different effects on the crystallization behavior of the mixtures with halogenated benzene are related to the difference in enthalpy of the functionalized DPAs themselves. **$(Si_7)_2$DPA** has a high crystallization enthalpy due to strong DPA interactions, whereas the DPA interactions are less strong for **$(Si_{15})_2$DPA**. Therefore, co-crystallization of DPA and the halogenated benzenes is less of an enthalpic penalty for **$(Si_{15})_2$DPA**. For all mixtures, the presence of one crystallization and one melting peak, albeit with multiple maxima, indicates successful incorporation of the halogenated benzene into the **$(Si_n)_2$DPA** crystal structure.

Table 4. Thermal properties of **$(Si_n)_2$DPA** with and without **DBTFB** and **DITFB**.

Mixture composition	T_m[a] [°C]	ΔH_m[a,b] [kJ mol^{-1}]	T_c[a] [°C]	ΔH_c[a,b] [kJ mol^{-1}]
$(Si_7)_2$DPA	80 ±1[c]	46	67 ±1[c]	48
$(Si_7)_2$DPA:**DBTFB**	67 ±4	30	54 ±2	20
$(Si_{15})_2$DPA	47 ±2	39	31 ±2	42
$(Si_{15})_2$DPA:**DBTFB**	44 ±3	25	27 ±3	36
$(Si_{15})_2$DPA:**DITFB**	43 ±3	20	25 ±3	37

[a] Thermal transitions and enthalpies as determined by DSC from the second heating and cooling cycle with heating and cooling rates of 10 °C min^{-1}, measured between 0 and 100 °C. Error margins taken as the FWHM. [b] The error margin on the enthalpies is ~5%. [c] Transitions below 0 °C are omitted here for clearer comparison. Full characterization is reported in Chapter 5.

To further investigate the packing of the co-crystals, X-ray scattering was performed. For all three co-crystals, lamellar morphologies were observed with the same spacing as found without the halogenated benzene (Figure 10A–B). The WAXS region of the **$(Si_7)_2$DPA**:**DBTFB** mixture shows some clear differences from that of **$(Si_7)_2$DPA**. This indicates intercalation of the halogenated benzene in the crystalline DPA layer of **$(Si_7)_2$DPA** without changing the crystalline layer thickness. For **$(Si_{15})_2$DPA**, its lamellar spacing was also maintained upon mixing with **DBTFB** and **DITFB**, while the large amorphous contribution of *o*DMS hinders the observation of differences in the WAXS region. Thus, since the same spacings are observed, the halogenated benzenes are expected to intercalate the existing packing structure, as has also been reported for non-functionalized DPA.[74] Consequently, only a slight bathochromic shift of <3nm is observed in both absorption and emission of the co-crystal films compared to **$(Si_n)_2$DPA** (Figure 10C). This contrasts with the co-crystals of non-functionalized DPA and is attributed to the difference between the 3D crystals of non-functionalized DPA and the monolayer structure of the **$(Si_n)_2$DPA** mixtures. For the different halogenated benzenes,

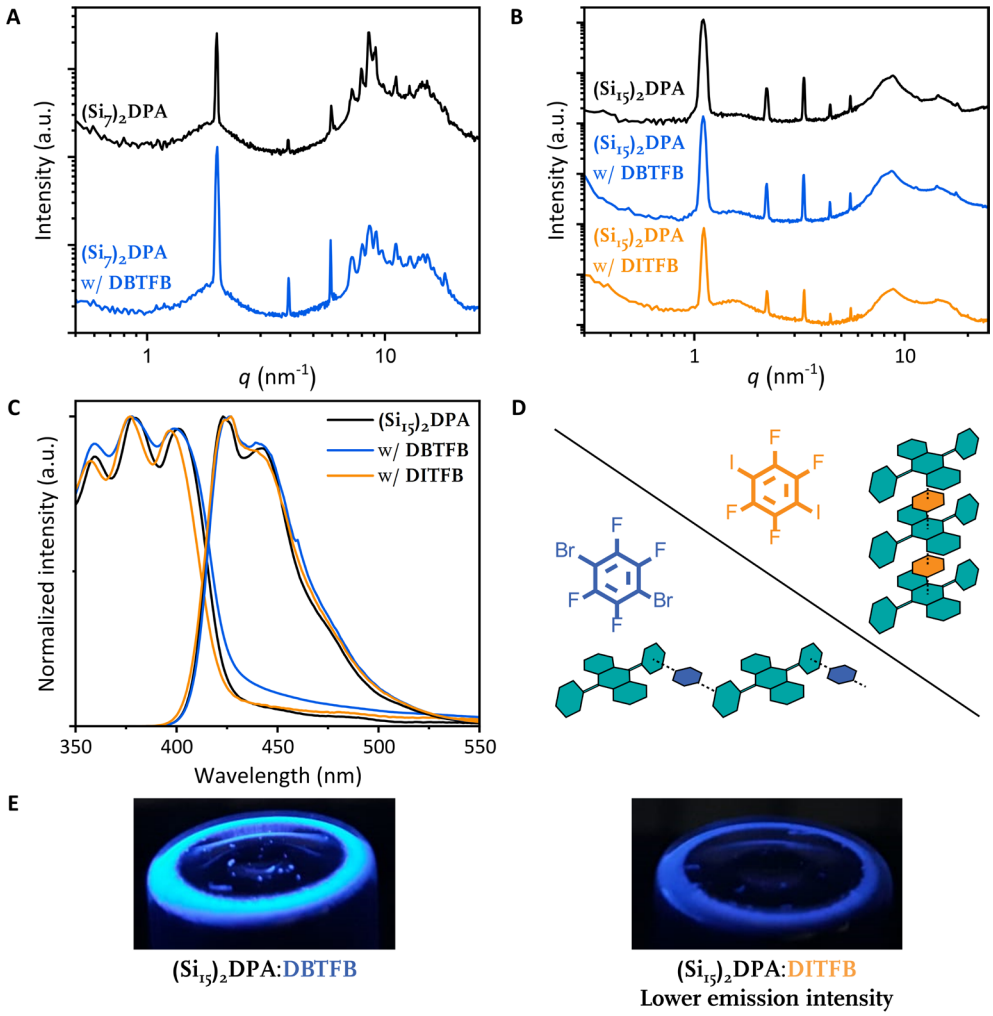

Figure 10. (A, B) 1-D transmission scattering profile of (A) **$(Si_7)_2$DPA** with (orange) and without (black) an equimolar amount of DBTFB, and (B) **$(Si_{15})_2$DPA** (black), in an equimolar mixture with DBTFB (blue) or DITFB (orange). Although **$(Si_7)_2$DPA** can form double lamellae upon careful thermal processing, the 1-D transmission scattering profiles are shown here after similar thermal processing of both **$(Si_7)_2$DPA** and the mixture. (C) Normalized absorption spectra of films of **$(Si_{15})_2$DPA** (black), in an equimolar mixture with DBTFB (blue) or DITFB (orange). (D) Schematic representation of the molecular packing in the co-crystal of diphenylanthracene with DBTFB (blue) or DITFB (orange) based on single-crystal X-ray diffraction data. Image adapted from the literature.[74] (E) Optical photographs of the waxy mixtures **$(Si_{15})_2$DPA:DBTFB** (left) and **$(Si_{15})_2$DPA:DITFB** (right) under UV light irradiation showing the visual difference in PLQY.

large differences are observed in emission intensity in the co-crystal with **$(Si_{15})_2$DPA**. As shown in Figure 10E, **$(Si_{15})_2$DPA:DITFB** has a significantly lower emission intensity than **$(Si_{15})_2$DPA:DBTFB**. These results are consistent with reported co-crystals of non-functionalized DPA, where co-crystals with DITFB have a photoluminescence quantum yield (PLQY) of 0.94%, while co-crystals with DBTFB have a significantly higher PLQY of 26.5%.[74] The PLQY of **$(Si_n)_2$DPA** is ~45% (see Chapter 5.4.1). The differences in PLQY

can be explained by the crystal structure of the mixtures. In the **DPA**:**DITFB** co-crystals, the halogenated benzene intercalates between the anthracene units, on which the greatest electron density is located due to the perpendicular orientation of the phenyl ring with respect to the anthracene core (Figure 10D). The interaction between the anthracene core and **DITFB** results in the lower emission efficiency. In contrast, **DBTFB** is intercalated between the phenyl rings and therefore DPA remains an efficient emitter. Based on literature, this might indicate an increase in electrochemiluminescence, which is not explored here.[74] These results show that halogenated benzenes can be incorporated into the DPA crystalline layer of **$(Si_n)_2$DPA** without changing the morphology or absorption spectra, while significantly reducing the emission intensity. Thus, halogen-bonding interactions can be used to tailor optical properties in block molecule systems.

3.5 Conclusions

In summary, we studied several binary and trinary mixtures in which at least one molecule was functionalized with *o*DMS. The other components were chosen to study the effect of homo-interactions and donor-acceptor interactions on the formed nanostructure. With PMDI-centered block molecules, we show that the incorporation of small molecules increases the distance between *o*DMS groups, decreasing their relative bulkiness and enabling the formation of lamellar morphologies. To this end, strong charge transfer (CT) interactions between the block molecule and the small molecule are preferred over the weaker PMDI-PMDI homo-interactions. The lower interaction strength of PMDI-PMDI compared to PMDI-pyrene is demonstrated in mixtures with telechelic PMDI block molecules. In mixtures based on homo-interactions, self-sorting occurs, leading to coexisting phases. In contrast, single morphologies are obtained when the arylene diimide systems are mixed with pyrene through the formation of stronger CT interactions. The minimal interaction strength between the small molecule and block molecule remains to be elucidated. CT formation is visualized by the formation of CT bands in the absorption spectrum. Based on the ternary mixtures of viologen, bromide ions and tetrathiafulvalene derivatives, we further prove that specific interactions between different components such as CT interactions lead to better defined morphologies than solely matching the shape of the core. The results of this chapter confirm the findings of Chapter 2, where a minimum available space for the *o*DMS of ~ 7 Å is shown to be required to form lamellar morphologies. We add to that knowledge that ~ 7 Å acts as a lower bound when there are strong interlayer interactions. Thus, also the crystal structure of co-assemblies can be used when designing new block molecule mixtures.

Moreover, halogen bonding was studied for its donor-acceptor interaction with DPA block molecules. Halogenated benzenes are known to intercalate the DPA structure, preserving the morphology of the DPA block molecules. However, the PLQY is significantly altered due to cocrystal formation. Combined with the aforementioned formation of CT bands, this demonstrates how co-assembly in *o*DMS block molecules can alter the optical properties of the studied system and how these co-assemblies can be designed. Therefore, assembled structures of *o*DMS block molecules are promising for tuning optoelectronic properties with modification or preservation of order at the nanoscale, increasing their applicability in optoelectronic devices.

Overall, we show how mixing donor and acceptor molecules can influence optical properties when one component is a block molecule. Based on the results reported here and those previously published on pyrene and naphthalene diimide block molecules,[39] it appears that the best defined co-assemblies are obtained when only one component is a block molecule. The strongest CT interactions are reported when both the donor and acceptor cores are attached with a single *o*DMS chain, due to either a higher effective molarity or a smaller number of assembly possibilities compared to separate donor and acceptor molecules.[39] However, we show here that mixing of a small molecule and a block molecule can also be used to obtain donor acceptor co-assemblies. This increases the scope of donor acceptor block molecule as functionalization of either the donor or acceptor molecule is not always synthetically accessible, for example for tetracyanoquinodimethane (TCNQ) that has been extensively studied for its strong electron-accepting properties.[2,36] The knowledge gained by studying these donor acceptor co-assemblies can accelerate the development of conductive, nanoscale assemblies that, when aligned, are promising for active elements in organic light-emitting diodes, organic solar cells and organic field-effect transistors.

3.6 Experimental section

3.6.1 Materials and methods

All chemicals were purchased from commercial sources and used as received. For the hydrosilylation reactions, the following preparation of Karstedt's catalyst from Sigma Aldrich is used; Platinum(0)-1,3-divinyl-1,1,3,3-tetramethyldisiloxane complex solution in xylene, Pt ~2 %. All solvents were purchased from Biosolve and the dry solvents were obtained using the MBraun solvent purification system (MB SPS-800). Glassware for all reactions carried out under argon was flame-dried to remove residual water. Analytical thin-layer chromatography (TLC) was performed on 60-F_{254} silica gel plates from Merck and visualized with a 254 nm ultraviolet lamp. Automated column chromatography was performed on a Biotage Isolera One system with Biotage KP-SIL Silica Flash or Biotage Sfär cartridges. The methods used for nuclear magnetic resonance (NMR), matrix assisted laser desorption/ionization time of flight mass spectroscopy (MALDI-ToF-MS), differential scanning calorimetry (DSC), recycling GPC, bulk small angle X-ray scattering (SAXS) and crystal lattice energy calculations are described in Chapter 2. **Polarized optical microscopy** samples were placed between two glass substrates and imaged using a Nikon Xfinity1 Lumenera microscope with two crossed linear polarizers before and after the sample. The samples were heated using a Linkam heating stage mounted in the POM set-up. **Absorption** spectra were measured on a PerkinElmer Lambda 1050 UV-VIS spectrophotometer with a PerkinElmer 3D WB Detector module (λ = 300 – 800 nm; $\Delta\lambda$ = 1 nm). The absorption spectra of the liquid **Si_7PMDISi_7**, **Si_7NDISi_7** and their mixtures with pyrene were measured by applying a drop of the liquid material on the glass slide, followed by smearing of this drop due to gravitational forces. This results in an inhomogeneous solvent-free film. **Emission** spectra were recorded on a luminescence spectrometer LS50B from PerkinElmer using a XBO xenon short arc discharge lamp (≤450W) from Osram (non-coherent excitation with λ_{ex} = 350 nm or 532 nm). Appropriate bandpass filters were used to remove scattered light.

3.6.2 Synthesis

The discrete length oligodimethylsiloxane **HSi$_7$** was synthesized by Bas de Waal according to literature procedure.[75] The synthesis of the DPA derivatives is reported in Chapter 5. Alex van de Ven synthesized **Si$_7$VSi$_7$Br** as reported in his master thesis.[65] **C$_5$PMMI**, **C$_5$PMDIC$_{5u}$**, **PMDI-Si$_8$-PMDI** and **PMDI-Si$_{40}$-PMDI** were synthesized and characterized by Stefan Maessen.[48]

C$_{5u}$PMDIC$_{5u}$
PMDA (296 mg g, 1.36 mmol, 1 eq.) and 4-pentene-1-amine (288 mg, 3.38 mmol, 2.5 eq) were dissolved in 4 mL of DMF in a 5 mL microwave reaction vessel. The mixture was reacted in the microwave for 5 minutes at 75 °C, followed by 15 minutes at 140 °C. After the reaction, the solution was reduced in vacuo, poured in DI water and filtered by gravity filtration. Subsequent recrystallization from hot chloroform through the addition of methanol gave the pure product as an off white solid after gravity filtration and drying the residue in the vacuum oven at 80 °C (335 mg, 70%).
^{1}H NMR (400 MHz, $CDCl_3$): δ = 8.27 (s, 2H), 5.81 (m, 2H), 5.21 – 4.81 (m, 4H), 3.92 – 3.62 (m, 4H), 2.30 – 2.02 (m, 4H), 1.82 (p, *J* = 7.4 Hz, 4H) ppm. ^{13}C NMR (100 MHz, $CDCl_3$): δ = 166.25, 137.24, 136.97, 118.16, 115.58, 38.26, 30.94, 27.42 ppm.

C$_{5u}$NDIC$_{5u}$
Naphthalenetetracarboxylic dianhydride (247 mg g, 0.92 mmol, 1 eq.) and 4-pentene-1-amine (186 mg, 2.18 mmol, 2.4 eq) were dissolved in 4 mL of DMF in a 5 mL microwave reaction vessel. The mixture was reacted in the microwave for 5 minutes at 75 °C, followed by 15 minutes at 140 °C. After the reaction, the solution was reduced in vacuo, poured in DI water and filtered by gravity filtration. Subsequent recrystallization from hot chloroform through the addition of methanol gave the pure product as an off white solid after gravity filtration and drying the residue in the vacuum oven at 80 °C (314 mg, 85%).
^{1}H NMR (400 MHz, $CDCl_3$): δ 8.76 (s, 4H), 5.87 (m, 2H), 5.18 – 4.85 (m, 4H), 4.35 – 4.05 (m, 4H), 2.42 – 2.06 (m, 4H), 1.99 – 1.69 (m, 4H) ppm. ^{13}C NMR (100 MHz, $CDCl_3$): δ = 162.83, 137.45, 130.96, 126.71, 126.63, 115.26, 40.53, 31.19, 27.04 ppm.

General method for Karstedt's hydrosilylation reaction
Under argon, *o*DMS and the crystalline block were dissolved in dry DCM and stirred. Subsequently, Karstedt's catalyst (2 wt% in xylene) was added (1-2 drops) and the reaction was stirred overnight until full conversion of the double bond. Hereafter, DCM was removed in vacuo and the product was purified using automated column chromatography and dried overnight.

Si$_7$PMDISi$_7$
Starting from **C$_{5u}$PMDIC$_{5u}$** (45 mg, 0.13 mmol, 1 eq.) and **HSi$_7$** (236 mg, 0.40 mmol, 3.1 eq), **Si$_7$PMDISi$_7$** was obtained using the general method. The product was reduced in vacuo and purified by column chromatography (Liquid injection from heptane, eluent heptane/$CHCl_3$ 100/0 – 0/100). The pure product was obtained after evaporation of the solvent as a colorless oil (55 mg, 31%).
^{1}H NMR (400 MHz, $CDCl_3$): δ 8.26 (s, 2H), 3.73 (m, 4H), 1.74 – 1.65 (m, 4H), 1.40 – 1.35 (m, 8H), 0.56-0.50 (m, 4H), 0.12 – 0.03 (m, 90H) ppm. ^{13}C NMR (100 MHz, $CDCl_3$): δ 166.27, 137.24, 118.07, 38.72, 30.53, 28.17, 22.81, 18.12, 1.79, 1.17, 1.15, 1.08, 1.06, 0.14 ppm. MALDI-ToF-MS M_w calculated for $C_{50}H_{112}N_2O_{16}Si_{14}$: 1388.5 Da, m/z found = 1412.4 Da $[M+Na]^+$.

Si$_7$NDISi$_7$
Starting from **C$_{5u}$NDIC$_{5u}$** (32 mg, 0.08 mmol, 1 eq.) and **HSi$_7$** (140 mg, 0.24 mmol, 3 eq), **Si$_7$NDISi$_7$** was obtained using the general method. The product was reduced in vacuo and purified by column chromatography (Liquid injection from heptane, eluent heptane/$CHCl_3$ 100/0 – 0/100). The pure product was obtained after evaporation of the solvent as a yellow oil (59 mg, 52%).
^{1}H NMR (400 MHz, $CDCl_3$): δ 8.76 (s, 4H), 4.22 - 4.16 (m, 4H), 1.80 – 1.70 (m, 4H), 1.51 – 1.36 (m, 8H), 0.60 – 0.53 (m, 4H), 0.11 – 0.02 (m, 90H) ppm. ^{13}C NMR (100 MHz, $CDCl_3$): δ 162.82, 130.91, 126.65, 40.96, 30.79, 27.82, 23.00, 18.18, 1.79, 1.18, 1.15, 1.08, 1.07, 0.16 ppm. MALDI-ToF-MS M_w calculated for $C_{54}H_{114}N_2O_{16}Si_{14}$: 1438.5 Da, m/z found = 1463.5 Da $[M+Na]^+$.

3.7 References

(1) Chen, J.; Chen, Y.; Feng, L. W.; Gu, C.; Li, G.; Su, N.; Wang, G.; Swick, S. M.; Huang, W.; Guo, X.; Facchetti, A.; Marks, T. J. *EnergyChem* **2020**, *2*, 100042.
(2) Jiang, H.; Hu, P.; Ye, J.; Zhang, K. K.; Long, Y.; Hu, W.; Kloc, C. *J. Mater. Chem. C* **2018**, *6*, 1884.
(3) Baeg, K. J.; Binda, M.; Natali, D.; Caironi, M.; Noh, Y. Y. *Adv. Mater.* **2013**, *25*, 4267.
(4) Zhu, L.; Yi, Y.; Li, Y.; Kim, E. G.; Coropceanu, V.; Brédas, J. L. *J. Am. Chem. Soc.* **2012**, *134*, 2340.
(5) Torrance, J. B.; Mayerle, J. J.; Bechgaard, K.; Silverman, B. D.; Tomkiewicz, Y. *Phys. Rev. B* **1980**, *22*, 4960.
(6) Kobayashi, H.; Nakayama, J. *Bull. Chem. Soc. Jpn.* **1981**, *54*, 2408.
(7) Emge, T. J.; Wiygul, F. M.; Chappell, J. S.; Bloch, A. N.; Ferraris, J. P.; Cowan, D. O.; Kistenmacher, T. J. *Mol. Cryst. Liq. Cryst.* **1982**, *87*, 137.
(8) Ishibashi, S.; Kohyama, M. *Phys. Rev. B* **2000**, *62*, 7839.
(9) Sing, M.; Schwingenschlögl, U.; Claessen, R.; Blaha, P.; Carmelo, P.; Martelo, M.; Sacramento, D.; Dressel, M.; Jacobsen, S. *Phys. Rev. B* **2003**, *68*, 1.
(10) Alves, H.; Molinari, A. S.; Xie, H.; Morpurgo, A. F. *Nat. Mater.* **2008**, *7*, 574.
(11) Blackburn, A. K.; Sue, A. C. H.; Shveyd, A. K.; Cao, D.; Tayi, A.; Narayanan, A.; Rolczynski, B. S.; Szarko, J. M.; Bozdemir, O. A.; Wakabayashi, R.; Lehrman, J. A.; Kahr, B.; Chen, L. X.; Nassar, M. S.; Stupp, S. I.; Stoddart, J. F. *J. Am. Chem. Soc.* **2014**, *136*, 17224.
(12) Torrance, J. B. *Acc. Chem. Res.* **1979**, *12*, 79.
(13) Bolton, O.; Lee, K.; Kim, H. J.; Lin, K. Y.; Kim, J. *Nat. Chem.* **2011**, *3*, 205.
(14) Horiuchi, S.; Ishii, F.; Kumai, R.; Okimoto, Y.; Tachibana, H.; Nagaosa, N.; Tokura, Y. *Nat. Mater.* **2005**, *4*, 163.
(15) Tayi, A. S.; Shveyd, A. K.; Sue, A. C. H.; Szarko, J. M.; Rolczynski, B. S.; Cao, D.; Jackson Kennedy, T.; Sarjeant, A. A.; Stern, C. L.; Paxton, W. F.; Wu, W.; Dey, S. K.; Fahrenbach, A. C.; Guest, J. R.; Mohseni, H.; Chen, L. X.; Wang, K. L.; Fraser Stoddart, J.; Stupp, S. I. *Nature* **2012**, *488*, 485.
(16) Ferraris, J.; Cowan, D. O.; Walatka, V.; Perlstein, J. H. *J. Am. Chem. Soc.* **1973**, *95*, 948.
(17) Zhang, J.; Geng, H.; Virk, T. S.; Zhao, Y.; Tan, J.; Di, C. A.; Xu, W.; Singh, K.; Hu, W.; Shuai, Z.; Liu, Y.; Zhu, D. *Adv. Mater.* **2012**, *24*, 2603.
(18) Saito, G.; Yoshida, Y. *Chem. Rec.* **2011**, *11*, 124.
(19) Dar, A. A.; Rashid, S. *CrystEngComm* **2021**, *23*, 8007.
(20) Wang, Y.; Wu, H.; Zhu, W.; Zhang, X.; Liu, Z.; Wu, Y.; Feng, C.; Dang, Y.; Dong, H.; Fu, H.; Hu, W. *Angew. Chem. Int. Ed.* **2021**, *60*, 6344.
(21) Pandeeswar, M.; Senanayak, S. P.; Narayan, K. S.; Govindaraju, T. *J. Am. Chem. Soc.* **2016**, *138*, 8259.
(22) Bartocci, S.; Berrocal, J. A.; Guarracino, P.; Grillaud, M.; Franco, L.; Mba, M. *Chem. Eur. J.* **2017**.
(23) Das, A.; Ghosh, S. *Chem. Commun.* **2011**, *47*, 8922.
(24) Liu, K.; Wang, C.; Li, Z.; Zhang, X. *Angew. Chem. Int. Ed.* **2011**, *50*, 4952.
(25) Chakraborty, S.; Barman, R.; Ghosh, S. *J. Mater. Chem. B* **2020**, *8*, 2909.
(26) Chidchob, P.; Jansen, S. A. H.; Meskers, S. C. J.; Weyandt, E.; van Leest, N. P.; de Bruin, B.; Palmans, A. R. A.; Vantomme, G.; Meijer, E. W. *Org. Mater.* **2021**, *03*, 174.
(27) De, S.; Koley, D.; Ramakrishnan, S. *Macromolecules* **2010**, *43*, 3183.
(28) Imato, K.; Nakajima, H.; Yamanaka, R.; Takeda, N. *Polym. J.* **2021**, *53*, 355.
(29) Deepthi, K.; Amal, R. R. B.; Rajeev, V. R.; Unni, K. N. N.; Gowd, E. B. *Macromolecules* **2019**, *52*, 2889.
(30) Mukherjee, A.; Barman, S.; Ghosh, A.; Datta, A.; Datta, A.; Ghosh, S. *Angew. Chem. Int. Ed.* **2022**, *61*, e202203817.
(31) Alvey, P. M.; Reczek, J. J.; Lynch, V.; Iverson, B. L. *J. Org. Chem.* **2010**, *75*, 7682.
(32) Jacob, L.; Rzeszotarska, E.; Koyioni, M.; Jakubowski, R.; Pociecha, D.; Pietrzak, A.; Kaszyński, P. *Chem. Mater.* **2022**, *34*, 6476.
(33) Zhang, Y.; Wu, G.; Liu, H.; Tian, R.; Li, Y.; Wang, D.; Chen, R.; Zhao, J.; Liu, S.; Li, Z.; Zhao, Y. *Mater. Chem. Front.* **2021**, *5*, 6575.
(34) Jalani, K.; Kumar, M.; George, S. J. *Chem. Commun.* **2013**, *49*, 5174.
(35) Berdugo, C.; Nalluri, S. K. M.; Javid, N.; Escuder, B.; Miravet, J. F.; Ulijn, R. V. *ACS Appl. Mater. Interfaces* **2015**, *7*, 25946.
(36) Guerrini, M.; Valencia, A. M.; Cocchi, C. *J. Phys. Chem. C* **2021**, *125*, 20821.
(37) van Son, M. H. C.; Berghuis, A. M.; Eisenreich, F.; de Waal, B.; Vantomme, G.; Gómez Rivas, J.; Meijer, E. W. *Adv. Mater.* **2020**, *32*, 2004775.
(38) Yang, W.; Zhang, W.; Luo, L.; Lyu, X.; Xiao, A.; Shen, Z.; Fan, X. H. *Chem. Commun.* **2020**, *56*, 10341.
(39) Lamers, B. A. G.; Van Son, M. H. C.; De Graaf, F. V.; Van Den Bersselaar, B. W. L.; De Waal, B. F. M.; Komatsu, K.; Sato, H.; Aida, T.; Berrocal, J. A.; Palmans, A. R. A.; Vantomme, G.; Meskers, S. C.

J.; Meijer, E. W. *Mater. Horizons* **2022**, *9*, 294.
(40) Yang, W.; Liu, D.; Luo, L.; Li, P.; Liu, Y.; Shen, Z.; Lei, T.; Yang, H.; Fan, X. H.; Zhou, Q. F. *Chem. Commun.* **2022**, *58*, 108.
(41) Zhang, W.; Yang, W.; Pan, H.; Lyu, X.; Xiao, A.; Liu, D.; Liu, Y.; Shen, Z.; Yang, H.; Fan, X. H. *Soft Matter* **2022**, *18*, 3430.
(42) Ishiwari, F.; Okabe, G.; Ogiwara, H.; Kajitani, T.; Tokita, M.; Takata, M.; Fukushima, T. *J. Am. Chem. Soc.* **2018**, *140*, 13497.
(43) Wang, Z.; Huang, K.; Wan, X.; Liu, M.; Chen, Y.; Shi, X.; Wang, S. *Angew. Chem. Int. Ed.* **2022**, *61*, e202211495.
(44) Lamers, B. Nanostructured Siloxane-Based Materials, 2021.
(45) Molla, M. R.; Das, A.; Ghosh, S. *Chem. Eur. J.* **2010**, *16*, 10084.
(46) Lamers, B. A. G.; Van Son, M. H. C.; De Graaf, F. V.; Van Den Bersselaar, B. W. L.; De Waal, B. F. M.; Komatsu, K.; Sato, H.; Aida, T.; Berrocal, J. A.; Palmans, A. R. A.; Vantomme, G.; Meskers, S. C. J.; Meijer, E. W. *Mater. Horizons* **2022**, *9*, 294.
(47) Knappert, M.; Jin, T.; Midgley, S. D.; Wu, G.; Scherman, O. A.; Grau-Crespo, R.; Colquhoun, H. M. *Polym. Chem.* **2019**, *10*, 6641.
(48) Maessen, S. J. D. Predicting the Formation of Lamellae in Block Molecules by Crystal Structure Energy Calculations, 2022.
(49) Lynch, D. E.; Hamilton, D. G. *Acta Cryst.* **2004**, *60*, 597.
(50) Hurd, C. B. *J. Am. Chem. Soc.* **1946**, *68*, 364.
(51) Wolff, S. K.; Grimwood, D. J.; McKinnon, J. J.; Turner, M. J.; Jayatilaka, D.; Spackman, M. A. *Crystal Explorer*; 2012.
(52) Hiraoka, S.; Tahara, H.; Mori, S.; Okujima, T.; Takase, M.; Nakae, T.; Uno, H. *Tetrahedron* **2017**, *73*, 957.
(53) Maranda-Niedbała, A.; Krzyżewska, K.; Kotwica, K.; Skórka, Ł.; Drapała, J.; Jarzembska, K. N.; Zagórska, M.; Proń, A.; Nowakowski, R. *Langmuir* **2020**, *36*, 15048.
(54) Inoue, S.; Minemawari, H.; Tsutsumi, J.; Chikamatsu, M.; Yamada, T.; Horiuchi, S.; Tanaka, M.; Kumai, R.; Yoneya, M.; Hasegawa, T. *Chem. Mater.* **2015**, *27*, 3809.
(55) Im, H.; Choi, M. Y.; Moon, C. J.; Kim, T. H. *Acta Crystallogr.* **2017**, *73*, 838.
(56) Kato, K.; Hagi, S.; Hinoshita, M.; Shikoh, E.; Teki, Y. *Phys. Chem. Chem. Phys.* **2017**, *19*, 18845.
(57) Krishna, G. R.; Devarapalli, R.; Lal, G.; Reddy, C. M. *J. Am. Chem. Soc.* **2016**, *138*, 13561.
(58) Tosaka, M.; Tashiro, K. *Polym. J.* **2018**, *153*, 507.
(59) Kamatham, N.; Ibraikulov, O. A.; Durand, P.; Wang, J.; Boyron, O.; Heinrich, B.; Heiser, T.; Lévêque, P.; Leclerc, N.; Méry, S. *Adv. Funct. Mater.* **2021**, *31*, 1.
(60) Zha, R. H.; de Waal, B.; Lutz, M.; Teunissen, A. J. P.; Meijer, E. W. *J. Am. Chem. Soc.* **2016**, *138*, 5693.
(61) Lee, S.; Gillard, T. M.; Bates, F. S. *AIChE J.* **2013**, *59*, 3502.
(62) Zhao, F.; Yuan, Y.; Ding, Y.; Wang, Y.; Wang, X.; Zhang, G.; Gu, X.; Qiu, L. *Macromolecules* **2021**, *54*, 5440.
(63) Mu, Z.; Yang, B.; Chen, J.; Ju, Z.; Huang, W.; Luo, L.; Yang, C.; Zhang, J. *Sci. Sin. Chim.* **2022**, *52*, 347.
(64) Lamers, B. A. G.; Graf, R.; De Waal, B. F. M.; Vantomme, G.; Palmans, A. R. A.; Meijer, E. W. *J. Am. Chem. Soc.* **2019**, *141*, 15456.
(65) Ven, A. P. A. van de. Exploring nanostructured viologen-siloxane block molecules with controllable electrical conductivity, 2021.
(66) Sagade, A. A.; Rao, K. V.; George, S. J.; Datta, A.; Kulkarni, G. U. *Chem. Commun.* **2013**, *49*, 5847.
(67) Striepe, L.; Baumgartner, T. *Chem. Eur. J.* **2017**, *23*, 16924.
(68) Tahara, H.; Tanaka, Y.; Yamamoto, S.; Yonemori, S.; Chan, B.; Murakami, H.; Sagara, T. *Chem. Sci.* **2021**, *12*, 4872.
(69) Santos, W. G.; Budkina, D. S.; da Costa, P. F. G. M.; Cardoso, D. R.; Tarnovsky, A. N.; Forbes, M. D. E. *Mater. Adv.* **2022**, 3862.
(70) Rahman, B.; Akutsu, H.; Yamada, J. I.; Nakatsuji, S. *Molecules* **2007**, *12*, 853.
(71) Simonsen, K. B.; Zong, K.; Rogers, R. D.; Cava, M. P.; Becher, J. *J. Org. Chem.* **1997**, *62*, 679.
(72) Berville, M.; Choua, S.; Gourlaouen, C.; Boudon, C.; Ruhlmann, L.; Bailly, C.; Cobo, S.; Saint-Aman, E.; Wytko, J.; Weiss, J. *ChemPhysChem* **2017**, *18*, 796.
(73) Lau, J.; Nielsen, M. B.; Thorup, N.; Cava, M. P.; Becher, J. *EurJOC.* **1999**, No. 12, 3335.
(74) Fan, G.; Yan, D. *Adv. Opt. Mater.* **2016**, *4*, 2139.
(75) Van Genabeek, B.; de Waal, B. F. M.; Gosens, M. M. J.; Pitet, L. M.; Palmans, A. R. A.; Meijer, E. W. *J. Am. Chem. Soc.* **2016**, *138*, 4210.

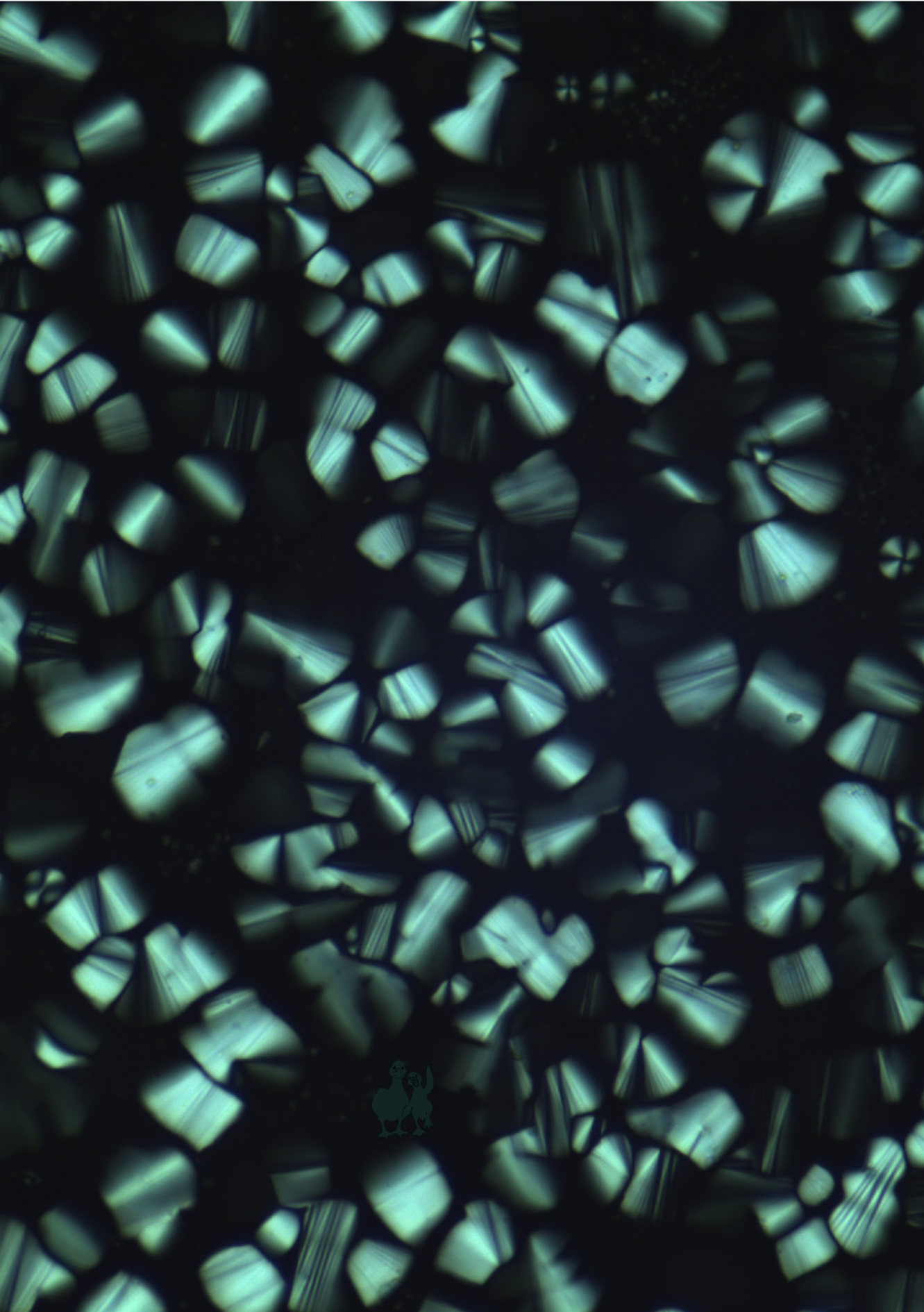

Chapter 4

Highly ordered supramolecular materials of phase-separated block molecules for long-range exciton transport

ABSTRACT: Efficient energy transport over long distances is essential for optoelectronic and light-harvesting devices. Although self-assembled nanofibers of organic molecules have been shown to exhibit long exciton diffusion lengths, aligning these nanofibers into films with large, organized domains with similar properties remains challenging, limiting their use in devices. Here we show how the functionalization of C_3-symmetric carbonyl-bridged triarylamine trisamides (CBT) with oligodimethylsiloxane (*o*DMS) side chains of discrete length leads to fully covered surfaces with aligned domains up to 125x70 μm^2 in which exciton transport occurs over long distances. The nanoscale morphology within the domains consists of highly ordered nanofibers within an insulating *o*DMS matrix with discrete intercolumnar spacings. The soft amorphous *o*DMS prevents bundling of the CBT fibers, reducing the number of defects in the CBT cylinders. As a result, the cylinders have a high degree of coherence, leading to exciton diffusion lengths of several hundred nanometers with exciton diffusivities comparable to those of single-crystal tetracene (0.04 $cm^2\ s^{-1}$). These findings represent the first steps toward fully covered surfaces of highly aligned nanofibers with high exciton diffusion rates and long exciton diffusion lengths.

Part of the work presented in this chapter will be published:
M. H. C. van Son, A. M. Berghuis, B. F. M. de Waal, F. A. Wenzel, K. Kreger, H.-W. Schmidt, J. Gómez Rivas, G. Vantomme, E. W. Meijer, *Submitted*.

4.1 Introduction

The transport of excitation energy over length scales beyond the optical absorption depth of >100 nm can greatly enhance fluorescence sensors or light-harvesting devices such as solar cells.[1,2] Crucial for long-range energy transport is the order at the nanoscale as densely packed molecules provide strong electronic Coulomb coupling, while minimization of both electronic and structural disorder improves exciton delocalization.[3] In solution, these requirements of strong coupling and low disorder can be met with supramolecular systems. Directed noncovalent interactions between C_3- or C_4-symmetric molecules provide a dynamic system with a well-defined spatial arrangement of the building blocks.[4,5] In defect-free single crystals, the molecular arrangement is constant throughout the crystal, leading to singlet excitons diffusion lengths (L_D) of a few 100 nm.[6] However, the processing of these crystals remains challenging due to their polydisperse dimensions, while devices require precisely defined dimensions.[7] In contrast, most organic semiconducting conjugated polymers can be easily processed for solid-state applications. However, local imperfections or variations in the crystalline packing will lead to exciton trapping at low-energy sites. This disorder limits their L_D to only ~10 – 20 nm.[8,9]

In attempts to combine processability with defect-free nanofibers, previous research has used solution-based self-assembly to obtain nanofibers up to 5 µm long that consist of ordered aggregates.[4,7,10] These nanofibers remain intact when deposited on a surface, and their structural order leads to long diffusion lengths and large exciton diffusivities (0.5 – 1 $cm^2\ s^{-1}$). These nanofibers have only been studied as isolated fibers on a surface because fiber bundling increases the energetic disorder, making them unsuitable for complete surface coverage.[10–14] This was shown most clearly for carbonyl-bridged triarylamine trisamides (CBT), where single fibers were found to have an exciton diffusivity of ~1 $cm^2\ s^{-1}$, while the exciton diffusivity of bundled CBT fibers was lower but still high for organic molecules at 0.05 $cm^2\ s^{-1}$. This reduction for bundles is attributed to the interacting periphery leading to local electronic perturbations.[10] Similar high exciton diffusion lengths and diffusivities are found in films of poly(3-hexylthiophene) (P3HT), where nanofibers are embedded in disordered P3HT domains.[9] Although alignment of these nanofibers is possible through blade-coating, the aligned nanofibers possess a lower structural order than nanofibers isolated on a surface.[7,15] Thus, the next step toward organic energy transport materials is to combine the highly ordered structures of supramolecular fibers with the film-forming ability of semiconductor polymers to form large domains of aligned structures with high exciton diffusivities.[3]

Recently, oligodimethylsiloxane (*o*DMS) has been attached to various aromatic cores to create highly ordered structures at the nanoscale.[16–22] In one such example, domains of millimeter-sized aligned 2D crystalline sheets could be obtained by slow cooling from their melt.[16] For this purpose, *o*DMS blocks of discrete length are covalently linked to diphenylanthracene (DPA) as discussed in detail in Chapter 5. In this system, the nanophase separation of *o*DMS with the aromatic core leads to assembly into highly ordered 2D DPA sheets separated by *o*DMS layers. As a result of the well-defined crystalline DPA packing within these monolayers, energy transport was found to be highly effective. This was shown by a two orders of magnitude increase in triplet-triplet annihilation photon upconverted photoluminescence of the aligned material compared

to its amorphous counterpart. In addition, phase separation with *o*DMS prevents interaction between adjacent nanostructures, reducing electronic disorder in the system. In semiconducting polymers, *o*DMS side chains are found to enhance energy transport compared to their alkyl counterparts.[23–26] These properties make functionalization with *o*DMS promising for creating large domains of aligned nanofibers with favorable energy transport characteristics. Although functionalization of "hard" crystalline molecular blocks with soft *o*DMS blocks has been used to form highly ordered aromatic nanofibers in an *o*DMS matrix, this approach has mainly been used for asymmetric, C_2- or C_4-symmetric systems where the nanostructure formed depends on the *o*DMS volume fraction.[19,27] However, C_3-symmetric molecules such as CBT have an inherent preference to form nanofibers and are thus more suitable to combine with *o*DMS functionalization to achieve micrometer-sized domains of highly ordered nanofibers for energy transfer applications.[28]

Here we report on the synthesis, assembly and molecular and photophysical characterization of C_3-symmetric carbonyl-bridged triarylamine trisamide (CBT) functionalized with linear and branched discrete length oligodimethylsiloxane. We show how phase separation induced by the peripheral *o*DMS chains leads to better order within the columns by preventing fiber bundling, thereby effectively increasing the degree of coherence (exciton delocalization). The CBT derivatives form micrometer-sized domains with the same hexagonally packed columnar morphology for which high exciton diffusivities and long exciton diffusion lengths are reported.

4.2 Molecular design and synthesis of CBT block molecules

The molecular structure and synthetic route of the CBT derivatives with discrete oligodimethylsiloxane (*o*DMS) chains are shown in Scheme 1. Two different *o*DMS chains are used that have the same length and molecular formula but are attached to the CBT alkene either at the first silicon atom (Si_{15}) or at the seventh silicon atom (Si_{15b}). These two different chains make it possible to study the effect of branching of the *o*DMS chain on the physical behavior and nanoscale morphology of C_3 symmetric molecules, illustrated here with a CBT core. The strong core-core interactions between the CBT cores along with the flexible nature of *o*DMS make these block molecules ideal for creating hard, isolated aromatic columns in a soft matrix.

The synthesis of these *o*DMS functionalized CBT molecules begins with the synthesis of the *o*DMS side chains. The linear *o*DMS chain **HSi$_{15}$** is synthesized according to a previously described procedure.[29] The branched *o*DMS chain **HSi$_{15b}$** is synthesized by coupling **HOSi$_7$** on either side of dichloromethylsilane to obtain the desired branched *o*DMS.[29] The hydrogen-functionalized discrete *o*DMS is then coupled with Karstedt's catalyst to the alkene-functionalized 2,6,10-triamino-CBT (**CBT(Alk)$_3$**). **CBT(Alk)$_3$** was kindly provided by Felix Wenzel and Klaus Kreger from the research group of Hans-Werner Schmidt.[30] Although this type of hydrosilylation reaction is generally rapid,[31] the reaction here was let to react for two weeks because strong supramolecular aggregation of the cores is thought to prevent easy access to the terminal alkenes. The final *o*DMS functionalized CBT molecules were purified with recycling GPC to yield

CBT(Si$_{15}$)$_3$ and **CBT(Si$_{15b}$)$_3$**, containing linear and branched *o*DMS, respectively, as orange waxy compounds. The yields were low (1 – 6%) but with high purity of the material, as the strong core aggregation prevented easy separation. The structure and the purity of the molecules were confirmed by ^{1}H NMR, ^{13}C NMR, MALDI-ToF-MS, and GPC.

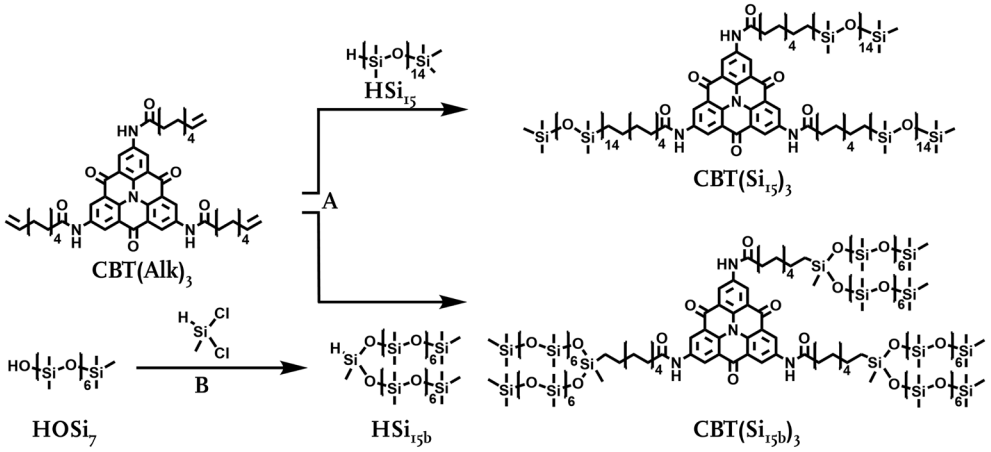

Scheme 1. Synthetic route to the formation of **CBT(Si$_{15}$)$_3$** and **CBT(Si$_{15b}$)$_3$**. (A) Karstedt's catalyst, dry DCM, RT, 2 weeks, 1 – 6%. (B) Toluene, pyridine, 0 °C to RT, 4h, 33%.

4.3 Effect of *o*DMS branching on thermal properties and nanostructure

The thermal properties of **CBT(Si$_{15}$)$_3$** and **CBT(Si$_{15b}$)$_3$** were characterized by differential scanning calorimetry (DSC) and polarized optical microscopy (POM). Similar to the properties of other CBT molecules reported previously, no obvious thermal transitions were observed up to 350 °C using DSC.[32] The lack of clear thermal transitions is attributed to very broad transitions, which were identified using POM measurements at variable temperature (Figure 1A). The width of these transitions is attributed to the strong aggregation of the core. For the POM measurement, the compound is placed between two microscopy slides and heated at 10 °C min^{-1} until the isotropic melt. At room temperature, both molecules **CBT(Si$_{15}$)$_3$** and **CBT(Si$_{15b}$)$_3$** showed clear birefringence and do not flow. Upon heating, material flow was observed at 100 – 110 °C for **CBT(Si$_{15}$)$_3$** and at 130 – 140 °C for **CBT(Si$_{15b}$)$_3$** upon applied external pressure. This flow is attributed to softening of the side chains, as the birefringence, which indicates core-core interactions, was maintained. The higher softening temperature of the side chain ($T_{exo\text{-}R}$) for **CBT(Si$_{15b}$)$_3$** (130 – 140 °C) compared to **CBT(Si$_{15}$)$_3$** (100 – 110 °C) indicates that the $T_{exo\text{-}R}$ is not determined by the absolute length of the *o*DMS side chain, but rather by its relative length. Branched **Si$_{15b}$** can also be considered as two *o*DMS side chains of length 7, and it is known that shorter *o*DMS side chains often lead to higher melting temperatures.[16] Upon further heating, the materials became isotropic between 210 and 255 °C for **CBT(Si$_{15}$)$_3$** and between 180 and 255 °C for **CBT(Si$_{15b}$)$_3$**. The loss of birefringence is related to the breaking of the CBT-CBT interactions and the resulting loss of order. The lowest isotropization temperature reported refers to the initial loss of birefringence, while the highest temperature indicates the isotropic melt. The lower initial isotropization

temperature of **CBT(Si$_{15b}$)$_3$** is attributed to the greater bulkiness of branched *o*DMS compared to linear *o*DMS. Both molecules are completely isotropic at the same temperature, indicating similar core-core interactions once the side chains become flexible. Upon cooling the material from their isotropic phase at 1 °C min^{-1}, the birefringence is restored for both materials. This occurred faster for **CBT(Si$_{15b}$)$_3$** due to a larger number of nucleation points of the core. The birefringent domains averaged 20 – 50 µm in length, although highly ordered domains up to 100 µm in length were observed for both compounds (Figure 1B, C). The largest domains of 125x70 µm^2 were observed for **CBT(Si$_{15}$)$_3$**.

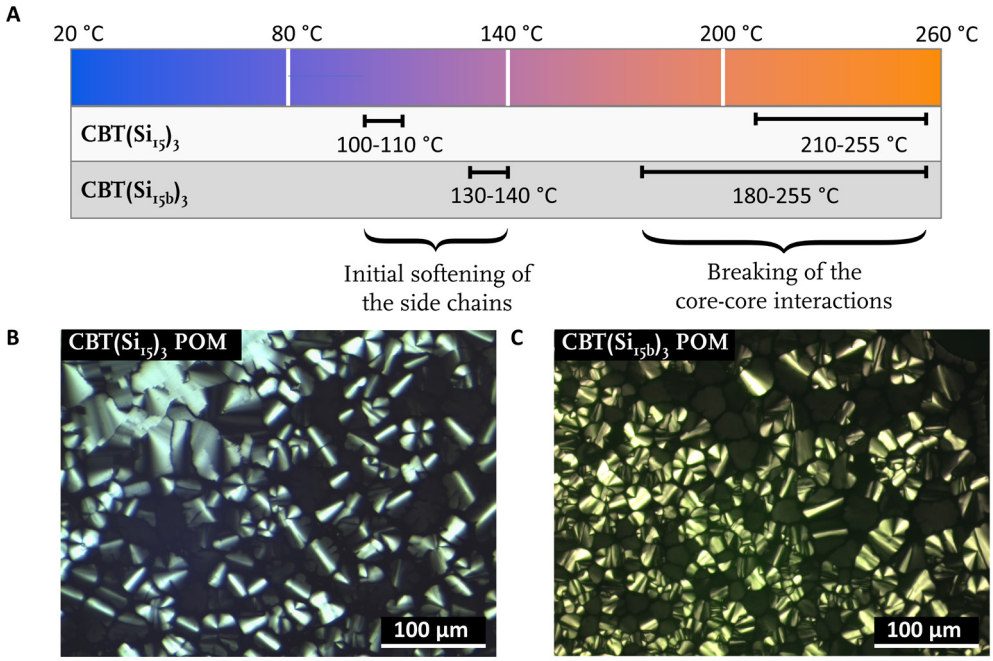

Figure 1. Thermal and photonic characterization of **CBT(Si$_{15}$)$_3$** and **CBT(Si$_{15b}$)$_3$**. (A) Thermal transitions for **CBT(Si$_{15}$)$_3$** (white bar) and **CBT(Si$_{15b}$)$_3$** (gray bar) as observed by POM upon heating and cooling at 10 °C min^{-1} where the softening of the side chains is observed as the free flowing of the material at applied pressure and the breaking of the core-core interactions as reversible loss of birefringence. (B, C) Polarized optical microscopy images of (B) **CBT(Si$_{15}$)$_3$** and (C) **CBT(Si$_{15b}$)$_3$** with domains of 20 - 100 µm length. Image taken with the material in between crossed polarizers.

Upon rotation of the material between the crossed polarizers of the POM setup, bright regions become dark and dark regions become bright. This observed anisotropy in the film occurs through spontaneous directional alignment of the molecules during the domain formation. This alignment was further studied with polarized photoluminescence (PL) measurements. As shown in Figure 2B and D, a dark line is visible through the center of a single domain when a polarizer is present between the material and the detector. This dark line becomes as bright as the surrounding material when rotated by 90° (Figure 2D). Thus, the PL in this region is highly polarized, as confirmed by polarizer angle-dependent PL measurements that can be fitted with a sinusoidal wave function (Figure 2A and C). For **CBT(Si$_{15b}$)$_3$**, a slight decrease in PL

intensity is observed across the different polarizer angles due to bleaching, whereas bleaching was not observed for **CBT(Si$_{15}$)$_3$**. These results, combined with the different isotropization behavior, indicate different core-core packing due to the different oDMS chains. In agreement with the POM results, the highest degree of polarization is observed on the dark line (Figure 2A). In these measurements, the area whose PL is measured is slightly larger than the width of the dark line. As such, the polarization angle dependence of emitted light shown in Figure 2A is only a lower value but still indicates the high degree of alignment inside a domain. Although the microscopic domains could not be aligned over millimeter distances with either shear force or rubbed polyimide layers, the domains of aligned cylinders are several orders of magnitude larger than the length of the previously reported nanofibers with high exciton diffusivities.[7,9,10] Due to the low quantity of material, it was not attempted to align the material by electric field, a method that has been used to align materials between two electrodes for other C_3-symmetric molecules with a π-stacking core, H-bonding dipole flipping group and flexible side chains.[33]

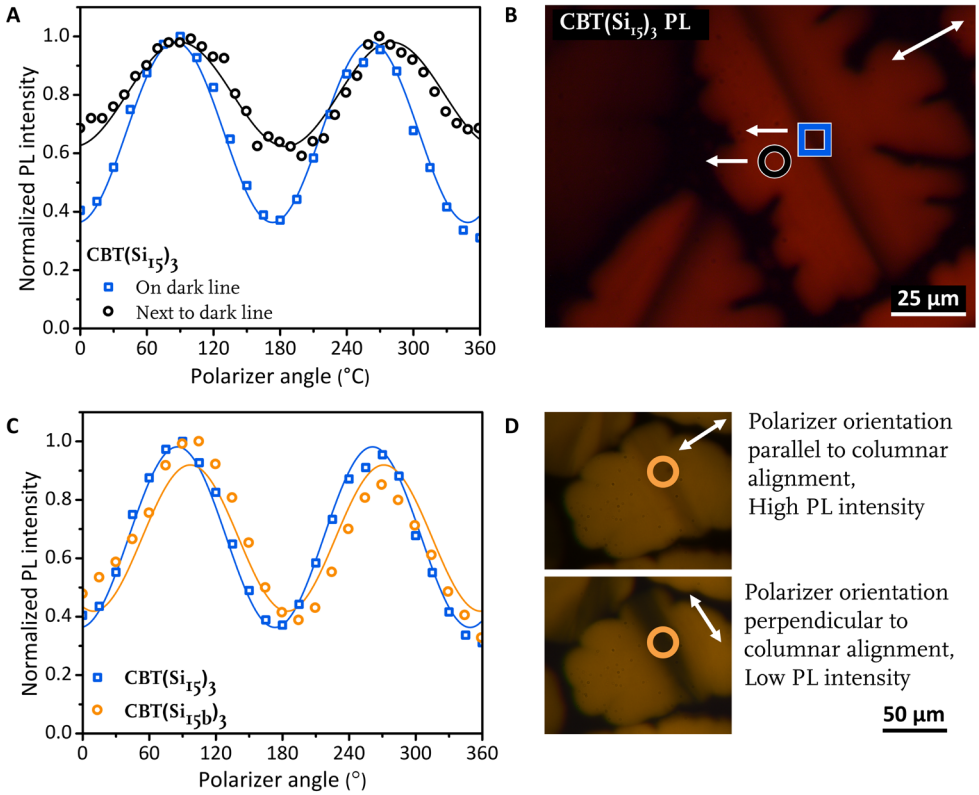

Figure 2. (A) Angle dependence of the PL intensity of **CBT(Si$_{15}$)$_3$** as measured on (blue) and next to (black) the dark line shown in (B). (B) Photoluminescence image of **CBT(Si$_{15}$)$_3$** were a single polarizer is used between the sample and detector, with the polarization direction shown by the double-sided arrow. (C) Angle dependence of the PL intensity of **CBT(Si$_{15}$)$_3$** (blue) and **CBT(Si$_{15b}$)$_3$** (orange). (D) PL images of **CBT(Si$_{15b}$)$_3$** with the area measured under (C) is indicated by an orange circle. The polarization direction of the linear polarizer in between the sample and the detector is indicated by the arrow. These two perpendicular polarizer directions clearly show the alignment of the columnar **CBT(Si$_{15b}$)$_3$** in the dark line.

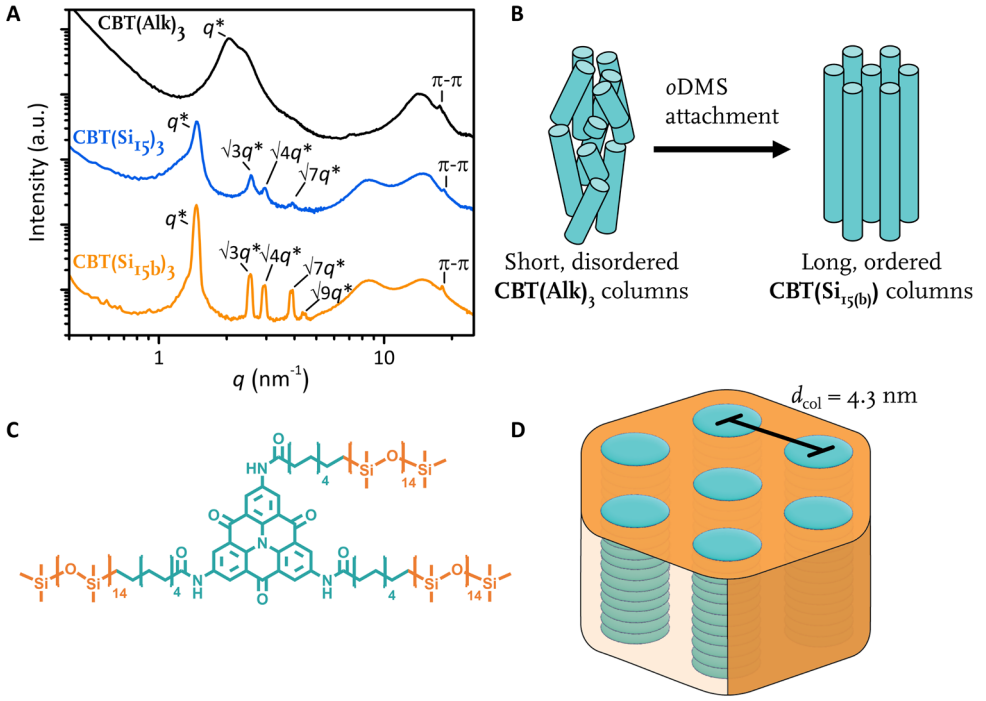

Figure 3. Molecular arrangement of **CBT(Si$_{15}$)$_3$** and **CBT(Si$_{15b}$)$_3$**. (A) Room-temperature X-ray scattering profiles showing amorphous **CBT(Alk)$_3$** (black), and columnar ordered **CBT(Si$_{15}$)$_3$** (blue) and **CBT(Si$_{15b}$)$_3$** (orange) after annealing. (B) Schematic representation of the effect of functionalization with *o*DMS to induce increased columnar order. (C) Molecular structure of **CBT(Si$_{15}$)$_3$** to indicate the color scheme used in D. The discrete length *o*DMS side chains are orange and the CBT core with alkyl spacers is turquoise. (D) Schematic representation of hexagonally packed columns of **CBT(Si$_{15}$)$_3$** and **CBT(Si$_{15b}$)$_3$** with an intercolumnar distance of 4.3 nm where the intercolumnar space is filled with *o*DMS.

The nanoscale morphologies of **CBT(Si$_{15}$)$_3$** and **CBT(Si$_{15b}$)$_3$** and their precursor **CBT(Alk)$_3$** were investigated using medium- and wide-angle X-ray scattering (MAXS and WAXS). The samples could not be fully brought to their isotropic state due to the high temperature required. Since the samples used for the optical characterization were prepared from the isotropic state, for those measurements the material is expected to have a higher degree of order than observed by X-ray scattering. In the MAXS region of Figure 3A ($1 < q < 7$ nm^{-1}), both **CBT(Si$_{15}$)$_3$** and **CBT(Si$_{15b}$)$_3$** exhibit a sharp principal scattering peak q^*, followed by reflection peaks indicative of long-range columnar packing (q^*, $\sqrt{3}q^*$, $\sqrt{4}q^*$, $\sqrt{7}q^*$, $\sqrt{9}q^*$, ...).[34] The shoulder of the principal scattering peak at lower q values is present because the sample could not be fully brought to its isotropic state. The average center-to-center distance of adjacent CBT columns was calculated from the principal scattering peak at $d_{col} = 2\pi/q^* = 4.3$ nm, with the packing schematically shown in Figure 3D. Both the sharpness and number of scattering peaks indicate a long-range columnar ordering with little to no defects.[29] In contrast, for **CBT(Alk)$_3$**, only a broad initial scattering peak is observed without clear reflection peaks, indicating a poorly defined morphology. In the WAXS region ($7 < q < 25$ nm^{-1}), a broad bump centered around 8.6 nm^{-1} is observed for both **CBT(Si$_{15}$)$_3$** and **CBT(Si$_{15b}$)$_3$**, which corresponds to

the amorphous halo of *o*DMS. For all three molecules, a pronounced π-π distance is observed around ~0.34 nm, comparable to other CBT compounds.[10,35–37] These results show that functionalization with *o*DMS greatly improves ordering at the nanoscale, which translates to a reduced number of defects in the CBT columns, while favorable orbital overlap between adjacent CBT molecules is maintained.

4.4 Exciton transport characteristics

4.4.1 The photonic properties of CBT block molecules

The high structural order and close π-π distance make these materials promising for long-range exciton migration.[38–41] To first understand the photonic properties of these molecules, absorption and photoluminescence (PL) spectra were recorded in 40 µM solutions of THF and dodecane and annealed films (Figure 4). In THF, a clear vibronic progression can be observed with PL maxima at 487 and 533 nm for both **CBT(Si$_{15}$)$_3$** and **CBT(Si$_{15b}$)$_3$**. These peaks are attributed to the electronic (0,0) π-π* transition of the CBT core in a molecularly dissolved state.[10] In contrast, the absorption spectrum in dodecane is broader than in THF and blue-shifted, while the PL spectrum is broader and red-shifted ~50 nm, indicating aggregation of the CBT cores. Aggregation is further confirmed by measuring the fluorescence lifetime. The molecularly dissolved compound in THF follows a single exponential decay, whereas in dodecane an additional longer lifetime component indicates aggregation in this solvent (Table 1). Comparing the absorption and emission spectra of the annealed films with the aggregates in solution, a significant suppression of the (0,0) transition at 533 nm can be observed for **CBT(Si$_{15b}$)$_3$**, while the (0,0) transition is even absent for **CBT(Si$_{15}$)$_3$**. The greater suppression of the (0,0) transition for **CBT(Si$_{15}$)$_3$** indicates a higher degree or electronic order within the π-stacked columns than for **CBT(Si$_{15b}$)$_3$**, due to a lower amount of defect. The formation of H-type aggregates indicates significant electronic Coulomb coupling between adjacent cores and strong exciton delocalization.[42,43] Together with the micrometer-sized domains of perfectly aligned columns, these supramolecular materials are ideal for studying their long-range energy transport.[3,9,10,36,44,45]

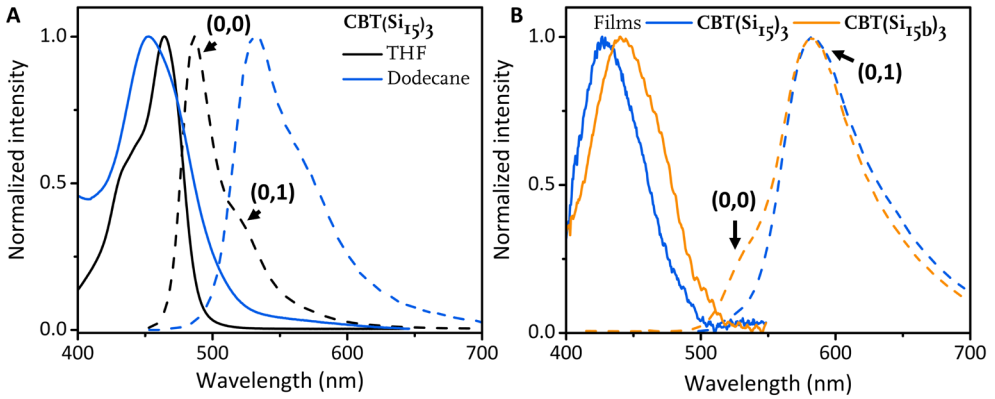

Figure 4. Absorption and emission spectra of (A) **CBT(Si$_{15}$)$_3$** in 40 µM THF (black line) and dodecane (blue). Comparable spectra were observed for **CBT(Si$_{15b}$)$_3$**. (B) Film absorption and emission spectra of **CBT(Si$_{15}$)$_3$** (blue) and **CBT(Si$_{15b}$)$_3$** (orange). The suppression of the (0,0) transition is clearly visible when comparing the solution and film spectra.

Table 1. Photoluminescence lifetimes of **CBT(Si$_{15}$)$_3$** and **CBT(Si$_{15b}$)$_3$** as measured in solutions of THF and dodecane, as well as in annealed films. For the THF solution, a single exponential function was used for the fit. For the dodecane solution and the annealed film, a bi-exponential function was used to fit the experimental data ($y = y_o + a_1 * e^{-x/t_1} + a_2 * e^{-x/t_2}$).

Compound		t_1 (ns)	a_1	t_2 (ns)	a_2
CBT(Si$_{15}$)$_3$	40 µM THF[a]	2.92			
	40 µM dodecane[b]	1.39	88	5.24	12
	Annealed film[c]	1.84	55	7.61	45
CBT(Si$_{15b}$)$_3$	40 µM THF[a]	2.94			
	40 µM dodecane[b]	2.06	57	5.58	43
	Annealed film[c]	3.33	49	14.79	51

[a] Monitored at 485 nm. [b] Monitored at 535 nm. [c] Monitored at 500 to 600 nm.

4.4.2 Exciton diffusivity of CBT block molecules

With this detailed knowledge of the photonic properties of the system in hand, the solid-state exciton diffusivity was measured in close cooperation with Matthijs Berghuis of the Applied Physics Department. For this purpose, the annealed thin films obtained during the optical microscopy measurements are used. Exciton diffusivity was measured by a combination of a fixed pulsed laser excitation (λ = 470 nm) with a spatially resolved emission detection that measures the exciton lifetime using a time-correlated single-photon counting setup. After initial excitation, photoluminescence occurs mainly at the excitation site. However, as the excitons diffuse in the material before their (radiative) decay, the area from where PL occurs widens over time. By plotting the broadening of the Gaussian fits of the emission as a function of time, the exciton diffusivity can be derived (Figure 5A, B). Very low exciton fluxes are used for these measurements to exclude artifacts due to saturation, photobleaching, and exciton-exciton annihilation.[10] Although the POM and PL measurements showed anisotropy of the material, anisotropy was not observed in the diffusivity measurements. The average exciton diffusivities were determined to be D(**CBT(Si$_{15}$)$_3$**) = 0.047 ±0.036 cm^2 s^{-1} and D(**CBT(Si$_{15b}$)$_3$**) = 0.028 ±0.021 cm^2 s^{-1} as measured at different locations of the same sample and evaluated for t < 2 ns. As can be seen in Figure 5C, for **CBT(Si$_{15}$)$_3$** also exciton mobilities above 0.1 cm^2 s^{-1} were measured. The slightly higher average exciton diffusivity of **CBT(Si$_{15}$)$_3$** than **CBT(Si$_{15b}$)$_3$** can be explained by the lower amount of defects, based on the larger suppression of the (0,0) transition in the emission spectra. When taking an average diffusion constant of 0.04 cm^2 s^{-1} (4 nm^2 ps^{-1}) and the intrinsic radiative lifetime of molecularly dissolved **CBT(Si$_{15}$)$_3$** or **CBT(Si$_{15b}$)$_3$** at τ = 2900 ps (Table 1), a diffusion length $L_D = (D\tau)^{1/2}$ of >100 nm can be estimated.[46,47] This corresponds to an exciton transport over more than 300 cohesive CBT cores aligned within one-dimensional fibers in an insulating *o*DMS matrix, as calculated with their π-π distance of 0.34 nm. The exciton diffusivity and diffusion length agree with the theoretically calculated values for CBT nanofibers.[36] The measured diffusion values are similar to tetracene crystals (0.04 cm^2 s^{-1}), polyfluorenes (0.029 cm^2 s^{-1}), or zinc porphyrins (0.014 cm^2 s^{-1}), while the diffusion length is an order of magnitude larger than typically reported for amorphous and polycrystalline organic semiconductors.[41,46,48,49] These results clearly show how the functionalization of organic π-conjugated molecules with *o*DMS side chains can result in fast exciton diffusion over

long distances without the requirement of 3D crystallinity, covalent polymerization or heavy atoms. Although higher diffusion coefficients have been reported for organic nanofibers (0.5 – 1 $cm^2\ s^{-1}$),[7,10] these values were obtained for isolated nanofibers on a surface while the approach reported here with 125x70 μm^2 domains is the next step toward complete surface coverage by isolating the nanofibers at the nanoscale.

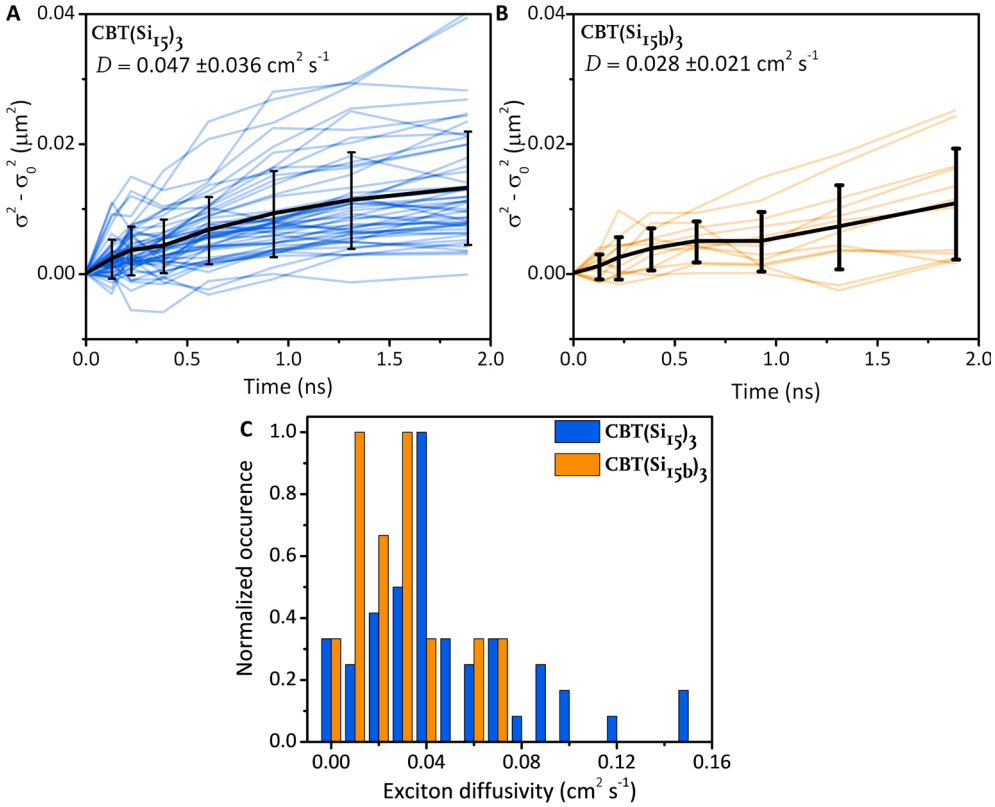

Figure 5. Temporal evolution of the variance of the exciton distribution for (A) **CBT(Si$_{15}$)$_3$** and (B) **CBT(Si$_{15b}$)$_3$**. The colored lines indicate the fitted data, and the black line the calculated mean and standard deviation. (C) Distribution of the exciton diffusivity of **CBT(Si$_{15}$)$_3$** (blue) and **CBT(Si$_{15b}$)$_3$** (orange), evaluated for $t < 2$ ns and binned in steps of 0.01 $cm^2\ s^{-1}$.

4.5 Conclusions

In conclusion, carbonyl-bridged triarylamine trisamides (CBT) have been functionalized with oligodimethylsiloxane (*o*DMS) of discrete length to obtain **CBT(Si$_{15}$)$_3$** and **CBT(Si$_{15b}$)$_3$** that differ only in the attachment point of the *o*DMS to the core. The bulk morphology of these discrete C_3-symmetric molecules consists of single isolated nanofibers of the CBT chromophores in a matrix of insulating *o*DMS with a regular intercolumnar spacing of 4.3 nm, forming microscale aligned domains with dimensions up to 125x70 μm^2. Within these columns, the well-defined arrangement of the cores allows diffusion lengths of > 100 nm, corresponding to exciton transport over more than 300 molecules. Both **CBT(Si$_{15}$)$_3$** and **CBT(Si$_{15b}$)$_3$** showed the same order of magnitude for the exciton diffusivity values, ranging from 0.028 to 0.048 cm^2 s^{-1}. These values are relatively high for organic molecules. The exciton diffusion is thought to be directional based on the polarized transmission and PL. This Chapter is a first step to bridge the gap between isolated organic fibers on a surface and processable materials with complete and homogeneous surface coverage. The work reported here extends the general approach to functionalization with well-defined *o*DMS from C_2- to C_3-symmetric molecules, where the high chemical incompatibility of the flexible *o*DMS with aromatic groups repeatedly leads to highly ordered nanophase-separated structures and long-range alignment. Moreover, *o*DMS functionalization induces intermolecular interactions that maximize energy transport, which, combined with the thermal processability of the materials, is promising for nanophotonics or nanoelectronics.

4.6 Experimental section

4.6.1 Materials and methods

All chemicals were purchased from commercial sources and used as received. For the hydrosilylation reactions, the following preparation of Karstedt's catalyst from Sigma Aldrich is used; Platinum(0)-1,3-divinyl-1,1,3,3-tetramethyldisiloxane complex solution in xylene, Pt ~2 %. Carbonyl-bridged triarylamine trisamide (CBT) with alkyl side chains was synthesized by Felix Wenzel and Klaus Kreger and used as received. The discrete length monohydride oligodimethylsiloxanes (monohydroxoxy of length 7 (**HOSi$_7$**), monohydride of length 15 (**HSi$_{15}$**)) were synthesized following literature procedures by Bas de Waal,[29,30] who also synthesized the branched *o*DMS. The methods used for nuclear magnetic resonance (NMR), matrix assisted laser desorption/ionization time of flight mass spectroscopy (MALDI-ToF-MS), differential scanning calorimetry (DSC) and bulk small angle X-ray scattering (SAXS) are described in Chapter 2. The method for recycling GPC is described in Chapter 2. **Polarized optical microscopy** samples were placed between two glass substrates and imaged using a Nikon Xfinity1 Lumenera microscope with two crossed linear polarizers in before and after the sample. The samples were heated using a Linkam heating stage mounted in the POM set-up. **Absorption** and **emission** were measured on a Princeton Instruments SP2300 spectrometer. For the emission measurement, the sample was excited with the UV lamp X-Cite 120 in combination with a band pass filter, λ_{ex} = 420 ±40 nm. **Time-resolved fluorescence experiments** were carried out with a 400 nm excitation pulse obtained from a Picoquant LDH C400 laser, operating at a repetition rate of 1 MHz. The fluorescence light, collected in a backward scattering geometry, was dispersed by a 0.34 m double monochromator, allowing for a spectral resolution of 1 nm. Time-resolved emission spectra were recorded with the time-correlated single-photon counting technique in reversed mode using a microchannel plate photomultiplier (Hamamatsu R3809u-51) and a time-to-amplitude converter. The width of the instrument response function amounts to 60 ps FWHM. Using a single channel analyzer (EG&G), fluorescence spectra can be recorded within a variable, narrow time window after the excitation pulse. The maximum photon count rate was kept low (< 10^8 s^{-1}) to prevent distortion of the spectra due to pulse pile-up effects. Fluorescence lifetimes were determined by fitting the initial decay with an exponential decay. **Exciton diffusion measurements** were performed in a Nikon Ti-E inverted microscope. A 820 nm, 80 MHz laser from a Ti:Sapph oscillator (MaiTai) was tuned to 470 nm in a OPO (Inspire HF, Spectra Physics). The repetition rate was reduced to 5 MHz in a pulse picker (APE pulseSelect) and the laser power was reduced using optical density filters. The laser beam was focused on the sample through a high NA oil objective (Nikon CFI Plan APO Lambda D 60x Oil, NA 1.45) resulting a small spot of ~300 nm diameter with a power of ~10-20 nW. The temporal and spatially resolved emission were collected by scanning the excited area using a Nikon C2 scanning head, sending the light to a TCSPC module (TimeHarp 300, Picoquant). Only the light in the range of 500 to 600 nm was collected using a long pass 500 nm filter, and a short pass 600 nm filter. The data is collected in the SymPhoTime 64 software. The spatial excitation profiles at different times after arrival of the laser pulse were analyzed in MatLab, by fitting the profile of the spot with a 2D Gaussian function. **Film preparation**. A small amount (<1 mg) of material was placed on clean glass slides on which a 0.17 mm thin glass slide was added to sandwich the sample. Annealing of the samples was performed with the POM set-up reported above. All samples were heated to their isotropic phase and subsequently cooled with 1 °C min^{-1} until room temperature.

4.6.2 Synthesis

Branched *o*DMS: HSi_{15b}
To toluene (25 ml), cooled with an ice/water bath, was added dichloromethylsilane (1.25 ml, 12.0 mmol, 1 eq.), followed by dry pyridine (5.10 ml, 62.5 mmol, 5.2 eq.). A solution of **$MeSi_7OH$** (13.17 g, 24.62 mmol, 2.05 eq.) in toluene (27 ml) was added dropwise over 7 minutes. The cooling was removed after 20 minutes and the reaction was let to stir at room temperature under argon. After 25 hours, the reaction mixture was diluted with toluene (200ml) and the reaction mixture was shaken with DI water (3 times 100 ml) in a separatory funnel. The organic phase was concentrated with rotary evaporator and the product was coevaporated with acetonitrile (100 ml) to remove water. The crude product was washed with acetonitrile (3 times 25 ml) to remove low molecular weight siloxane compounds. The remaining liquid (12.0 g) was purified by column chromatography (Liquid injection, eluent heptane/chloroform 100/0 – 80/20) The product was obtained as a clear liquid (9.18 g, 65%).
^{1}H-NMR (400 MHz, $CDCl_3$): δ = 4.68 (q, J = 1.6 Hz, 1H, H-Si-CH_3), 0.15 (d, J = 1.6 Hz, 3H, H-Si-CH_3), 0.10 (d, J = 1.1 Hz, 12H, H-Si-O-Si-(CH_3)$_2$), 0.09 (s, 18H, (CH_3)$_3$-Si), 0.08-0.07 (m, 48H, CH_3), 0.05 (s, 12H, CH_3) ppm. ^{13}C NMR (100 MHz, $CDCl_3$) δ = 32.21, 29.34, 23.01, 14.42, 2.37, 2.08, 1.62, 1.44, 1.35, 1.32, 1.27, 1.16 ppm. ^{29}Si NMR (79 MHz, $CDCl_3$) δ = 7.23, -20.57, -21.41, -21.66, -21.87, -21.96, -22.08, -37.59 ppm. MALDI-ToF-MS: m/z calcd. for $C_{31}H_{94}O_{14}Si_{15}$+$Na^+$ 1133.32 Da, found: 1133.27 Da $[M+Na]^+$.

CBT(Alk)$_3$
In a Schlenk flask, 0.56 g (1.53 mmol, 1 eq.) of 2,6,10-triamino-carbonyl-bridged triarylamine was dissolved in 30 ml of dry NMP and 0.62 ml (7.635 mmol, 5 eq.) of dry pyridine under argon atmosphere. The solution was cooled to 5°C with an ice bath and 1.64 ml (7.635 mmol, 5 eq.) of 10-undecenoyl chloride was added dropwise. The reaction mixture was warmed to room temperature and stirred for 48 h. Subsequently, it was poured into 300 ml of water and the precipitated crude product was filtered by gravity filtration and dried in the oven at 80 °C. The crude product was purified by column chromatography (eluent EtOAc/DMF 10/1) and then recrystallized from EtOAc. After freeze-drying from 5 mL of dioxane, the product was obtained as an orange solid (355 mg, 27%).
1H NMR (300 MHz, THF-d8): δ = 9.66 (s, 3H, H-N), 8.67 (s, 6H, H-Ar), 5.81 (m, 6H, CH2-CH=CH2), 4.98 (m, 3H, CH=CH-HA), 4.91 (m, 3H, CH=CH-HB), 2.54-2.43 (m, 6H, (CO)CH2), 2.06 (q, 6H, CH2(CH=CH2)), 1.88-1.75 (m, 6H, CH2), 1.55-1.28 (m, 30H, 5xCH2) ppm. ^{13}C NMR was not measured due to its low solubility. M/z calcd. for $C_{54}H_{66}N_4O_6$: 867.1 Da, found: 867.5 Da $[M]^+$.

CBT(Si_{15b})$_3$
In a flame dried Schlenk tube, **CBT(Alk)$_3$** (32 mg, 37 µmol, 1 eq.) and **HSi_{15b}** (284 mg, 744 µmol, 20.2 eq.) were dispersed in 0.6 ml dry DCM. To this suspension, 10 µL catalyst solution (1:9 v:v Karstedt's catalyst:dry DCM, Karstedt's catalyst was 2% in xylene) was added. After reacting for 24h under argon, an additional 10 µL catalyst solution was added to the yellow solution, as well as 0.2 mL dry DCM to account for evaporated solvent. This was repeated after 72h, 96h, 162h and 240h. After reacting for 14 days, NMR showed a conversion of 96% alkene conversion. The crude mixture was impregnated on celite and purified by column chromatography (Solid loading, eluent heptane/chloroform 100/0 – 0/100 – 100/0 (Removal of **HSi_{15b}**), heptane/EtOAc 100/0 – 0/100(removal of the product)). The product was further purified using recycling GPC with unstabilized THF to give the product as a dark orange waxy solid (10 mg, 6% yield). Strong core aggregation prevented complete reaction to the three times reacted target compound and hampered subsequent work-up.
^{1}H NMR (400 MHz, THF-d_8) δ 9.66 (s, 3H), 9.01 (s, 6H), 2.46 (s, 6H), 1.85-1.78 (m, 6H), 1.52-1.35 (m, 42H), 0.64-0.56 (m, 6H), 0.17-0.07 (m, 279H) ppm. ^{13}C NMR (100 MHz, THF-d_8) δ 175.73, 171.89, 133.44, 124.16, 123.91, 37.63, 34.28, 32.68, 30.61, 30.57, 30.50, 30.45, 30.34, 30.32, 18.24, 14.24, 1.77, 1.30, 1.28, 1.24, 1.21, 1.19, 1.16, 0.26 ppm. MALDI-ToF-MS M_w calculated for $C_{147}H_{348}N_4O_{48}Si_{45}$: 4204.2 Da, m/z found = 4226.1 Da $[M+Na]^+$.

CBT(Si_{15})$_3$
In a flame dried Schlenk tube, **CBT(Alk)$_3$** (34 mg, 39 µmol, 1 eq.) and **HSi_{15}** (303 mg, 795 µmol, 20.4 eq.) were dispersed in 1.8 ml dry DCM. To this suspension, 10 µL catalyst solution (1:9 v:v Karstedt's catalyst (2% in xylene):dry DCM) was added. After reacting for 24h under argon, an additional 10 µL catalyst solution was added to the orange suspension, as well as dry DCM to account for evaporated solvent. This was repeated after 90h, 114h, 170h, 312h, 336 and 360h. After reacting for 16 days, the gelated reaction mixture was reduced in vacuo. The crude mixture was impregnated on celite and purified by column chromatography (Solid loading, eluent heptane/chloroform 100/0 – 0/100 – 100/0 (Removal of **HSi_{15}**), heptane/EtOAc 100/0 – 0/100(removal of the product)). The product was further purified using recycling GPC with unstabilized THF to give the

product as a dark orange waxy solid (2 mg, 1% yield). Strong core aggregation prevented complete reaction to the three times reacted target compound and hampered subsequent work-up.
^{1}H NMR (400 MHz, THF-*d*$_8$) δ 9.66 (s, 3H), 9.09 (s, 6H), 2.46 (s, 6H), 1.85-1.77 (m, 6H), 1.48-1.34 (m, 42H), 0.64-0.57 (m, 6H), 0.17-0.07 (m, 279H) ppm. ^{13}C NMR (100 MHz, THF-*d*$_8$) δ 34.37, 32.69, 30.53, 30.46, 30.42, 14.25, 1.76, 1.25, 1.19, 1.15, 0.24 ppm. Due to the strong aggregation and low quantity of the material, not all carbon signals could be observed. MALDI-ToF-MS M_w calculated for $C_{147}H_{348}N_4O_{48}Si_{45}$: 4204.2 Da, m/z found = 4225.0 Da $[M+Na]^+$.

4.7 References

(1) Cheng, C.; Gong, Y.; Guo, Y.; Cui, L.; Ji, H.; Yuan, H.; Jiang, L.; Zhao, J.; Che, Y. *Angew. Chem. Int. Ed.* **2021**, *60*, 5827.
(2) Zhu, T.; Wan, Y.; Guo, Z.; Johnson, J.; Huang, L. *Adv. Mater.* **2016**, *28*, 7539.
(3) Eisele, D. M.; Arias, D. H.; Fu, X.; Bloemsma, E. A.; Steiner, C. P.; Jensen, R. A.; Rebentrost, P.; Eisele, H.; Tokmakoff, A.; Lloyd, S.; Nelson, K. A.; Nicastro, D.; Knoester, J.; Bawendi, M. G. *Proc. Natl. Acad. Sci. U. S. A.* **2014**, *111*, E3367.
(4) Haedler, A. T.; Kreger, K.; Issac, A.; Wittmann, B.; Kivala, M.; Hammer, N.; Köhler, J.; Schmidt, H. W.; Hildner, R. *Nature* **2015**, *523*, 196.
(5) Dumele, O.; Chen, J.; Passarelli, J. V.; Stupp, S. I. *Adv. Mater.* **2020**, *32*, 1907247.
(6) Wang, Y.; Sun, L.; Wang, C.; Yang, F.; Ren, X.; Zhang, X.; Dong, H.; Hu, W. *Chem. Soc. Rev.* **2019**, *48*, 1492.
(7) Jin, X.; Price, M. B.; Finnegan, J. R.; Boott, C. E.; Richter, J. M.; Rao, A.; Menke, S. M.; Friend, R. H.; Whittell, G. R.; Manners, I. *Science* **2018**, *360*, 897.
(8) Spanggaard, H.; Krebs, F. C. *Sol. Energy Mater. Sol. Cells* **2004**, *83*, 125.
(9) Sneyd, A. J.; Fukui, T.; Paleček, D.; Prodhan, S.; Wagner, I.; Zhang, Y.; Sung, J.; Collins, S. M.; Slater, T. J. A.; Andaji-Garmaroudi, Z.; MacFarlane, L. R.; Garcia-Hernandez, J. D.; Wang, L.; Whittell, G. R.; Hodgkiss, J. M.; Chen, K.; Beljonne, D.; Manners, I.; Friend, R. H.; Rao, A. *Sci. Adv.* **2021**, *7*, eabh4232.
(10) Wittmann, B.; Wenzel, F. A.; Wiesneth, S.; Haedler, A. T.; Drechsler, M.; Kreger, K.; Köhler, J.; Meijer, E. W.; Schmidt, H. W.; Hildner, R. *J. Am. Chem. Soc.* **2020**, *142*, 8323.
(11) Eisele, D. M.; Knoester, J.; Kirstein, S.; Rabe, J. P.; Vanden Bout, D. A. *Nat. Nanotechnol.* **2009**, *4*, 658.
(12) Ma, J.; Lu, G.; Huang, X.; Feng, C. *Chem. Commun.* **2021**, *57*, 13259.
(13) Kim, T.; Ham, S.; Lee, S. H.; Hong, Y.; Kim, D. *Nanoscale* **2018**, *10*, 16438.
(14) Clark, K. A.; Krueger, E. L.; Vanden Bout, D. A. *J. Phys. Chem. Lett.* **2014**, *5*, 2274.
(15) Chu, P. H.; Kleinhenz, N.; Persson, N.; McBride, M.; Hernandez, J. L.; Fu, B.; Zhang, G.; Reichmanis, E. *Chem. Mater.* **2016**, *28*, 9099.
(16) van Son, M. H. C.; Berghuis, A. M.; Eisenreich, F.; de Waal, B.; Vantomme, G.; Gómez Rivas, J.; Meijer, E. W. *Adv. Mater.* **2020**, *32*, 2004775.
(17) Yang, W.; Zhang, W.; Luo, L.; Lyu, X.; Xiao, A.; Shen, Z.; Fan, X. H. *Chem. Commun.* **2020**, *56*, 10341.
(18) Lamers, B. A. G.; Van Son, M. H. C.; De Graaf, F. V.; Van Den Bersselaar, B. W. L.; De Waal, B. F. M.; Komatsu, K.; Sato, H.; Aida, T.; Berrocal, J. A.; Palmans, A. R. A.; Vantomme, G.; Meskers, S. C. J.; Meijer, E. W. *Mater. Horizons* **2022**, *9*, 294.
(19) Yang, W.; Liu, D.; Luo, L.; Li, P.; Liu, Y.; Shen, Z.; Lei, T.; Yang, H.; Fan, X. H.; Zhou, Q. F. *Chem. Commun.* **2022**, *58*, 108.
(20) Zhang, W.; Yang, W.; Pan, H.; Lyu, X.; Xiao, A.; Liu, D.; Liu, Y.; Shen, Z.; Yang, H.; Fan, X. H. *Soft Matter* **2022**, *18*, 3430.
(21) Ishiwari, F.; Okabe, G.; Ogiwara, H.; Kajitani, T.; Tokita, M.; Takata, M.; Fukushima, T. *J. Am. Chem. Soc.* **2018**, *140*, 13497.
(22) Wang, Z.; Huang, K.; Wan, X.; Liu, M.; Chen, Y.; Shi, X.; Wang, S. *Angew. Chem. Int. Ed.* **2022**, *61*, e202211495.
(23) Zhao, F.; Yuan, Y.; Ding, Y.; Wang, Y.; Wang, X.; Zhang, G.; Gu, X.; Qiu, L. *Macromolecules* **2021**, *54*, 5440.
(24) Heintges, G. H. L.; Hendriks, K. H.; Colberts, F. J. M.; Li, M.; Li, J.; Janssen, R. A. J. *RSC Adv.* **2019**, *9*, 8740.
(25) Mei, J.; Bao, Z. *Chem. Mater.* **2014**, *26*, 604.
(26) Kamatham, N.; Ibraikulov, O. A.; Durand, P.; Wang, J.; Boyron, O.; Heinrich, B.; Heiser, T.; Lévêque, P.; Leclerc, N.; Méry, S. *Adv. Funct. Mater.* **2021**, *31*, 1.

(27) Lamers, B. A. G.; Graf, R.; De Waal, B. F. M.; Vantomme, G.; Palmans, A. R. A.; Meijer, E. W. *J. Am. Chem. Soc.* **2019**, *141*, 15456.
(28) Van Gorp, J. J.; Vekemans, J. A. J. M.; Meijer, E. W. *J. Am. Chem. Soc.* **2002**, *124*, 14759.
(29) Van Genabeek, B.; de Waal, B. F. M.; Gosens, M. M. J.; Pitet, L. M.; Palmans, A. R. A.; Meijer, E. W. *J. Am. Chem. Soc.* **2016**, *138*, 4210.
(30) Haedler, A. T.; Beyer, S. R.; Hammer, N.; Hildner, R.; Kivala, M.; Köhler, J.; Schmidt, H.-W. *Chem. Eur. J.* **2014**, *20*, 11708.
(31) Meister, T. K.; Riener, K.; Gigler, P.; Stohrer, J.; Herrmann, W. A.; Kühn, F. E. *ACS Catal.* **2016**, *6*, 1274.
(32) Gorbunov, A. V.; Haedler, A. T.; Putzeys, T.; Zha, R. H.; Schmidt, H. W.; Kivala, M.; Urbanavičiutec, I.; Wübbenhorst, M.; Meijer, E. W.; Kemerink, M. *ACS Appl. Mater. Interfaces* **2016**, *8*, 15535.
(33) Butkevich, A. A.; Kemerink, M. *Adv. Mater. Technol.* **2022**.
(34) Hamley, I. W.; Castelletto, V. *Small-angle scattering of block copolymers*; 2008.
(35) Haedler, A. T.; Meskers, S. C. J.; Zha, R. H.; Kivala, M.; Schmidt, H. W.; Meijer, E. W. *J. Am. Chem. Soc.* **2016**, *138*, 10539.
(36) Saikin, S. K.; Shakirov, M. A.; Kreisbeck, C.; Peskin, U.; Proshin, Y. N.; Aspuru-Guzik, A. *J. Phys. Chem. C* **2017**, *121*, 24994.
(37) Hamzehpoor, E.; Perepichka, D. F. *Angew. Chem. Int. Ed.* **2020**, *59*, 9977.
(38) Adam, D.; Schuhmacher, P.; Simmerer, J.; Häussling, L.; Siemensmeyer, K.; Etzbachi, K. H.; Ringsdorf, H.; Haarer, D. *Nature* **1994**, *371*, 141.
(39) Henson, Z. B.; Müllen, K.; Bazan, G. C. *Nat. Chem.* **2012**, *4*, 699.
(40) Park, S. K.; Kim, J. H.; Park, S. Y. *Adv. Mater.* **2018**, *30*, 1.
(41) Mikhnenko, O. V.; Blom, P. W. M.; Nguyen, T. Q. *Energy Environ. Sci.* **2015**, *8*, 1867.
(42) Kasha, M.; Rawls, H. R.; El-Bayoumi, M. A. *Pure Appl. Chem.* **1965**, *11*, 371.
(43) Chaudhuri, D.; Li, D.; Che, Y.; Shafran, E.; Gerton, J. M.; Zang, L.; Lupton, J. M. *Nano Lett.* **2011**, *11*, 488.
(44) Giannini, S.; Carof, A.; Ellis, M.; Yang, H.; Ziogos, O. G.; Ghosh, S.; Blumberger, J. *Nat. Commun.* **2019**, *10*, 1.
(45) Hestand, N. J.; Spano, F. C. *Acc. Chem. Res.* **2017**, *50*, 341.
(46) Huijser, A.; Suijkerbuijk, B. M. J. M.; Gebbink, R. J. M. K.; Savenije, T. J.; Siebbeles, L. D. A. *J. Am. Chem. Soc.* **2008**, *130*, 2485.
(47) Hisamitsu, S.; Yanai, N.; Kouno, H.; Magome, E.; Matsuki, M.; Yamada, T.; Monguzzi, A.; Kimizuka, N. *Phys. Chem. Chem. Phys.* **2018**, *20*, 3233.
(48) Campillo, A. J.; Hyer, R. C.; Shapiro, S. L.; Swenberg, C. E. *Chem. Phys. Lett.* **1977**, *48*, 495.
(49) Zaikowski, L.; Mauro, G.; Bird, M.; Karten, B.; Asaoka, S.; Wu, Q.; Cook, A. R.; Miller, J. R. *J. Phys. Chem. B* **2015**, *119*, 7231.

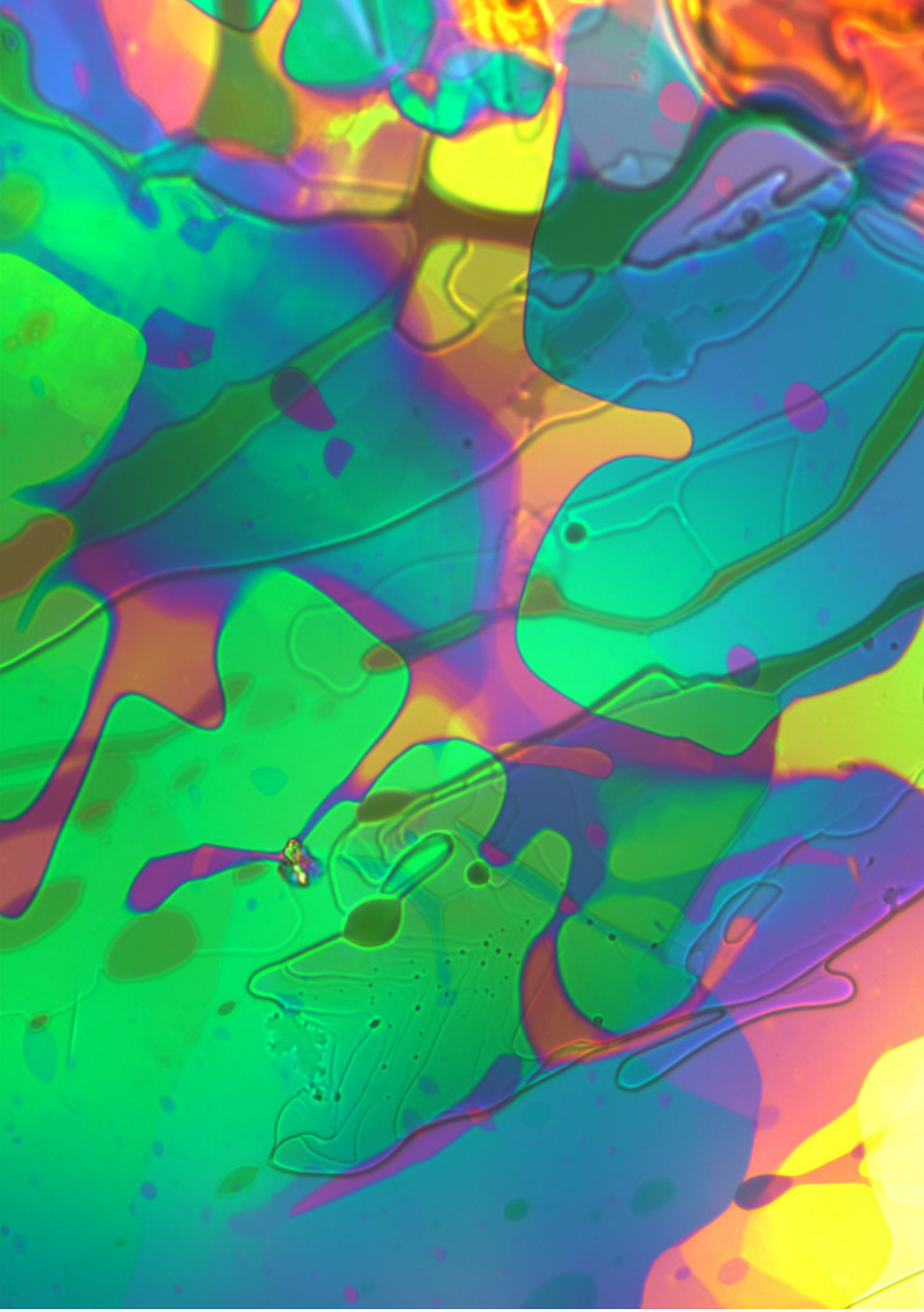

Chapter 5

Highly ordered 2D-assemblies of phase-separated block molecules for upconverted, linearly polarized emission

ABSTRACT: Materials based on the laminar ordering of self-assembled molecules have a unique potential for applications requiring efficient energy migration through densely packed chromophores. Here, we report on employing molecular assemblies of core-centered block molecules for triplet-triplet annihilation upconversion (TTA-UC) based on triplet energy migration with linearly polarized emission. By covalently attaching discrete length oligodimethylsiloxane (*o*DMS) to 9,10-diphenylanthracene (DPA), highly ordered 2D crystalline DPA sheets separated by *o*DMS layers are obtained. Transparent films of this material doped with small amounts of triplet sensitizer Pt(II) octaethylporphyrin show air-stable TTA-UC under non-coherent excitation. Upon annealing, an increase in TTA-UC up to two orders of magnitude is observed originating from both an improved molecular ordering of DPA and an increased dispersion of the sensitizer. The molecular alignment in millimeter-sized domains leads to upconverted linearly polarized emission without alignment layers. By using a novel technique, Upconversion Imaging Microscopy, the TTA-UC intensity is spatially resolved on a micrometer scale to visually demonstrate the importance of molecular dispersion of sensitizer molecules for efficient TTA-UC. The reported results are promising for anti-counterfeiting and 3D night vision applications, but also exemplify the potential of discrete oligodimethylsiloxane functionalized chromophores for highly aligned and densely packed molecular materials.

Part of this work is published in:
M. H. C. van Son, A. M. Berghuis, F. Eisenreich, B. F. M. de Waal, G. Vantomme, J. Gómez Rivas, E. W. Meijer, *Adv. Mater.* **2020**, *32*, 48, 2004775.

5.1 Introduction

Organic 2D nanomaterials have unique physical and chemical properties deviating from their bulk counterparts as a result of their reduced dimensionality. One of these properties is fast exciton diffusion through aligned and densely packed chromophores.[1–6] The highest exciton mobilities are obtained for large domains due to fewer grain boundaries and lower number of defects with respect to their polycrystalline counterparts.[7–9] By relying on fast exciton diffusion for energy transfer, aligned systems overcome the fundamental issues of slow molecular diffusion in solid-state.[10–12] Large domains of aligned chromophores are thus promising for the utilization of energy transfer processes generally studied in solution for solid-state applications. Triplet-triplet annihilation upconversion (TTA-UC) is one of these processes that benefits from efficient energy transfer for bulk applications[3,10,12,13] such as photovoltaics,[14–16] photocatalysis,[17] anti-counterfeiting,[18] and night vision[19]. In the TTA-UC process, dopant levels of sensitizer molecules absorb low-energy light and higher energy light is emitted by the annihilator chromophores (Figure 1). The required energy transfer processes for TTA-UC can only occur for certain sensitizer-annihilator pairs where all energetic requirements are met.[14,20,21] The most investigated donor-acceptor pair is Pt(II) octaethylporphyrin (PtOEP) and 9,10-diphenylanthracene (DPA) or derivatives thereof for the upconversion of green (532 nm) to blue (440 nm) light. TTA-UC has been shown in various solid-state systems such as polymers with either tethered or dispersed annihilators,[14,22,23] and organic glasses[24,25]. The difficulty with these rigid systems is the restricted diffusion of excited triplet molecules, thereby reducing the efficiency of the energy transfer.[26,27] To overcome the problem of limited diffusion, supramolecular approaches have been developed utilizing aligned chromophores for fast exciton diffusion, known as triplet energy migration-based upconversion (TEM-UC).

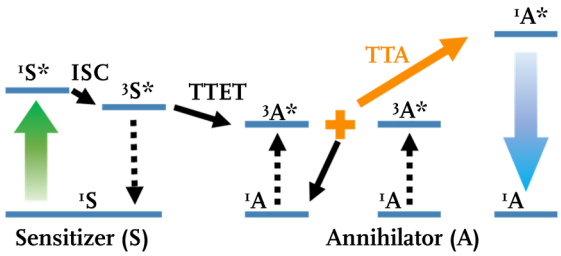

Figure 1. Jablonski diagram showing the mechanism of TTA-UC. Excitation of the sensitizer molecule (green arrow, low energy light) generates a photo-excited sensitizer singlet state $^1S^*$ that undergoes intersystem crossing (ISC) to the triplet excited state $^3S^*$. This energy is transferred via triplet-triplet energy transfer (TTET) to form annihilator triplets $^3A^*$. Two annihilator triplets undergo triplet-triplet annihilation (TTA) thereby forming a ground state annihilator singlet ^1A and a higher energy annihilator singlet $^1A^*$ that produces upconverted delayed fluorescence (blue arrow, higher energy light).

Triplet energy migration-based photon upconversion has been realized in condensed amorphous systems,[12] ordered self-assembled structures in liquid,[28–30] gels[5,31], molecular crystals[32–34] and MOFs[35] with various reviews written about this topic.[10–12] In most of these approaches, the annihilator is functionalized with side chains or ionic groups. This functionalization results in dense self-assembled structures in liquid or quasi-solid phases by exploiting solvophobic interactions, hydrogen bonding,

and electrostatic interactions. These interactions are also used to bring the sensitizer in close proximity to the annihilator for efficient Dexter-type energy transfer between both chromophoric units.[28,33,36] Furthermore, self-assembly approaches in liquids have been shown to prevent unfavorable oxygen quenching of triplet excited states.[28,30,37] A different approach for TTA-UC in solid state is achieved by doping pure acceptor DPA crystals with the donor PtOEP. In molecular crystals, triplet excitons can diffuse effectively due to the dense chromophore packing, which is promising for efficient TTA-UC. However, PtOEP tends to aggregate resulting in low triplet energy transfer efficiency to the acceptor molecules.[32,38,39] Donor aggregation could be prevented by changing the DPA chromophore structure to monophenylanthracene with added alkyl side chains and hydrogen bonding interactions.[33] Although this approach has dense chromophore packing structure and molecular dispersion of the donor, it does not fulfil the other requirements for solid state TTA-UC, namely solution processability and control over defects.[3] In addition, this is not a general approach for TTA-UC in solid state with different chromophores as the DPA structure was significantly altered to obtain molecular dispersion of the donor. Thus for solid-state upconverting systems, self-assembly of soft annihilator crystals is a promising but relatively unexplored approach that could even lead to polarized upconverted emission.[10,11,33,40,41] Until now, upconverted circularly polarized emission has been realized for chiral annihilators in solution,[42–44] or dispersed in a liquid crystalline matrix.[45] Upconverted linearly polarized emission has only been shown for aligned lanthanide crystals[18,46] and for annihilator molecules dispersed in a liquid crystalline matrix.[47] However, matrix-free upconverted linearly polarized emission in films from ordered annihilator molecules remains a challenge that, when solved, can find applications in optical storage, optical anti-counterfeiting, and 3D night vision.[18,19,46,48]

To obtain ordered morphologies such as cylinders or lamellae in films, block copolymers and liquid crystals are most often used. In polymeric systems, phase segregation dictates the feature size and morphology. Phase segregation is influenced by the composition and immiscibility of its constituents as well as (post-)processing parameters such as solvent choice or thermal annealing. Recently, we developed block molecules that combine phase segregation with crystallization in discrete molecular weight molecules for highly ordered structures in bulk through functionalization with oligodimethylsiloxane (*o*DMS).[49–56] These block molecules bridge the gap between block copolymers and liquid crystals.[54] By using "soft" *o*DMS of discrete lengths and "hard" crystalline molecular blocks, ordered lamellar structures with sub-10 nm spacings can be obtained.[53,54,56] Furthermore, functionalization with *o*DMS can result in the formation of millimeter-sized domains of ordered crystalline monolayers, which has been demonstrated with hydrazone derivatives.[56] The hydrazone block molecules could additionally be aligned, resulting in linearly polarized absorption. The high degree of long-range order, large domain size, and polarized characteristics make *o*DMS block molecules promising for upconverted linearly polarized emission.

Here, we report on the synthesis as well as molecular and photophysical characterization of the benchmark TTA-UC annihilator 9,10-diphenylanthracene (DPA) functionalized with discrete length oligodimethylsiloxane. We demonstrate air-stable TEM-UC through ordered annihilator molecules in films doped with triplet sensitizer PtOEP. Topographic mapping of the upconverted emission intensity was used to study

the effect of sensitizer aggregation. For the DPA derivative with the shortest *o*DMS chains, millimeter-sized domains with regular chromophore alignment were obtained during annealing and this block molecule is therefore studied for polarization-dependent absorption and upconverted emission. The specific TTA-UC measurement were performed in close collaboration with Matthijs Berghuis of the Applied Physics Department

5.2 Synthesis of DPA block molecules

The molecular structure and synthetic route of the 9,10-diphenylanthracene derivatives **$(Si_n)_2$DPA** functionalized with discrete oligodimethylsiloxane (*o*DMS) chains with lengths of 7, 11 or 15 repeating units are shown in Scheme 1. The side chains are attached at the periphery of the core to maintain the spectroscopic properties of unfunctionalized DPA,[40,57] as well as to allow the investigation of *o*DMS functionalization as a general approach for inducing nanoscale organization of block chromophore structures. The flexible nature of *o*DMS and the crystalline nature of DPA make these block molecules small coil-rod-coil structures of discrete length.

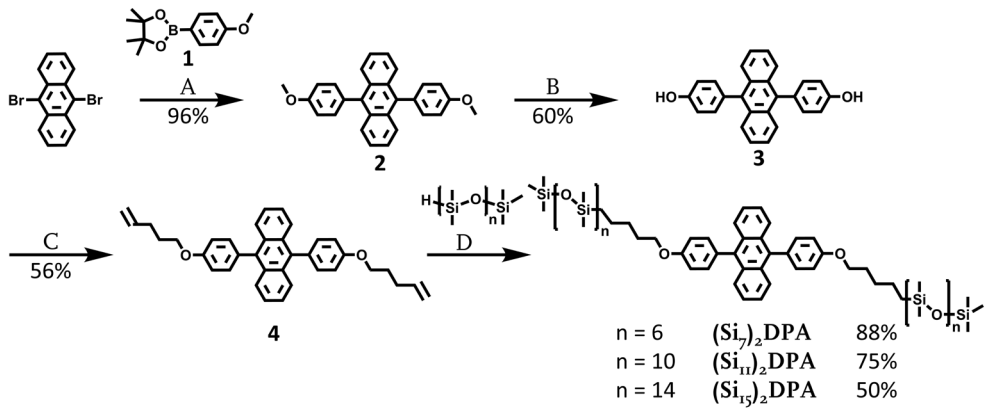

Scheme 1. Synthetic route of 9,10-difunctionalized anthracenes **$(Si_n)_2$DPA**. (A) Suzuki coupling; arylboronic ester, $Pd(PPh_3)_2Cl_2$, Na_2CO_3, DME:water (5:1), 100 °C, 16 h. (B) BBr_3, dry DCM, RT, 21 h. (C) Williamson etherification; 5-bromo-1-pentene, K_2CO_3, dry DMF, 80 °C, 18 h. (D) Terminal hydride functionalized discrete oligodimethylsiloxane,[50] Karstedt's catalyst, dry DCM, RT, 3 h.

The first step in the **$(Si_n)_2$DPA** synthesis is a Suzuki coupling to obtain 9,10-dianisylanthracene (**2**).[40] After deprotection of the methoxy groups with boron tribromide (**3**), the hydroxy groups were derivatized with a terminal alkene spacer via Williamson ether synthesis (**4**). In the last step, Karstedt's catalyst was used for the hydrosilylation of the terminal alkene with hydride-functionalized discrete *o*DMS. The liquid *o*DMS chains were synthesized by Bas de Waal using a previously reported procedure.[50] The final products were purified with recycling GPC to yield **$(Si_7)_2$DPA**, **$(Si_{11})_2$DPA**, and **$(Si_{15})_2$DPA** as light-yellow waxy compounds of which **$(Si_7)_2$DPA** crystallized over time into a brittle light-yellow solid. The purity of the block molecules was confirmed by ^{1}H-NMR, ^{13}C-NMR, and MALDI-ToF-MS.

Table 1. Thermal and morphological characterization data for **$(Si_n)_2$DPA**.

Compound	T_m [a,b] [°C]	ΔH_m [a,c] [kJ mol^{-1}]	T_c [a,b] [°C]	ΔH_c [a,c] [kJ mol^{-1}]	d_{lam} [d] [nm]
DPA	247	28	172		-
$(Si_7)_2$DPA	80 ±1	46	68 ±1	43	3.1 [e]
	−39 ±1	17	−44 ±1	15	
$(Si_{11})_2$DPA	59 ±2	29	40 ±2	35	4.3
$(Si_{15})_2$DPA	47 ±3	39	33 ±1	40	5.7

[a] Thermal transitions and enthalpies as determined by DSC from the second heating and cooling cycle with heating and cooling rates of 10 °C min^{-1}. [b] Error margins taken as the FWHM. [c] The error margin on the enthalpies is ~5%. [d] Lamellar domain spacing from SAXS data, calculated as $d_{lam} = 2\pi/q^*$. [e] An additional principal scattering peak was observed at 3.2 nm at room temperature. At −70 °C only a single lamellar structure was observed with 3.2 nm spacing.

5.3 Impact of *o*DMS length on the thermal properties and nanostructure

Differential scanning calorimetry (DSC) and polarized optical microscopy (POM) were used to investigate the thermal properties of **$(Si_n)_2$DPA**. For all block molecules, a melting transition to the isotropic phase is observed between 47 °C and 80 °C (Figure 2A) that corresponds to a loss in birefringence observed with POM. The melting point decreases upon increasing the length of the flexible *o*DMS side chains (Table 1). The melting enthalpies of about ~ 30 – 45 kJ mol^{-1} are similar to unfunctionalized DPA as well as DPA functionalized with alkyl chains and indicate crystallinity in the system.[40,58] The highest enthalpy with the sharpest transition, and thus strongest intermolecular interactions, is observed for **$(Si_7)_2$DPA**. **$(Si_7)_2$DPA** shows an additional melting and crystallization peak around −40 °C. Additional thermal transitions are also likely for the other two molecules, but these could not be resolved as the DSC could not cool below −70 °C. For all block molecules, cooling from the isotropic phase restored the birefringence in micrometer-sized domains showing the reversibility of the thermal transitions. Interestingly, upon slow cooling (1 °C min^{-1}), multiple crystalline domains with millimeter dimensions were obtained and can be observed by eye for **$(Si_7)_2$DPA** and **$(Si_{11})_2$DPA** (Figure 2B). On the contrary, faster cooling (10 °C min^{-1}) gave smaller domains due to an increased number of nucleation sites. Careful thermal treatment can thus induce regular chromophore alignment over large areas. This is more facile for shorter *o*DMS due to the higher volume fraction of crystalline DPA.

The nanoscale morphologies of the **$(Si_n)_2$DPA** after annealing were examined using medium and wide-angle X-ray scattering (MAXS and WAXS), respectively (Figure 2C). All block molecules show equally spaced reflection peaks from the principal scattering peak (q^*, $2q^*$, $3q^*$, ...) indicating long-range lamellar ordering.[59] This ordering, schematically shown in Figure 2D, is the combined result of both crystallization of the DPA core and phase separation with the amorphous *o*DMS leading to alternating layers of both molecular blocks.[51] For **$(Si_7)_2$DPA**, an additional principal scattering q' was observed without any reflection peaks. Therefore, this peak is assigned to a single layer with a slightly different core packing than the majority of the lamellae between which it is located. The observed increase in lamellar spacing, $d_{lam} = 2\pi/q^*$, from 3.2 nm to 5.7 nm for **$(Si_7)_2$DPA** and **$(Si_{15})_2$DPA**, respectively, is explained by increased volumes of

oDMS resulting in larger distances between monolayers of the crystalline DPA cores. The increase in spacing matches the reported volume of oDMS.[60] Interestingly, **$(Si_7)_2$DPA** displays pronounced spots in the 2D WAXS region indicating strong regular crystalline interactions of the DPA cores throughout the material. In the WAXS region of **$(Si_{11})_2$DPA** and **$(Si_{15})_2$DPA**, the crystalline interactions are less pronounced than for **$(Si_7)_2$DPA** due to both weaker DPA packing as evidenced by the lower enthalpies as well as an increased contribution of the amorphous halo originating from the longer oDMS chains.

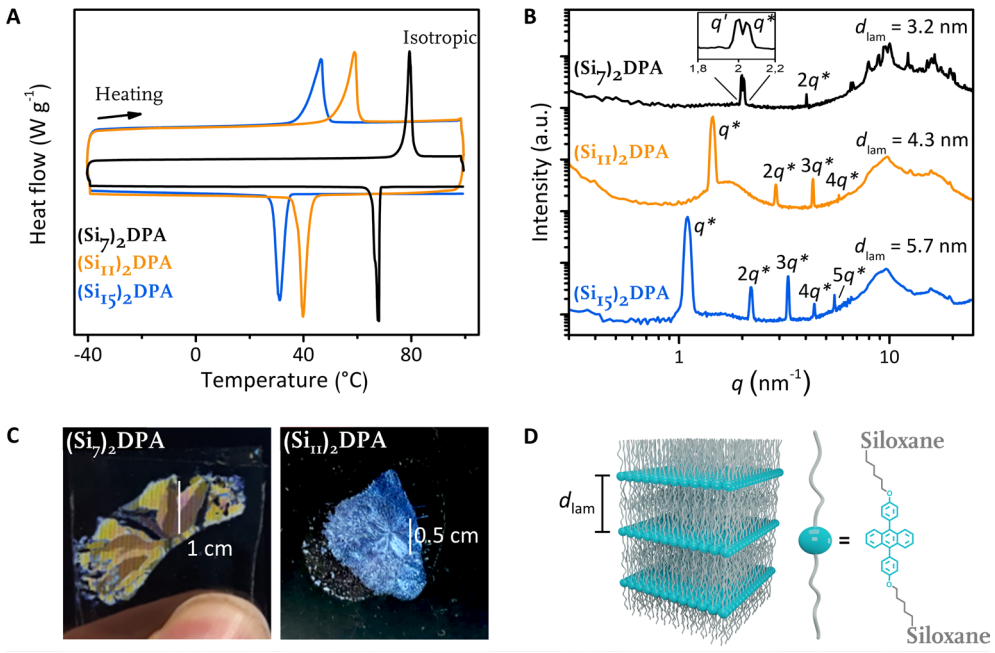

Figure 2. Characterization of **$(Si_n)_2$DPA**. (A) Differential scanning calorimetry traces of the second cycle of **$(Si_7)_2$DPA** (black), **$(Si_{11})_2$DPA** (orange), and **$(Si_{15})_2$DPA** (blue) with 10 °C min^{-1} showing melting and crystallization peaks (exothermic down). Only the thermal transitions above room temperature are shown. (B) Room temperature X-ray scattering profiles for **$(Si_7)_2$DPA** (black), **$(Si_{11})_2$DPA** (orange), and **$(Si_{15})_2$DPA** (blue) after annealing showing lamellar order. (C) Optical photographs of annealed films of **$(Si_7)_2$DPA** (left) and **$(Si_{11})_2$DPA** (right) between two crossed linear polarizers showing domains with dimensions of 10 and 5 mm respectively obtained after annealing. (D) Schematic representation of the multilayer lamellar ordering of self-assembled 2D crystalline DPA sheets (blue) separated by the discrete length side chains (gray).

5.4 Triplet-triplet annihilation upconversion with DPA block molecules

5.4.1 Energetic requirements for TTA-UC

The high order and large domains observed for **$(Si_n)_2$DPA** make these materials promising for TEM-UC if the energetic requirements for upconversion are met. The optical properties are thus studied in solution and film. In 25 µM chloroform solutions, the absorption and emission spectra are identical between the three **$(Si_n)_2$DPA** block molecules. In these spectra, the typical vibronic progression of unfunctionalized DPA is observed (Table 2, Figure 3a), albeit less pronounced and slightly red-shifted (~15 nm) in emission. The spectra obtained for the drop-cast films of **$(Si_n)_2$DPA** are comparable to the solution spectra and differ only in relative intensities of the emission peaks at ~425 nm and ~444 nm. Although excimers have been reported for unfunctionalized DPA in bulk,[61] they are not observed in the drop-cast films as confirmed by comparable monoexponential fluorescence decays in solution and film (Table 2). The absence of excimers is beneficial as they act as a loss channel for the overall upconversion efficiency.[11,62] In addition, the observed red-shifted emission increases the upconversion efficiency due to a smaller overlap with the absorption profile of PtOEP and corresponding lower reabsorption of upconverted light.[63,64] The fluorescence quantum yields in deoxygenated cyclohexane solution were determined to be 0.90, 0.95, and 0.93 for **$(Si_7)_2$DPA**, **$(Si_{11})_2$DPA** and **$(Si_{15})_2$DPA**, respectively, relative to unfunctionalized DPA (Φ_{FL} = 0.97 in cyclohexane, Table 2).[65] In thin film, slightly lower quantum yields (0.43. 0.46, and 0.49 for **$(Si_7)_2$DPA**, **$(Si_{11})_2$DPA** and **$(Si_{15})_2$DPA**, respectively) are obtained as the high concentration in condensed film leads to reabsorption of the emitted light. These spectroscopic results prove that the **$(Si_n)_2$DPA** block molecules can be used as annihilator in solution as well as in films with PtOEP as sensitizer, provided PtOEP can be dispersed in the film.[32]

Table 2. Optical characterization data for **$(Si_n)_2$DPA**.

Compound	λ_{abs} [a] [nm]	λ_{em} [a] [nm]	τ_{soln} [a,b] [ns]	τ_{film} [b] [ns]	$\tau_{film,Pt}$ [b,c] [ns]	$\Phi_{FL,soln}$ [d] [-]	$\Phi_{FL,film}$ [-]
DPA	357; 375; 396	412 432	-	-	-	0.97[65]	-
$(Si_7)_2$DPA	360; 378; 398	429	4.7	4.3	6.6	0.90	0.43
$(Si_{11})_2$DPA	360; 379; 399	430	4.8	5.6	6	0.95	0.46
$(Si_{15})_2$DPA	360; 378; 399	428	4.9	5.6	6.4	0.93	0.49

[a] Peak values recorded in 25 µM chloroform solution. [b] Fluorescence lifetimes at 440 nm under 400 nm excitation fitted to a single exponential decay. [c] Film doped with PtOEP (PtOEP:annihilator = 1:300). [d] Recorded in cyclohexane solution.

5.4.2 TTA-UC in film

To investigate triplet-triplet annihilation upconversion in films, chloroform solutions of 1 mg **$(Si_n)_2$DPA** with ~3 mol% PtOEP were deoxygenated by freeze-pump-thaw and reduced from 1 mL to 0.1 mL before drop-casting in a glovebox on clean glass slides. After overnight evaporation of the solvent, the films were laminated with a second glass slide and sealed with UV-curing glue. Sealing is required since under ambient conditions the singlet oxygen present through triplet sensitization of oxygen with PtOEP can react to form non-emissive oxidized DPA cores. The laminated films were transparent even at 4.6 µm thickness with a very light pink color due to the presence of PtOEP. Transparency indicates only a minor contribution of scattering to the overall loss of the TTA-UC efficiency. Upon 532 nm laser excitation of the films, upconverted photoluminescence (UCPL) was clearly visible by eye as blue emission (Figure 3B). The emission spectra under 532 nm excitation show the UCPL with maxima at 422 nm for both **$(Si_{11})_2$DPA** and **$(Si_{15})_2$DPA** and at 444 nm for **$(Si_7)_2$DPA**, identical to the spectra obtained for the doped **$(Si_n)_2$DPA** films under direct excitation of the DPA core with 350 nm light (Figure 3B). Residual PtOEP phosphorescence is observed even with low donor concentrations (PtOEP:annihilator = 1:10.000), indicating that the energy transfer from donor to annihilator is not complete. Interestingly, the upconversion reported here is obtained with a non-coherent light source which is paramount for practical applications in photovoltaics.[66] Although non-coherent excitation has been shown for diffusion-based TTA-UC in flexible polymers,[14,22,23,67] this is the first time that non-coherent excitation is reported for TEM-UC (*vide infra*).

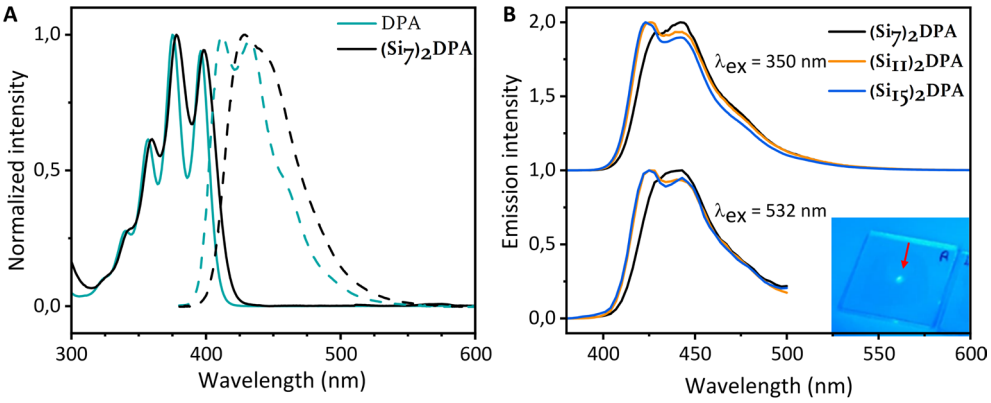

Figure 3. Optical spectroscopy analysis. (A) Absorption (full line) and emission (dotted line) spectra in 25 µM $CHCl_3$ solutions of unfunctionalized DPA (green) and **$(Si_7)_2$DPA** (black). (B) Fluorescence spectra of doped films (PtOEP:annihilator = 1:300) of **$(Si_7)_2$DPA** (black), **$(Si_{11})_2$DPA** (orange), and **$(Si_{15})_2$DPA** (blue) under direct excitation (λ_{ex} = 350 nm, top) and under upconversion conditions through indirect excitation (λ_{ex} = 532 nm, bottom) using a non-coherent light source. Inset shows a photographic image of **$(Si_7)_2$DPA** (PtOEP:annihilator = 1:300) under 532 nm laser irradiation with a 500 nm lowpass filter to remove reflected green light. Upconverted photoluminescence (UCPL) is observed by naked eye as a blue spot, here indicated with a red arrow.

5.4.3 Sensitizer aggregation

Before analyzing whether the upconversion is based on diffusion or triplet energy migration, the aggregation state of the PtOEP sensitizer is examined by absorption measurements and optical microscopy. Aggregated PtOEP reduces the efficiency of the triplet energy transfer processes and should thus be minimized.[32] As comparable results were obtained for the three block molecules, only the results of **$(Si_{11})_2$DPA** are shown in Figure 4. The absorption spectrum of the drop-cast film displays a broad peak ranging from 530-560 nm with contributions of both molecularly dispersed PtOEP at 536 nm and aggregated PtOEP at 552 nm (blue line in Figure 4A).[33] The red-shifted Q-band absorption of aggregated PtOEP originates from the intermolecular interactions in the aggregate.[3] Aggregated PtOEP is observed by optical microscopy for various ratios PtOEP:annihilator (1:300, 1:600, 1:1000) and likely occurs during the drop-casting process as the concentration increases during the overnight solvent evaporation.[34,68] Optimization of the PtOEP concentration is not investigated for this study. After annealing of the films, analysis by optical microscopy reveals two distinct

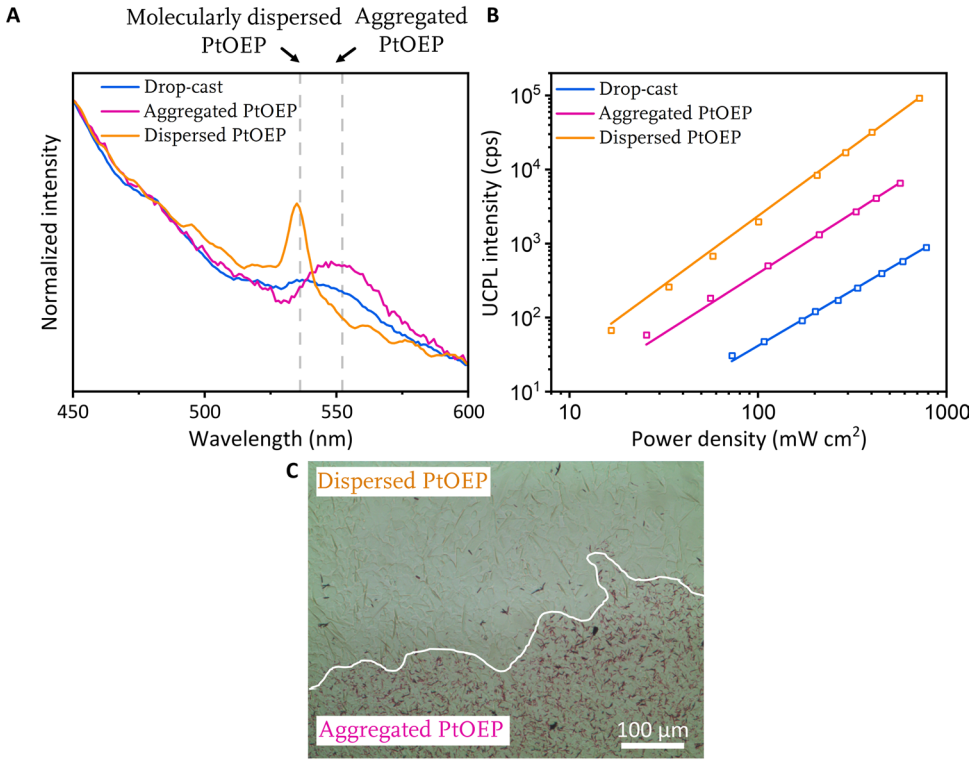

Figure 4. PtOEP aggregation correlated with UCPL intensity of a **$(Si_{11})_2$DPA** film (PtOEP:annihilator = 1:300). (A) Normalized absorption spectra, (B) optical microscopy image after annealing showing the boundary (red line) of regions with mostly dispersed PtOEP and mostly aggregated PtOEP. The PtOEP aggregates are observed as pink clusters and are mainly located at the bottom of the image. (C) power density dependence of UCPL intensity (laser excitation, λ_{ex} = 532 nm). The blue line indicates the results before annealing and the pink and orange line after annealing. The pink line indicates regions with a large fraction of the PtOEP aggregated, while the orange line shows the results from regions with molecularly dispersed PtOEP. The PL intensity is integrated up to 500 nm.

regions of which the boundary is indicated by a white line (Figure 4C). In the lower region, aggregated PtOEP is present as pink clusters while these aggregates are mainly absent in the upper region. The assignment of the pink solid as aggregated PtOEP is confirmed by significant absorption at 552 nm in this region (pink line in Figure 4A). The upper region, where pink aggregates are mostly absent, absorbs only around 536 nm indicating molecularly dispersed PtOEP (orange line in Figure 4A). Annealing can thus increase the molecular dispersion of PtOEP, although in some regions the aggregates remain.

With the aim of improving the donor dispersion, PtOEP was replaced by a porphyrin functionalized with *o*DMS synthesized by Elisabeth Weyandt (Figure 5). Upconverted emission was observed by eye for both unannealed and annealed films. However, within two days the UCPL was not visible anymore, while repeating the annealing step resulted again in a UCPL active film. This is attributed to demixing of the sensitizer and annihilator cores facilitated by the increased miscibility of the sensitizer in the *o*DMS matrix. As a result of the separation between sensitizer and annihilator, efficient Dexter-type energy transfer is hindered due to the increased distance in the demixed state. As such, triplet sensitization of the DPA cores is not possible. The observed initial UCPL is therefore likely the result of kinetic trapping of the sensitizer close to the annihilator core during the cooling, while the UCPL in the molten, unordered state is likely diffusion based. Thus, the immiscibility of PtOEP with *o*DMS is beneficial as the phase separation between these components brings the sensitizers close to the DPA cores resulting in a stable upconverting system. The rest of the upconversion studies are therefore performed with PtOEP.

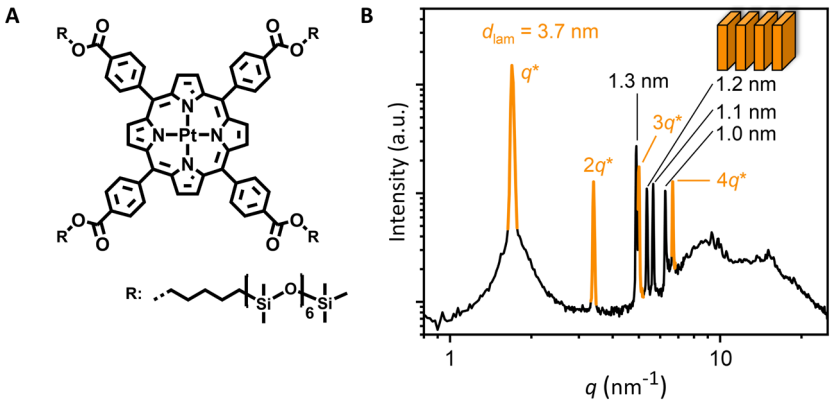

Figure 5. (A) Molecular structure of the studied platinum porphyrin with four pendant *o*DMS chains. (B) 1-D scattering transmission data of the molecule showing a lamellar ordering (orange) and peaks corresponding to the molecular dimensions of the aromatic core in a crystalline packing (1.3 – 1.0 nm).

Additional information on the relation between PtOEP aggregation and UCPL intensity was obtained from spatially resolving the UCPL by correlating optical microscopy (OM) with Upconversion Imaging Microscopy (UCIM) (Figure 6). By using UCIM, the UCPL intensity is spatially resolved with micrometer resolution in a region of 1.25 x 1.25 mm of doped **$(Si_7)_2$DPA** film, containing both aggregated and molecularly dispersed PtOEP. This novel technique gives a visual correlation between PtOEP aggregation and UCPL intensity with a magnification of two orders of magnitude higher than previously reported for a 0.4 × 0.5 mm² single crystal of DPA doped with PtOEP.[32] In the OM and UCIM images of Figure 6, red and white lines, respectively, are drawn to indicate the grain boundary of the two crystalline regions identified by POM (Figure 6C). Upon superposition of the OM and UCIM images by visual comparison, a clear distinction can be made between both regions. The highest average UCPL intensity is obtained on the right side of the grain boundary where PtOEP is mostly dispersed. On the contrary, the average UCPL intensity on the left side of the grain boundary is lower due to the aggregation of PtOEP. This aggregation is visible in the OM image as dark aggregates and corresponds to regions in the UCIM image with a complete absence of UCPL (dark blue color). The results of the UCIM measurements show visually that even micrometer sized PtOEP aggregates are detrimental for UCPL. Interestingly, also an absence of UCPL is observed in some regions where aggregation in the OM image is not visible. These features may be as small as the pixel size of the UCIM image (10 x 10 μm²), which has similar dimensions as the excitation laser beam. The absence of UCPL from these small features may be the result of inhomogeneous PtOEP dispersion or defects in the DPA crystal lattice and illustrates the complexity of obtaining homogeneous upconverting solid materials.

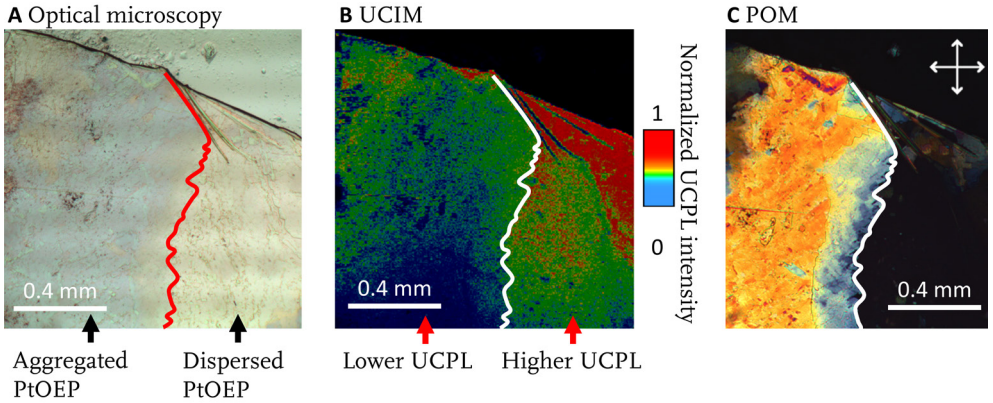

Figure 6. Correlation of the effect of PtOEP aggregation on the UCPL intensity. (A) Optical microscopy, (B) Upconversion Imaging Microscopy (UCIM), (C) Polarized Optical Microscopy images of an annealed doped **$(Si_7)_2$DPA** film showing the grain boundary of different crystalline regions with mostly aggregated PtOEP (left region) and mostly molecularly dispersed PtOEP (right region). The grain boundary is indicated by a red or white line in the OM and UCIM image, respectively. The UCIM image shows the UCPL intensity under 532 nm laser irradiation with a 500 nm short-pass filter. In the UCIM image blue regions correspond to low UCPL (<33% of maximum UCPL) while red regions correspond to high UCPL (>50% of maximum UCPL). Aggregated PtOEP is visible as dark spots in the optical microscopy image and corresponds to the dark blue regions in the UCIM image.

Table 3. Fitted slope values (b, fitted with $y = ax^b$) of the UCPL intensity dependency on excitation energy.

Slope values of excitation energy versus UCPL intensity	Dispersed PtOEP	Aggregated PtOEP	Drop-cast
$(Si_7)_2$DPA	1.9	1.5	2.3
$(Si_{11})_2$DPA	1.9	1.6	1.5
$(Si_{15})_2$DPA	1.4	1.5	1.4

5.4.4 Distinguishing between molecular diffusion and triplet-energy migration based TTA-UC

By measuring the dependency of the excitation energy on the maximum UCPL, more information on the upconversion process is obtained. In all measurements, a linear correlation was found between the UCPL intensity and excitation energy, with slopes between 1.4 – 2.2 (Figure 4B, Table 3). These slopes indicate that besides triplet-triplet annihilation and upconverted emission, other deactivation channels are also present for the annihilator excited states.[27,36] For the annealed films (pink line) up to 10-fold higher UCPL intensities are found compared with the drop-cast films (blue line). This is attributed to the increased chromophore alignment in the annealed films through which triplet-energy migration can occur more efficiently, proving TEM-UC in the studied system. TEM-UC is additionally shown by shorter upconverted emission lifetimes after annealing (on average 42 µs before, and 33 µs after annealing) as the enhanced triplet energy migration results in a higher probability for triplet-triplet annihilation. Additionally, ~20% shorter upconverted emission lifetimes are observed with higher excitation energies for the unannealed films of **$(Si_{11})_2$DPA** and **$(Si_{15})_2$DPA**. At higher excitation energy, more triplets are formed and therefore annihilation can occur more rapidly. The risetime of the UCPL intensity could be observed for the annealed film of **$(Si_7)_2$DPA** and maximum UCPL signal was measured after 12 µs. As discussed in the previous paragraph, besides inducing chromophore alignment, annealing leads to an increase in PtOEP dispersion in some regions (orange line, Figure 4). The combination of increased chromophore alignment and better PtOEP dispersion leads to a remarkable 50 to 100-fold increase in UCPL intensity for **$(Si_{11})_2$DPA** when compared with the drop-cast film.

5.4.5 Oxygen dependence

Air-stability of the UCPL is expected for annealed films of **$(Si_n)_2$DPA** due to its dense chromophore packing, which has been shown in liquids to prevent oxygen quenching.[10,28–30,37] Time-dependent UCPL measurements were thus performed for drop-cast and annealed films between two glass plates of **$(Si_7)_2$DPA** prepared in air without prior deoxygenation of the solvent (Figure 7). For the annealed film, a constant UCPL intensity was observed over the studied time-range. In contrast, the UCPL intensity of the drop-cast film showed a gradual decrease of ~20 – 40% in the first 10 to 30 minutes attributed to the reaction of residual singlet oxygen with the DPA cores as confirmed by ^{1}H-NMR, and MALDI-ToF-MS.[69] After this initial decrease, the UCPL intensity remained constant for over a week. Measurements of the same films after two months showed a complete loss of upconverted emission while oxygen-free sealed films were stable for more than a year. These results indicate that molecular self-assembly is also an effective approach in condensed systems to minimize oxygen-related problems.

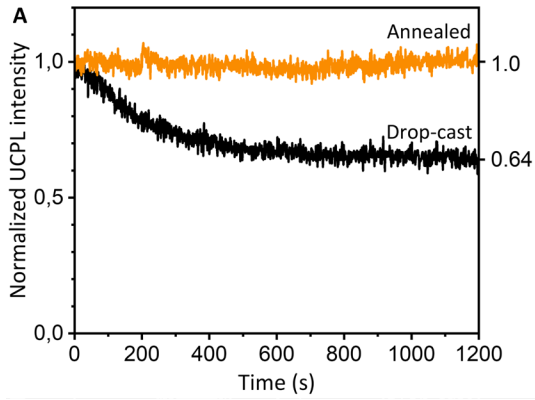

Figure 7. Time dependence of the UCPL intensity at 440 nm of **$(Si_7)_2$DPA** films (PtOEP:annihilator = 1:300) drop-cast in air without prior deoxygenation (non-coherent excitation, λ_{ex} = 532 nm). After 5 days in air the films were laminated, but not sealed on all sides to allow continuous exposure to air. The drop-cast film (black line) shows a gradual decrease in the initial 10 minutes of ~35%, while the annealed film (orange line) shows constant UCPL intensity over time.

5.4.6 Linearly polarized UCPL

During the annealing of **$(Si_7)_2$DPA**, domain growth in two perpendicular directions was observed by polarized optical microscopy (Figure 8A) and resulted in millimeter-sized domains. Although perpendicular alignment of the chromophores is observed in some polymorphs of unsubstituted DPA, atomic resolution could not be obtained for **$(Si_n)_2$DPA** and therefore no comparison with the DPA polymorphs can and will be made.[70,71] The long-range ordering of the **$(Si_7)_2$DPA** crystals was confirmed by measuring the absorption intensity at 380 nm for one of the ~20 mm² single domains shown in Figure 2C while varying the orientation of the incoming linearly polarized light (Figure 8B). The sharpness of the peak at ~160 degrees indicates a very high degree of ordering over a large surface with minimal defects. The degree of polarization (ρ = $(I_{max} - I_{min})/(I_{max} + I_{min})$ is calculated to have a lower limit of 0.41 as the maximum absorption could not be measured truthfully due to machine limitations. The maximum and minimum absorption intensities have a periodicity of 90 degrees as a result of chromophore alignment along crystallographic axes.[72] This confirms that the perpendicular alignment observed by POM occurs throughout the film. As a result of this perpendicular alignment, both the emission under direct excitation as well as the UCPL emission are linearly polarized (Figure 8C, D). The degree of polarization (ρ = $(I_{max} - I_{min})/(I_{max} + I_{min})$ under direct excitation was calculated to be 0.89, while a significantly lower value of 0.09 is found under indirect excitation. This discrepancy is likely related to the dispersion of PtOEP. Under direct excitation, the majority of the aligned DPA cores emit. In contrast, when only the PtOEP is excited, emission occurs only in the regions where PtOEP is present, and therefore only probes a smaller region of the DPA molecules. PtOEP additionally may act as a very local defect in the lamellar packing, thereby lowering the degree of polarization. Although a higher degree of polarization is required for practical applications, the reported approach based on organic

coil-rod-coil block molecules serves as a first step for rare earth metal-free linearly polarized UCPL without the use of alignment layers. Linearly polarized UCPL may find applications in solar-cells or optical anti-counterfeiting. Additionally, when extended to upconversion of NIR light, linear polarized UCPL can be used for 3D night vision.[19,48]

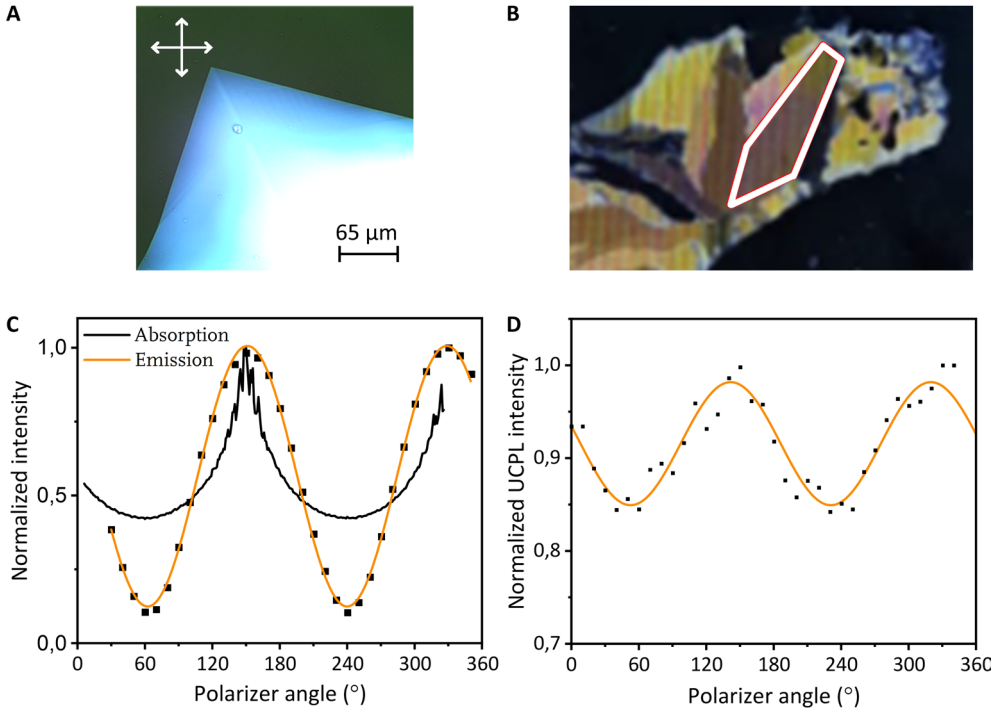

Figure 8. Linear polarized properties resulting from perpendicular domain growth directions. (A) Polarized optical microscopy image of **$(Si_7)_2$DPA** during slow cooling from the melt (0.5 °C min^{-1}) showing a preferential ±90° angle in domain growth directions. Scale bar indicates 65 µm. In (B) the 1 cm long domain that is used for the polarization experiments is indicated with white lines. Linear polarization dependent (C) absorption at 380 nm (black line) and direct emission of 440 nm with λ_{ex} = 375 nm and (D) upconverted photoluminescence of 440 nm with λ_{ex} = 532 nm for the ~20 mm^2 domain of **$(Si_7)_2$DPA** (PtOEP:annihilator = 1:300) shown in (B).

5.5 Conclusion

In conclusion, 9,10-diphenylanthracene has been functionalized with discrete length oligodimethylsiloxane (*o*DMS) to yield the three derivatives **$(Si_7)_2$DPA**, **$(Si_{11})_2$DPA** and **$(Si_{15})_2$DPA** while retaining the required energy levels for TTA-UC in solution and bulk. The bulk morphology of these discrete core-centered block molecules consists of 2D monolayers of crystalline DPA chromophores separated by layers of amorphous *o*DMS with spacings of 3-6 nm. Transparent films were prepared by drop-casting materials doped with ~3 mol% PtOEP that show air-stable upconverted light emission (UCPL) of ~440 nm under non-coherent excitation (λ_{ex} = 532 nm). Annealing of these films leads to an increase in chromophore alignment and the corresponding increase in UCPL intensities proves that the reported TTA-UC relies on triplet energy migration through ordered chromophores. Annealing additionally induces better molecular dispersion of PtOEP that, combined with the increase in chromophore alignment, leads up to a 100-fold increase in UCPL intensity when compared to the unannealed film. For films of **$(Si_7)_2$DPA**, millimeter-sized domains with regular alignment are obtained from which linearly polarized absorption and UCPL emission were observed. This is the first report of matrix-free polarized upconverted emission in organic films. The spatial dependence of the upconversion intensity as shown by Upconversion Imaging Microscopy is a crucial factor to consider in upconversion research as displacements of only a few micrometers already can give different UCPL intensities. The work presented here highlights the potential of nanophase separation with discrete length *o*DMS as a general approach for optoelectronic applications where dense chromophore packing and alignment are required in bulk, such as singlet fission[73,74] or nanoelectronics.[4,7,75]

5.6 Experimental section

5.6.1 Materials and methods

All chemicals were purchased from commercial sources and used as received. The K_2CO_3 that was used was in anhydrous powder form and of analytical grade. For the hydrosilylation reactions, the following preparation of Karstedt's catalyst from Sigma Aldrich is used; Platinum(0)-1,3-divinyl-1,1,3,3-tetramethyldisiloxane complex solution in xylene, Pt ~2 %. The discrete length monohydride oligodimethylsiloxanes with lengths 7, 11, and 15 (**HSi_7**, **HSi_{11}** and **HSi_{15}**, respectively) were synthesized according to literature procedure by Bas de Waal.[50] Elisabeth Weyandt synthesized the *o*DMS functionalized porphyrin. All solvents were purchased from Biosolve and dry solvents were obtained using MBraun solvent purification system (MB SPS-800). The glassware for all reactions carried out under argon was flame-dried to remove residual water. Analytical thin-layer chromatography (TLC) was performed on 60-F_{254} silica gel plates from Merck and visualized with a 254 nm ultraviolet lamp. Automated column chromatography was conducted on a Biotage Isolera One system using Biotage KP-SIL Silica Flash or Biotage Sfär cartridges. The methods used for nuclear magnetic resonance (NMR), matrix assisted laser desorption/ionization time of flight mass spectroscopy (MALDI-ToF-MS), differential scanning calorimetry (DSC) and bulk small angle X-ray scattering (SAXS) are described in Chapter 2. **Recycling GPC** was performed in chloroform solution with a Jaigel-2H column from JAI using a Shimadzu LC-10AD VP liquid chromatograph. A Shimadzu SPD-10AV VP was used as UV-VIS detector in conjunction with Dax 9.0 software from Van Mierlo Software Consultancy. **Optical microscopy** samples were placed between two glass substrates and imaged using a Nikon Xfinity1 Lumenera microscope with 16x and 25x magnification. The same instrument was used for **polarized optical microscopy** (POM) with two crossed linear polarizers before and after the sample. The samples were heated using a Linkam heating stage mounted in the POM set-up. **Unpolarized absorption** has been measured on a PerkinElmer Lambda 1050 UV-VIS spectrophotometer with a PerkinElmer 3D WB Detector module (λ = 300 – 800 nm; $\Delta\lambda$ = 1 nm). For **linear polarized absorption**, a PerkinElmer Lambda 750 spectrometer was used with a rotatable polarizer in front of the beam. A black cardboard mask was used to only measure a single domain. **Emission** spectra were recorded on a luminescence spectrometer LS50B from PerkinElmer using a XBO xenon short arc

discharge lamp (≤450W) from Osram (non-coherent excitation with λ_{ex} = 350 nm or 532 nm). Appropriate bandpass filters were used to remove scattered light. **Polarized emission** was measured with a 100 mW 532nm continuous-wave laser from Laser2000 with appropriate neutral density filters to prevent bleaching of the sample. The measurements were conducted with a Princeton Instruments SP2300 spectrometer and a Princeton Instruments ProEN:512 CCD camera. A 500 nm premium short pass filter from ThorLabs was used to remove scattered incident light. A rotatable Prinz polarizing filter suitable for 400 – 700 nm was placed between the sample and the detector. The angle was varied manually. Bleaching was not observed during the measurement as for the same polarization the same intensity was measured at the start, middle, and end of the measurement series. **Time-resolved fluorescence experiments under direct excitation** were carried out with a 400 nm excitation pulse obtained from a Picoquant LDH C400 laser, operating at a repetition rate of 1 MHz. The fluorescence light, collected in a backward scattering geometry, was dispersed by a 0.34 m double monochromator, allowing for a spectral resolution of 1 nm. Time-resolved emission spectra were recorded with the time-correlated single-photon counting technique in reversed mode using a microchannel plate photomultiplier (Hamamatsu R3809u-51) and a time-to-amplitude converter. The width of the instrument response function amounts to 60 ps FWHM. Using a single channel analyzer (EG&G), fluorescence spectra can be recorded within a variable, narrow time window after the excitation pulse. The maximum photon count rate was kept low (< 10^8 s^{-1}) to prevent distortion of the spectra due to pulse pile-up effects. Fluorescence lifetimes were determined by fitting the initial decay with a monoexponential decay. **Time-resolved fluorescence experiments under 532 nm excitation** were carried out with a 800 nm laser from a 5 KHz amplified laser system (Astrella, Coherent) that was converted to 532 nm in an OPA Topas-C optical parametric oscillator from Light Converison. The 532 nm laser was focused on the sample to a spot size with a diameter of ~50 µm. Upconverted emission was collected by an objective lens and residual laser light was removed by a 500 nm short pass filter (FESH500, Thorlabs). The signal was detected by a PDA100A Si amplified photodiode from Thorlabs that was read out at a rate of $2*10^6$ samples/second by a USB-6366 data acquisition card from National Instruments. Each measurement integrated the signal of $2*10^5$ laser pulses. **Time-dependent air-stability of UCPL** at 440 nm is recorded on a Luminescence Spectrometer LS50B from PerkinElmer (non-coherent excitation with λ_{ex} = 532 nm). The slid width of the detector was adjusted to obtain similar initial UCPL intensities. **Photoluminescence quantum yield in deoxygenated cyclohexane solutions** was measured by relative means with 9,10-diphenylanthracene (24 µM in deoxygenated cyclohexane, Φ_{PL} = 0.97[65]) as the fluorescence standard. Deoxygenation was performed by freeze-pump-thaw (3 cycles). The emission spectra were integrated from 375 - 600 nm (λ_{ex} = 355 nm, 0.1 nm excitation slid width). **Photoluminescence quantum yield in thin film** was determined using the absolute method with a RT-060-SF integrating sphere from Labsphere under 375nm excitation using a Picoquant laser (LDH series) at a power of ~1 mW.[76] The scattered fluorescence and laser light were collected through an optic fiber by a USBS2000+ spectrometer from Ocean Optics. The spectrometer was calibrated with a HL-2000-FHSA calibration lamp from Mikropack. **Upconversion Imaging Microscopy** (UCIM) was measured on a Nikon Ti-E inverted microscope with a C2 confocal scanning head. A 100 mW continuous wave laser from Laser2000 (λ_{ex} = 532 nm) was sent through a fiber coupled to a time-correlated single-photon counting detector from TimeHarp 300 Picoquant, triggered at 80 MHz. The software for this measurement was SymPhoTime 64 from PicoQuant. A 500 nm premium short pass filter from ThorLabs was used to remove scattered incident light. **Laser intensity dependent TTA-UC emission** was measured using the same set-up as for UCIM with a series of variable neutral density filters replacing the optical fiber to modify the incoming excitation intensity. The UCPL intensity was integrated up to 500 nm. The laser spot size was taken as the area in which the laser illumination was higher than the maximum intensity times $1/e^2$. The measurements were performed on the area with the highest UCPL intensity as determined by first scanning the UCPL intensity of the entire sample. **Film preparation** A solution of ~1 mg **$(Si_7)_2$DPA**, **$(Si_{11})_2$DPA**, or **$(Si_{15})_2$DPA** with corresponding amounts of PtOEP (0.3 mol%) was prepared from a chloroform stock solution in 1 mL spectroscopic grade chloroform. The solutions were deoxygenated by freeze-pump-thaw (3-5 cycles) until upconverted emission was observed visually as blue light emission upon radiation with a 532 nm laser. The deoxygenated solution was reduced in vacuo to ~0.1 mL and transferred to an argon-filled glovebox. The concentrated solution was drop-cast under argon atmosphere on clean glass slides. After overnight evaporation of the solvent, another glass slide was laminated on top of the sample with UV-curing glue (Norland UVS91) on the edges. The glass slides were clamped in place with paper clamps. Aluminum foil was used as a mask for the sample during the UV-curing of the glue (20 minutes per side). **Film annealing** of the samples was performed with the POM set-up reported above. All samples were heated to their isotropic phase (20 °C above their melting point, isothermal for 10 minutes) and subsequently cooled with 5 °C min^{-1} to their melting point (80 °C, 59 °C, and 47 °C for **$(Si_7)_2$DPA**, **$(Si_{11})_2$DPA** or **$(Si_{15})_2$DPA**, respectively). The samples were further cooled with 2 °C min^{-1} until the first birefringence was observed. The cooling rate was then lowered to 1 °C min^{-1} and the samples cooled to 73 °C, 52 °C, and 40 °C for **$(Si_7)_2$DPA**,

$(Si_{11})_2$DPA or **$(Si_{15})_2$DPA**, respectively. The samples were held at this temperature for 5 minutes and were then cooled to room temperature with 5 °C min^{-1}.

5.6.3 Synthesis

The NMR spectra of compounds **1**, **2** and **3** (Scheme 1) matched with their reported values.[40,77]

2-(4-methoxyphenyl)-4,4,5,5-tetramethyl-1,3,2-dioxaborolane (1)
4-Bromoanisole (2.7 ml, 22 mmol, 1 eq.) was dissolved in dry THF (100 mL) and cooled to –78 °C before dropwise adding *n*-BuLi (2.5 M in hexanes, 11 mL, 28 mmol, 1.3 eq.). After stirring at –78 °C for 30 min, 2-isopropoxy-4,4,5,5-tetramethyl-1,3,2-dioxaborolane (6 ml, 30 mmol, 1.4 eq.) was added. After an additional 30 min the cooling bath was removed and the reaction was let to warm up to room temperature for 45 min after which MeOH (20 mL) was added to quench excess *n*-BuLi. The reaction mixture was diluted with DI water and the THF and MeOH were evaporated off using a rotary evaporator. The product was then extracted with ETOAc. The organic layer was dried with $MgSO_4$ and reduced in vacuo to 4.6 g slightly yellow oil. This was purified by column chromatography (Liquid loading from heptane, eluent heptane/EtOAc 100/0 – 80/20) to give 3.5 g colorless oil (70%).
^{1}H NMR (400 MHz, $CDCl_3$): δ 7.75 (d, J = 8.6 Hz, 2H), 6.59 (d, J = 8.6 Hz, 2H), 3.82 (s, 3H), 1.32 (s, 12H) ppm.

9,10-bis(4-methoxyphenyl)anthracene (2)
In a flame-dried Schlenk tube was charged 9,10-dibromoanthracene (501 mg, 1.49 mmol, 1 eq.), 4-methoxyphenyl boronic acid pinacol ester **1** (907 mg, 3.87 mmol, 2.6 eq.), Na_2CO_3 (326 mg, 3.08 mmol, 2.1 eq.) and $Pd(PPh_3)_2Cl_2$ (78 mg, 7mol%) under argon. After evacuation-and-backfill with argon (3 cycles), 1,2-dimethoxyethane (7.5 ml) and DI water (1.5 ml) was added. The reaction mixture was deoxygenated by freeze-pump-thaw (4 cycles) and subsequently heated to 100 °C for 16 h after which NMR showed no anthracene starting material. The reaction mixture was let to cool down to RT, diluted with DI water, and vacuum filtered. The dark green solids were purified by recrystallization from $CHCl_3$ yielding the product as a light green solid (560 mg, 96%).
^{1}H NMR (400 MHz, $CDCl_3$): δ 7.76 – 7.72 (m, 4H), 7.39 (m, 4H), 7.35 – 7.31 (m, 4H), 7.14 (m, 4H), 3.97 (s, 6H) ppm.

9,10-bis(4-hydroxyphenyl)anthracene (3)
9,10-Bis(4-methoxyphenyl)anthracene **2** (310 mg, 0.77 mmol, 1 eq.) was charged in a round-bottom flask, evacuated and backfilled with argon before being dissolved in 12 ml of dry DCM. At 0°C BBr_3 (7ml, 1M in DCM, 7 mmol, 9 eq.) was added dropwise, turning the dark green solution from deep red to dark blue. The reaction mixture was let to warm up to room temperature. After 21h the reaction was dark green and a suspension had formed. To quench the BBr_3 isopropanol was added slowly, then ethanol and lastly water turning the solution light red. Extraction was performed with water and ethyl acetate. After drying with $MgSO_4$ the organic phase was reduced in vacuo to yield the product as as light green solids that became light yellow over time (177 mg, 60%).
^{1}H NMR (400 MHz, $CDCl_3$): δ 7.76 – 7.72 (m, 4H), 7.36 – 7.31 (m, 8H), 7.13 (m, 4H), 4.89 (s, 2H) ppm.

9,10-bis(4-(pent-4-en-1-yloxy)phenyl)anthracene (4)
A solution of 9,10-bis(4-hydroxyphenyl)anthracene **3** (175 mg, 0.48 mmol, 1 eq.), K_2CO_3 (186 mg, 1.34 mmol, 2.8 eq.) and 5-bromopent-1-ene (0.23 ml, 2 mmol, 4.2 eq.) in dry DMF (12 ml) was heated at 80 °C under argon atmosphere. After 18h the mixture was cooled to RT. Addition of water resulted in a precipitate that was vacuum filtered to give 136 mg of the final compound as light yellow solid (56%, m.p. = 167.7 °C, ΔH_m = 23.6 kJ mol^{-1}). ^{1}H NMR (400 MHz, $CDCl_3$): δ 7.76 – 7.72 (m, 4H), 7.40 – 7.30 (m, 8H), 7.13 (m, 4H), 6.00 – 5.86 (m, 2H), 5.18 – 5.02 (m, 4H), 4.13 (t, J = 6.4 Hz, 4H), 2.34 (q, J = 7.1 Hz, 4H), 2.00 (quint, J = 6.9 Hz, 4H) ppm.
^{13}C NMR (100 MHz, $CDCl_3$): δ 158.86, 138.26, 137.13, 132.72, 131.38, 130.61, 127.41, 125.19, 115.59, 114.76, 67.86, 30.59, 28.95 ppm.

General procedure for hydrosilylation reactions
In a flame dried Schlenk tube, **4** (1 eq.) and oligodimethylsiloxane with a terminal hydride (1.9-2.8 eq.) were charged. The compounds are suspended in dry DCM after which 1-2 drops Karstedt's catalyst were added under argon. After 15 minutes the suspensions became a transparent liquid mixture. After complete conversion (indicated by the absence of the *H*-Si hydrogen in ^{1}H-NMR at 4.70 ppm in $CDCl_3$, or by the absence of alkene peaks at 6.00-5.86 and 5.18-5.02 ppm) the mixture was diluted with DCM and reduced in vacuo to obtain waxes. Excess oligodimethylsiloxane was removed by column chromatography (Liquid loading from heptane, eluent heptane/DCM 100/0 – 0/100). The products were further purified with recycle GPC (chloroform) to remove all byproducts.

$(Si_7)_2$DPA
9,10-bis(4-(pent-4-en-1-yloxy)phenyl)anthracene (44.7 mg, 0.09 mmol, 1 eq.), **HSi_7** (131 mg, 0.25 mmol, 2.8 eq.), dry DCM (3.5 ml), Karstedt's catalyst (1 drop). After recycle GPC, the final product was obtained as a yellowish wax that crystallized into a brittle solid (92 mg, 67%).
^{1}H NMR (400 MHz, $CDCl_3$): δ 7.79 – 7.75 (m, 4H), 7.41 – 7.37 (m, 4H), 7.36 – 7.32 (m, 4H), 7.17 – 7.12 (m, 4H), 4.16 – 4.10 (t, *J* = 6.6 Hz, 4H), 1.97 – 1.87 (m, 4H), 1.66 – 1.56 (m, 4H), 1.56 – 1.46 (m, 4H), 0.70 – 0.62 (m, 4H), 0.16 – 0.06 (m, 90H) ppm. ^{13}C NMR (100 MHz, $CDCl_3$): δ 158.96, 137.17, 132.71, 131.27, 130.63, 127.43, 125.18, 114.73, 68.46, 30.25, 29.57, 23.54, 18.64, 2.17, 1.59, 1.53, 1.49, 1.47, 1.46, 0.61 ppm. MALDI-ToF-MS M_w calculated for $C_{66}H_{126}O_{14}Si_{14}$: 1534.6 Da, m/z found: 1534.6 Da $[M]^+$.

$(Si_{11})_2$DPA
9,10-bis(4-(pent-4-en-1-yloxy)phenyl)anthracene (56.2 mg, 0.11 mmol, 1 eq.), **HSi_{11}** (172.8 mg, 0.21 mmol, 1.9 eq.), dry DCM (5 ml), Karstedt's catalyst (2 drops). After recycle GPC, the final product was obtained as a yellowish wax (165 mg, 75%).
^{1}H NMR (400 MHz, $CDCl_3$): δ 7.77 – 7.70 (m, 4H), 7.40 – 7.29 (m, 8H), 7.15 – 7.09 (m, 4H), 4.15 – 4.05 (t, *J* = 6.6 Hz, 4H), 1.95 – 1.83 (m, 4H), 1.64 – 1.41 (m, 8H), 0.66 – 0.60 (m, 4H), 0.12 – 0.03 (m, 138H) ppm. ^{13}C NMR (100 MHz, $CDCl_3$): δ 158.97, 137.18, 132.71, 131.29, 130.65, 127.44, 125.18, 114.74, 68.47, 30.26, 29.58, 23.55, 18.65, 2.16, 1.59, 1.52, 1.48, 1.46, 1.43, 0.61 ppm. MALDI-ToF-MS M_w calculated for $C_{82}H_{174}O_{22}Si_{22}$: 2126.7 Da, m/z found: 2126.8 Da $[M]^+$.

$(Si_{15})_2$DPA
9,10-bis(4-(pent-4-en-1-yloxy)phenyl)anthracene (44.4 mg, 0.09 mmol, 1 eq.), **HSi_{15}** (268 mg, 0.23 mmol, 2.6 eq.), dry DCM (2 ml), Karstedt's catalyst (1 drop). After recycle GPC, the final product was obtained as a yellowish wax (120 mg, 50%).
^{1}H NMR (400 MHz, $CDCl_3$): δ 7.77 – 7.72 (m, 4H), 7.40 – 7.34 (m, 4H), 7.34 – 7.29 (m, 8H), 7.15 – 7.10 (m, 4H), 4.13 – 4.07 (t, *J* = 6.6 Hz, 4H), 1.95 – 1.84 (m, 4H), 1.63 – 1.52 (m, 4H), 1.52 – 1.42 (m, 4H), 0.68 – 0.59 (m, 4H), 0.28 – 0.03 (m, 186H) ppm. ^{13}C NMR (100 MHz, $CDCl_3$): δ 158.95, 137.16, 132.70, 131.26, 130.62, 127.42, 125.17, 114.71, 68.47, 30.24, 29.56, 23.53, 18.63, 2.14, 1.57, 1.50, 1.46, 1.44, 1.41, 0.59 ppm. MALDI-ToF-MS M_w calculated for $C_{98}H_{222}O_{30}Si_{30}$: 2718.9 Da, m/z found: 2718.9 Da $[M]^+$.

5.7 References

(1) O'Neill, M.; Kelly, S. M. *Adv. Mater.* **2011**, *23*, 566.
(2) Jin, X.; Price, M. B.; Finnegan, J. R.; Boott, C. E.; Richter, J. M.; Rao, A.; Menke, S. M.; Friend, R. H.; Whittell, G. R.; Manners, I. *Science* **2018**, *360*, 897.
(3) Joarder, B.; Yanai, N.; Kimizuka, N. *J. Phys. Chem. Lett.* **2018**, *9*, 4613.
(4) Park, S. K.; Kim, J. H.; Park, S. Y. *Adv. Mater.* **2018**, *30*, 1.
(5) Qin, X.; Han, J.; Yang, D.; Chen, W.; Zhao, T.; Jin, X.; Guo, P.; Duan, P. *Chinese Chem. Lett.* **2019**, *30*, 1923.
(6) Shi, Y. L.; Zhuo, M. P.; Wang, X. D.; Liao, L. S. *ACS Appl. Nano Mater.* **2020**, *3*, 1080.
(7) Jiang, L.; Dong, H.; Meng, Q.; Li, H.; He, M.; Wei, Z.; He, Y.; Hu, W. *Adv. Mater.* **2011**, *23*, 2059.
(8) Yao, Y.; Zhang, L.; Orgiu, E.; Samorì, P. *Adv. Mater.* **2019**, *31*, 1.
(9) Wang, Y.; Sun, L.; Wang, C.; Yang, F.; Ren, X.; Zhang, X.; Dong, H.; Hu, W. *Chem. Soc. Rev.* **2019**, *48*, 1492.
(10) Yanai, N.; Kimizuka, N. *Chem. Commun.* **2016**, *52*, 5354.
(11) Gray, V.; Moth-Poulsen, K.; Albinsson, B.; Abrahamsson, M. *Coord. Chem. Rev.* **2018**, *362*, 54.
(12) Kimizuka, N.; Yanai, N.; Morikawa, M. A. *Langmuir* **2016**, *32*, 12304.
(13) Zhou, J.; Liu, Q.; Feng, W.; Sun, Y.; Li, F. *Chem. Rev.* **2015**, *115*, 395.
(14) Singh-Rachford, T. N.; Castellano, F. N. *Coord. Chem. Rev.* **2010**, *254*, 2560.
(15) McKenna, B.; Evans, R. C. *Adv. Mater.* **2017**, *29*.
(16) Felter, K. M.; Fravventura, M. C.; Koster, E.; Abellon, R. D.; Savenije, T. J.; Grozema, F. C. *ACS Energy Lett.* **2020**, *5*, 124.
(17) Hagstrom, A. L.; Weon, S.; Choi, W.; Kim, J. H. *ACS Appl. Mater. Interfaces* **2019**, *11*, 13304.
(18) Ye, S.; Gao, J.; Juan, A.; Guo, J. *Mol. Cryst. Liq. Cryst.* **2018**, *669*, 36.
(19) Liu, S. W.; Lee, C. C.; Yuan, C. H.; Su, W. C.; Lin, S. Y.; Chang, W. C.; Huang, B. Y.; Lin, C. F.; Lee, Y. Z.; Su, T. H.; Chen, K. T. *Adv. Mater.* **2015**, *27*, 1217.
(20) Pun, A. B.; Campos, L. M.; Congreve, D. N. *J. Am. Chem. Soc.* **2019**, *141*, 3777.
(21) Mcculloch, I.; Heeney, M.; Chabinyc, M. L.; Delongchamp, D.; Kline, R. J.; Cölle, M.; Duffy, W.; Fischer, D.; Gundlach, D.; Hamadani, B.; Hamilton, R.; Richter, L.; Salleo, A.; Shkunov, M.; Sparrowe, D.; Tierney, S.; Zhang, W. *Adv. Mater.* **2009**, *21*, 1091.
(22) Singh-Rachford, T. N.; Lott, J.; Weder, C.; Castellano, F. N. *J. Am. Chem. Soc.* **2009**, *131*, 12007.
(23) Islangulov, R. R.; Lott, J.; Weder, C.; Castellano, F. N. *J. Am. Chem. Soc.* **2007**, *129*, 12652.
(24) Vadrucci, R.; Weder, C.; Simon, Y. C. *J. Mater. Chem. C* **2014**, *2*, 2837.
(25) Raišys, S.; Kazlauskas, K.; Juršenas, S.; Simon, Y. C. *ACS Appl. Mater. Interfaces* **2016**, *8*, 15732.
(26) Hagstrom, A. L.; Lee, H. L.; Lee, M. S.; Choe, H. S.; Jung, J.; Park, B. G.; Han, W. S.; Ko, J. S.; Kim, J. H.; Kim, J. H. *ACS Appl. Mater. Interfaces* **2018**, *10*, 8985.
(27) Duan, P.; Yanai, N.; Kurashige, Y.; Kimizuka, N. *Ang. Chem. Int. Ed.* 2015, pp 7544–7549.
(28) Ogawa, T.; Yanai, N.; Monguzzi, A.; Kimizuka, N. *Sci. Rep.* **2015**, *5*, 1.
(29) Kouno, H.; Ogawa, T.; Amemori, S.; Mahato, P.; Yanai, N.; Kimizuka, N. *Chem. Sci.* **2016**, *7*, 5224.
(30) Kouno, H.; Sasaki, Y.; Yanai, N.; Kimizuka, N. *Chem. Eur. J.* **2019**, *25*, 6124.
(31) Duan, P.; Yanai, N.; Nagatomi, H.; Kimizuka, N. *J. Am. Chem. Soc.* **2015**, *137*, 1887.
(32) Monguzzi, A.; Tubino, R.; Hoseinkhani, S.; Campione, M.; Meinardi, F. *Phys. Chem. Chem. Phys.* **2012**, *14*, 4322.
(33) Hosoyamada, M.; Yanai, N.; Ogawa, T.; Kimizuka, N. *Chem. Eur. J.* **2016**, *22*, 2060.
(34) Ogawa, T.; Yanai, N.; Kouno, H.; Kimizuka, N. *J. Photonics Energy* **2017**, *8*, 1.
(35) Gharaati, S.; Wang, C.; Förster, C.; Weigert, F.; Resch-Genger, U.; Heinze, K. *Chem. Eur. J.* **2020**, *26*, 1003.
(36) Monguzzi, A.; Mézyk, J.; Scotognella, F.; Tubino, R.; Meinardi, F. *Phys. Rev. B - Condens. Matter Mater. Phys.* **2008**, *78*, 2.
(37) Duan, P.; Yanai, N.; Kimizuka, N. *J. Am. Chem. Soc.* **2013**, *135*, 19056.
(38) Goudarzi, H.; Keivanidis, P. E. *ACS Appl. Mater. Interfaces* **2017**, *9*, 845.
(39) Karpicz, R.; Puzinas, S.; Gulbinas, V.; Vakhnin, A.; Kadashchuk, A.; Rand, B. P. *Chem. Phys.* **2014**, *429*, 57.
(40) Kerkhof, L. C. Van Den; Allan, K. M.; McGrath, K. M.; Spencer, J. L.; Hodgkiss, J. M. *Int. J. Nanotechnol.* **2017**, *14*, 432.
(41) Wang, Y.; Shi, J.; Chen, J.; Zhu, W.; Baranoff, E. *J. Mater. Chem. C* **2015**, *3*, 7993.
(42) Han, J.; Duan, P.; Li, X.; Liu, M. *J. Am. Chem. Soc.* **2017**, *139*, 9783.
(43) Yang, D.; Han, J.; Liu, M.; Duan, P. *Adv. Mater.* **2019**, *31*, 1.
(44) Zhao, T.; Han, J.; Qin, X.; Zhou, M.; Duan, P. *J. Phys. Chem. Lett.* **2020**, *11*, 311.

(45) Yang, X.; Han, J.; Wang, Y.; Duan, P. *Chem. Sci.* **2019**, *10*, 172.
(46) Murali, G.; Kaur, S.; Kim, J.; Nam, S. H.; Lee, J. H.; Suh, Y. D.; In, I.; Lee, S. H. *J. Mater. Chem. C* **2019**, *7*, 10918.
(47) Börjesson, K.; Rudquist, P.; Gray, V.; Moth-Poulsen, K. *Nat. Commun.* **2016**, *7*.
(48) Francis, L. S. Contact lenses for viewing 3D films. GB 2469996 A, 2009.
(49) Nickmans, K.; Murphy, J. N.; de Waal, B.; Leclère, P.; Doise, J.; Gronheid, R.; Broer, D. J.; Schenning, A. P. H. J. *Adv. Mater.* **2016**, *28*, 10068.
(50) Van Genabeek, B.; de Waal, B. F. M.; Gosens, M. M. J.; Pitet, L. M.; Palmans, A. R. A.; Meijer, E. W. *J. Am. Chem. Soc.* **2016**, *138*, 4210.
(51) Zha, R. H.; de Waal, B.; Lutz, M.; Teunissen, A. J. P.; Meijer, E. W. *J. Am. Chem. Soc.* **2016**, *138*, 5693.
(52) Van Genabeek, B.; Lamers, B. A. G.; De Waal, B. F. M.; Van Son, M. H. C.; Palmans, A. R. A.; Meijer, E. W. *J. Am. Chem. Soc.* **2017**, *139*, 14869.
(53) Berrocal, J. A.; Zha, R. H.; de Waal, B. F. M.; Lugger, J. A. M.; Lutz, M.; Meijer, E. W. *ACS Nano* **2017**, *11*, 3733.
(54) Zha, R. H.; Vantomme, G.; Berrocal, J. A.; Gosens, R.; De Waal, B.; Meskers, S.; Meijer, E. W. *Adv. Funct. Mater.* **2018**, *28*, 1.
(55) Lamers, B. A. G.; van Genabeek, B.; Hennissen, J.; de Waal, B. F. M.; Palmans, A. R. A.; Meijer, E. W. *Macromolecules* **2019**, *52*, 1200.
(56) Lamers, B. A. G.; Graf, R.; De Waal, B. F. M.; Vantomme, G.; Palmans, A. R. A.; Meijer, E. W. *J. Am. Chem. Soc.* **2019**, *141*, 15456.
(57) Gray, V.; Dzebo, D.; Lundin, A.; Alborzpour, J.; Abrahamsson, M.; Albinsson, B.; Moth-Poulsen, K. *J. Mater. Chem. C* **2015**, *3*, 11111.
(58) Lu, F.; Jang, K.; Osica, I.; Hagiwara, K.; Yoshizawa, M.; Ishii, M.; Chino, Y.; Ohta, K.; Ludwichowska, K.; Kurzydłowski, K. J.; Ishihara, S.; Nakanishi, T. *Chem. Sci.* **2018**, *9*, 6774.
(59) Hamley, I. W.; Castelletto, V. *Small-angle scattering of block copolymers*; 2008.
(60) Hurd, C. B. *J. Am. Chem. Soc.* **1946**, *68*, 364.
(61) Nandi, A.; Manna, B.; Ghosh, R. *Phys. Chem. Chem. Phys.* **2019**, *21*, 11193.
(62) Hestand, N. J.; Spano, F. C. *Acc. Chem. Res.* **2017**, *50*, 341.
(63) Gray, V.; Dreos, A.; Erhart, P.; Albinsson, B.; Moth-Poulsen, K.; Abrahamsson, M. *Phys. Chem. Chem. Phys.* **2017**, *19*, 10931.
(64) Raišys, S.; Juršėnas, S.; Simon, Y. C.; Weder, C.; Kazlauskas, K. *Chem. Sci.* **2018**, *9*, 6796.
(65) Suzuki, K.; Kobayashi, A.; Kaneko, S.; Takehira, K.; Yoshihara, T.; Ishida, H.; Shiina, Y.; Oishi, S.; Tobita, S. *Phys. Chem. Chem. Phys.* **2009**, *11*, 9850.
(66) Gertsen, A. S.; Koerstz, M.; Mikkelsen, K. V. *Phys. Chem. Chem. Phys.* **2018**, *20*, 12182.
(67) Haefele, A.; Blumhoff, J.; Khnayzer, R. S.; Castellano, F. N. *J. Phys. Chem. Lett.* **2012**, *3*, 299.
(68) Zhang, Q. G.; Lu, Y.; Wang, F. X.; Wei, Y.; Liu, Y. Q.; Yang, B.; Pan, G. B. *RSC Adv.* **2014**, *4*, 47325.
(69) Wasserman, H. H.; Scheffer, J. R.; Cooper, J. L. *J. Am. Chem. Soc.* **1972**, *94*, 4991.
(70) Liu, X.; Zhu, T.; Hu, Q.; Dong, L.; Tan, Z. *Crystals* **2019**, *9*, 512.
(71) Salzillo, T.; Della Valle, R. G.; Venuti, E.; Brillante, A.; Siegrist, T.; Masino, M.; Mezzadri, F.; Girlando, A. *J. Phys. Chem. C* **2016**, *120*, 1831.
(72) Lewis, T. P.; Eaton, W. A. *J. Am. Chem. Soc.* **1997**, *93*, 2054.
(73) Pensack, R. D.; Tilley, A. J.; Parkin, S. R.; Lee, T. S.; Payne, M. M.; Gao, D.; Jahnke, A. A.; Oblinsky, D. G.; Li, P. F.; Anthony, J. E.; Seferos, D. S.; Scholes, G. D. *J. Am. Chem. Soc.* **2015**, *137*, 6790.
(74) Pensack, R. D.; Grieco, C.; Purdum, G. E.; Mazza, S. M.; Tilley, A. J.; Ostroumov, E. E.; Seferos, D. S.; Loo, Y. L.; Asbury, J. B.; Anthony, J. E.; Scholes, G. D. *Mater. Horizons* **2017**, *4*, 915.
(75) Li, X.; Tang, M. L. *Chem. Commun.* **2017**, *53*, 4429.
(76) De Mello, J. C.; Wittmann, H. F.; Friend, R. H. *Adv. Mater.* **1997**, *9*, 230.
(77) Dzhevakov, P. B.; Topchiy, M. A.; Zharkova, D. A.; Morozov, O. S.; Asachenko, A. F.; Nechaev, M. S. *Adv. Synth. Catal.* **2016**, *358*, 977.

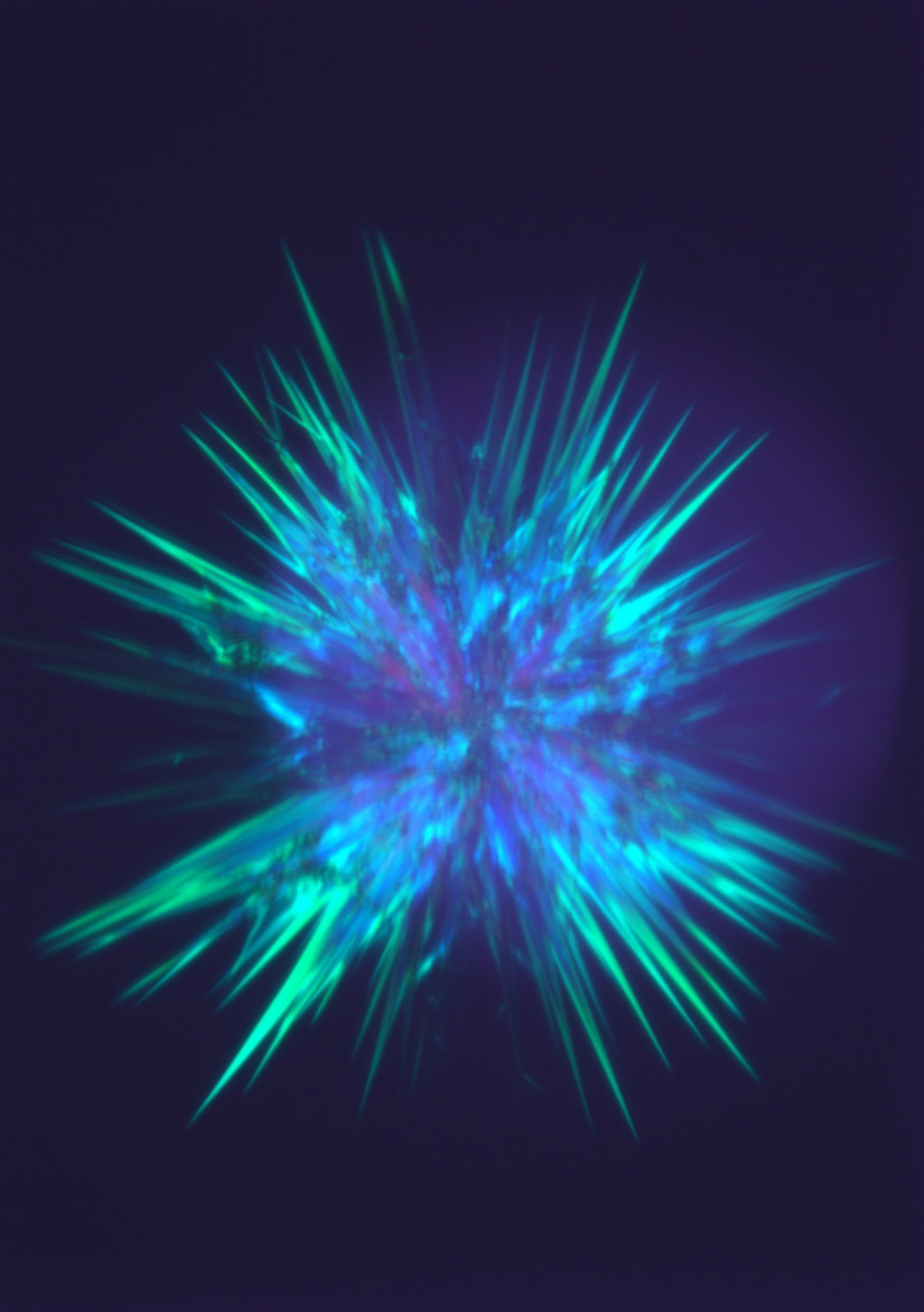

Chapter 6

Epilogue

ABSTRACT: Control over the nanostructure of organic molecules gives control over their macroscopic properties. Therefore, understanding how self-assembly into multiscale ordered domains can be directed is promising for improving the optoelectronic properties of the materials. For this purpose, we synthesized novel block molecules in which order at the nanoscale was induced by a combination of phase separation and crystallization. Reported crystal structures and space-filling arguments can be used to predict whether 2D nanostructures are formed. After demonstrating the potential of these block molecules for high exciton diffusivities and enhanced triplet-triplet annihilation upconverted photoluminescence, their applicability for singlet fission is studied. To this end, TIPS-pentacene block molecules were studied with femtosecond transient absorption measurements. Although singlet fission was observed, the relationship between the morphology and singlet fission characteristics could not be resolved because the thickness of the layer of the block molecule could not be controlled.

The singlet fission analysis was performed in close collaboration with Dr. Guiying He and Professor Matthew Y. Sfeir from the Advanced Science Research Center in New York, and Dr. Dino Wu and Professor Luis M. Campos from Columbia University in New York.

6.1 The aim revisited

In the introduction of this thesis, we show that control over the nanostructure of organic molecules gives control over their macroscopic properties. In the following chapters, we showed how nanostructured chromophores can be obtained by functionalization of aromatic cores with discrete oligodimethylsiloxane (*o*DMS). For these block molecules, phase separation and space filling are key features to control the order at the nanoscale.

Analysis of all newly reported molecules shows how the intermolecular distances in reported crystal structures can be used to design block molecules assembled in 2D lamellar morphologies, allowing *a priori* rationalization of molecular design. We show that the distance between *o*DMS attachment points should preferably be greater than ~7 Å, the *o*DMS diameter, to ensure that the *o*DMS does not interfere with the crystalline packing. Thus, a core-centered architecture with a grafting density of two *o*DMS chains per core should only be used for bulky aromatic molecules. For denser aromatic molecules, a lower grafting density of one *o*DMS chain per core is more appropriate. This lower graft density can be achieved in either a core-*o*DMS or a telechelic core-*o*DMS-core architecture. The former has a lower tendency for lamella formation as the *o*DMS chain can coil onto itself, leading to an increased bulkiness of the *o*DMS which stabilizes lamella formation. This coiling is prevented in the telechelic architecture due to the interconnection of multiple aromatic assemblies via the more stretched *o*DMS chains. Compared to linear *o*DMS, branched *o*DMS is bulkier and therefore leads to less strongly packed assemblies. By varying the bulkiness of the side groups, the interaction strength between the aromatic cores can thus be controlled which allows control over their optoelectronic properties.

The distance requirement can also be used when designing co-assemblies of block molecules. By mixing small molecules that intercalate with the cores of the block molecules, the distance between the *o*DMS attachment points can be increased. To do this, the interaction between the core of the block molecule and the small molecule must be sufficiently strong. We have demonstrated how co-assembly with block molecules results in nanoscale-ordered materials with charge transfer bands in the absorption spectrum, causing the material to change color, and how the photoluminescence quantum yield can be affected.

Moreover, in this thesis we have reported how the well-defined order that can be obtained by functionalization of aromatic cores with *o*DMS results in enhanced energy transfer between chromophores. This is demonstrated by the exciton diffusivity values obtained that are high for organic molecules and a 100-fold increase in the triplet-triplet annihilated upconverted signal compared to the non-ordered analog. In these two examples, order was not only obtained on the nanoscale, but the molecules even formed ordered domains 0.1 mm to 1 cm in size. As a result, the absorption and emission spectra were linearly polarized through these domains. This thesis has both increased knowledge of how block molecules form their morphologies at the nanoscale, enabling rationalized molecular design, and demonstrated how block molecules can be used to improve photonic properties. As such, it shows the potential of this type of material for optoelectronic applications such as transistors or solar cell components.

6.2 Future directions

6.2.1 Singlet fission

Although the potential of *o*DMS-containing block molecules has been demonstrated in this thesis, some aspects of these materials require further research before application in real-world devices is possible. This will be illustrated with a series of block molecules designed for singlet fission. Singlet fission (SF) is the process by which a singlet exciton splits into two triplet excitons, thereby increasing the number of charge carriers. This multiple exciton generation process has significant potential for technological applications such as photodetectors[1], fluorescence imaging[2], or electroluminescent OLEDs[3]. However, SF is best known for its potential in single-junction solar cells to double the photocurrent and thus increase the maximum achievable efficiency by overcoming the Shockley-Queisser limit. Since SF is a multi-chromophore phenomenon, it strongly depends on the orbital overlap in the bulk. Moreover, the energy of the lowest-lying excited state singlet $E(S_1)$ must be more than twice the energy of an excited state triplet $E(T_1)$. Because of their favorable slipped cofacial π-π packing and favorable energy levels, pentacene and its derivatives are one of the most studied SF materials.[4,5]

By varying the side groups of pentacene, it was found that SF can occur with interchromophore distances of > 5 Å, although SF rates were several orders of magnitude faster with tighter packing.[6] Similarly, by changing the pentacene core to an aza-derivative, tighter packing and therefore faster singlet fission can be obtained.[7] Shearing TIPS-pentacene can induce several polymorphs with tighter packing, leading to twice as high maximum mobilities.[8] However, in addition to short-range spatial ordering, long-range spatial ordering is also important for efficient SF, since both rapid diffusion of singlets to favorable sites for SF and rapid exciton diffusion of triplets after separation of triplet pairs is required.[6,9–13] SF is usually studied in crystalline films or isolated dimers with only a few reports using locally high concentration systems, such as polymers with pendant pentacenes or micelles of pentacene-functionalized poly(ethylene glycol).[14,15] However, the effect of different long-range nanoscale morphologies on SF remains to be elucidated. To this end, pentacene block molecules have been designed, synthesized, and characterized.

6.2.2 General challenges for block molecules, illustrated with TIPS-pentacene block molecules

Two different pentacene derivatives were chosen for the design of the pentacene block molecules (Figure 1 and Figure 2) and their properties are related to the reported crystal structures of the non-functionalized cores. For mesitylene-pentacene shown in Figure 1, the crystal structure shows that the adjacent molecules are packed perpendicular to each other in densely packed 1D stacks, which would result in a columnar morphology. However, the corresponding block molecule **$(Si_{15})_2$Pentacene** showed a lamellar morphology. We hypothesize that another pentacene polymorph is favored with an alkyl spacer on the pentacene. This shows that the influence of the alkyl side chains is very important because the additional intermolecular interactions and the minimization of the free volume around the alkyl chains can cause a different arrangement of the aromatic groups relative to each other.[16,17] Thus, when using reported

crystal structures for the design of block molecules, all reported polymorphs should be studied. Furthermore, the chromophore whose crystal structure is known should preferably have similar alkyl spacers as the chromophore to be functionalized with *o*DMS.

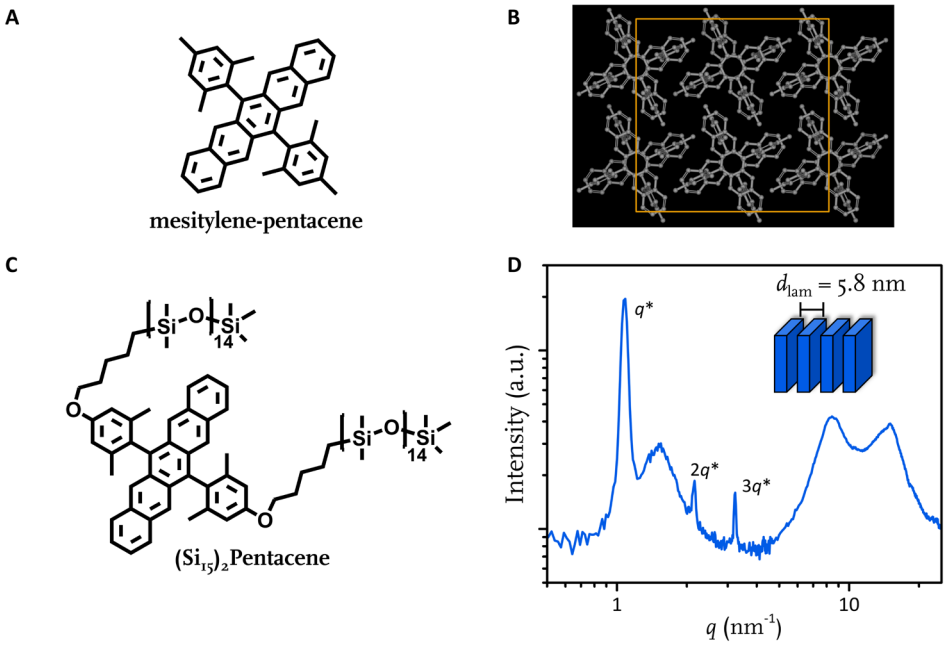

Figure 1. Molecular structure of (A) mesitylene-pentacene and (B) the mesitylene-pentacene block molecule **$(Si_{15})_2$Pentacene**. (B) The crystal structure of mesitylene-pentacene showing a columnar rectangle arrangement. (D) 1D transmission spectra of **$(Si_{15})_2$Pentacene** showing lamellar morphology. This molecule was synthesized by Dr. Dino Wu at Columbia University in the laboratory of Prof. Luis Campos.

Crystal structures are not reported for all molecules, which would prevent *a priori* block molecule design using the approach introduced in this thesis of comparing distances between the *o*DMS attachment points, and the ongoing study on calculated interaction energies. However, the crystal structure of similar compounds can still be used to rationalize which molecular architecture to choose. For TIPS-pentacene, the *o*DMS attachment points in a core-centered architecture would be too close together (< 6 Å) to maintain the packing reported in the crystal structure, and therefore functionalization with a single *o*DMS chain was chosen.[18] This yielded the molecules **Pent-Si_7**, **Pent-Si_{15}**, **Pent-Si_{15b}** and **Pent-Si_{16}-Pent** shown in Figure 2. Unlike the other structures in this thesis, the volume fraction of the core in **Pent-Si_7** is larger than the volume fraction of *o*DMS (Table 1, page 126). According to block copolymer theory, **Pent-Si_7** should assemble in a columnar morphology consisting of *o*DMS cylinders in a pentacene matrix. **Pent-Si_{16}-Pent** has a similar volume fraction and the telechelic architecture was thought to result in a lamellar morphology. However, **Pent-Si_{16}-Pent** was amorphous down to at least −70°C. Therefore, the effect of the molecular architecture when the core volume exceeds the *o*DMS volume remains to be elucidated.

Lamellar morphologies were obtained for **Pent-Si$_{15}$** and **Pent-Si$_{15b}$**, with the higher thermal transitions and enthalpies for **Pent-Si$_{15b}$** indicating a more stable morphology. In this head-tail architecture, the minimum distance between attachment points > 11.5 Å is significantly larger than the *o*DMS diameter of ~7 Å, when assuming the packing reported for TIPS-pentacene crystals.[18] Therefore, the bulkier branched *o*DMS **Si$_{15b}$** can better fill the available space than the linear **Si$_{15}$**, which results in a more stable morphology for **Pent-Si$_{15b}$**. In Chapter 3 we argue that strong intermolecular interactions are required when the distances between the attachment points of *o*DMS are larger than 10 Å. While we briefly show in Chapters 2 and 3 that we can calculate the intermolecular interactions using the program CrystalExplorer,[19] the chemical structure of TIPS-pentacene was too large to perform these calculations. The approach of calculating the intermolecular interaction energies is currently being developed in collaboration with Bart van den Bersselaar and Tobias Schnitzer and will further advance the *a priori* rationalization of block molecule design.

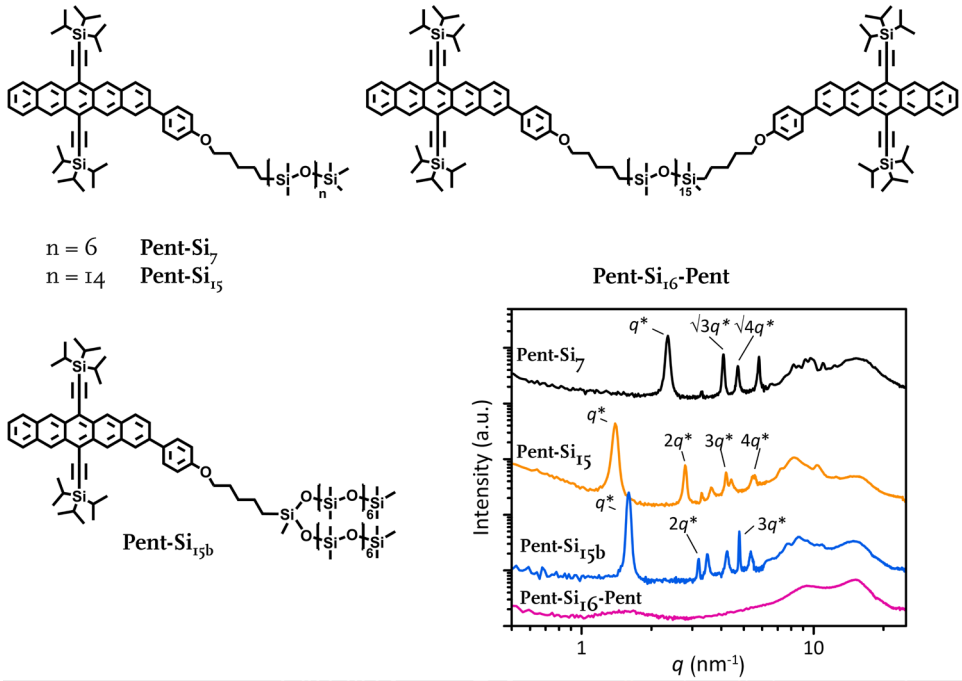

Figure 2. Molecular structures of the four TIPS-pentacene block molecules. As shown by the reflection peaks of the principal scattering peak in the 1D transmission spectra, **Pent-Si$_7$** forms a columnar hexagonal morphology, **Pent-Si$_{15}$** and **Pent-Si$_{15b}$** form lamellar morphologies, while **Pent-Si$_{16}$-Pent** is amorphous. The data were recorded after slow cooling from the melt. The unassigned peaks correspond to distances within the crystal structure of the material.

Table 1. Thermal and morphological characterization data for the *o*DMS functionalized pentacene derivatives.

Compound	T_m[a] [°C]	ΔH_m[a] [kJ mol^{-1}]	T_c[a] (°C)	ΔH_c[a] [kJ mol^{-1}]	f_{Pent}[b]	Phase[c]	d[c] [nm]
Pent-Si$_{16}$-Pent	n.o.	-	n.o.	-	0.55 – 0.66	-	-
Pent-Si$_7$	100	12	64	11	0.58 – 0.69	Col$_h$	2.7
Pent-Si$_{15}$	84	9	51	9	0.40 – 0.51	Lam	4.5
Pent-Si$_{15b}$	93	14	30	11	0.40 – 0.51	Lam	3.9

[a] Thermal transitions and enthalpies as determined by DSC from the second heating and cooling cycle with heating and cooling rates of 10 °C min^{-1}. [b] A range of values is given because the crystal structure of the core is not known. The lower limit was calculated using the volume of TIPS-pentacene,[18] and the upper limit was calculated using the volume of dibrominated TIPS-pentacene.[20] [c] Determined from the SAXS data. Col$_h$ is columnar hexagonal with the columns formed by *o*DMS; Lam is lamellar. Domain spacings were calculated using $d = 2\pi/q^*$.

As can be seen in the POM images of the TIPS-pentacene block molecules, large domains are formed with the head-tail architecture (Figure 3). It has been attempted to control the orientation and size of these domains with rubbed polyimide layers or shear force, both techniques from the field of liquid crystals, although without success. Fortunately, continued advances in materials processing in other areas are likely to promote block molecule processing as well, further improving the applicability of block molecules for use in devices by controlling their domain orientation and size.[8,21–28]

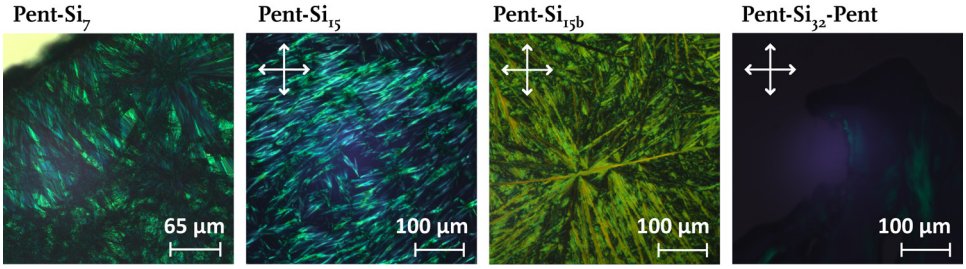

Figure 3. Optical microscopy images of the TIPS-pentacene block molecules. Two perpendicular arrows indicate that the image was taken with the material between crossed polarizers.

The TIPS-pentacene block molecules have been studied for their singlet fission properties using femtosecond transient absorption (fsTA). These measurements were performed by Guiying He from the group of Prof. Matthew Sfeir at the Advanced Science Research Center in New York. The fsTA spectrum with kinetic traces at 470 and 530 nm is shown in Figure 4 for annealed **Pent-Si$_{15b}$** as a representative example. At early times, we observe a signal at ~470 nm corresponding to the bright singlet (S_1). Concomitantly, the characteristic T-T absorption band of the pentacene develops at 530 nm.[6] Singlet fission is the most likely pathway for triplet formation, since the population of triplets formed by intersystem crossing is negligible at this time scale.[29] The signal at 470 nm does not decay to zero due to overlap with the spectral feature of the triplet, although the intrinsic singlet fission is expected to be completed within the time frame of 1 ps. This fast decay is also observed in polymers with pendent pentacenes and implies minimization of areas with poor orbital overlap due to suppressed motion of the individual molecules in the material.[15] A bi-exponential equation is used for the initial phase of triplet formation, as shown in Figure 4B.[30] The initial triplet pair formation

occurs with a time constant, τ_1, ranging from 210 – 350 fs. These values are consistent with polycrystalline films of TIPS-Pentacene (~100 – 400 fs) and may vary due to differences in sample preparation, transient absorption measurements, and data analysis.[31] This fast phase of triplet formation is attributed to the intrinsic time scale of SF, while the second slower triplet formation phase with time constant τ_2 is attributed to singlet fission limited by energy migration. Here, the singlets formed are not initially located on molecules with the appropriate packing for singlet fission, and thus must first diffuse to sites suitable for singlet fission.[30]

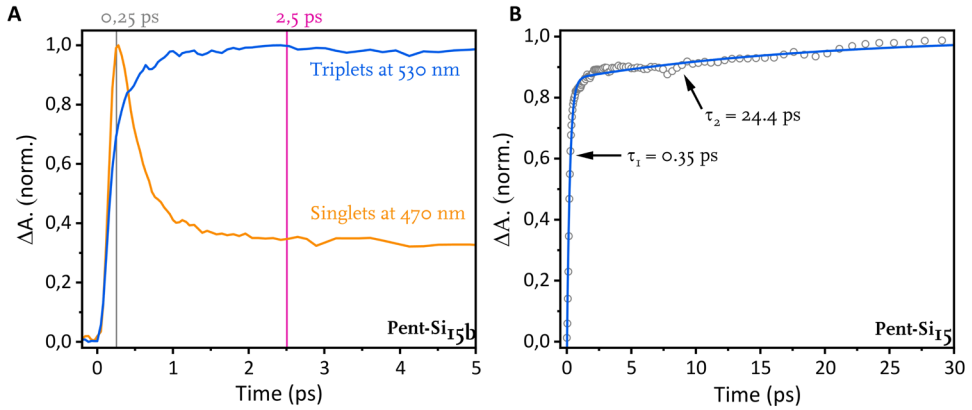

Figure 4. (A) Singlet (orange) and triplet (blue) kinetics at 470 and 530 nm, respectively, for an annealed **Pent-Si$_{15b}$** film. After photoexcitation, the depopulation of the S_1 state at 470 nm is accompanied by the increase of the triplet signal at 530 nm. (B) Triplet kinetics at 530 nm for a **Pent-Si$_{15}$** film showing clearly the fast intrinsic triplet formation related to τ_1, and the energy-migration limited triplet formation with the slower time constant τ_2.

The four different TIPS-pentacene block molecules would allow a comparison of the different morphologies on the singlet fission characteristics. However, to properly compare the transient absorption results, the absorption of the different materials must be comparable. The layer thickness and hence the absorption cannot be controlled during the thermal treatment of block molecules between two glass slides as the material flows around the temperature required to obtain the highest order. The thickness of the material can be controlled with spacers between the glass slides. However, this is only possible with a minimum spacing of 5 – 10 µm which gives too high absorption for the TIPS-pentacene block molecules. In processing techniques such as spin coating, inhomogeneous surface coverage is usually obtained for block molecules because the low interaction energy of block molecules with glass or quartz leads to surface dewetting. For TIPS-pentacene polymers, surface modification with phenyltrichlorosilane and octadecyltrimethoxysilane was used to change the interaction energy between material and surface, a technique that could also help in the processing of block molecules.[32] Spatial control of block molecules up to the millimeter would be a great addition to the knowledge gained on obtaining ordered materials at the nanoscale, accelerating the development of block molecules for devices.

6.2.3 General challenges for block molecules, illustrated with DPA-*o*DMS alternating polymers

The ordering of most block molecules is sensitive to external stimuli such as pressure, because of their general waxy or brittle solid properties, or exposure to oxygen or solvent vapors. While this is not necessarily a problem for multilayer devices, where adjacent layers can improve the stability of the block molecules, the development of ordered materials with favorable bulk properties would benefit product development. Since polymers have tunable bulk properties through control of their dispersity and molecular weight, an alternating *o*DMS-core polymer was synthesized to study whether polymerization can yield ordered polymer materials at the nanoscale. For this, dialkylated diphenylanthracene was polymerized with difunctional **HSi$_{16}$H** to obtain the polymer **(DPA-Si$_{16}$)$_n$** (Figure 5). After polymerization with Karstedts' catalyst and removal of the solvent, a free-standing polymer film was obtained. However, the material had no long-range ordering. Moreover, the catalyst could not be removed by Soxhlet extraction, column chromatography or dialysis. In contrast, *o*DMS-containing polymers formed by supramolecular assembly have been shown to yield both favorable bulk properties and well-defined ordering at the nanoscale, making these approaches preferable to covalent polymerization when one wants to combine bulk properties with well-defined ordering. One approach utilized the supramolecular polymerization of telechelic block molecules to obtain a brittle polymer with long-range ordered lamellae through quadruple hydrogen bonding of the ureidopyrimidone motifs.[33] The second approach was shown with core-centered terthiophene block molecules that formed columnar morphologies through the phase separation with the *o*DMS chains.[34] The *o*DMS chains were functionalized with pendant acrylate groups that allowed for photopolymerization with retention of the ordered nanostructure and charge transport capabilities. This second approach is more generalizable as it relies on the phase separation of aromatic groups with *o*DMS instead of relying on specific core-core interactions of the former approach. These initial results indicate that phase separation followed by photopolymerization is preferred over covalent or supramolecular polymerization when targeting highly-ordered nanostructures with favorable physical properties for optoelectronic applications.

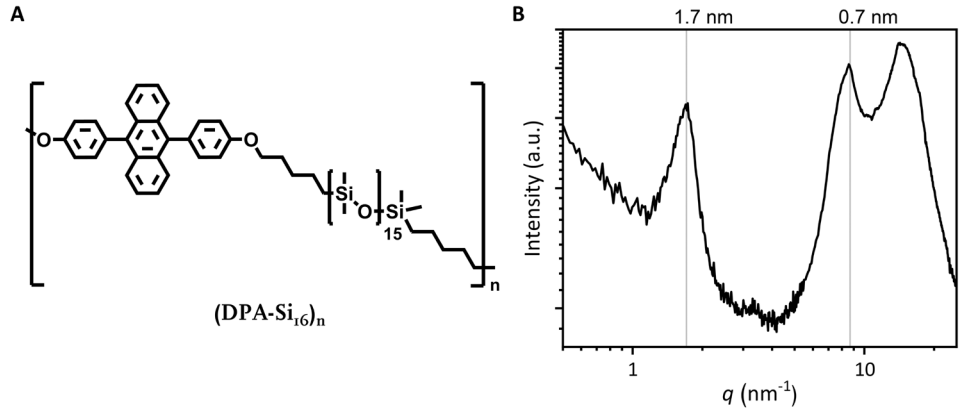

Figure 5. (A) Molecular structure of the *o*DMS-diphenylanthracene polymer **(DPA-Si$_{16}$)$_n$** forming an amorphous phase, as visible in the 1D transmission spectrum under (B). A distance of 1.7 nm is observed between the ill-defined DPA assemblies, while the signal at 7 Å corresponds to the *o*DMS diameter.

6.3 Experimental section

6.3.1 Materials and methods

All chemicals were purchased from commercial sources and used without further purification. For the hydrosilylation reactions, the following preparation of Karstedt's catalyst from Sigma Aldrich is used; Platinum(0)-1,3-divinyl-1,1,3,3-tetramethyldisiloxane complex solution in xylene, Pt ~2 %. **$(Si_{15})_2$Pentacene** was synthesized by Dino Wu and phenol-decorated TIPS-pentacene was synthesized by Kealan Fallon, both from Campos Research Group. The discrete length oligodimethylsiloxanes (*o*DMS) monohydride with a length of 7 (**HSi_7**) or 15 (**HSi_{15}**) silicon atoms, and *o*DMS dihydride with a length of 16 silicon atoms (**$HSi_{16}H$**) were synthesized according to literature procedure.[1] The synthesis of **HSi_{15b}** is described in Chapter 4. Synthesis of 9,10-bis(4-(pent-4-en-1-yloxy)phenyl)anthracene is described in Chapter 5. Dry solvents were obtained with an MBRAUN solvent purification system (MB-SPS). Flame-dried Schlenk flasks were used for all reactions carried out under argon atmosphere. Reactions were followed by thin-layer chromatography (TLC) using 60-F254 silica gel plates from Merck and visualized by UV light at 254 nm. Automated column chromatography was conducted on a Grace system using Biotage KP-SIL Silica Flash Cartridges. The methods used for nuclear magnetic resonance (NMR), matrix assisted laser desorption/ionization time of flight mass spectroscopy (MALDI-ToF-MS), and bulk small angle X-ray scattering (SAXS) are described in Chapter 2. **Differential scanning calorimetry (DSC)** data were collected on a DSC Q2000 from TA instruments, calibrated with an indium standard. The samples (2-3 mg) were weighed directly into aluminium pans and hermetically sealed. The samples were initially heated to 120 °C and then subjected to two cooling/heating cycles from 0 °C to 120 °C with a rate of 2 K min^{-1} as well as two cooling/heating cycles from -50 °C to 120 °C with 10 K min^{-1}. The data that is presented, represents the second heating and/or cooling cycle, with the third cycle similar to the second. The thermal transition temperatures were assigned at the maximum of the transition. **Polarized Optical Microscopy** (POM) samples were sandwiched between glass substrates and imaged using Nikon ECLIPSE Ci-POL microscope with 4x, or 16x magnification. The samples were heated and cooled using a Linkam LTS 420 heating stage mounted in the POM set-up. All samples were heated to their isotropic phase (10-20 °C above their melting point, isothermal for 5-10 minutes) and subsequently cooled with 5 °C min^{-1} to their melting point. The samples were further cooled with 1 °C min^{-1} to form birefringent domains. **Volume fractions** were estimated as the ratio between the *o*DMS volume and the core volume. For this, the bulk density of PDMS was taken as 0.95 g ml^{-1} which was converted to volume with the respective molecular weights of the three lengths *o*DMS (M_{w,CH_3Si_7H} = 519.1 g mol^{-1} gives $V_{CH_3Si_7H} \approx 546$ ml mol^{-1}; $M_{w,CH_3Si_{15}H}$ = 1112.4 g mol^{-1} gives $V_{CH_3Si_{15}H} \approx 1170$ ml mol^{-1}; $M_{w,HSi_{16}H}$ = 1173 g mol^{-1} gives $V_{HSi_{16}H} \approx 1261$ ml mol^{-1}).[35] The volumes of linear and branched *o*DMS with length 15 were assumed to be the same. The volumes of the cores were calculated using the densities of the crystal structures of compounds similar to used cores. The crystal densities were estimated from the crystal structures of unfunctionalized TIPS-pentacene[18] and dibrominated TIPS-pentacene[20] by dividing the unit cell volume in $Å^3$ with the number of molecules in the unit cell followed by conversion to ml mol^{-1}. For the calculations for the volume of the cores, their molecular weights were taken including alkyl spacer on both sides. The samples for the **singlet fission** experiments were prepared on glass slides that were cleaned by sonication in isopropanol (2x 10 minutes), followed by sonication in acetone (2x 10 minutes). The glass slides were dried with compressed air. In a glovebox (oxygen level below 1.5 ppm), roughly 1 mg was put on one of the glass slides before using a second glass slide to smear the material over a larger area. The edges of the two glass slides were aligned and sealed with UV-curing glue (Norland UVS91). Aluminum foil was used as a mask for the sample during the UV-curing of the glue (30 minutes). **Femtosecond transient absorption** were performed by Guiying He from SfeirLab Photonics.

6.3.2 Synthesis

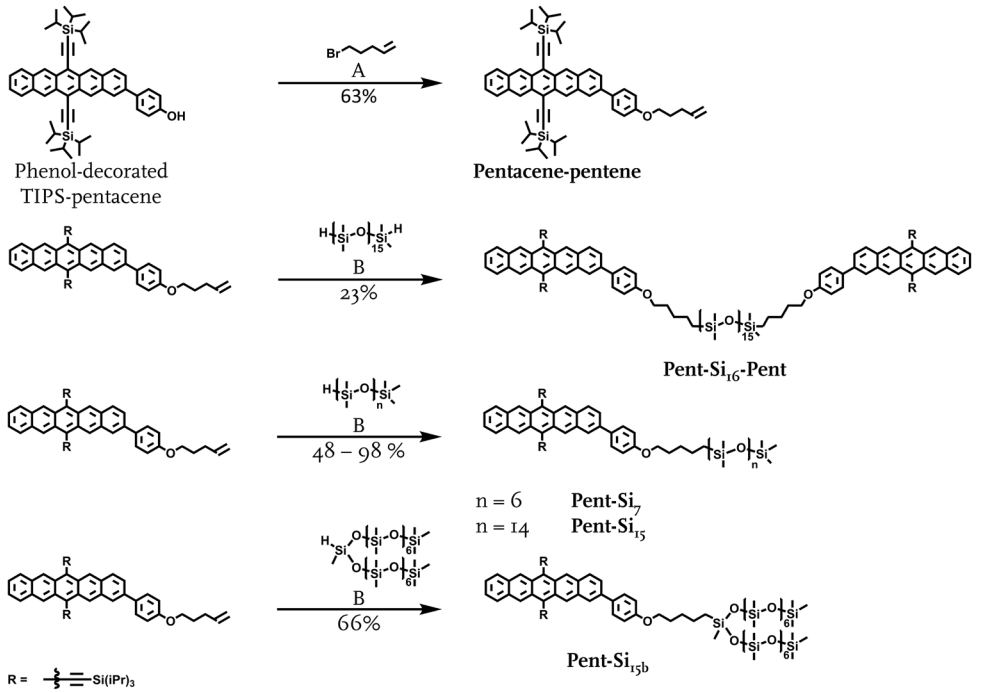

Scheme 1. Synthetic scheme of the pentacene derivatives. (A) Williamson etherification; K_2CO_3, dry DMF, 80 °C, 48 h. (B) Karstedt's catalyst, dry DCM, RT, 3h.

Pentacene-pentene
Phenol-decorated TIPS-pentacene (308 mg, 0.42 mmol, 1 eq.), K_2CO_3 (127 mg, 0.92 mmol, 2.18 eq.) and 5-bromopent-1-ene (0.5 mL, 4.09 mmol, 9,7 eq.) were dissolved in 10 mL dry DMF and heated to 80 °C. After 48 hours, the mixture was cooled to room temperature before adding DI water. The target compound was extracted with EtOAc until the aqueous phase was colorless. The organic phase was dried with $MgSO_4$ and reduced in vacuo to 370 mg crude product as dark green solid that was impregnated on celite and purified by column chromatography (Solid loading, eluent heptane/EtOAc 100/0 – 95/5). The target product was obtained as dark green solid (210 mg, 63% yield).
^{1}H NMR (400 MHz, $CDCl_3$): δ 9.30 (s, 4H), 8.07 (s, 1H), 8.03 (d, J = 9.0 Hz, 1H), 8.00 – 7.95 (m, 2H), 7.76 – 7.67 (m, 3H), 7.43- 7.39 (m, 2H), 7.07 (d, J = 8.7 Hz, 2H), 5.96 – 5.83 (m, 1H), 5.15 – 5.00 (m, 2H), 4.05 (t, J = 6.4 Hz, 2H), 2.33 – 2.26 (m, 2H), 2.00 – 1.91 (m, 2H), 1.45 – 1.30 (m, 42H) ppm. ^{13}C NMR (100 MHz, $CDCl_3$): δ 159.14, 138.04, 137.94, 133.29, 132.72, 132.44, 132.38, 131.50, 131.12, 130.88, 130.81, 130.70, 129.37, 128.82, 128.43, 126.59, 126.46, 126.44, 126.31, 126.20, 126.15, 126.13, 124.89, 118.56, 118.27, 115.43, 115.18, 107.29, 107.21, 104.91, 104.85, 67.48, 30.30, 28.61, 19.18, 19.17, 11.85 ppm.
MALDI-ToF-MS: m/z calc. for $C_{55}H_{66}OSi_2$ 799.30 Da; found 798.51 Da [M^+].

General procedure for hydrosilylations
In a flame dried Schlenk flask, **pentacene-pentene** (1 eq.) and oligodimethylsiloxane with terminal hydride(s) (0.4 – 2.8 eq.) were dissolved in dry DCM. After addition of Karstedt's catalyst (1 – 2 drops), the reaction was let to run under argon. After 3 hours, the reaction mixture was diluted with DCM and impregnated on celite. Excess oligodimethylsiloxane was removed with column chromatography (solid loading on celite, SiO_2 column, gradient pure heptane to either up to 40% chloroform or DCM). The purity of the green waxes was confirmed by ^{1}H-NMR, ^{13}C-NMR, and MALDI-ToF-MS.

Pent-Si$_7$
Pentacene-pentene (50 mg, 0.06 mmol, 1 eq.), **HSi$_7$** (90 mg, 0.17 mmol, 2.79 eq.), dry DCM (2 ml), Karstedt's catalyst (2 drops). After column chromatography (pure heptane gradient to 20% DCM in heptane), the compound was obtained as a dark green wax (81 mg, 98%).
^{1}H NMR (400 MHz, $CDCl_3$): δ 9.31 (s, 4H), 8.08 (s, 1H), 8.03 (d, *J* = 9.0 Hz, 1H), 8.00 – 7.95 (m, 2H), 7.76 – 7.67 (m, 3H), 7.44- 7.40 (m, 2H), 7.07 (d, *J* = 8.4 Hz, 2H), 4.05 (t, *J* = 6.5 Hz, 2H), 1.89 – 1.80 (m, 2H), 1.59 - 1.49 (m, 2H), 1.48 – 1.40 (m, 2H), 1.39 (s, 24H), 1.38 (s, 12H), 0.66 – 0.58 (m, 2H), 0.11 - 0.04 (m, 45H) ppm. ^{13}C NMR (100 MHz, $CDCl_3$) δ 159.26, 138.09, 133.18, 132.74, 132.45, 132.38, 131.52, 130.81, 130.71, 129.36, 128.83, 128.42, 126.62, 126.47, 126.45, 126.30, 126.20, 126.15, 126.13, 124.87, 118.56, 118.28, 115.16, 107.29, 107.20, 104.93, 104.86, 68.32, 32.05, 29.96, 29.87, 29.24, 23.29, 22.86, 19.18, 18.41, 14.28, 11.86, 1.96, 1.95, 1.37, 1.32, 1.32, 1.31, 1.27, 1.25, 1.21, 0.38, 0.16 ppm. MALDI-ToF-MS: m/z calc. for $C_{70}H_{112}O_7Si_9$ 1318.42 Da, found 1317.68 Da [M^+].

Pent-Si$_{15}$
Pentacene-pentene (26 mg, 0.03 mmol, 1 eq.), **HSi$_{15}$** (24 mg, 0.02 mmol, 0.67 eq.), dry DCM (3 ml), Karstedt's catalyst (2 drops). After column chromatography (pure heptane gradient to 40% chloroform in heptane), the compound was obtained as a dark green wax (21 mg, 48%). The compound has a purity of 95% with 5% unfunctionalized pentacene-pentene according to NMR.
^{1}H NMR (400 MHz, $CDCl_3$): δ 9.30 (s, 4H), 8.08 (s, 1H), 8.03 (d, *J* = 9.0 Hz, 1H), 8.00 – 7.95 (m, 2H), 7.76 – 7.67 (m, 3H), 7.44- 7.40 (m, 2H), 7.07 (d, *J* = 8.4 Hz, 2H), 4.04 (t, *J* = 6.5 Hz, 2H), 1.89 – 1.80 (m, 2H), 1.59 - 1.49 (m, 2H), 1.48 – 1.40 (m, 2H), 1.39 (s, 24H), 1.37 (s, 12H), 0.66 – 0.58 (m, 2H), 0.11 – 0.04 (m, 93H) ppm. ^{13}C NMR (100 MHz, $CDCl_3$) δ 159.26, 138.09, 133.18, 132.74, 132.45, 131.52, 131.12, 130.88, 130.81, 130.71, 129.36, 128.83, 128.42, 126.62, 126.46, 126.44, 126.30, 126.20, 126.15, 124.87, 118.56, 118.26, 115.16, 107.29, 107.20, 104.86, 68.32, 29.95, 29.24, 23.28, 19.17, 18.40, 11.86, 1.94, 1.58, 1.36, 1.33, 1.30, 1.25, 1.21, 0.84, 0.37, 0.15, -0.41 ppm. MALDI-ToF-MS: m/z calc. for $C_{89}H_{160}O_{15}Si_{17}$ 1911.66 Da, found 1910.57 Da [M^+].

Pent-Si$_{15b}$
Pentacene-pentene (48 mg, 0.06 mmol, 1 eq.), **HSi$_{15b}$** (103 mg, 0.09 mmol, 1.55 eq.), dry DCM (0.8 ml), Karstedt's catalyst (1 drop). After column chromatography (pure heptane gradient to 20% chloroform in heptane), the compound was obtained as a dark green wax (75 mg, 66%).
^{1}H NMR (400 MHz, $CDCl_3$): δ 9.30 (s, 4H), 8.08 (s, 1H), 8.03 (d, *J* = 9.0 Hz, 1H), 8.00 – 7.95 (m, 2H), 7.76 – 7.67 (m, 3H), 7.44- 7.40 (m, 2H), 7.07 (d, *J* = 8.4 Hz, 2H), 4.04 (t, *J* = 6.5 Hz, 2H), 1.89 – 1.80 (m, 2H), 1.59 – 1.49 (m, 2H), 1.48 – 1.40 (m, 2H), 1.39 (s, 24H), 1.37 (s, 12H), 0.61 – 0.55 (m, 2H), 0.11 – 0.04 (m, 93H) ppm. ^{13}C NMR (101 MHz, $CDCl_3$) δ 159.27, 138.10, 133.16, 132.74, 132.44, 132.37, 131.51, 131.12, 130.81, 130.70, 129.35, 128.82, 128.41, 126.62, 126.45, 126.30, 126.19, 126.15, 126.12, 124.85, 118.56, 118.26, 115.14, 107.28, 107.20, 104.85, 77.48, 77.16, 76.84, 68.33, 32.04, 29.84, 29.28, 23.06, 22.85, 19.17, 17.63, 14.28, 11.85, 1.94, 1.30, 1.30, 1.26, 1.24, 1.23, 0.16, -0.29 ppm. MALDI-ToF-MS: m/z calc. for $C_{89}H_{160}O_{15}Si_{17}$ 1911.66 Da, found 1910.58 Da [M^+].

Pent-Si$_{16}$-Pent
HSi$_{16}$H (33 mg, 0.03 mmol, 1 eq.), **pentacene-pentene** (53 mg, 0.07 mmol, 2.36 eq.), dry DCM (2 ml), Karstedt's catalyst (2 drops). After column chromatography (3 columns, pure heptane gradient to 20% DCM in heptane), the compound was obtained as a tough dark green wax (18 mg, 23%).
^{1}H NMR (400 MHz, $CDCl_3$): δ 9.30 (s, 8H), 8.08 (s, 2H), 8.03 (d, *J* = 9.0 Hz, 2H), 8.00 – 7.95 (m, 4H), 7.76 – 7.67 (m, 6H), 7.44 – 7.40 (m, 4H), 7.07 (d, *J* = 8.4 Hz, 4H), 4.04 (t, *J* = 6.5 Hz, 4H), 1.89 – 1.80 (m, 4H), 1.59 – 1.49 (m, 4H), 1.48 – 1.40 (m, 4H), 1.39 (s, 48H), 1.37 (s, 24H), 0.66 – 0.58 (m, 4H), 0.11 – 0.04 (m, 96H) ppm. ^{13}C NMR (101 MHz, $CDCl_3$) δ 159.27, 138.10, 133.16, 132.74, 132.44, 132.37, 131.51, 131.12, 130.81, 130.70, 129.35, 128.82, 128.41, 126.62, 126.45, 126.30, 126.19, 126.15, 126.12, 124.85, 118.56, 118.26, 115.14, 107.28, 107.20, 104.85, 77.48, 77.16, 76.84, 68.33, 32.04, 29.84, 29.28, 23.06, 22.85, 19.17, 17.63, 14.28, 11.85, 1.94, 1.30, 1.30, 1.26, 1.24, 1.23, 0.16, -0.29 ppm. MALDI-ToF-MS: m/z calc. for $C_{141}H_{230}O_{17}Si_{20}$ 2771.09 Da, found 2770.22 Da [M^+].

(DPA-Si$_{16}$)$_n$
9,10-bis(4-(pent-4-en-1-yloxy)phenyl)anthracene (193 mg, 387 µmol, 1 eq.), **HSi$_{16}$H** (454 mg, 387 µmol, 1 eq.), 2.6 mL dry DCM, Karstedt's catalyst (1 drop, and after 3h another drop). The product was purified by dialysis in THF to remove unreacted DPA. The product was obtained as a transparent light brown film (575 mg, 88% from maximum obtainable weight). The final product contained ~20% oxidized product.
^{1}H NMR (400 MHz, $CDCl_3$): δ 7.76 – 7.70 (m, 4H), 7.40 – 7.33 (m, 4H), 7.33 – 7.29 (m, 4H), 7.15 – 7.09 (m, 4H), 4.13 – 4.05 (m, 4H), 1.93 – 1.83 (m, 4H), 1.61 – 1.40 (m, 8H), 0.67 – 0.58 (m, 4H), 0.12 – 0.03 (m, 96H) ppm. ^{13}C NMR (100 MHz, $CDCl_3$): 159.25, 158.96, 140.92, 137.16, 136.14, 132.70, 131.27, 130.63, 128.99, 127.87, 127.42, 125.87, 125.16, 123.76, 114.72, 114.58, 84.29, 68.47, 34.59, 30.69, 30.24, 30.20, 30.06, 29.57, 29.49, 23.53, 23.51, 21.54, 18.63, 18.61, 1.78, 1.57, 1.46, 1.44, 1.41, 1.04, 0.59 ppm. ^{13}C NMR signal also contained the signals for the oxidized DPA core. MALDI-ToF-MS showed oligomer peaks at 1670.6 Da (DPA-Si$_{16}$), 2169.9 Da (DPA-Si$_{16}$-DPA), 3342.1 Da (DPA-Si$_{16}$-DPA-Si$_{16}$), 3841.4 (DPA-Si$_{16}$-DPA-Si$_{16}$-DPA), 5512.6 Da (DPA-Si$_{16}$-DPA-Si$_{16}$-DPA-Si$_{16}$-DPA). GPC: M_n = 10 kDa, M_w = 120 kDa, $Đ$ = 12.

6.4 References

(1) Lee, J.; Jadhav, P.; Baldo, M. A. *Appl. Phys. Lett.* **2009**, *95*, 10.
(2) Piland, G. B.; Burdett, J. J.; Dillon, R. J.; Bardeen, C. J. *J. Phys. Chem. Lett.* **2014**, *5*, 2312.
(3) Liu, H.; Jia, W. Y.; Zhang, Y.; Zhang, Q. M.; Lei, Y. L.; Lu, C. L.; Ling, Y. Z.; Xiong, Z. H. *Synth. Met.* **2014**, *198*, 6.
(4) Kolata, K.; Breuer, T.; Witte, G.; Chatterjee, S. *ACS Nano* **2014**, *8*, 7377.
(5) Smith, M. B.; Michl, J. *Chem. Rev.* **2010**, *110*, 6891.
(6) Yost, S. R.; Lee, J.; Wilson, M. W. B.; Wu, T.; McMahon, D. P.; Parkhurst, R. R.; Thompson, N. J.; Congreve, D. N.; Rao, A.; Johnson, K.; Sfeir, M. Y.; Bawendi, M. G.; Swager, T. M.; Friend, R. H.; Baldo, M. A.; Van Voorhis, T. *Nat. Chem.* **2014**, *6*, 492.
(7) Herz, J.; Buckup, T.; Paulus, F.; Engelhart, J.; Bunz, U. H. F.; Motzkus, M. *J. Phys. Chem. Lett.* **2014**, *5*, 2425.
(8) Giri, G.; Verploegen, E.; Mannsfeld, S. C. B.; Atahan-Evrenk, S.; Kim, D. H.; Lee, S. Y.; Becerril, H. A.; Aspuru-Guzik, A.; Toney, M. F.; Bao, Z. *Nature* **2011**, *480*, 504.
(9) Wan, Y.; Guo, Z.; Zhu, T.; Yan, S.; Johnson, J.; Huang, L. *Nat. Chem.* **2015**, *7*, 785.
(10) Zhu, T.; Wan, Y.; Guo, Z.; Johnson, J.; Huang, L. *Adv. Mater.* **2016**, *28*, 7539.
(11) Tayebjee, M. J. Y.; Schwarz, K. N.; MacQueen, R. W.; Dvořák, M.; Lam, A. W. C.; Ghiggino, K. P.; McCamey, D. R.; Schmidt, T. W.; Conibeer, G. J. *J. Phys. Chem. C* **2016**, *120*, 157.
(12) Jones, A. C.; Kearns, N. M.; Ho, J. J.; Flach, J. T.; Zanni, M. T. *Nat. Chem.* **2020**, *12*, 40.
(13) Pensack, R. D.; Grieco, C.; Purdum, G. E.; Mazza, S. M.; Tilley, A. J.; Ostroumov, E. E.; Seferos, D. S.; Loo, Y. L.; Asbury, J. B.; Anthony, J. E.; Scholes, G. D. *Mater. Horizons* **2017**, *4*, 915.
(14) Pensack, R. D.; Tilley, A. J.; Grieco, C.; Purdum, G. E.; Ostroumov, E. E.; Granger, D. B.; Oblinsky, D. G.; Dean, J. C.; Doucette, G. S.; Asbury, J. B.; Loo, Y. L.; Seferos, D. S.; Anthony, J. E.; Scholes, G. D. *Chem. Sci.* **2018**, *9*, 6240.
(15) Yablon, L. M.; Sanders, S. N.; Li, H.; Parenti, K. R.; Kumarasamy, E.; Fallon, K. J.; Hore, M. J. A.; Cacciuto, A.; Sfeir, M. Y.; Campos, L. M. *J. Am. Chem. Soc.* **2019**, *141*, 9564.
(16) Ohta, A.; Hattori, K.; Kusumoto, Y.; Kawase, T.; Kobayashi, T.; Naito, H.; Kitamura, C. *Chem. Lett.* **2012**, *41*, 674.
(17) Maranda-Niedbała, A.; Krzyżewska, K.; Kotwica, K.; Skórka, Ł.; Drapała, J.; Jarzembska, K. N.; Zagórska, M.; Proń, A.; Nowakowski, R. *Langmuir* **2020**, *36*, 15048.
(18) Anthony, J. E.; Eaton, D. L.; Parkin, S. R. *Org. Lett.* **2002**, *4*, 15.
(19) Wolff, S. K.; Grimwood, D. J.; McKinnon, J. J.; Turner, M. J.; Jayatilaka, D.; Spackman, M. A. *Crystal Explorer*; 2012.
(20) Okamoto, T.; Jiang, Y.; Becerril, H. A.; Hong, S.; Senatore, M. L.; Tang, M. L.; Toney, M. F.; Siegrist, T.; Bao, Z. *J. Mater. Chem.* **2011**, *21*, 7078.
(21) Yao, Y.; Zhang, L.; Orgiu, E.; Samorì, P. *Adv. Mater.* **2019**, *31*, 1.
(22) Krishna, G. R.; Devarapalli, R.; Lal, G.; Reddy, C. M. *J. Am. Chem. Soc.* **2016**, *138*, 13561.
(23) Cao, M.; Zhang, C.; Cai, Z.; Xiao, C.; Chen, X.; Yi, K.; Yang, Y.; Lu, Y.; Wei, D. *Nat. Commun.* **2019**, *10*, 1.
(24) Park, S. K.; Kim, J. H.; Park, S. Y. *Adv. Mater.* **2018**, *30*, 1.
(25) Shi, Y. L.; Zhuo, M. P.; Wang, X. D.; Liao, L. S. *ACS Appl. Nano Mater.* **2020**, *3*, 1080.
(26) Yang, F.; Cheng, S.; Zhang, X.; Ren, X.; Li, R.; Dong, H.; Hu, W. *Adv. Mater.* **2018**, *30*, 1702415.
(27) Wang, Z.; Jingjing, Q.; Wang, X.; Zhang, Z.; Chen, Y.; Huang, X.; Huang, W. *Chem. Soc. Rev.* **2018**,

47, 6128.
(28) He, Z.; Chen, J.; Li, D. *J. Vac. Sci. Technol. A* **2019**, *37*, 040801.
(29) Walker, B. J.; Musser, A. J.; Beljonne, D.; Friend, R. H. *Nat. Chem.* **2013**, *5*, 1019.
(30) Roberts, S. T.; McAnally, R. E.; Mastron, J. N.; Webber, D. H.; Whited, M. T.; Brutchey, R. L.; Thompson, M. E.; Bradforth, S. E. *J. Am. Chem. Soc.* **2012**, *134*, 6388.
(31) Pensack, R. D.; Tilley, A. J.; Parkin, S. R.; Lee, T. S.; Payne, M. M.; Gao, D.; Jahnke, A. A.; Oblinsky, D. G.; Li, P. F.; Anthony, J. E.; Seferos, D. S.; Scholes, G. D. *J. Am. Chem. Soc.* **2015**, *137*, 6790.
(32) Jiang, Y.; Hong, S.; Oh, J. H.; Mondal, R.; Okamoto, T.; Verploegen, E.; Toney, M. F.; McGehee, M. D.; Bao, Z. *J. Mater. Chem.* **2012**, *22*, 4356.
(33) Lamers, B. A. G.; Van Der Tol, J. J. B.; Vonk, K. M.; De Waal, B. F. M.; Palmans, A. R. A.; Meijer, E. W.; Vantomme, G. *Macromolecules* **2020**, *53*, 10289.
(34) Sakaino, H.; Meskers, S. C. J.; Meijer, E. W.; Vantomme, G. *Chem. Commun.* **2022**, *3*, 12819.
(35) Van Genabeek, B.; de Waal, B. F. M.; Gosens, M. M. J.; Pitet, L. M.; Palmans, A. R. A.; Meijer, E. W. *J. Am. Chem. Soc.* **2016**, *138*, 4210.

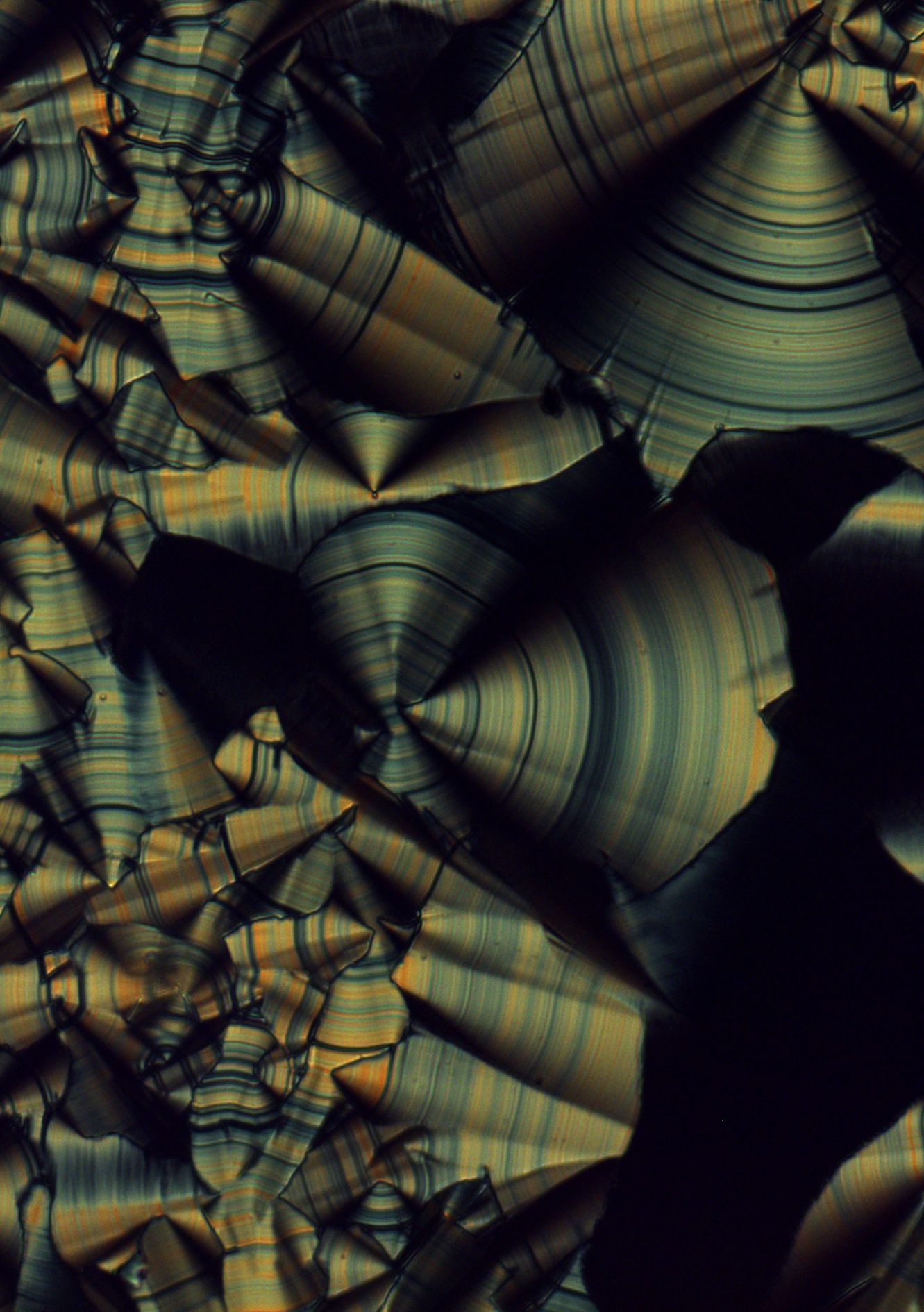

Summary

Understanding how to control the nanostructure of organic molecules is directly related to improving their performance in optoelectronic devices such as organic solar cells or transistors. For block copolymers (BCPs) and liquid crystals (LCs), hierarchically ordered nanostructures are formed via phase separation and supramolecular driving forces. Advances in processing techniques enabled the formation of monolayer crystals, which can transport energy more efficiently than the bulk material. Recently, another way to obtain nanoscale ordered materials has been developed using block molecules that consist of organic molecules attached to discrete length oligodimethylsiloxane (*o*DMS). For these block molecules, the order is induced through directional interactions of the organic molecules and phase separation with the *o*DMS. *o*DMS was chosen for its high χ parameter or immiscibility with many organic molecules. This makes functionalization with *o*DMS a general approach for well-defined nanostructures, although several fundamental design questions remain. Similar to 2D organic materials, the long-range order and well-defined nanodomains of these discrete block molecules are expected to enhance energy transport through the material. In this thesis, we study the structure-property relationship to enable rationalized design of discrete block molecules and show how their arrangement at the nanoscale improves energy transport.

Chapter 1 introduces how nanoscale ordering in materials can be controlled and how this can improve the resulting optoelectronic properties. To this end, 2D organic crystals, BCPs and LCs are introduced. The driving forces for ordering at the nanoscale are related to ongoing advances in materials processing. In addition, the main principles of discrete block molecules are discussed and the remaining open questions in this field are highlighted, leading to the aim of the research described in the thesis.

We describe how the molecular design of block molecules affects the formed nanostructure in **Chapter 2**. To this end, three molecular architectures are studied with either a central aromatic group with peripheral *o*DMS (core-centered), central *o*DMS with peripheral aromatic groups (telechelic) or an asymmetric design with a single aromatic group and single *o*DMS chain (head-tail). The *o*DMS length was varied to have a similar volume fraction for all block molecules of roughly 0.3, which would lead to columnar phases according to traditional BCP theory. The directional interactions of the rigid aromatic groups result in lamellar morphologies only when the *o*DMS fits the available space. The available space can be determined from reported crystal structures and should be at least 7 Å, the diameter of *o*DMS. While the *o*DMS can coil onto itself in the head-tail architecture, this is prevented in the telechelic architecture making the latter more reliable when targeting lamellar morphologies. The symmetry of the aromatic group was also studied by varying the peripheral alkyl length for the telechelic and head-tail architectures. Lamellar morphologies are only formed when the peripheral alkyl length matches the alkyl spacer between the *o*DMS and the aromatic group. The lamellar morphology formation is again explained by space-filling arguments. With shorter peripheral alkyls, the block molecules form columnar phases to minimize the free volume in the alkane region that would otherwise exist in a lamellar morphology. For the core-centered architecture with diphenylanthracene (DPA), the length of the alkyl spacer connecting the oDMS and the aromatic group was varied from C_4 to C_{11}. The highest thermal transitions and related enthalpies as well as the largest domain sizes upon slow

cooling from the melt were observed for a C_5 spacer. When assuming stretched alkyl spacers, free volume is introduced in the alkane region for C_6 to C_{11} as the cross-sectional area of alkanes is half that of *o*DMS. This leads to various co-existing nanostructures. This Chapter introduces how reported crystal structures can be used in the design of block molecules by considering space-filling arguments.

Chapter 3 focuses on the effect of mixing small molecules with block molecules to change their optical properties. To this end, arylene diimide block molecules are mixed with either non-functionalized arylene diimide or pyrene. The systems consisting of non-functionalized and *o*DMS-functionalized arylene diimide formed less-defined morphologies as compared to the mixtures with pyrene. This is ascribed through stronger interactions of the arylene diimide with pyrene due to charge transfer (CT) complexation. This CT formation caused a bathochromic absorption shift compared to the parent arylene diimide block molecules which is visually observed as a color change. Charge transfer complexation is also observed in mixtures with viologen block molecules, extending the observations to charged compounds. DPA block molecules were mixed with halogenated benzene rings that intercalate in the crystalline DPA layer, resulting in reduced photoluminescence quantum yields while retaining the same nanostructure. Moreover, we extend the space-filling arguments introduced in Chapter 2 to multicomponent systems.

The effect of ordering at the nanoscale on macroscopic properties is first shown in **Chapter 4**. Here, we report the differences between alkyl-functionalized and *o*DMS-functionalized carbonyl-bridged triarylamines (CBT). While the alkyl-functionalized CBT was amorphous, well-defined columnar stacks were formed after functionalization with *o*DMS. Here, the *o*DMS induces the required phase separation for the column formation while preventing interaction of adjacent columns that would otherwise lead to higher energetic disorder in the system. The columns were aligned in micrometer-sized domains resulting in highly polarized absorption and emission. The improved order after functionalization with *o*DMS results in high exciton mobilities usually found in crystals, but here in a thermal- and solution-processable material.

The well-defined nanoscale ordering of diphenylanthracene block molecules is explored in **Chapter 5** to study the effect of the ordering on the efficiency of photon upconversion (UC). The nanoscale ordering is retained upon mixing with dopant levels sensitizer molecules and the material can still form domains up to a centimeter in size. This enhanced order in the system compared to its unannealed state results in more efficient triplet energy migration (TEM) through the system. As such, the chance for triplet-triplet annihilation is enhanced, which leads to a 100-fold increase in the TEM-UC photoluminescence. Moreover, the large size of the domains resulted in linearly polarized upconverted emission.

In **Chapter 6**, we summarize the findings reported in this thesis on discrete block molecules, which allows for rationalization of their design, while highlighting how their nanoscale arrangement improves energy transfer. Moreover, using pentacene block molecules studied for their singlet fission properties, we report on outstanding fundamental questions and provide guidelines for future optoelectronic research directions.

Samenvatting

Voor het verbeteren van de optische en elektronische eigenschappen van bijvoorbeeld organische zonnecellen en transistoren, is het nodig om de relatie tussen deze eigenschappen en de nanostructuur van organische moleculen te begrijpen. Nanostructuren worden doorgaans gevormd door polymeren bestaande uit meerdere verschillende blokken, zogeheten blokcopolymeren (BCPs), of door vloeibare kristallen (liquid crystals, LCs). De nanostructuur in BCPs en LCs wordt gevormd door een combinatie van aantrekkende krachten tussen vergelijkbare blokken en het ontmengen van verschillende blokken die wel zijn verbonden. Bij kristallen is ontdekt dat 2D kristallen met de dikte van een enkel molecuul energie efficiënter kunnen transporteren dan een dikker 3D kristal. Onlangs is een manier ontwikkeld om de verbeterde eigenschappen van 2D kristallen te behouden in een 3D materiaal, door voort te bouwen op de kennis van BCPs en LCs. Hiervoor worden blokmoleculen gebruikt die bestaan uit organische moleculen die zijn gekoppeld aan korte dimethylsiloxane polymeren (*o*DMS) van een enkele lengte. Juist omdat *o*DMS totaal niet mengt met het organische molecuul waaraan het wordt gekoppeld, worden nanostructuren met een hoge mate van ordering gevormd. Eerder onderzoek naar blokmoleculen focuste op hoe precies geordende nanostructuren kunnen worden gemaakt en hoe dit kan leiden tot georiënteerde gebieden van meerdere tientallen micrometers. In dit proefschrift bouw ik voort op deze kennis, beantwoord ik enkele openstaande fundamentele onderzoeksvragen omtrent het moleculaire ontwerp van deze blokmoleculen en zet ik de eerste stappen naar hun toepassing.

Hoofdstuk 1 introduceert hoe nanostructuren kunnen worden gemaakt en hoe dit hun optische en elektronische eigenschappen verbetert. Vervolgens worden de eerder bestudeerde *o*DMS blokmoleculen en de openstaande onderzoeksvragen behandeld. In **Hoofdstuk 2** variëren we meerdere parameters van het moleculaire ontwerp van de blokmoleculen. Hieruit volgt dat we eerder gepubliceerde kristalstructuren kunnen gebruiken voor het moleculaire ontwerp door rekening te houden met de beschikbare ruimte voor de *o*DMS in de beoogde nanostructuur. **Hoofdstuk 3** focust op het mengen van blokmoleculen met chemisch andere kleine moleculen. Als beide moleculen sterke interacties aan kunnen gaan, kan de nanostructuur worden behouden terwijl de optische eigenschappen veranderen. Dit leidt tot ofwel een kleurverandering of minder efficiënte uitzending van licht. In **Hoofdstuk 4** laten we zien hoe de verhoogde orde op nanoschaal door de *o*DMS zorgt voor efficiëntere energieoverdracht tussen naburige moleculen. De gemeten energieoverdracht is hoger dan wat normaal wordt gevonden voor materialen die gemakkelijk verwerkt kunnen worden. De verhoogde orde op nanoschaal en de daardoor efficiëntere energieoverdracht wordt in **Hoofdstuk 5** bestudeerd met zonnecellen als beoogde toepassing. Licht met een lange golflengte kan normaliter niet door zonnecellen worden opgenomen, maar kan door fysische processen worden omgezet naar licht dat wel kan worden opgenomen. Deze omzetting is, vergeleken met een niet geordend systeem, 100 keer efficiënter nadat door de *o*DMS een hoge mate van orde is bereikt. Tot slot vat ik de eerdergenoemde conclusies in **Hoofdstuk 6** samen en benoem ik de nog openstaande onderzoeksvragen voor toekomstig vervolgonderzoek.

Curriculum Vitae

Martin van Son was born on April 24th, 1995 in Eindhoven, The Netherlands. After completing his secondary education at the Eckartcollege in Eindhoven in 2013, he studied Chemical Engineering at Eindhoven University of Technology (TU/e). During his bachelor's degree, he worked as a tutor for university Calculus and Nanotechnology, as well as high school Maths, Chemistry and Physics. Furthermore, he worked as an atomic force microscopy analyst and researcher of the Miller-Urey experiment in collaboration with the NEMO Science Museum, both in the group of prof. dr. E. W. Meijer. In this group, he concluded his bachelor's degree by synthesizing new block molecules and studying the effect of dispersity on their bulk self-assembly behavior. He then completed an internship in the research group of prof. dr. C. J. Hawker (University of California, Santa Barbara) on novel polymer synthesis. His graduation project in the group of prof. dr. E. W. Meijer focused on the synthesis of luminescent fluorene copolymers to elucidate the requirements for high chiral order. In addition, he did an industrial internship at Topsoe in Kongens Lyngby, Denmark, where he prepared, tested and improved homogeneous zeolite catalysts for the synthesis of renewable monomers. After obtaining his master's degree in 2018, he starter his PhD in the laboratory for Macromolecular and Organic Chemistry under the supervision of prof. dr. E. W. Meijer and dr. G. Vantomme. During this period, he focused on the requirements for obtaining highly ordered nanostructures using siloxane-based block molecules as well as how this order can improve their optoelectronic properties. The most important results are presented in this thesis.

Martin van Son is geboren op 24 april 1995 in Eindhoven. Nadat hij in 2013 zijn middelbare schoolopleiding aan het Eckartcollege in Eindhoven had afgerond, studeerde hij Chemical Engineering aan de Technische Universiteit Eindhoven (TU/e). Tijdens zijn bacheloropleiding werkte hij als tutor voor universitaire Calculus en Nanotechnologie, en gaf bijles in middelbare school wiskunde, scheikunde en natuurkunde. Verder werkte hij als atoomkrachtmicroscopie analist en onderzoeker van het Miller-Urey experiment in samenwerking met het NEMO Science Museum, beide in de groep van prof. dr. E. W. Meijer. In deze groep sloot hij zijn bachelor af met het synthetiseren van nieuwe blokmoleculen en het bestuderen van het effect van dispersie op hun bulk assemblage gedrag. Vervolgens liep hij stage in de onderzoeksgroep van prof. dr. C. J. Hawker (University of California, Santa Barbara), waar hij werkte aan nieuwe polymeersynthese. Zijn afstudeerproject in de groep van prof. dr. E. W. Meijer richtte zich op de synthese van lichtgevende fluoreen-copolymeren om de vereisten voor een hoge chirale orde te bestuderen. Daarna deed hij een industriële stage bij Topsoe in Kongens Lyngby, Denemarken, waar hij nieuwe homogene zeolietkatalysatoren bestudeerde voor de synthese van hernieuwbare monomeren. Na het behalen van zijn ingenieurstitel in 2018, startte hij zijn promotieonderzoek in het laboratorium voor Macromoleculaire en Organische Chemie onder supervisie van prof. dr. E. W. Meijer en dr. G. Vantomme. Tijdens deze periode richtte hij zich op de vereisten voor het verkrijgen van sterk geordende nanostructuren met behulp van siloxaan-gebaseerde blokmoleculen en hoe de hoge orde opto-elektronische eigenschappen kan verbeteren. De belangrijkste resultaten van dit onderzoek staan beschreven in dit proefschrift.

List of Publications

M.H.C. van Son, A.M. Berghuis, B.F.M. de Waal, F.A. Wenzel, K. Kreger, H.-W. Schmidt, J. Gómez Rivas, G. Vantomme, E.W. Meijer, Highly Ordered Supramolecular Materials of Phase-Separated Block Molecules for Long-range Exciton Transport, *Submitted*

M.H.C. van Son, B.W.L. van den Bersselaar, B.F.M. de Waal, G. Vantomme, E. W. Meijer, Targeting 2D Morphologies in Phase-Separated Materials through Molecular Architecture, *Manuscript in preparation*

M.H.C. van Son, M. Beslać, B.F.M. de Waal, G. Vantomme, E.W. Meijer, The Effect of the Alkyl Spacer Length on Block Molecule Morphology, *Manuscript in preparation*

T. Schnitzer, B.W.L. van den Bersselaar, B.A.G. Lamers, M.H.C. van Son, S.J.D. Maessen, F.V. de Graaf, B.F.M. de Waal, N. Trapp, G. Vantomme, E.W. Meijer, Crystal Lattice Analysis for Morphology Prediction of Phase-Separated 2D materials, *Manuscript in preparation*

M.H.C. van Son, A.M. Berghuis, F. Eisenreich, B.F.M. de Waal, G. Vantomme, J. Gómez Rivas, E.W. Meijer, Highly Ordered 2D-Assemblies of Phase-Segregated Block Molecules for Upconverted Linearly Polarized Emission, *Advanced Materials*, **2021**, *32*, 2004775

B.A.G. Lamers, M.H.C. van Son, F.V. de Graaf, B.W.L. van den Bersselaar, B.F.M. de Waal, K. Komatsu, H. Sato, T. Aida, J.A. Berrocal, A.R.A. Palmans, G. Vantomme, E.W. Meijer, Tuning the Donor-Acceptor Interactions in Phase-Segregated Block Molecules, *Mater. Horiz.* **2021**, *9*, 294

C. Kulkarni, M.H.C. van Son, D. Di Nuzzo, S.C.J. Meskers, A.R.A. Palmans, E.W. Meijer, Molecular Design Principles for Achieving Strong Chiroptical Properties of Fluorene Copolymers in Thin-Films, *Chem. Mater.* **2019**, *31*, 6699

A. Anastasaki, B. Oschman, J. Willenbacher, A. Melker, M.H.C. van Son, N. Phuoc Truong, M.W. Schultze, E.H. Discekici, A.J. McGrath, T.P. David, C.M. Bates, C.J. Hawker, One Pot Synthesis of ABCDE Multiblock Copolymers with Hydrophobic, Hydrophilic, and Semi-Fluorinated Segments, *Angew. Chem. Int. Ed.* **2017**, *56*, 14483

B. van Genabeek, B.A.G. Lamers, B.F.M. de Waal, M.H.C. van Son, A.R.A. Palmans, E.W. Meijer, Amplifying (Im)perfection: The Impact of Crystallinity in Discrete and Disperse Block Co-oligomers, *J. Ac. Chem. Soc.* **2017**, *139*, 14869

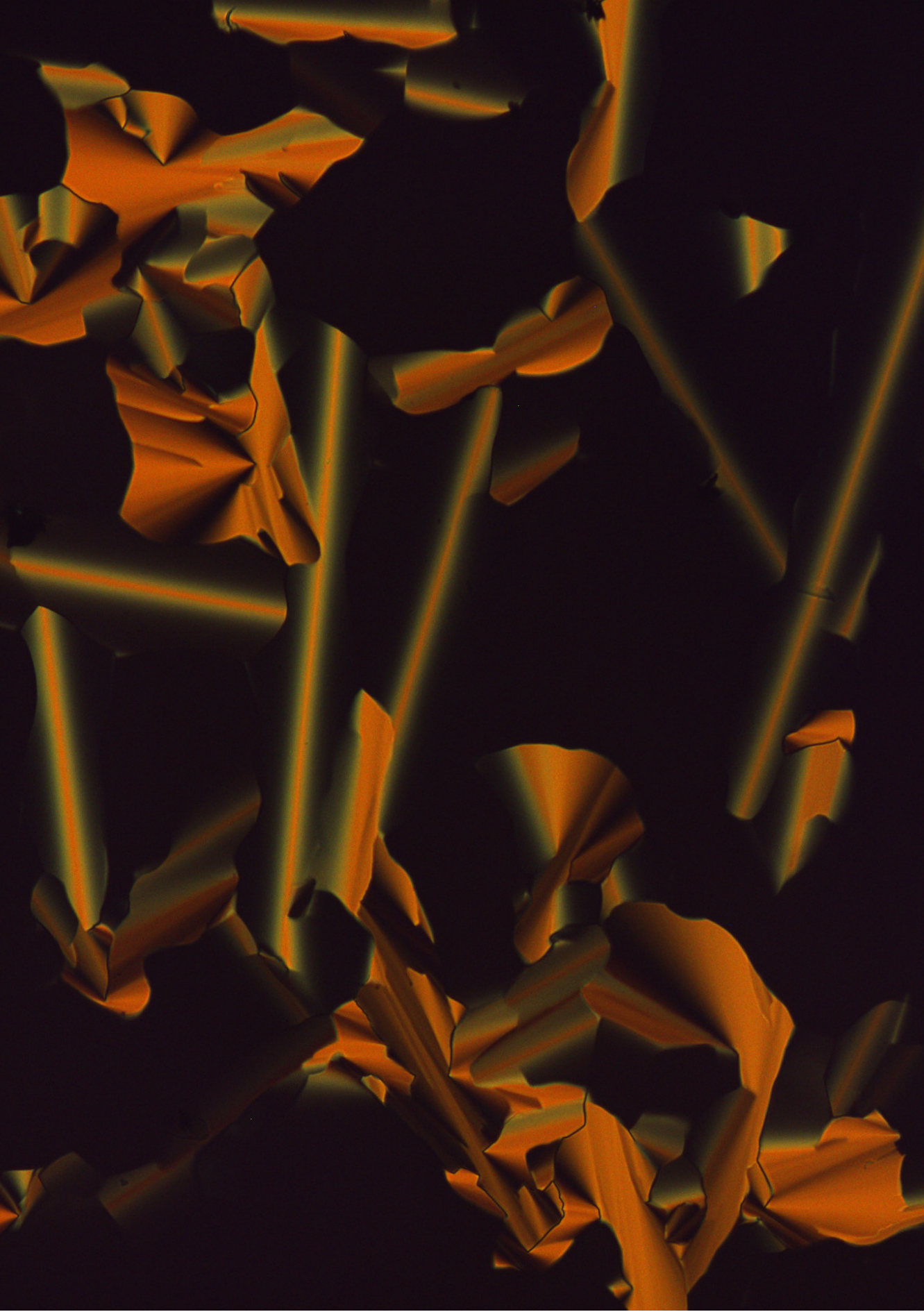

Acknowledgements | Dankwoord

De afgelopen 4 jaar ben ik omringd geweest met vele mensen die me zowel inhoudelijk, of juist niet inhoudelijk, enorm hebben geholpen. Ik wil jullie hier graag voor bedanken!

Allereerst wil ik graag *Bert* bedanken. Door de kans die je me gaf om een PhD te doen ligt dit proefschrift nu voor ons, waar ik met de nodige tegenslagen maar vooral met plezier aan heb mogen werken. Ik waardeer heel erg dat ik aan het eind van het eerste jaar mijn eigen plan mocht trekken en projecten mocht verzinnen. Door het vertrouwen in mij als onderzoeker heb ik met plezier en passie aan mijn zelf bedacht upconversion project kunnen werken, terwijl pas na de afronding bleek dat je initieel helemaal niet in dit project geloofde. Ik had dit project ook niet kunnen afronden als je me niet had geïntroduceerd bij de groep van Jaime Gómez Rivas waar ik met Matthijs de nodige uren heb doorgebracht om interessante metingen te doen. Bedankt in het vertrouwen in mij, zowel voor als tijdens mijn PhD. Ik heb veel kunnen leren en ik kijk er naar uit mijn kennis en vaardigheden toe te passen buiten de academische wereld.

Ghislaine, I would like to thank you for your contagious enthusiasm during discussions and for dreaming about what we could eventually achieve one day. You also helped me by being realistic and forward-looking whenever I walked into your office when something small had succeeded or failed. You were able to help me turn frustration into purposeful action. I wish you much success in the rest of your academic career, and I hope I meet another person as passionate as you in my next job.

I also would like to thank my committee. *Anja*, tijdens mijn bachelor project, master project en aan het begin van mijn PhD zat je er tijdens de lunchmeetings bij en wist je altijd verrassende, kritische vragen te stellen vanuit een andere invalshoek. Dit heeft mij geleerd om een stap terug te nemen en kritisch te kijken naar de vooruitgang, bedankt hiervoor. Ook wens ik je een goede toekomst toe voor de Palmans Research Group. *Jaime*, I can't thank you enough for opening the doors to your facilities and initiating the collaboration with Matthijs. Without all the work I have done in your lab, my research would only have been half the fun and this thesis would be half as interesting. I also want to thank you for your feedback on the manuscripts that followed the research in your lab. *Luis*, I want to thank you for your help with the upconversion project and your continuous enthusiasm in all the discussions that we had. Every time we talked, you were thinking about the bigger picture and came up with great ideas while staying realistic. I really enjoyed getting inspired by the topics your group worked on and I learned a lot from our collaborations. I also want to thank you again for your hospitality when I visited New York. *Stefan*, ik wil jou graag bedanken voor je hulp tijdens optische metingen en het vergroten van mijn begrip tijdens de daaropvolgende discussies als we data bespraken. Je deur stond altijd open en ik heb meer en sneller van je kunnen leren dan wat mogelijk zou zijn vanuit literatuur. Je manier van uitleggen vond ik enorm prettig omdat je altijd precies aanvoelde wat ik meteen snapte en wat iets meer aandacht nodig had. *Fabian*, you started as a post-doc in Berts group who helped me with the upconversion project and now you are in my committee as an assistant professor. Who could have known?

Thank you for your help and I wish you good luck in your new position. Furthermore, I would like to thank you for introducing me to acrylic pour art, which resulted in lots of nice paintings around my apartment and lots of fun whilst making them.

Bart, ook met jou heb ik veel samengewerkt, vooral richting het einde van mijn PhD. Hoe kon het ook anders als de enige twee PhD'ers die aan siloxanen werkten. Maar dat neemt niet weg dat ik de samenwerking ook erg prettig vond. Toen ik met het voorstel kwam om samen aan het architectuur project te werken, stond je daar meteen voor open. Je nam de helft van de synthese uit mijn handen, maar misschien wel meer dan de helft van het denkwerk omdat we het samen konden doen. Ik hoop dat je de opgedane kennis kan blijven gebruiken in de rest van jouw onderzoek. Uiteraard wil ik je ook bedanken voor de vele SAXS-metingen die je hebt gedaan. Succes met de rest van je PhD, je hebt mooie projecten in het verschiet om de fundamentele aspecten en toepassingen van siloxaan materialen verder te verduidelijken. Bedankt dat je mijn paranimf bent. Ajeto.

Marle, ook jou wil ik bedanken dat je mijn paranimf bent. Je bent iets later dan ik begonnen aan je PhD en je projecten waren totaal niet vergelijkbaar met die van mij. Maar we hebben juist wel altijd goed kunnen bespreken hoe het onderzoek doen verloopt met alle tegenslagen en successen. Ook bracht je een gezellige energie als we samen op het lab stonden, waarbij ik jouw muziekkeuze zeker kon waarderen. Ik hoop dat we blijven afspreken om bij te praten en spelletjes te doen en ik wens je enorm veel succes met het afronden van je eigen PhD.

Matthijs, zonder jou was dit boekje maar half zo dik en met een stuk minder diepgang. Door samen metingen te doen in het donkere lab in Flux kon ik daadwerkelijk de functie van mijn materiaal bestuderen, terwijl ik enorm veel leerde van de discussies die we tijdens de metingen voerde. Ik vond het ook erg leuk om met je samen te werken en van je te leren, waardoor het helemaal niet erg was dat we regelmatig samen metingen aan het doen waren die net zo goed door een persoon gedaan konden worden. We zijn meerdere projecten samen gestart en ik heb altijd gevonden dat we de projecten echt samendeden. Je was nieuwsgierig naar de scheikundige kant van zaken terwijl je mij nieuwsgierig bleef maken naar jouw onderzoek en perspectief. Hierdoor hebben we twee mooie manuscripten kunnen afronden en heb ik veel van je kunnen leren. Bedankt!

Bas, ik kan met zekerheid zeggen dat dit boekje leeg zou zijn zonder jou. Tijdens mijn bachelor project werkte ik al met de siloxanen die jij had gemaakt en ik vind het enorm leuk om te zien hoe de blok moleculen zijn geëvolueerd naar daadwerkelijke functie, allemaal geïnitieerd door jouw synthese vaardigheden. Ook wil ik je bedanken voor je aanstekelijke, zichtbare passie voor siloxanen tijdens de lunchmeetings. Dit uitte zich ook toen ik vroeg om vertakte siloxanen, die je toen in mum van tijd had gemaakt. Bedankt Bas, niet alleen voor je hulp met de synthese, maar ook voor het plezier wat je hebt gebracht.

Dat ik zo goed mijn onderzoek heb kunnen doen komt ook omdat de groep goed draaiende gehouden wordt door *Carla*, *Martina* en *Margot*. Ik wil jullie hiervoor bedanken. Specifiek wil ik Carla bedanken omdat je altijd wel een gaatje wist te vinden in de drukke agenda van Bert en het altijd erg gezellig was als ik op je kantoor moest wachten voordat Bert tijd had voor onze meeting.

Lou, I want to thank you for keeping the recycle GPC running and trying to get it to work as fast as possible when it was broken. Especially when I found our results make more sense after the molecules are purified by recycle GPC, the functioning of the GPC was paramount for my research. Thanks for always being helpful and kind.

Ook wil ik graag de mensen helpen die me hebben geholpen met mijn experimenten. Allereerst *Jolanda*, bedankt dat je ervoor zorgde dat lab 2 altijd in de beste staat was om in te werken en dat we 's ochtends de dag goed begonnen met het het foute uur. *Brigitte*, jou wil ik bedanken voor de discussies aan het begin van mijn PhD, de samenwerking tijdens het NDI-pyrene project en natuurlijk de SAXS-metingen die je voor me hebt gedaan. *Chidambar*, after teaching me how to be an independent researcher during my master project, you kept guiding me throughout the beginning of my PhD. This really helped me to keep my focus on the goal of the project when things were not working out in the lab. *Sandra*, ook aan jou heb ik enorm veel gehad aan het begin van mijn PhD. Je zorgde voor enorm veel gezelligheid (en lekkere baksels) en wist dagen vol frustratie toch een leuk randje te geven. Ik waardeer het enorm dat we blijven afspreken. *Christiaan*, omdat we tegelijk waren begonnen aan onze PhD liepen we vaak tegen dezelfde dingen aan. Ik vond het enorm fijn om dit proces te kunnen delen en van elkaar te kunnen leren. Ik ben blij dat je een mooie baan bij ASML hebt gevonden waar je vaardigheden goed tot recht komen.

I would also like to thank the students that helped me with the synthesis of the diphenylanthracene molecules. *Sachi*, you did the initial synthesis for the upconversion project when you came here as a summer intern. Although the progress was slower than we both expected, it helped me understand what didn't work synthetically. You were the start of the successes during my PhD for which I am grateful, and I hope that you also enjoyed your stay in Eindhoven. *Marko*, I also would like to thank you for all the hard work you did in the lab. Although it took some time before we found the right method to make our molecules because the MALDI was broken, in the end we managed to synthesize and study all of them. Good luck with the rest of your research efforts that, based on your independence and knowledge already during your bachelor studies, will lead to very interesting discoveries.

Dino, during your stay in Eindhoven we started some projects together and I really enjoyed having you in the lab as a collaborator. I would also like to thank you again for hosting me when I came to New York.

Verder wil ik ook graag *Tom*, *Sterre* en *Lisette* bedanken voor de wekelijkse gezelligheid tijdens de cohortlunch samen met Marle. Het was altijd erg fijn om een vast moment in de week te hebben om met jullie bij te praten. Ik heb daar erg van genoten

en vind het jammer dat we dit niet kunnen blijven voortzetten. Tom, ik wens je enorm veel succes toe in Zweden, maar vooral plezier. Ook wil ik je nog bedanken voor de inhoudelijke discussies die we konden voeren over mijn optische metingen. Sterre, het blijft altijd leuk om met jou en Olivier spelletjes te spelen en ik hoop dat we dat ook zullen doen in jullie nieuwe huis. Heel veel plezier met je nieuwe baan. Lisette, jou wil ik enorm veel succes wensen voor de rest van je PhD en ik weet zeker dat ze in jou een goed persoon hebben gekozen om te helpen met de onderwijshervormingen.

Of course, I would also like to thank the rest of the people in the group. *Stef* and *Freek*, ik leerde jullie kennen tijdens jullie afstuderen en toen al kon ik jullie humor en vrolijkheid waarderen. *Joost*, we hebben samen de AFM-cursus gedaan en ik heb je leren kennen als enorm gemotiveerd en ondernemend persoon die altijd een feestje op gang kan brengen, nadat je zelf een biertje hebt gehad. *Magda* and *Marco*, I started a project with the both of you individually, but the results and synthesis were not really as we hoped. However, it was very nice to work with you and to discuss the next steps. *Tobi*, thank you for taking the lead in the CrystalExplorer project. I hope we can send it somewhere nice once it is finished. Good luck with your new position as a group leader. *Anjana*, *Linlin* and *Stefan*, I would like to thank you for always being calm and happy in the lab and making the atmosphere pleasant to work in. I'd also like to thank all the people I've got to meet during my PhD for your input and memorable time: *Simone, Lafayette, Jesús, Hao, Laura, Shikha, Fan, Giulia, Huachuan, Diederik, Roy, Eveline, Annelore, Roy, Paul, Muhabbat, Andreas, Elisabeth, David, Hailin, Osamu, Tessa, Piers, Rik* en *Esmee*.

Uiteraard wil ook alle vrienden buiten het lab bedanken voor de gezellige avonden en weekenden! Hoewel het niet altijd over mijn PhD ging, hielp jullie aanwezigheid zeker mee door de nodige ontspanning te brengen. Bedankt *Appie, Carlos, Ward, Lotte, Maartje, Saske, Yaëll, Ward, Sanne* en *Tim* voor de vriendschap al sinds de middelbare school. Bedankt *Joost, Wouter, Esmee* en *Bram* voor de gezellige braspartijen. Bedankt *Max, Wouter, Inge, Youri, Silvie, Jaimie, Annemarie* voor de gezellige dansmomenten.

Uiteraard wil ik ook graag mijn *ouders*, *Henri* en *Ilona* en de rest van de *familie* bedanken voor de steun en interesse, hoewel het niet altijd duidelijk zal zijn geweest wat ik precies aan het doen was.

Naomi, zonder jou had ik het niet gekund. Als het tegenzat op het lab kon je me altijd weer laten ontspannen door me het werk tijdelijk los te laten. Door jou danste ik door mijn PhD en hebben we zoveel moois mee kunnen maken wat ik anders nooit zelf zou hebben ondernomen. Bedankt voor je onvoorwaardelijk steun en dat je me helpt waar je ook maar kan.

Martin